



UNIVERSITA' DEGLI STUDI DI NAPOLI "FEDERICO II"

Di.S.T.A.R. - Department of Earth Sciences, Environment
and Resources Sciences

Doctorate School in

GROUND DEFORMATION ANALYSIS IN APENNINE AREAS,
SEISMICALLY ACTIVE OR ASEISMIC, USING DATA FROM SAR
INTERFEROMETRY AND INTEGRATION OF GEOMORPHOLOGICAL AND
STRUCTURAL DATA.

XXXI Cycle

Ph.D. Thesis

student: Sergio Nardò

Advisors:

Prof. Alessandra Ascione

Coordinator of Doctorate School:

Prof. Maurizio Fedi

Co-Advisor:

Prof. Domenico Calcaterra

Prof. Stefano Mazzoli

Summary

Summary	2
ABSTRACT	4
CHAPTER 1 - INVESTIGATION OF GROUND DEFORMATION.....	7
1. INTRODUCTION	7
1.1. Objectives	8
1.2. Short Historical Compendium about thesis' topics	9
1.3. Previous personal experience with the PS technique and the reason why a PhD project about this topic	10
CHAPTER 2 - MATERIALS AND METHODS.....	12
2.1 Earth Observation with Synthetic Aperture Radar (SAR)	12
2.1.1 Satellite missions	12
2.2 Advanced DInSAR techniques	15
2.2.1 Potential and limitations of multi-interferogram techniques	17
2.2.2 Interferogram stacking techniques	18
2.3 PS (Persistent Scatterers)-based or PSI (Persistent Scatterer Interferometry) techniques	18
2.3.1 SAR acquisition geometry.....	20
2.4 Extraordinary Plan of Environmental Remote Sensing (PST-A) by Ministry of the Environment and Territory and Sea Protection (MATTM).....	22
2.5 Basic statistics	23
2.6 PSs data mining. How make selection in a large dataset.....	27
2.6.1. PSs Classification using frequency distribution	27
2.6.2. PSs mean velocity values spatial clustering	29
2.6.2.1 Hot Spot Analysis mapping tool (Getis-Ord G_i^*).....	29
2.6.2.2 Cluster and Outlier Analysis mapping tool (Anselin Local Moran's I).....	30
2.7 Map interpolation: IDW method	31
2.8 Time series.....	32
2.9 Selection, Analysis and Mapping Procedures in the various case studies	32
CHAPTER 3 - GEOLOGICAL FRAMEWORK	34
3.1 The Apennines tectonic framework.....	34
3.2 Seismotectonic framework of the Apennines	38
3.3 Structural setting	42
3.3.1 Structure of the Northern Apennines	43
3.3.2 Structure of the central Apennines	44
3.3.3 Structure of the southern Apennines.....	46
CHAPTER 4 - INVESTIGATION OF POST-SEISMIC GROUND DEFORMATION: THE 1980 IRPINIA EARTHQUAKE CASE STUDY	49
4.1 Introduction	49
4.2 Geological framework.....	53
4.3 Data analysis: construction of ground deformation maps based on PSs mean vertical velocity....	53

4.3.1 IDW analysis of “native” PS datasets.....	53
4.3.2 Geospatial analysis: Hot Spot and Cluster and Outlier.....	56
4.4 Discussion and Concluding remarks.....	67
CHAPTER 5 - INVESTIGATION OF PRE-SEISMIC GROUND DEFORMATION IN THE 1997 COLFIORITO EARTHQUAKE	70
5.1 Geological framework.....	70
5.2 Seismotectonic and SAR remote sensing background of the 1997 Colfiorito earthquake.....	72
5.3 PSs and time series analysis in Colfiorito earthquake area.....	74
5.4 Discussion and Concluding remarks.....	76
CHAPTER 6 - INVESTIGATION OF PRE-SEISMIC GROUND DEFORMATION IN THE 2009 L'AQUILA EARTHQUAKE	77
6.1 Seismotectonic and SAR Remote Sensing background of the 2009 L'Aquila earthquake.....	77
6.2 Materials and method.....	78
6.3 Results	80
6.3.1 ERS dataset analysis.....	80
6.3.2 ENVISAT dataset analysis.....	80
6.4 Discussion and concluding remarks.....	83
CHAPTER 7 - INVESTIGATION OF PRE-SEISMIC GROUND DEFORMATION IN THE 2013 LUNIGIANA EARTHQUAKE	86
7.1 Geologic and tectonic setting	86
7.2 Materials and method.....	88
7.2.1 Time series.....	89
7.3 Discussion and Concluding remarks	91
CHAPTER 8 - INVESTIGATION OF A-SEISMIC GROUND DEFORMATION IN THE CAMPANIA PLAIN	92
8.1 Introduction	92
8.2 Geological framework.....	92
8.2 Geomorphological analysis of the northern sector of the Campana Plain	99
8.2.1 The Volturno Plain	100
8.2.2 The Canello Plain.....	102
8.3 PSs vertical Vmean, ground deformation maps of Fiume Volturno Campana Plain.....	103
8.4 ERS Time Series analysis	115
8.5 ENVISAT Time Series analysis.....	119
8.6 Discussion.....	122
8.7 Discussion and Concluding remarks	125
CHAPTER 9 - CONCLUDING REMARKS.....	126
REFERENCES	128
Aknowledgements	154

ABSTRACT

The core of the study herein has been the analysis of PS-InSAR datasets aimed at providing new constraints to the active tectonics framework, and seismotectonics, of several regions of the Apennines. The analysed Permanent Scatterers datasets result from processing of large amounts of temporally continuous series of radar images acquired with the ERS (1992-2000), ENVISAT (2003-2010) and COSMO SKYMED (2011-2014) satellite missions. Such datasets, which are available in the cartographic website (Geoportale Nazionale) of the Italian Ministry of Environment (MATTM) have been collected through time by the MATTM in the frame of the "Extraordinary Remote Sensing Plan" (Piano Straordinario di Telerilevamento Ambientale, PST-A, law n. 179/2002 - article 27), with the aim of supporting local administrations in the field of environmental policies. The database was realized through three phases: the first one (2008-2009), which involved the interferometric processing of SAR images acquired throughout the country by the ERS1/ERS2 and ENVISAT satellites in both ascending and descending orbits, from 1992 to 2008; the second one (2010-2011) integrated the existing database with the processing of the SAR images acquired by the ENVISAT satellite from 2008 to 2010; the third phase (2013-2015) provided an upgrading and updating of the previously developed database on critical areas, based on StripMap H image acquired with a 16-day recurrence, either in ascending or descending orbit, using the Italian national satellite system, the COSMO SKYMED.

With this study, a massive use of Permanent Scatterer datasets is applied for the first time at assessment of ground deformation of large (hundreds of km² wide) regions of Italy over the last decades, in order to unravelling their current tectonic behaviour. To date in the field of tectonics – in particular, of earthquake geology - the SAR images have been used essentially through the DinSAR technique (comparison between two images, acquired pre- and post-event) in order to constrain the co- and post-seismic deformation (Massonet et al., 1993; Peltzer et al., 1996, 1998; Stramondo et al., 1999; Atzori et al., 2009; Copley and Reynolds, 2014), while the approach that has been used in the case studies that are the object of the research herein is based on analyses of data that (with the exception of the Lunigiana case study) cover an about 20-year long time window. The opportunity of analysing so long, continuous SAR records has allowed detection of both coseismic displacement of moderate earthquakes (i.e., the M 6.3 2009 L'Aquila earthquake, and the M 5 2013 Lunigiana earthquake), and subdued ground displacements - and acceleration – on time scale ranging from yearly to decades.

The specific approach used in this study rests on a combination of various techniques of analysis and processing of the PS datasets. In general, as the analyses that have been carried out aimed at identifying motion values with wide areal extent, a statistical filtering has been applied to PSs velocity values in order to discard from the initial, "native", dataset fast-moving PSs that may be associated with the occurrence of local-scale phenomena (e.g., landslides, sediment compaction, water extraction, etc.). Furthermore, an in depth inspection of time series of PSs from all of the investigated areas has been carried out with the aim of identifying changing (LoS-oriented) motion trends over the analysed time windows.

A distinctive feature of this study was the estimation of vertical ground displacements. In fact, while most studies on ground deformation are based on analysis of SAR data recorded along either ascending or descending satellite orbits (thus based on LoS-oriented motions), a specific focus of this study was to obtain - starting from LoS-oriented PS velocity values - displacement values in the vertical plane oriented west-east. In order to evaluate vertical displacements, a geometrical relationship was applied to ascending - descending PSs pairs. As PS from ascending and descending tracks are neither spatially coincident nor synchronous, each image pair was obtained by selecting ascending-descending radar images with a time separation within one month. In the L'Aquila region case study, the combination of data recorded along both the ascending and descending satellite orbits has been crucial to the identification of pre-seismic ground motions, undetected in previous works that – similarly – had addressed assessment of possible pre-seismic satellite-recorded signals.

In the various case studies, different kinds of GIS-aided geostatistical analyses were used to extract and synthesise information on ground deformation through the construction of both raster maps of displacement values for the ascending and descending LoS, respectively, and maps of the vertical (z, up - down) component of the "real" displacement vector.

In the Campania plain case study, the PS-InSAR data analysis and processing have been integrated by detail scale geomorphological-stratigraphical analysis. Results of analyses of the two independent data sets are consistent, and point to tectonically-controlled ground displacements in a large part of the northern part of the study area (Volturno plain) during the 1992-2010 analysed time span. In particular,

the integrated data sets show that the boundaries of the area affected by current subsidence follow fault scarps formed in the 39 ka old Campania Ignimbrite, while the horst blocks of such faults are substantially stable (or slightly uplifting) during the analysed time window.

Furthermore, mean rates of current subsidence and long-term (Late Pleistocene to present) mean subsidence rates are comparable, pointing to current vertical displacement assessed through the PS-InSAR data analysis as the expression of the recent tectonics of the analysed sectors of the Campania plain. The Campania plain substantially lacks strong historical seismicity. Such evidence suggests that the detected surface displacements result at least in part from aseismic fault activity.

The Monte Marzano case study has allowed assessment of subdued deformation along both the major structures that were activated with the Irpinia 1980 earthquake, i.e. the NE-dipping Monte Marzano fault and the SW-dipping Conza fault, respectively. Ground deformation associated with such structures appears decreasing from the time window covered by the ERS satellites (1992-2000) to that covered by the ENVISAT (2003-2010). These data suggest that post-seismic slip of the M 6.9 has continued until 20 years after the main shock to become very weak in the following ten years. Furthermore, the PS-InSAR data analysis has shown that wide areas located between the Monte Marzano and Conza faults (i.e., in the one that is recognised as the graben structure bounded by those structures) show uplift in the range of 0-2 mm/yr, more evident in the period surveyed by the ERS satellites (1992-2000) and less evident in the 2003-2010 time span (ENVISAT). Such uplift might be related to the occurrence, at depth, of a fluid reservoir that has been independently identified by seismic tomography (Amoroso et al., 2014).

In depth analysis of pre-seismic periods have been carried out in three study areas, i.e. those of the 1997 Colfiorito earthquake, of the 2009 L'Aquila earthquake and of the 2013 Lunigiana earthquake.

The Colfiorito case study has not provided any significant information on possible pre-seismic ground deformation, most probably due to the PS spatial distribution in that region too much discontinuous to allow identification of both net signals from inspection of the rare and sparse PS time series, and statistically meaningful surface displacement patterns.

Both in the L'Aquila and Lunigiana case studies, ground deformation signals in the pre-seismic period have been detected from inspection of PS time series. Pre-seismic ground deformation signals detected in the Lunigiana area (which was affected by a strike-slip faulting earthquake; Eva et al., 2014, Pezzo et al., 2014, Stramondo et al., 2014) are questionable, as they are quite complex and difficult to be interpreted and framed within the local tectonic scenario.

Conversely, very clear and net pre-seismic signals have been identified in the region hit by the L'Aquila normal faulting earthquake. There, in the time span predating of some four years the 6th April 2009 main shock, ground deformation with distinct spatial patterns, and orientations, have been detected. In particular, the PS-InSAR analysis has shown that the hanging wall block of the Paganica fault (the surface expression of the structure activated with the main shock; e.g., Galli et al., 2010) has been subject to slow uplift and eastward horizontal motion from 2005 to September/October 2008, and then (October 2008-March 2009) subject to subsidence and westward oriented horizontal motion. Following coseismic collapse, in the early post-seismic period (April-May 2009), subsidence extended eastwards beyond the Paganica fault trace.

The region affected by opposite pre-seismic motions covers the area in which the 6th April main shock and most of both foreshocks and aftershocks (Valoroso et al., 2013) were recorded, while the inversion of the pre-seismic displacements is coeval with onset of the foreshocks (October 2008; Di Luccio et al., 2010). In addition, such a region includes both topographic highs and lows. All of such features point to a correlation of the detected motions with the seismic phenomena, and suggest a deep-seated causative mechanism, such as volume changes in response to vertical/lateral fluids migration and fracturing processes at depth, with all phenomena having been documented in connection with the 2009 earthquake in the study region (e.g., Di Luccio et al., 2010; Lucente et al., 2010; Moro et al., 2017).

Pre-seismic ground deformation that has been detected in the L'Aquila region could represent a precursor signal of the 2009, M 6.3 earthquake. Such a hypothesis should be tested, in the future, through the continuous monitoring through SAR satellites, but also high-resolution geodetic techniques, of seismically active regions worldwide aimed at detecting the possible occurrence of pre-seismic signals.

However, the results of this study point to the long-term (yearly scale) PS-InSAR technique as a tool crucial to the detection of ground deformation in areas struck by recent earthquakes, and to monitoring active – possibly aseismic - structures. Such knowledge may strongly support strategies addressed at territorial planning and mitigation of seismic hazard, and represent an important sustenance for actions ruled by Civil Protection. On the other hand, the results of this study highlight the importance of the existing PS database, and the importance of continuing implementing such an instrument in the future.

CHAPTER 1 - INVESTIGATION OF GROUND DEFORMATION

1. INTRODUCTION

Remote sensing data by SAR interferometry (InSAR) provide a one-dimensional measurement of change in distance along the look direction of the radar spacecraft (Line of Sight or LoS) for two orbit geometries, ascending and descending, whose combination results are two - vertical and horizontal - displacement vectors in a vertical plane east-west oriented. Similarity between maps of LoS displacement rate from ascending and descending tracks suggest that the observed displacements may be interpreted as reflecting mostly vertical surface displacement or, conversely, LoS displacements in opposite directions, approaching and moving away from satellite, indicate a horizontal component presence.

Such a technique is largely used to detect and monitor ground deformations induced by landslides, volcanism, tectonics and anthropic processes in urbanized areas (Massonnet et al., 1993; Achache et al., 1995; Carnec et al., 1996; Fruneau et al., 1996; Kimura & Yamaguchi, 2000; Berardino et al., 2002; Corsini et al., 2006; Tizzani et al., 2007; Vilardo et al., 2009, Di Martire et al., 2017).

The development of new techniques, based on the analysis of large datasets and, more in general, the Advanced Differential SAR Interferometry approach (A-DInSAR), has significantly increased the potential of SAR remote sensing for ground deformation detection. The SAR technique has proved to be a powerful tool for exploring the slow motion of the Earth's surface at local (Ferretti et al., 2000; Prati et al., 2010) and sub-regional scale (Bürgmann et al., 2006; Corsini et al., 2006; Meisina et al., 2006). The SAR technique has also provided fundamental constraints to modelling of earthquake source mechanisms (e.g., Stramondo et al., 1999; Atzori et al., 2009; D'Agostino et al., 2012; Cheloni et al., 2017). Such a technique is also well suited for the detection of ground deformation possibly predating seismic events, a task crucial to forecasting strategies based on the search for diagnostic precursor signals of severe earthquakes (Jordan et al., 2011). In recent years, research has been pushed forward towards the identification of pre-seismic ground deformation patterns through the use of SAR-based techniques, which are being acknowledged among the most promising tools for the search of earthquake precursors (Moro et al., 2017). Within such a framework, the interferometric Extraordinary Environmental Remote Sensing Plan (PST-A) archive, by Italian Ministry of the Environment (MATTM), retains the millimetre ground deformation data that could be, actually, the most important marker of accumulation of crustal seismogenic stress. Such a dataset may provide fundamental information on the pre-seismic phase of moderate to strong earthquakes that have hit Italy in recent years.

The ground deformation mechanisms that characterize a seismic cycle can provide information about the possible earthquake genetic causes. A great earthquake instantaneously disturbs the existing stress balance within the crust.

Knowledge of how the resultant stress concentrations are relaxed, both temporally and spatially, can that Postseismic transients with durations of a few months to years are seen by Peltzer et al. (1996, 1998) and Savage and Svarc (1997) using Synthetic Aperture Radar (SAR) and Global Positioning System (GPS) data.

Copley and Reynolds, 2014, have measured surface displacements post-seismic signal, from 2 to 16 years following the 1994 Sefidabeh earthquake sequence in east Iran, using Differential Interferometry SAR (DInSAR) data from the ERS and Envisat satellites on descending track only.

Geodetic data spanning the first decades after an event are more likely to provide information about long period relaxation of structures in the crust. The problem is that post-seismic data of this temporal extent are generally unavailable because of the relatively recent advent of sufficiently accurate geodetic measurement

The post-seismic deformation following an earthquake can be measured with terrestrial geodetic stations. Such measurements, in the context of a recurring seismic cycle, actually can be obtained with the dense spatial coverage provided by satellite radar interferometry (Massonnet et al., 1994).

Italy has a medium-high seismic hazard (due to the frequency and intensity of phenomena), very high vulnerability (due to the fragility of building, infrastructural, industrial, production and service assets) and an extremely high exposure (due to population density and its historical, artistic and monumental heritage that is one of its kind in the world). Our peninsula therefore has a high seismic risk, in terms of victims, damage to buildings and direct and indirect costs expected after an earthquake.

In Italy we have numerous studies and documents regarding the seismicity of our peninsula, representing a historic heritage that is without equal worldwide. In the nineteenth century, with the development of seismological sciences, the research into the causes and geographic distribution of earthquakes started to

be published. Wider use of seismic instruments from the end of the nineteenth century and monitoring networks in the twentieth century finally provided input for studies into seismic characterisation in Italy. Science today is not yet able to forecast the exact time and place for future earthquakes. The only forecast possible is of a statistical kind, based on knowledge of past seismicity in Italy therefore on the recurrence of earthquakes. We know which areas in the country run a high seismic risk, for earthquake frequency and intensity and therefore where it is most likely that a big seismic event will happen, but it is not possible to exactly determine when it will happen.

Over recent years science has made considerable progress in the study of seismic precursors, in other words the chemical and physical parameters of the ground and underground subject to the variations that can be observed before an earthquake happens. In the future, systematic study of these precursors could allow the initial moment of the earthquake to be fixed, even if false alarms must be avoided, which could prove to be even more harmful.

Research into earthquake precursors has concentrated on:

- Seismological precursors: before a big seismic event a series of microtremors may occur, only detectable by instruments.
- Geophysical precursors: anomalies in the P and S wave speeds, variations in magnetic and electric characteristics of rocks.
- Geochemical precursors: variation in underground waters of the concentration of some chemical elements, in particular of radon, a radioactive gas.
- Geodetic precursors: alterations in the level and slope of ground surface.

Forecasting of earthquakes based on precursors has so far brought disappointing contradictory results. No precursor happens regularly before each important earthquake, for this reason research is moving towards simultaneous observation of different phenomena.

1.1. Objectives

The objectives of the thesis concern the possibility to identify, through the use of more or less recent technologies and techniques of remote sensing (over 20 years of applications), the deformations that the Earth's surface undergoes through the seismic cycles (inter-, pre-, co- and post-seismic) in seismogenic areas and, sometimes, in aseismic ones.

The Ministry of the Environment and Territory and Sea Protection (MATTM), in the context of the Extraordinary Plan of Environmental Remote Sensing (PST-A), have a representative "historical" database of the national territory (see par. 5.), containing the measurements of ground movements obtained by means of SAR interferometry, available through the MATTM National Cartographic Portal (<http://www.pcn.minambiente.it/mattm/progetto-pst-prodotti-interferometrici/#9>).

The database realization was assigned by the MATTM to the temporary business grouping by e-GEOS S.p.A., as the parent company, and by the Telerilevamento Europa T.R.E. s.r.l and Compulab s.r.l.

The database was obtained by processing ERS 1/2, ENVISAT images, acquired between 1992-2000 and 2003-2010 by ESA, with an almost total coverage of the Italian territory, and very few 2011 - 2014 COSMO SKYMED (ASI) images, all through the multi-interferogram technique.

The Multi-Pass interferometry or A-DInSAR (Advanced Differential SAR Interferometry) techniques are based on radar multi-image analysis. The products of these analyzes derive from complex processing chains of satellite images, called *PS (Persistent Scatterers)-based* or *PSI (Persistent Scatterer Interferometry) techniques*.

The PS data, not much used by public administrations, for environmental and territorial control and monitoring, in the scientific field they have been used mainly in the geo-applicative field concerning the issue of hydrogeological risk, for slope gravitational and subsidence phenomena monitoring.

The PS data, unlike the DInSAR, has been not much used in seismological field too.

Therefore, in this thesis they were collected several PS ERS 1/2 and ENVISAT PS dataset, and few COSMO SKYMED ones, over portions of the Apennine chain, and they were subject to post-processing mapping, geostatistical tools, and inspections about the deformation time series.

A very exciting challenge was to investigate if there were, in the "historical" MATTM interferometric database, any "signal" that can reveal the existence of pre-seismic deformation phenomena, that is a geodetic precursors.

From what has been said before, as summarized in this paragraph and in the introductory one, areas of interest have been identified for the topics related to post- and pre-seismic ground deformation and ground deformation in almost aseismic areas.

The areas of interest of this PhD project are located in several site of Italian peninsula.

- **Monte Marzano**, Campania region, 1980, 6.9 Mw Irpinia earthquake - topic objective: post-seismic ground deformation;
- **Colfiorito**, Umbria region, 1997, 5.7 and 6.0 Mw earthquake - topic objective: pre-seismic ground deformation;
- **L'Aquila**, Abruzzo region; 2009, 6. Mw earthquake - topic objective: pre-seismic ground deformation;
- **Lunigiana**, Toscana-Liguria regions boundary, 2013, 5.1 Mw earthquake - topic objective: pre-seismic ground deformation;
- **Lower Volturno Plain**, Campania region - topic objective: quasi aseismic ground deformation.

1.2. Short Historical Compendium about thesis' topics

The accuracy of the millimetre measurements so far realized by the SAR systems have provided impressive images of surface displacements in areas affected by strong earthquakes, which have contributed to constrain the geometric and kinematic features of earthquake generating faults. As a milestone, Massonet et al., 1993, 25 years ago, published a paper about geodetic data obtained by a space-based technique, the synthetic aperture radar (SAR). They used data from ERS1 ESA satellite to capture the movements produced by the 1992 7.3 Mw Landers earthquake (CA USA). Very impressive remains the "Image of an earthquake" published on 1993 Nature Journal cover (Fig. 1.1). The post-processing interferometric colored fringes, obtained with a pair of ERS1 SAR images, taken just before and little after the earthquake, let's we see and quantify the real areal ground deformation after the main shock. This was/is the differential radar interferometry (DInSAR) technique.

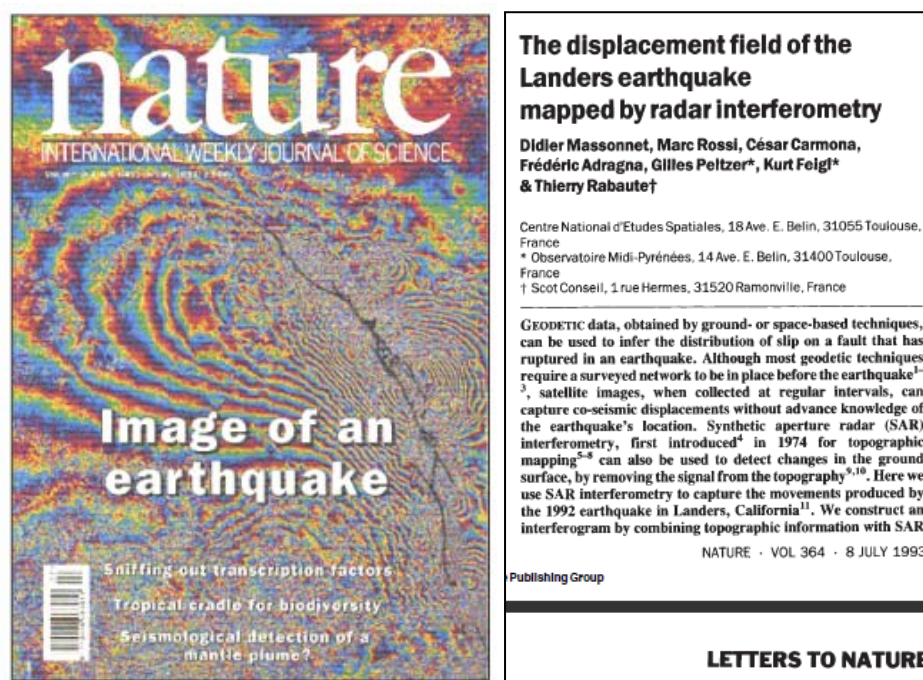


Fig. 1.1. Massonet et al., 1993, "Image of an earthquake"

The DInSAR technique is used nowadays for the identification of surface rupture areas (capable fault is an active fault whose coseismic displacement can intercept the ground surface Vittori et al., 1997; Machette, 2000; Galadini et al., 2012), characterization of the superficial deformation and for the reconstruction of the dynamics of the rupture along the fault plane that gave rise to the main and after shocks.

In the last few years several A-DInSAR multi-interferogram techniques have been developed, including Permanent Scatterers Interferometry SAR (PSInSAR) by Ferretti et al., 2001 and Small Baseline Subset (SBAS) by Berardino et al., 2002.

Vilardo et al., 2009, applied the Permanent Scatterers Synthetic Aperture Radar Interferometry (PS-InSAR, Ferretti et al., 2001) technique to the Campania region (southern Italy), using SAR images acquired in ascending and descending orbits from 1992 to 2001 by the European Remote Sensing satellites (ERS), with the aim to detect ground displacements at a regional scale. The study area, is characterized by intense urbanization, active volcanoes (Phlegraean Fields, Vesuvius and Ischia), seismogenic structures, landslides, hydrogeological instability and includes the southern Apennines chain and Plio-Quaternary structural depressions.

Perrone et al., 2013, used PS-InSAR techniques data to identify areas, in Piemonte region (northern Italy), with similar tectonic deformation rates, mean velocity values (V_{mean}), operating statistically on a PSs dataset, with help of GIS software, through spatial statistics analysis using a geostatistical analysis tool for PSs data. They derived "isokinematics maps" of the study area.

Costantini et al., 2017, debate how PSI technology is today an operational tool for mapping unstable areas and preventing geo-hazards. Ground deformations due to subsidence, landslides, earthquakes and volcanic activities, and their impact on buildings and infrastructures, can be monitored, even at a national scale. The authors say that many potential final users still ignore the capabilities of Earth observation sensors, and satellite SAR sensors are largely unknown.

Moro et al., 2017, analyzed pre- and post-seismic displacement time series of the PSs and presented evidence of ground deformation preceding the 2009 L'Aquila earthquake, occurred within two Quaternary basins filled with sediments hosting multi-layer aquifers, that are located close to the epicentral area, investigating the seismic cycle associated with the earthquake by applying advanced InSAR techniques to SAR datasets from various satellite missions (RADARSAT-2, ENVISAT and COSMO-SkyMed). The SAR images were processed with the SqueeSARTM, the IPTA and the Persistent Scatterer Pair (PSP) techniques, evolutions of PSInSAR and SBAS ones, which permits estimation of displacement time series for dense sets of locations that correspond to identified persistent scatterers. According to the authors, these techniques are suitable for the identification of earthquake precursors.

1.3. Previous personal experience with the PS technique and the reason why a PhD project about this topic

The 2003 SLAM project (Service for Landslide Monitoring), with some applications in Italy, implemented by the European Space Agency (ESA), use the Permanent Scatterers (PSInSAR) technique (Ferretti et al., 2001), a multi-image advanced differential radar interferometry (DInSAR) technique, for landslide investigations.

In 2006 the Agenzia Regionale per la Protezione dell'Ambiente del Piemonte (ARPA - regional environmental agency) obtained the covering of entire regional territory with interferometric PSInSAR technique data, using data from ERS1/2 satellites (1992-2001 time span). In 2010, ARPA Piemonte (regional environmental agency), in the framework of European Project RISK NAT carried out a study about western Alps using RADARSAT 1 images (2002-2009 time span) processed with the SqueeSAR technique (Ferretti et al., 2011).

The first approaches to the PSInSAR, in Campania territorial administration (Regione Campania), start in 2005 with the TELLUS Project. The writer of this thesis was a component of TELLUS Project team.

In the framework of Progetto Operativo per la Difesa del Suolo (PODIS) implemented by national authority of Italian Ministry of Environment (MATM), TELLUS had the aim to realize an advanced/integrated remote sensing/ground monitoring system mainly dedicated to gravitative ground deformations. In the following years (2007-2009), other types of ground deformations was taken in count (subsidence, tectonic, volcanic) in Vilardo et al., 2009 (where the writer was co-author).

In 2010, the entire experience of PODIS-TELLUS Project with the PSInSAR data sets from 1992 to 2010 from radar spaceborne systems ERS-1/2 SAR (ESA), RADARSAT-1 (Canadian Space Agency), ENVISAT ASAR (ESA), that covered Campania region, was transferred to Regione Campania (Settore Difesa del Suolo).

In that years TELLUS realized some collaboration with Federico II University of Napoli (Prof. D. Calcaterra), about specific geotechnical and geomorphological case studies, making dissemination about PSInSAR.

At the end of 2009 the writer became employed at ARPA Campania that, unlike ARPA Piemonte and other ARPA in northern Italy, did not have a sector dedicated to monitoring peculiar geologic phenomena like landslides, subsidence and ground deformations in general.

Despite this, in 2010, the writer published, as ARPA Campania membership, with other authors, the scientific article "L'utilizzo della tecnica PSInSAR™ per l'individuazione ed il monitoraggio di sinkholes in aree urbanizzate della Campania; i casi di Telesse Terme (BN) e di Sarno (SA)", in Atti 2° Workshop Internazionale - "I Sinkholes - Gli sprofondamenti catastrofici nell'ambiente naturale ed in quello antropizzato". ISPRA, Roma, 3-4 Dicembre 2009.

Unfortunately, after this, nothing has changed in ARPA Campania scientific organization. The question that arises is why ARPA Piemonte is monitoring the regional territory with interferometric PSInSAR technique while not ARPA Campania?

About at the end of 2015, the writer decides, in order not to disperse the acquired knowledge by TELLUS experience, to participate for XXXI° cycle Earth Sciences Phd selection at Federico II University of Napoli and, after the positive result, he took temporary leave from the ARPA Campania. The project idea was to apply the PSInSAR technique to try to identify some peculiar ground deformation signal in seismogenically active areas possibly comparing them with geomorphological and / or geostructural elements.

In 2016 it was created, by law (L. 132/2016), the Sistema Nazionale di Protezione Ambientale (SNPA) that integrates Istituto Superiore per la Protezione e Ricerca Ambientale (ISPRA national institute) and 21 regional ARPA in a same framework. The purpose of this system is to standardize technical-scientific activities (monitoring and control) throughout the national territory and to produce advanced research in environmental field.

At the end of 2016, it was constituted by ISPRA the Tavolo Nazionale dei Servizi Geologi Operativi (TNSGO) with the objective to promote the PS Journal Italia (operational service for monitoring the movements of the ground based on interferometric data), framed in the strategic plan "Space Economy" promoted by the Italian Presidency of the Council of Ministers and in particular in the Mirror Copernicus program (European Environmental Agency EEA), using requirements provided by Regional Authorities (Environmental Agencies and Geological Surveys).

At the same period too, the Government of the Campania Region has ruled, by law (L.R. 38/2016 and L.R. 10/1998), that ARPA Campania have to monitoring the hazardous and risk area (landslides, sinkholes, subsidence) about natural disasters.

In conclusion, the writer hope is that, when he resume in service, with the additional Phd experience, as well as of TELLUS one, he will find an adequate technical-scientific space in ARPA Campania, to work with the PSInSAR, SQUEESAR or others PS SAR techniques, with the most recent data obtained from the current SAR missions of the Sentinel 1A / 1B (ESA) and Cosmo Skymed (ASI) satellites, in order to comply with a specific legislative provision.

CHAPTER 2 - MATERIALS AND METHODS

2.1 Earth Observation with Synthetic Aperture Radar (SAR)

The earth observation through the remote sensing represents today one of the main technical-scientific disciplines that allows to obtain, from an external point of view to the terrestrial system, information, quantitative and qualitative, about areas of interest or specific targets located far from a sensor on satellite platforms, through measurements of an electromagnetic radiation naturally emitted (passive detection) or artificially transmitted and then reflected (active detection), that interacts with the involved surfaces.

The passive sensors allow a qualitative observation of an area, working mainly with optical data; in this case the electromagnetic energy is characterized by wavelengths belonging to the visible up to the infrared in the electromagnetic spectrum. The active sensors achieve quantitative information of an observed phenomenon working with wavelengths of the L-, C- or X-band (Fig. 2.1). In particular, radar (Radio Detection And Ranging) is an active sensors that use electromagnetic waves in the radio wavelengths and determine the distance of an object (registering the two-way travel time of the pulse) and its physical quantities measuring its backscatter intensity.

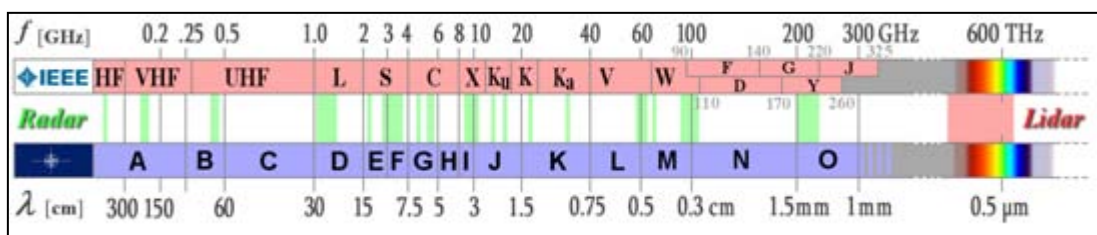


Fig. 2.1. RADAR wavelengths of the L-, C- or X-band

The limitation of physical antenna aperture was overcome through Synthetic Aperture Radar where signal processing is used to improve the resolution beyond (Curlander et. al., 1991). In others words, SAR “synthesizes” a very long antenna playing on the forward motion of the physical antenna.

These instruments, using microwaves, do not feel the effect of clouds and could achieve measures 24 hours a day obtaining radar images of wide areas.

Radar images are pixels matrixes and each of them it is associated a value of the phase and the amplitude relative to the wave emitted by the antenna and backscattered from the targets.

With two radar images referred to the same area, acquired with temporal and spatial baseline (at different times and in different orbit positions), it is possible to obtain, through a conventional technique called the DInSAR (Differential SAR Interferometry), a new image in which each pixel is associated to the difference of the phases. This image is called interferograms and the phase difference, pixel to pixel, between two SAR images is called the interferometric phase. It contains various contributions among which, the electromagnetic noise, the atmospheric features, the topography of the observed scene, and the possible soil deformation occurred in the interval of time between the two acquisitions. Subtracting the noise, atmospheric and topographic components it is possible to estimate that due to the displacement. Therefore, from a processing of the interferometric phase, compared with the ground topography, it is possible to obtain two kinds of results:

- High resolution Digital Elevation Models (DEMs);
- Deformation maps characterized by millimetre resolution.

2.1.1 Satellite missions

The satellites operating between 1990 and 2010 used SAR sensors to acquire in C band.

The main civil satellites equipped with SAR sensors in C band, that have surveyed Italian regions in recent past and no more working, was:

- ERS-1 and ERS-2 (ESA).
- ENVISAT (ESA).
- RADARSAT-1 (CSA).

Furthermore, the SAR sensors in C band currently working are:

- RADARSAT-2 (CSA).
- SENTINEL-1A and SENTINEL-1B (ESA).

The ESA's European Remote Sensing (ERS) satellites have been installed with SAR radar sensors with frequency of 5.3 GHz and wavelength $\lambda = 5.66$ cm. Their orbits (Fig. 2.2) are heliosynchronous and slightly inclined to the meridians (8.5°) and illuminate, from the altitude of 785 km, a strip of territory (swath) approximately 100 km wide. The sensor-target direction or Line of Sight (LOS) is perpendicular to the orbit of the satellite and is inclined on average by an angle equal to 23° (θ , off-nadir) with respect to the vertical (Fig. 2.2). The resolution is about 4 meters in azimuth and 8 meters in the direction of the range (the ground resolution is about 20 m.) The same nominal orbit is traced every 35 days and in a time of about 100 minutes.

The ERS-1 satellite acquired data from the end of 1991 to March 2000. From November 1993 to April 1995, the acquisitions were characterized by particular phases lasting a few months each, in which the acquisition parameters were modified for particular applications. and for acquisition in specific areas of the Earth, including the oceans and poles.

The ERS-2 satellite has been operational since the beginning of 1995 and, until the end of the ERS-1 mission, has performed a scan of the same scene but from a slightly different shooting point and one day after the passage of ERS-1. Thanks to this feature, ESA has guaranteed the availability of Tandem pairs from March 1995 to March 2000, through which it is possible to generate high resolution DEMs exploiting the spatial baseline of image pairs.

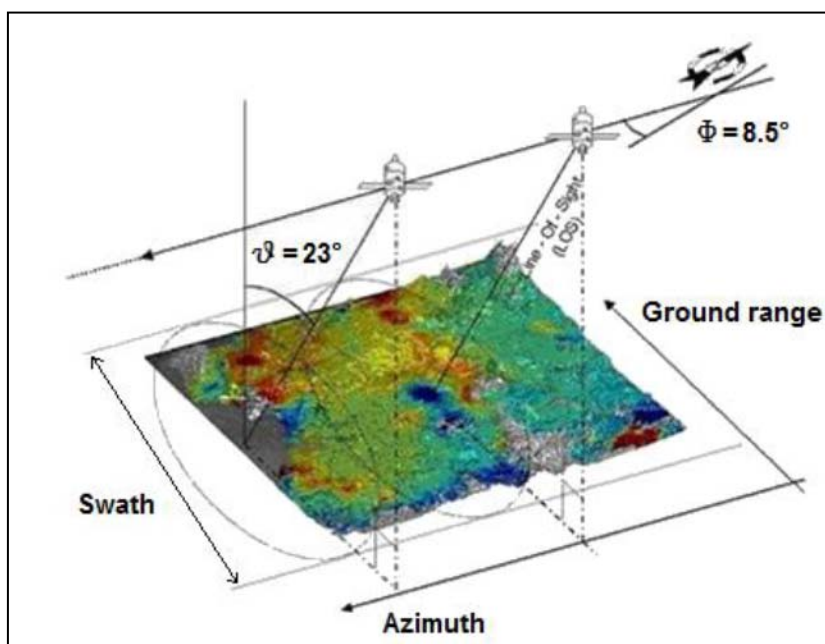


Fig. 2.2 Orbit and look features

The ESA satellite ENVISAT (ENVIRONMENTAL SATellite), launched in November 2002, replaced and expanded the functions of the ERS-1 and ERS-2 satellites. It is equipped with an ASAR sensor (Advanced Synthetic Aperture Radar), which represented an evolution of the SAR and used a series of antennas that could work with different polarizations and 7 different angles of incidence (between 15° and 45°) with consequent variation of the scene size observed in a single image. The satellite traveled through a helio-synchronous orbit with a retransmission time equal to that of the ERS satellites (35 days). The instrument acquires in C band (frequency of 5.331 GHz and wavelength of 5.63 cm) but with a slight shift in frequency with respect to ERS-1 and ERS-2 which makes it difficult but possible, through some technical devices, the combination of its data with ERS data to perform interferometric processing.

The RADARSAT-1 satellite of the Canadian Space Agency (CSA), launched in November 1995, used a sensor SAR in C band. The observation geometry is a lot flexible, in fact, the angles of incidence vary from 10° to 60° , the radar wave beam can be oriented and the width of the imaging bands can be varied

from 45 to 510 km wide, with resolutions respectively from 8 to 100 meters. The cycle repetition of the satellite's orbit was 24 days.

Unlike other satellites, RADARSAT-1 generally acquires on demand.

Thanks to an agreement between RADARSAT International and TRE (spin-off company of the Politecnico di Milano), from March 2003, images were acquired on Italian territory every 24 days in Standard mode, both along ascending or descending orbits. In addition, satellite acquisitions were requested in Fine Beam mode on some sensitive areas, such as Venice, Turin, Rome, Naples, Ancona and Crotona. Most of the Italian areas are covered by at least 60 RADARSAT-1 images in descending geometry and 60 in ascendant. Thanks to the high number of available acquisitions and the shorter acquisition frequency (24 days) compared to the ERS and ENVISAT satellites (35 days), these images allow a higher accuracy in the measurement of deformations, because they allow to limit the effects for the temporal decorrelation of the radar signal.

In December 2007, the satellite RADARSAT-2 was also launched. The orbit is the same as RADARSAT-1, but it is traversed with a 30-minute delay for interferometer entry during the period when the two satellites are both operational. The mission, ensures all the methods of acquisition of RADARSAT-1, will ensure continuity with the data obtained from the previous satellite. Its news is instead related to the different angles with which the system can work that contain up to a resolution of 3 m, both in range and in azimuth, to acquire images from both sides of the platform compared to the direction of flight double-sided imaging), and to emit and acquire the signal in all polarizations.

Finally, SENTINEL satellites are the last generation of Earth observation satellites of the ESA and the Copernicus group (program of the European Commission). The mission is composed of a constellation of two satellites, sharing the same orbital plane. SENTINEL-1A satellite was launched on April 3, 2014 and SENTINEL-1B on 25 April 2016. The SENTINEL-1 mission includes C-band imaging operating in four exclusive imaging modes with different resolution (down to 5 m) and coverage (up to 400 km). It provides dual polarisation capability, very short revisit times and rapid product delivery. For each observation, precise measurements of spacecraft position and attitude are available. The SENTINEL-1 mission includes C-band imaging operating in four exclusive imaging modes with different resolution (down to 5 m) and coverage (up to 400 km). It provides dual polarisation capability, very short revisit times (12 - 6 days) and rapid product delivery. For each observation, precise measurements of spacecraft position and attitude are available. They provides all-weather, day and night radar imaging for land and ocean services, such as: monitoring of Arctic sea-ice extent, routine sea-ice mapping, surveillance of the marine environment, including oil-spill monitoring, monitoring land-surface for motion risks, mapping of forests, water and soil management and to support humanitarian aid and crisis situations.

The satellites operating from 2007, using SAR sensors to acquire in X band, are:

- TerraSAR-X (DLR)
- COSMO-SkyMed (ASI)

The TerraSAR-X mission started on June 15, 2007; it is a German SAR satellite mission for scientific and commercial applications. The project is supported by BMBF (German ministry of Education and Science) and managed by DLR (German Aerospace Center). The science objectives were to make multi-mode and high-resolution X-band data available for a wide spectrum of scientific applications in fields as hydrology, geology, climatology, oceanography, environmental and disaster monitoring, and cartography (DEM generation). Its main features are: resolution up to 0.25 m (in-staring spotlight mode), an excellent radiometric accuracy, unique agility (rapid switches between imaging modes and polarizations). On June 21, 2010, the twin mission TanDEM-X started, and since then they fly in a close formation at distances of only few hundred meters and record data synchronously. This peculiar configuration allows the generation of WorldDEM, which is a DEM of the Earth's land surface with a vertical accuracy of 2 m (relative) and 10 m (absolute).

COSMO-SkyMed (Constellation of small Satellites for Mediterranean basin Observation) is a satellite mission ran by the ASI (Italian Space Agency) and the Italian Ministry of Defense. The CSK system is made up of four satellites and it is equipped with High-Resolution SAR, in sun-synchronous polar orbits, phased in the same orbital plane. This results in varied Constellation of small Satellites for Mediterranean basin Observation) is a satellite mission ran by the ASI (Italian intervals between the satellites along the same ground track of between 1 and 15 days. The first two satellites were launched in 2007, the remaining two in 2008 and 2010, respectively. Its main goal is to provide imagery for environmental monitoring and surveillance applications for the management of exogenous, endogenous and

anthropogenic risks, but also commercial products. The CSK system is made up of four satellites and it is equipped with High-Resolution SAR, in sun-synchronous polar orbits, phased in the same orbital plane. This results in varied intervals between the satellites along the same ground track of between 1 and 15 days. The first two satellites were launched in 2007, the remaining two in 2008 and 2010, respectively. Its main goal is to provide imagery for environmental monitoring and surveillance applications for the management of exogenous, endogenous and anthropogenic risks, but also commercial products.

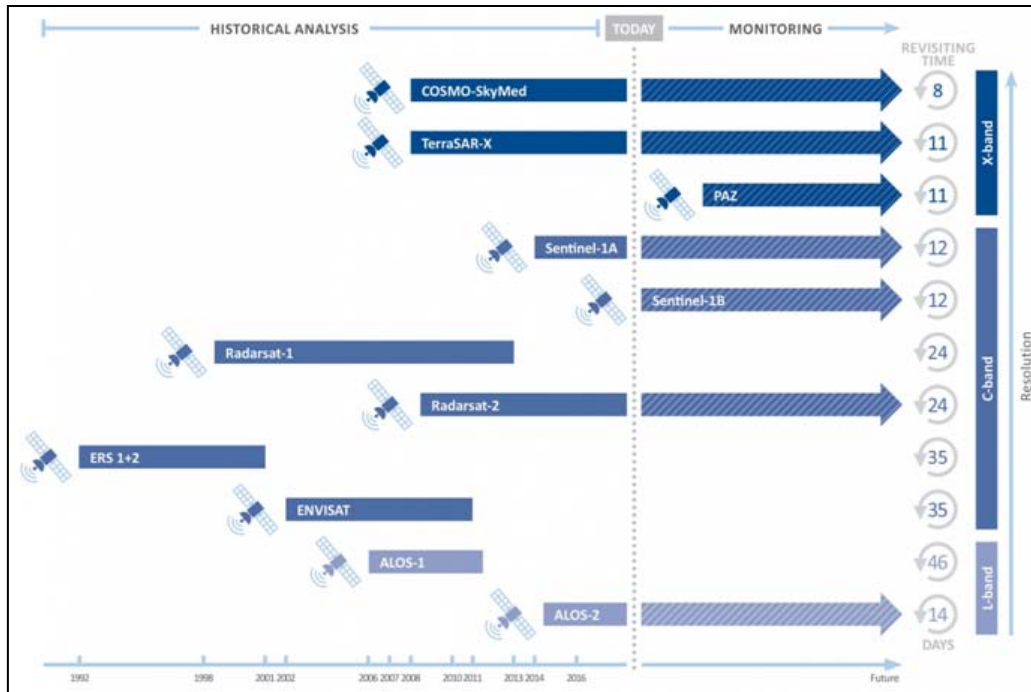


Fig. 2.3 The SAR satellites missions

2.2 Advanced DInSAR techniques

The A-DInSAR (Advanced Differential SAR Interferometry) techniques, or multi-pass interferometry, are based on multi-interferogram or multi-image analysis, that is, they use a long series of radar images related to the same area, from which they come identified some radar targets, which are used to measure displacements.

The multi-interferogram techniques allows to select almost all the SAR images acquired by the selected sensor on the area under examination.

In fact, to implement a multi-interferogram analysis, separate images from very high normal baseline can also be chosen (up to 1200 m with images acquired in C band; Colesanti et al., 2003b), with consequent improvement of the temporal sampling of the phenomena, unlike the differential interferometric technique, for which it is necessary to select only pairs of images characterized by low spatial baseline values (<200-300 m) with the consequent reduction of the sampling frequency.

In other words, while differential interferometry samples the deformation phenomenon under examination through the study of two acquisitions/images (the master, M, and the slave, S), estimating only the cumulative deformation occurred between the two acquisitions or, equivalently, the velocity of linear deformation recorded between them, the multi-interferogram analysis is able to provide the complete description of the temporal evolution of the deformations (Fig. 2.4). Obviously, this capacity is limited by the number and temporal distribution of available acquisitions.

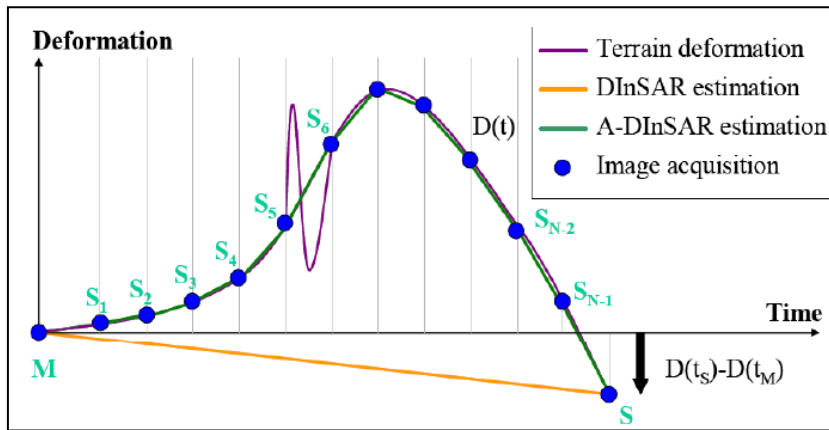


Fig. 2.4 Time sampling of a deformation phenomenon obtained by DInSAR analysis and multi-interferogram analysis. As A-DInSAR analyzes guarantee a better temporal sampling of the phenomenon, the movement occurring between the acquisition S5 and S6 can not be measured with the available images (Crosetto et al., 2005b).

The ability of multi-interferogram techniques to describe deformation phenomena, depends temporally on the number and distribution of images available on the study area and, spatially, on the availability of pixels affected by low levels of noise in phase information or pixels characterized by stability in reflection characteristics (Permanent or Persistent Scatterers - PS) during the entire period covered by the acquisitions (Crosetto et al., 2005b).

A-DInSAR techniques can allow to get from a few hundred up to over 1,000 points / km². We can therefore imagine the grid of radar targets as a dense network of natural GPS stations for monitoring large areas of interest, with a frequency of data updating equal to that of image acquisition (usually monthly or less) and with a spatial density of extremely high measurement points.

The A-DInSAR analysis yields a database of radar targets for which the following information is generally extracted (Fig. 2.5):

MONDRAGONE_RSAT_S3_D_T11										
FID	Shape *	CODE *	NORTH	EAST	V STDEV	COHERENCE	VEL	D20030322	D20030415	
0	Point	A8JDP	4557640,23	412094,81	0,67	0,97	-0,4	0	-3,19	
1	Point	A6BH1	4564371,61	396257,8	0,77	0,69	-0,56	0	-3,61	
2	Point	A6BB6	4564407,85	396252,01	0,99	0,73	-1,45	0	-6,18	
3	Point	A6A19	4564465,11	396265,75	0,77	0,88	0,87	0	-3,27	
4	Point	A6AX6	4564490,12	396265,92	0,78	0,96	-0,3	0	-1,85	
5	Point	A6AZT	4564470,56	396312,47	0,81	0,92	0,02	0	-2,51	
6	Point	A6ARR	4564515,73	396312,01	0,91	0,9	0,3	0	5,4	
7	Point	A6AP0	4564525,64	396312,52	0,86	0,79	0,2	0	1,14	
8	Point	A6AWE	4564487,9	396325,61	0,84	0,9	0,39	0	0,68	
9	Point	A6ACU	4564590,46	396338,25	0,77	0,73	0,94	0	-3,66	
10	Point	A5860	4564771,31	396359,78	0,9	0,84	0,59	0	-1,95	
11	Point	A6AAS	4564591	396384,41	0,81	0,9	-0,86	0	2,11	
12	Point	A59UL	4564663,57	396372,43	0,82	0,91	3,51	0	-0,66	
13	Point	A59MC	4564696,64	396382,13	0,89	0,77	0,39	0	-2,58	
14	Point	A585X	4564776,24	396360,13	0,86	0,72	-0,08	0	-4,36	
15	Point	A59R2	4564660,81	396434,76	0,91	0,71	-1,51	0	-3,99	
16	Point	A57RM	4564996,45	396531,75	0,78	0,92	-1,45	0	-1,34	
17	Point	A57QG	4565000,23	396537,68	0,8	0,8	-2,04	0	2,28	
18	Point	A6BH0	4564304,65	396584,53	0,98	0,76	0,71	0	1,87	
19	Point	A55WB	4565293,14	396672,11	0,77	0,96	0,42	0	-0,16	
20	Point	A6ABR	4564520,65	396703,4	0,9	0,73	-0,8	0	-2,13	
21	Point	A55ZD	4565271,32	396705,36	0,85	0,77	1,15	0	-7,16	
22	Point	A55A7	4565408,29	396721,08	0,76	0,89	0,17	0	-2,87	
23	Point	A542F	4565456,17	396731,81	0,81	0,82	0,47	0	-3,22	

Fig. 2.5 Example of A - DInSAR database

- target **position**: geographical coordinates (E, N, precision up to $\pm 2\text{-}6$ m) and altitude (accuracy up to $\pm 1.5\text{-}2$ m);
- **average** annual deformation **speed** (mm / year), with precision up to 0.1 mm / year (depends on the distance of the targets from the *reference point*);
- deformation **time series** with a measuring frequency equal to that of the review time of the used satellite, and with precision up to 1 mm on the single measurement;
- quality parameters, e.g. standard deviation associated with the estimate of the annual average velocity and **coherence** of each target.

The coherence provides a measure of the quality of the PS, and quantifies the correspondence of the behavior of the target with the deformation model used in the analysis (typically linear). The coherence

can assume values between 0 and 1, or respectively between the total absence of correspondence between the data and the model and their complete agreement. During processing, only radar targets that have consistency greater than a certain threshold are selected. This threshold value is established according to the number of images used for processing (they are inversely proportional) and so that the probability of error in the identification of the targets is contained (i.e. less than 10^{-5} ; TRE, 2008b).

All ground-deformation measurements derived from multi-interferometric analysis are detected along the sensor-target line (Line of Sight - LoS), and they are relative type in both space and time. The deformations are calculated with respect to the position of a reference point on the ground of known coordinates, supposedly fixed or expressly indicated by GPS measurements or optical leveling, and with respect to a reference image chosen within the dataset used for analysis. The displacement measured at each reading (SAR acquisition) therefore represents the difference between the ground altitude at the reading and that at the time of the reference acquisition (zero displacement).

In the last few years several A-DInSAR multi-interferogram techniques have been developed, including:

- PSInSAR (Permanent Scatterers Interferometry SAR) by Ferretti et al., 2001, TRE Milan Polytechnic spin off;
- SBAS (Small Baseline Subset) Berardino et al., 2002, CNR-IREA of Naples;
- IPTA (Interferometric Point Target Analysis) by Werner et al., 2003, Remote Sensing GAMMA, Switzerland;
- CPT (Coherent Pixel Technique) by Mora et al., 2003, Barcelona Polytechnic of Catalonia;
- SPN (Stable Point Network) by Arnaud et al., 2003, Altamira Information, Barcelona.
- StaMPS (Stanford Method for Persistent Scatterers) by Hooper et al., 2004, University of Stanford;
- PSP-DIFSAR (Persistent Scatterers Pairs - DIFSAR) by Constantini et al., 2008, e-GEOS, Rome;
- SqueeSAR by Ferretti et al., 2011, Altamira Information TRE.

The ground deformations over time are generally modeled by linear functions and, in other cases, more complex models are adopted, such as quadratic, sinusoidal (seasonal) functions or combinations.

The multi-interferometric techniques are distinguished according to the processing approach in the following two categories (Wasowski et al., 2007): PS (Persistent Scatterers) -based or PSI (Persistent Scatterer Interferometry), and interferogram stacking.

2.2.1 Potential and limitations of multi-interferogram techniques

As first, they do not require any intervention on the ground and make it possible to study large portions of land or areas that are difficult to access, with a consequent reduction in the time and costs of large-scale investigation. They also allow the analysis of phenomena that took place in the recent past thanks to the availability of SAR image archives established in recent years by the various space agencies (ERS archives (1992-2001) and ENVISAT (2002-2010) of ESA and RADARSAT-1 archive (2003-2008) of the CSA, and allow to study phenomena whose velocities are extremely reduced (mm / year) and for which conventional techniques would require years before they can provide meaningful measures.

The multi-interferogram approaches allow to monitor the soil deformations with high precision on the deformation trend (precision in the estimation of the average speed up to 0.1 mm/year, on the single measurement vertical displacement up to 1 mm and E-W displacement up to 1 cm).

In areas of high urbanization, the spatial density of radar targets reaches very high values, up to 400-700 PS/km², but also over 1,000 PS/km² with data from high resolution sensors, as Cosmo Skymed or TerraSAR-X. This spatial density of benchmarks is several orders of magnitude higher than that obtainable with conventional geodetic networks and provides higher precision (millimetric) than the GPS (centimeter) analysis in the calculation of vertical displacements.

In addition, radar targets are already present on the ground and, unlike the traditional measuring instruments (geodetic benchmarks, GPS, inclinometers), they do not require any installation or maintenance by operators. However, these approaches do not represent a substitute for other monitoring techniques, but are in complete synergy with them. The integration of multi-interferometric data with traditional geodetic measurements and GPS (Table 2.1), allows in fact to exploit all their advantages and obtain a more complete view on the evolution of the phenomena studied.

Multi-interferometric data	GPS measurements
<ul style="list-style-type: none"> - accurate measurements in the vertical direction - high spatial density - monthly update - optimization of the positioning of the permanent GPS stations - displacement measurements along the LoS 	<ul style="list-style-type: none"> - accurate measurements in the horizontal direction - low spatial density - good time sampling - removal of systematic errors in the results of the PS technique. Data calibration. - 3D displacement field

Table 2.1 The characteristics of the multi-interferometric measurements in relation to those of the GPS measurements, show that the two techniques are complementary (TRE, 2008a).

2.2.2 Interferogram stacking techniques

The interferogram stacking techniques are based on the combination of phase information deriving from the analysis of interferograms generated by the combination of all the acquisitions available on the area of interest (multiple masters) characterized by low baseline values spatial (e.g. <200-300 m). In contrast to the PSI techniques, these approaches exploit the signals deriving from the integration of several adjacent cells and through a multi-looking complex operation they combine and connect the time series of the phase values related to the deformations of the investigated surface. These techniques reduce the effects of decorrelation, maximizing the number of pixels used for the combination of phase contributions and consequently improving the signal to noise ratio, SNR (Signal-to-Noise Ratio). Examples of techniques belonging to this category are the SBAS and the CPT (Fig. 2.6).

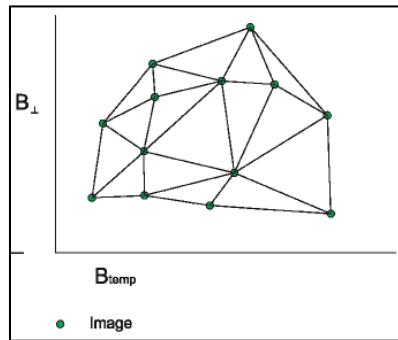


Fig. 2.6 Representative scheme of PSInSAR processing

2.3 PS (Persistent Scatterers)-based or PSI (Persistent Scatterer Interferometry) techniques

The radar targets (PS or PSI), used as benchmarks for the measurement of deformations, are immune to the effects of decorrelation, i.e. they maintain the same electromagnetic characteristics (reflectivity) in all the images, varying both the acquisition geometry and the climatic conditions, thus preserving the information of phase in time. The PSs generally correspond both to structures of anthropic origin, such as buildings, monuments, metal structures, dams, viaducts, poles, antennas, and to stable natural reflectors such as exposed rocks (Fig. 2.7).



Fig. 2.7 - RADAR targets on ground surface (from TRE, 2008b).

The techniques belonging to this category are the PSInSAR, IPTA, PSP-DIFSAR, StaMPS and SPN. Generally, processing is performed on datastacks composed of at least 30 SAR images acquired along the same nominal orbit and with the same acquisition geometry (Fig. 2.8). However, the number of acquisitions necessary to implement an analysis is related to the characteristics of the area of interest and the type of radar sensor used.

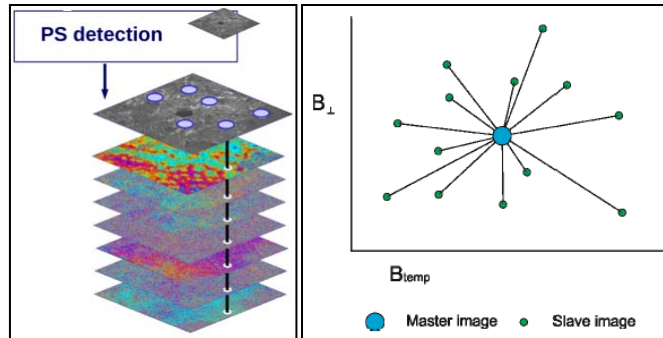


Fig. 2.8 - Representative scheme of generic PSI processing

If several SAR acquisitions on the same area are available, the PS grid can be used to discriminate the various phase contributions related to topography, deformation and atmosphere, taking advantage of their different characteristics with respect to time, space and acquisition geometry (Table 2.2). The atmospheric artifact is calculated as the interferometric phase component that is random in time but correlated in space, that is similar in correspondence of points close to each other.

	Time	Space	Acquisition Geometry (baseline)
deformation	correlated	variable	uncorrelated
topography	uncorrelated	variable	proportional
atmosphere	uncorrelated	correlated	uncorrelated

Table 2.2 Behavior of phase terms due to topography, deformations and atmosphere, against time, space and normal baseline.

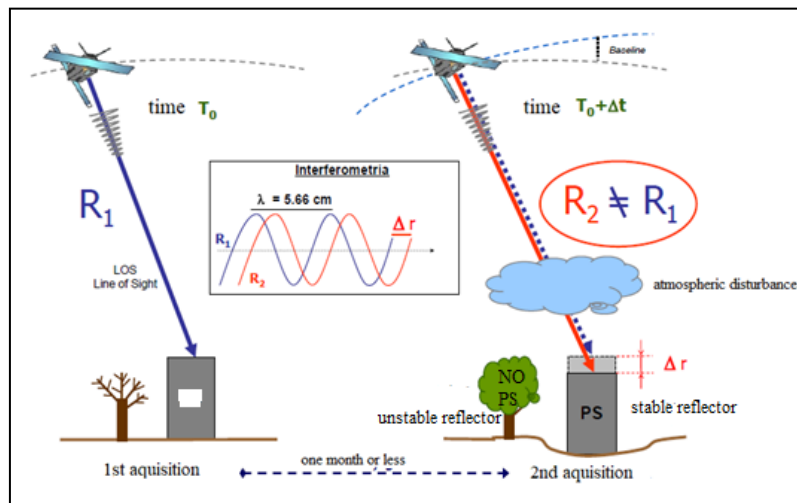


Fig. 2.9 Variation of the reflectivity component of the targets which gives rise to temporal decorrelation, variations of the normal baseline which give rise to geometric decorrelation, atmospheric disturbances (from TRE, 2008b).

The factors influencing the precision obtained with the PS technique are (Fig. 2.9):

- number and temporal distribution of the images available on the area of interest (the greater the number of data, the greater the probability of identifying PS, moreover the acquisitions are frequent, the better the estimate of the displacements);
- density of PS;
- uncertainty in the orbital parameters and changes in electromagnetic properties over time;
- atmospheric noise (possible residual errors in case of atmospheric conditions not perfectly simulated);
- distance of the PS from the reference point (as for traditional geodetic networks, the precision decreases with increasing distance from the reference point).

The PSI technique can be applied on different scales:

- *Local survey*, analyzed area of extension from 1 to 100 km², characterized by a very high degree of detail and with which the density of the points of measure can reach, in urban area, even 1,000 PS / km².

This analysis can be used for monitoring of circumscribed phenomena, such as landslides or sinkholes, for the purpose of urban planning, for the control of extraction basins or plants.

- *Regional survey*, analyzed area above 50 km², that it is a very useful operative tool to characterize phenomena of extended deformation. This analysis can be used for monitoring landslides, subsidies, seismic faults, oil or gas fields, storage basins and mines.

- *Linear structures survey*, such as pipelines (eg methane pipelines, gas pipelines), motorways, railways, etc., by which information is provided on a strip of 1,000 meters wide land around the structure track, as well as information about detail (the historical series of points) for a strip of 250 meters around the track.

- *Single Building survey* provides a targeted and circumscribed analysis of individual buildings in urban areas that refers to a portion of territory equal to 1 km², for which you want to receive precise information of movement (analysis of individual buildings, of architectural structures), etc).

2.3.1 SAR acquisition geometry

As mentioned before, the relative displacement measurements is only along the LoS, not in 3D geographic space. The combination of the satellites motion (quasi-polar, ascending and descending, orbits in Fig. 2.10 left) and the Earth rotation, makes it possible to look at the same area of interest from two opposite acquisition geometries. In fact, over the same geographic area, they are processed two distinct PS database, one for ascending and one for descending orbit.

Theoretically, considering the satellites moving exactly along meridians, components of the same real ground displacement, in the same ground point (very rare case), contained in a vertical plane E-W oriented, can be measured, with similar or different values, along both the ascending and descending LoS (Fig. 2.10 right),.

In other words, SAR sensors measure only two components along both the LoSs but not real 3D displacement.

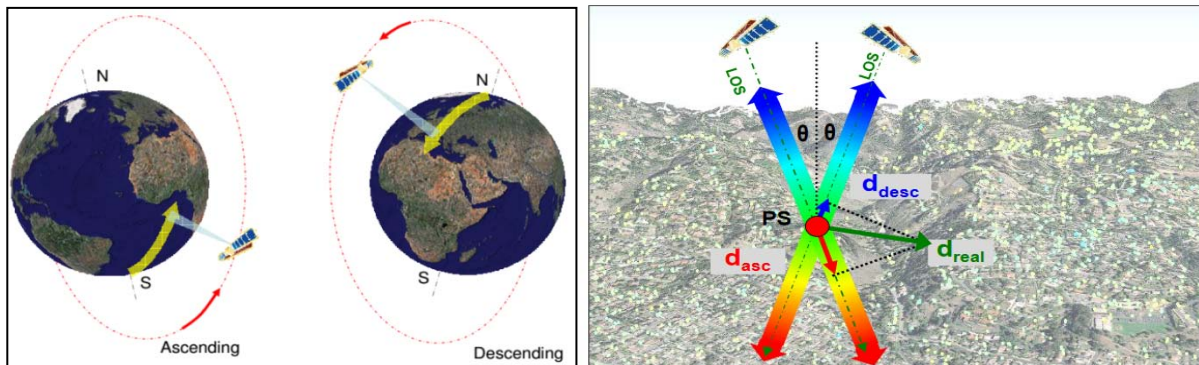


Figure 2.10 SAR image acquisition geometry. On the left, the ascending and descending orbit tracks; on the right, looking at the same ground point from two different point of view (from TRE, PSInSAR Handbook)

In fact, the simplified relationships (1) to (4) (Lundgren et al. 2004; Manzo et al., 2006; Lanari et al., 2007; Tofani et al., 2013) link the components measured along the LoSs and the incidence angle (θ) with the vertical and horizontal E-W oriented components (not with the horizontal N-S oriented component) of the real displacement (D) or mean velocity (V_{mean}) vectors.

$$(1) \quad Dz = (D_{LoSd} + D_{LoSa})/2\cos\theta$$

$$(2) \quad Deast = (D_{LoSd} - D_{LoSa})/2\sin\theta$$

$$(3) \quad Vz = (V_{LoSd} + V_{LoSa})/2\cos\theta$$

$$(4) \quad Veast = (V_{LoSd} - V_{LoSa})/2\sin\theta$$

Where: Dz is the vertical component of the displacement; $Deast$ is the horizontal component of the displacement; Vz is the vertical component of the mean velocity; $Veast$ is the horizontal component of the V_{mean} .

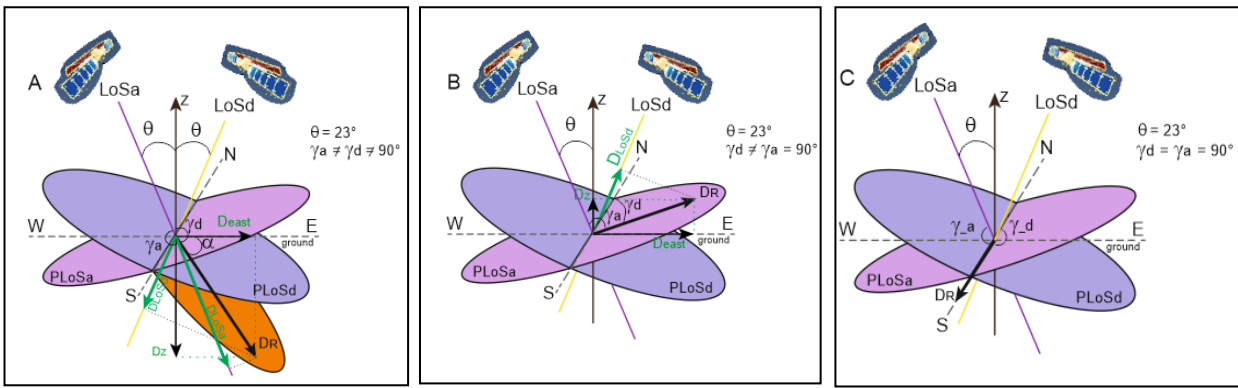


Fig. 2.11 A: generic case with LoSs measurements not null; B: case with null measurements on LoSa; C: case with null measurements on both the LoSs

In Fig. 2.11A, a real displacement vector (DR) is oriented along a generic plane in the geographic space: the DLoSa, DLoSd measurements and θ angle, through relationships (1) and (2), allow to calculate the Dz and Deast components of DR, in a vertical plane E-W oriented. In this example, Dz and Deast values are quite different numerically but they can become very similar the more Dr is vertical or horizontal.

In Fig. 2.11B, DR is oriented along the plane perpendicular to the LoSa; for this reason there is not projection of DR on LoSa, that is DLoSa is null.

In Fig. 2.11C, DR is oriented along N-S direction; for this reason there is not projection of DR on both LoSa and LoSd, that is both DLoSa and DLoSd are null. For this reason, the component N-S of any deformation can not be detected by SAR.

As a generic example, with ERS and ENVISAT satellites, where LoS incidence angle $\theta = 23^\circ$, in Fig. 2.12 is possible to see a quantitative relationship between the real displacement vector (blue arrow) and the components on the ascending LoS (yellow arrow) and descending one (green arrow).

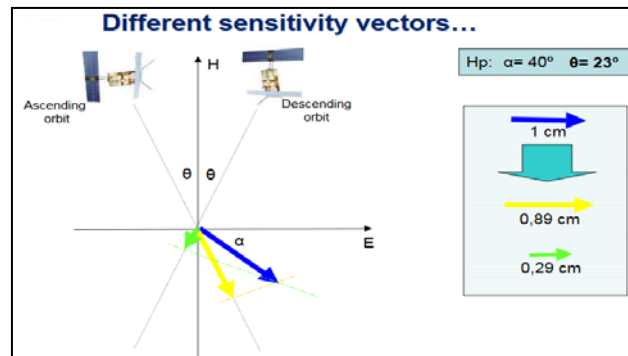


Fig. 2.12

Conventionally, PS that move along the LoS, away from the satellite, are represented with colors from yellow to red while, with colors from light blue to dark blue, are points moving towards the satellite, with green color they are considered stable (Fig. 2.13).

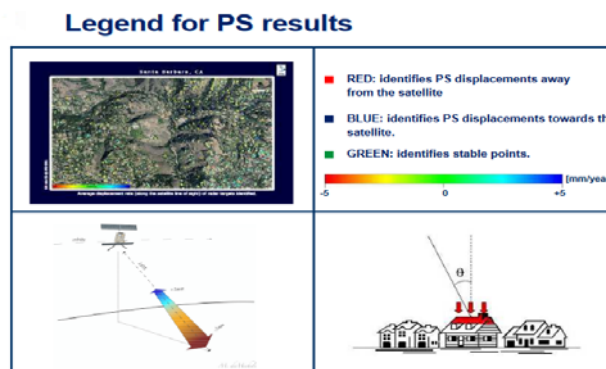


Fig. 2.13

2.4 Extraordinary Plan of Environmental Remote Sensing (PST-A) by Ministry of the Environment and Territory and Sea Protection (MATTM)

The PST-A is an information system. With it a representative database of the national territory was implemented, containing the measurements of the movements of the terrain obtained by means of SAR interferometry.

The database was obtained by processing, through the multi-interferogram technique generically defined as Persistent Scatterers Interferometry (PSI), all the available ERS and Envisat SAR data over Italy, and then at updating the PSI measurement database based on COSMO-SkyMed HIMAGE (stripmap) data stacks (Fig. 2.14). This was the first InSAR project at national scale, and has required the processing of about 20,000 SAR images acquired from 1992 to 2014 over the whole Italian territory (Costantini et al., 2017; Di Martire et al., 2017), with different spatial densities of measurement points on different types of land covers, although not everywhere with all sensors and acquisition geometries. For each measurement point (i.e. for each PS), both the average displacement rate (in mm/year) and the full time series of displacement (in mm), along the satellite line of sight, are provided.

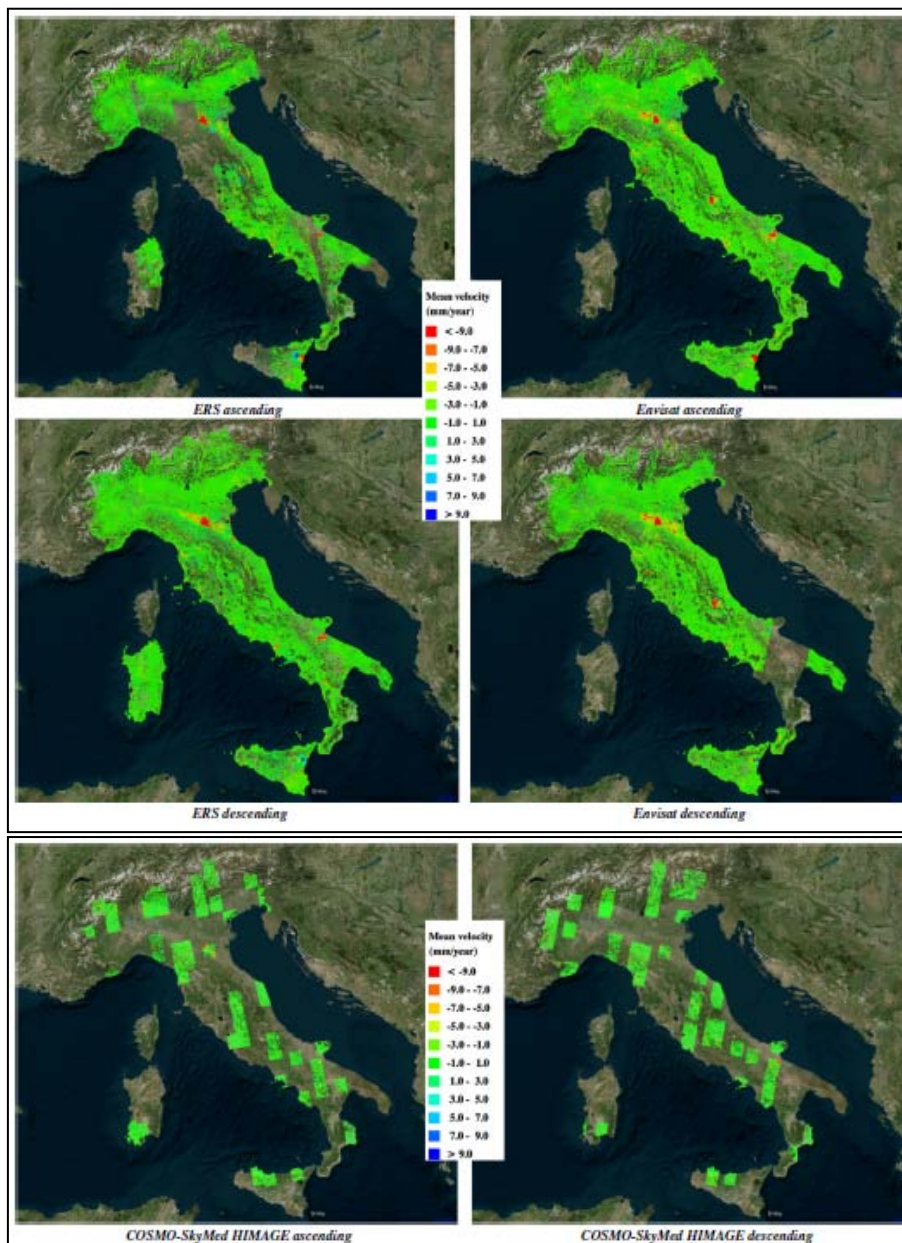


Fig. 2.14 PST-A project by PSI processing of C-band SAR data, ERS-1 and ERS-2 1992–2000 and Envisat 2002–2010, in upper panel and COSMO-SkyMed HIMAGE SAR data stacks (2011–2014), in lower panel, acquired in the two acquisition geometries, ascending and descending (from Costantini et al., 2017).

The data are available through the MATTM National Cartographic Portal, a publishing platform compliant with the guidelines of the European Directive INSPIRE for spatial information dissemination (<http://www.pcn.minambiente.it/mattm/progetto-pst-prodotti-interferometrici/#9>).

For realization assigned by the MATTM to the temporary business grouping by e-GEOS S.p.A., as the parent company, and by the Telerilevamento Europa T.R.E. s.r.l and Compulab s.r.l.

The processing of the PST-A InSAR data, under the coordination of e-GEOS, was shared between e-GEOS (which processed 70% of COSMOSkyMed and 60% of Envisat data) and TRE (which processed 30% of COSMO-SkyMed, 40% of Envisat, and all ERS data). Each of the companies relied on their own algorithms and processing chains, PSP (Costantini et al., 2008, 2009) by e-GEOS and PSInSAR and SqueeSAR by TRE (Ferretti et al., 2000, 2001, 2011).

A validation of the PSI measurements of the PST-A project vs GNSS measurements was performed by the CIRGEO department of the University of Padua at the end of the first phase of the PST-A project over the sites of Venice and Bologna. In particular, the standard deviation of the difference between the displacement rates determined by the two technologies ranges from a minimum of 0.5 mm/year up to 1 mm/year.

PSI techniques can provide not only a synoptic view of the displacement field affecting the area of interest in the period of time covered by the radar scenes, but also, for each PS, the time series of the displacements at the satellite acquisition dates, characterized by millimetric precision (Fig. 2.15). The deformation time series represent the most advanced PSI product. They provide the deformation history over the observed period and referred to the LoS of the SAR sensor, i.e. the line that connects the sensor and the target, which is fundamental for many applications, e.g. studying the kinematics of a given phenomenon (quiescence, activation, acceleration, etc.).

The interferometric measurements are freely accessible to everybody through the Portal. In addition, public administrations, both at central and at local level, as well as research institutes, universities, etc., can make agreements with the MATTM to download the data.

PST_ERS_T129_F819_CL003_TEANO_A																			
FID	Shape	code	vel	v_stddev	coherence	v_1992	vstd_1992	v_1993	vstd_1993	v_1994	vstd_1994	v_2000	vstd_2000	d19920614	d19930110	d19930214	d19930321	d19930425	
0	Point	A1G3O	1.95	0.56	0.7	-999	-999	8.58	3.26	-999	-999	3.51	12.31	4.96	0	-10.39	-2.8	-2.61	-1.93
1	Point	A1G3T	-0.79	0.65	0.75	-999	-999	1.54	6.67	-999	-999	3.7	-13.15	8.6	0	-6.06	-2.05	-3.92	5.71
2	Point	A1G3V	-3.14	0.58	0.76	-999	-999	-13.12	5.67	-999	-999	7.04	-19.79	6.75	0	-0.82	7.28	5.31	-9.21
3	Point	A1G3	-8.01	0.58	0.79	-999	-999	-22.54	3.85	-999	-999	7.64	-14.01	9.05	0	-1.71	0.85	3.48	-2.16
4	Point	A1G3Y	1.25	0.37	0.83	-999	-999	-0.91	6.91	-999	-999	2.67	-3.33	2.8	0	11.94	2.53	2.79	-10.27
5	Point	A1G3E	-5.63	0.55	0.7	-999	-999	-12.89	6.93	-999	-999	3.77	-9.51	3.42	0	-12.56	-0.63	-4.37	-7.44
6	Point	A1G4A	-4.65	0.5	0.88	-999	-999	-19.45	4.58	-999	-999	6.39	-21.07	3.35	0	-5.13	-3.35	0.06	-1.41
7	Point	A1G4G	0.44	0.61	0.7	-999	-999	8.58	4.26	-999	-999	3.31	-3.7	3.09	0	-9.09	-5.26	-4.67	-4.41
8	Point	A1G4H	0.54	0.47	0.65	-999	-999	7.86	3.81	-999	-999	5.73	-1.54	3.73	0	-0.28	-1.62	-2.49	-2.95
9	Point	A1G4L	-1.68	0.59	0.9	-999	-999	-3.65	3.24	-999	-999	3.93	-20.19	4.45	0	1.64	4.97	3.33	10.18
10	Point	A1G4M	-4.15	0.58	0.79	-999	-999	2.81	5.78	-999	-999	5.78	-19.09	3.06	0	15.56	14.81	1.24	12.49
11	Point	A1G4O	-9.95	0.63	0.77	-999	-999	-30.76	4.9	-999	-999	3.84	-27.63	6.67	0	-19.22	-13.1	-14.25	-14.28
12	Point	A1G4P	-10.84	0.61	0.92	-999	-999	-42.02	5.63	-999	-999	6.47	-26.34	5.49	0	-12.68	-11.6	-10.23	-12.75
13	Point	A1G4Q	-3.35	0.57	0.85	-999	-999	-16.65	3.51	-999	-999	12.58	-16.13	5.22	0	0.81	2.48	-0.61	-0.33
14	Point	A1G4R	0.61	0.39	0.93	-999	-999	-1.36	1.43	-999	-999	2.01	-7.47	3.43	0	0.87	-0.68	-1.54	-1.26
15	Point	A1G4U	-3	0.4	0.86	-999	-999	-12.38	3.46	-999	-999	1.46	0.95	4.99	0	-1.89	-9.9	-15.02	-8.97
16	Point	A1G4O	-4.24	0.51	0.67	-999	-999	-1.49	7.8	-999	-999	4.08	-4.63	5.64	0	-13.67	-13.88	-2.26	-1.84
17	Point	A1G4I	-6.41	0.52	0.89	-999	-999	-16.09	3.41	-999	-999	2.92	-11.65	4.18	0	-6.18	-0.96	-2.62	-2.18
18	Point	A1G4E	0.63	0.38	0.96	-999	-999	-2.74	1	-999	-999	1.53	-4.51	2.4	0	-3.39	-5.15	-5.2	-6
19	Point	A1G4T	-0.39	0.42	0.8	-999	-999	7.48	6.23	-999	-999	4.74	-5.21	1.91	0	-15.32	-14.73	-11.42	-10.32
20	Point	A1G48	1.49	0.41	0.85	-999	-999	5.06	2.63	-999	-999	1.72	2.71	2.89	0	-2.84	-8.23	-6.16	-6.9
21	Point	A1G5A	0.84	0.43	0.83	-999	-999	1.47	2.1	-999	-999	5.22	-2.18	2.18	0	1.58	1.74	0.63	0.2
22	Point	A1G5B	0.92	0.47	0.7	-999	-999	6.89	5.82	-999	-999	3.51	-0.43	5.32	0	-5.41	-1.57	-4.67	-4.84
23	Point	A1G5C	-0.18	0.48	0.83	-999	-999	-0.28	3.84	-999	-999	1.41	-11.65	4.42	0	-10.22	-11.52	-5.81	-1.88

Fig.2.15 Example of PS datasheet

2.5 Basic statistics

Some basic information on the statistical analysis of data. Data can be distributed (spread out) in different ways. It can be spread out more on the left or more on the right or it can be all jumbled up (Fig. 2.16).

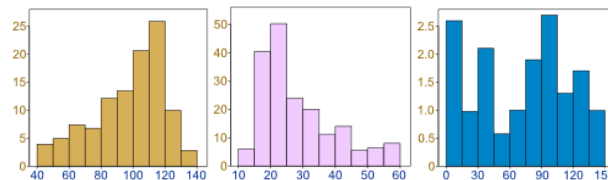


Fig. 2.16

If a variable (X values) can take on any value between two specified values, it is called a continuous variable; otherwise, it is called a discrete variable.

Just like variables, probability distributions can be classified as discrete or continuous.

With a discrete probability distribution, each possible value of the discrete random variable can be associated with a non-zero probability. Thus, a discrete probability distribution can always be presented in tabular form.

A continuous probability distribution differs from a discrete probability distribution in several ways. The probability that a continuous random variable will assume a particular value is zero. As a result, a continuous probability distribution cannot be expressed in tabular form. Instead, an equation or formula is used to describe a continuous probability distribution.

Even though the distribution of X values will be discrete, represented by a histogram or bar chart, this distribution can be approximated by a normal distribution, which is continuous.

A continuity correction factor is used when you approximate a discrete probability distribution with a continuous probability distribution.

For example, a binomial distribution can be approximated with a normal distribution (Fig. 2.17).

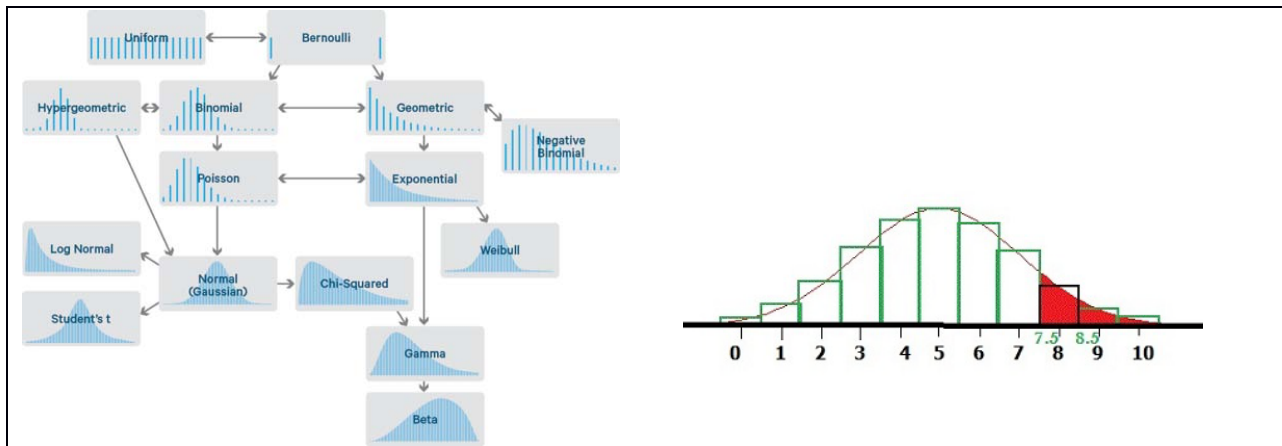


Fig. 2.17 Approximate a discrete probability distribution with a continuous probability normal distribution.

The normal distribution is a commonly encountered continuous probability distribution. There are many cases where the data tends to be around a central value with no bias left or right, and it gets close to a normal distribution.

The normal distribution is useful because of the central limit theorem. In its most general form it states that averages of samples of observations of random variables become normally distributed when the number of observations is sufficiently large.

The data is normally distributed when the distribution has (Fig. 2.18):

- mean = median = mode
- symmetry about the center
- 50% of values less than the mean and 50% greater than the mean

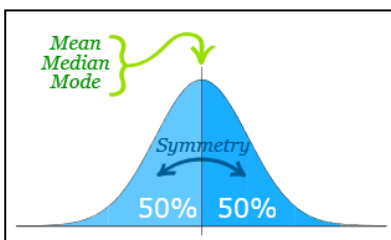


Fig. 2.18 (see text)

There are many different normal distributions (Fig. 2.19), with each one depending on two parameters: the population mean, μ , and the population standard deviation, σ .

The simplest case of the normal curves is called the standard normal distribution and it is a normal distribution with a mean of 0 and a standard deviation equal to 1.

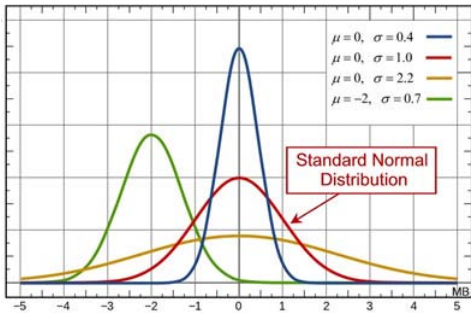
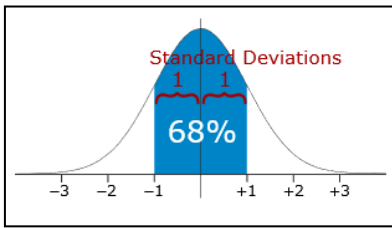
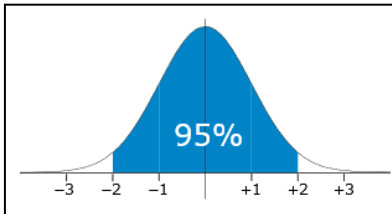


Fig. 2.19 Different normal distributions

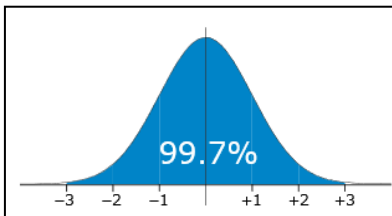
The standard deviation is a measure of how spread out numbers are. We find that generally (Fig. 2.20):



68% of values are within 1 standard deviation of the mean



95% of values are within 2 standard deviations of the mean



99,7% of values are within 3 standard deviations of the mean

Fig. 2.20 Standard deviations

It is good to know the standard deviation, because we can say that any value is:

- likely to be within 1 standard deviation (68 out of 100 should be)
- very likely to be within 2 standard deviations (95 out of 100 should be)
- almost certainly within 3 standard deviations (99,7 out of 100 should be)

The number of standard deviations from the mean is also called the "Standard Score", "sigma" or "z-score" (Fig. 2.21).

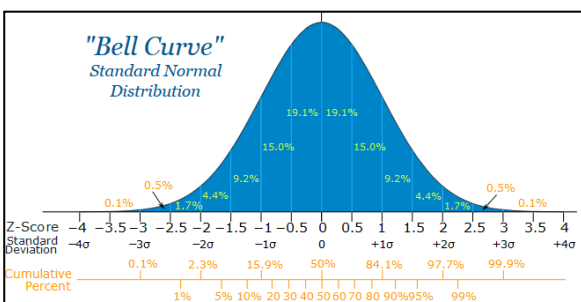


Fig. 2.21 Z-score

We can take any Normal Distribution and convert it to The Standard Normal Distribution.

To convert a value to a Standard Score ("z-score") (Fig. 2.22):

$$z = \frac{x - \mu}{\sigma}$$

- z is the "z-score" (Standard Score)
- x is the value to be standardized
- μ is the mean
- σ is the standard deviation



Fig. 2.22 (see text)

The interval about the mean, containing 50% of the data, is the interquartile range, IQR.

When working with box plots (Fig. 2.23), the IQR is computed by subtracting the first quartile (Q1) from the third quartile (Q3).

In a standard normal distribution: $IQR = Q3 - Q1 = 0.67448 - (-0.67448) = 1.34896$.

In any normal distribution (Fig.): $IQR = Q3 - Q1 = 0.67448\sigma - (-0.67448\sigma) = 1.34896\sigma$.

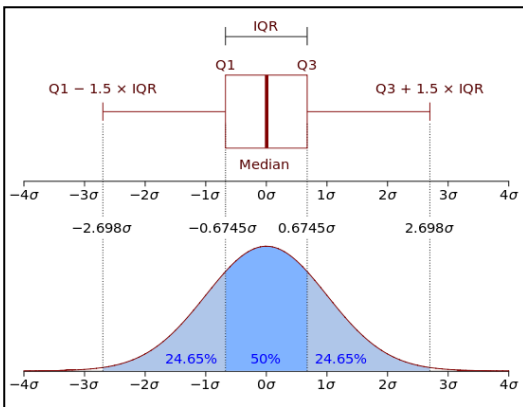


Fig. 2.23 Box plot and normal distribution

Skewness is the degree of distortion from the symmetrical bell curve, or normal distribution, in a set of data. Skewness can be negative, positive, zero or undefined (Fig. 2.24).

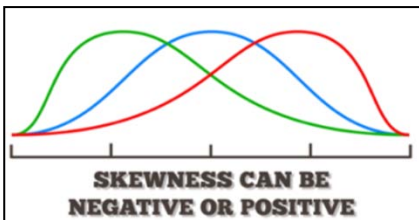


Fig. 2.24 (see text)

Kurtosis measures extreme values in either tail (Fig. 2.25).

Distributions with a positive value tells you that you have heavy-tails (i.e. a lot of data in your tails).

A negative value means that you have light-tails (i.e. little data in your tails).

The standard normal distribution has a kurtosis of 3.

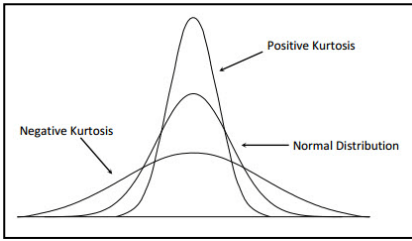


Fig. 2.25 (see text)

The value of *inner fence* is $Q1 - 1.5 * IQR$ and $Q3 + 1.5 * IQR$. At the same time, the value of *outer fence* is $Q1 + 3 * IQR$ and $Q3 + 3 * IQR$. The data between inner and outer fence values are called (*possible/suspected*) *outliers*; outside the fences they are called the *extreme (probable) outliers* (Fig. 2.26).

Outliers is an observation point that is distant from other observations and they are often bad data points/errors. But they should be investigated carefully. Often they contain valuable information about processes (like geological phenomena) under investigation. Before considering the possible elimination of these points from the data, one should try to understand why they appeared and whether it is likely similar values will continue to appear.

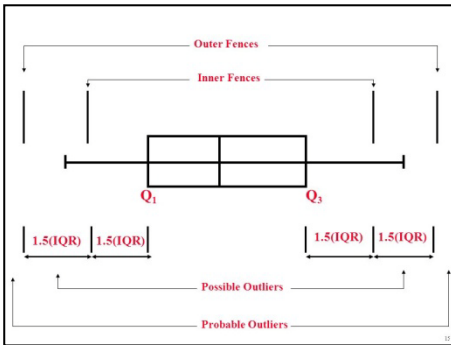


Fig. 2.26 - Outliers evaluation

2.6 PSs data mining. How make selection in a large dataset

Data mining is the process of sorting through large datasets to identify patterns and establish relationships to solve problems through data analysis. Data mining parameters include sequence or path analysis, classification, clustering and forecasting. We used classification and clustering.

2.6.1. PSs Classification using frequency distribution

From a table like that in Fig. 2.15, it is possible to obtain the frequency histogram of PSs Vmean values (Fig. 2.27). The frequency histogram is used to describe the main statistical features of an entire native dataset that, generally, is not a normal distribution because mean and median are quite different, skewness is negative and kurtosis is > 3 .

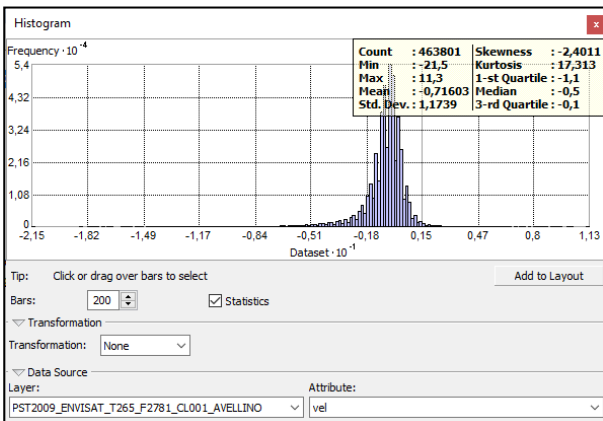


Fig. 2.27 Frequency distribution histogram, with statistics, of Vmean of an ENVISAT dataset with 463801 PSs.

In particular, the statistical parameters, 1st and 3rd Quartile (Q1 and Q3), are used for IQR calculation; so it is possible to compute the PS Normal, Outlier and Extreme-Outlier intervals, or subsets, in terms of Vmean values (Table 2.3).

Boundary (fences) calculation	Boundary values as Vmean	unit	Intervals or subsets
Q1	-1,10	mm/yr	
Q3	-0,10	mm/yr	
IQR = (Q3 - Q1)	1,00	mm/yr	
			PS PROBABLE OUTLIERS
[Q3 + (3×IQR)]	2,9	mm/yr	PS POSSIBLE OUTLIERS
[Q3 + (1.5×IQR)]	1,4	mm/yr	PS NORMAL DISTRIBUTION
[Q1 - (1.5×IQR)]	-2,6	mm/yr	
[Q1 - (3×IQR)]	-4,1	mm/yr	PS POSSIBLE OUTLIERS
			PS PROBABLE OUTLIERS

Table 2.3 Large dataset PSs classification using frequency distribution.

In Fig. 2.28 it is represented the histogram relative to the only PS normal subset ($-2.6 < Vmean < 1.4$) extract by native dataset, according to the Table ; the frequency distribution is discret but it can be represented like a normal distribution (continuous) because the number of observations is sufficiently large.

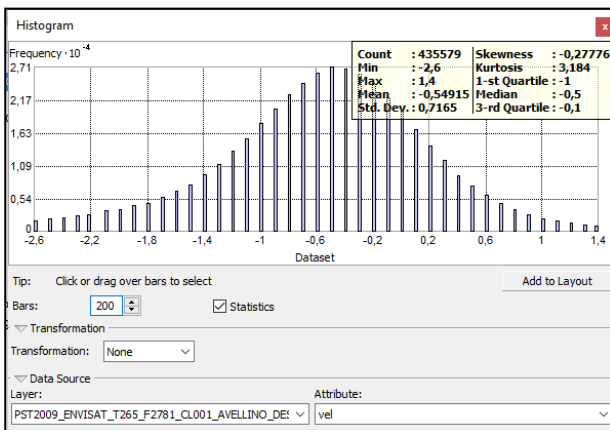


Fig. 2.28 Frequency distribution histogram of PSs normal subset derived from dataset of Table 2.3 above. The new dataset is composed by 435579 PSs (28222, 6%, PSs less respect to the native dataset) with a normal distribution: mean and median are almost the same.

In Fig. 2.29 it is represented the histogram relative to the only PS subsets external to inner fences ($Vmean < -2.6$ and > 1.4) extract by native dataset, according to the Table 2.3. There are two subsets (negative and positive outliers) with frequency distributions that seems like geometrical (discrete) or exponential (continuous) distribution.

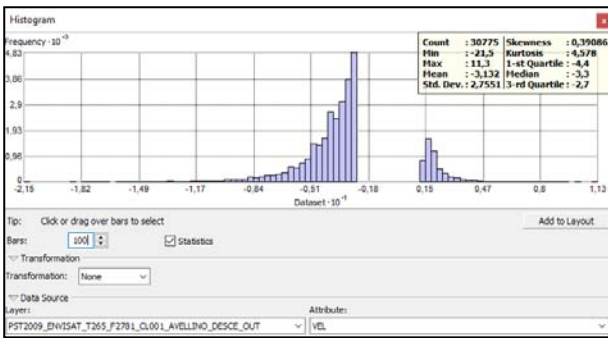


Fig. 2.29 histogram relative to the only PS subsets external to inner fences

Therefore it is possible to analyze different categories of data, statistically separated (or filtered) by the initial dataset, on the basis of the Vmean values. For example, the high negative velocity values in the dataset, i.e. negative outliers subset, are probably due to the occurrence of local phenomena (landslides and deep seated gravitational slope deformations) or compaction of sediments (geotechnical subsidence). Instead, slow or very slow subsidences or uplifts, with wider areal extent, regional or sub-regional, are probably included in the normal distribution subset and they can be relative to tectonic deformation.

2.6.2. PSs mean velocity values spatial clustering

PSs are spatial data, that is data related to space (Güting, 1994). The space of interest is the two-dimensional abstraction of the surface of the Earth where *"Everything is related to everything else but near things are more related than distant things"* is the first law of geography (Tobler, 1970).

In spatial data sets, clustering permits a generalization of the spatial component like explicit location and extension of spatial objects which define implicit relations of spatial neighborhood. Current spatial clustering techniques can be broadly classified into three categories; partitional, hierarchical and locality-based algorithms.

In locality-based algorithms a local index of spatial autocorrelation (the degree to which nearby features are more similar than distant ones, to identify relations between proximity and intensity) needs to measure the degree of autocorrelation for each geographical feature.

- Getis-Ord G_i^* high/low clustering (Hot Spot Analysis) (Getis and Ord, 1992) (Cliff & Ord, 1973).
Identifies features which are part of "hot spots": areas with unusual clustering of high or low values, based on the value of the G_i^* score (categorized according to the standard deviation: the higher the G_i^* score, the more nearby features have high values, and viceversa (it is possible to do a density map of using the Z-Score as weight).
- Anselin local of Moran's I (Anselin, 1995). To attribute to each feature a degree of high/low autocorrelation based on its (high/low) intensity being similar/dissimilar to nearby features.

2.6.2.1 Hot Spot Analysis mapping tool (Getis-Ord G_i^*)

Hot Spot Analysis (HSA) tool (and correspondent Cold Spot) works by looking at each data feature and its neighboring features in comparison to the overall spatial distribution of the phenomenon explored. If the difference between the local sum for a feature and its neighbors is highly larger than expected (the overall sum) a hot-spot is accepted (Fig. 2.30).

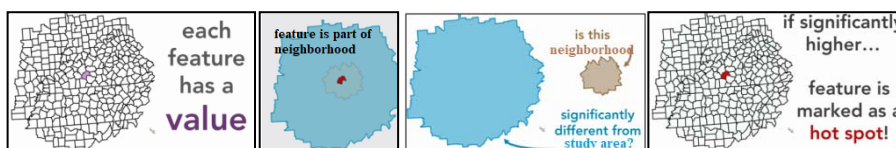


Fig. 2.30 How Hot Spot Analysis (HSA) tool works

Hot Spot local statistic, calculated for each feature (point, line, polygon) within the context of its neighbors determines:

- whether local pattern (feature and its neighbors) is statistically significant from global pattern (all features)
- null hypothesis: there is complete spatial randomness, no statistical significance exists in a set of given observations. The null hypothesis attempts to show that no variation exists between variables or that a single variable is no different than its mean. It is presumed to be true until statistical evidence nullifies it for an alternative hypothesis.

Hot Spot local statistic outputs produces:

- Z scores(standard deviations) and P values (probability). A high Z score and small P value for a feature indicates a significant hot spot. A low negative Z score and small P value indicates a significant cold spot. The higher (or lower) the Z score, the more intense the clustering. A Z score near zero means no spatial clustering.
- Hot spot: statistically significant cluster of features with high values
- Cold spot: statistically significant cluster of features with low values

The resultant Z score tells where features with either high or low values cluster spatially (Fig. 2.31).

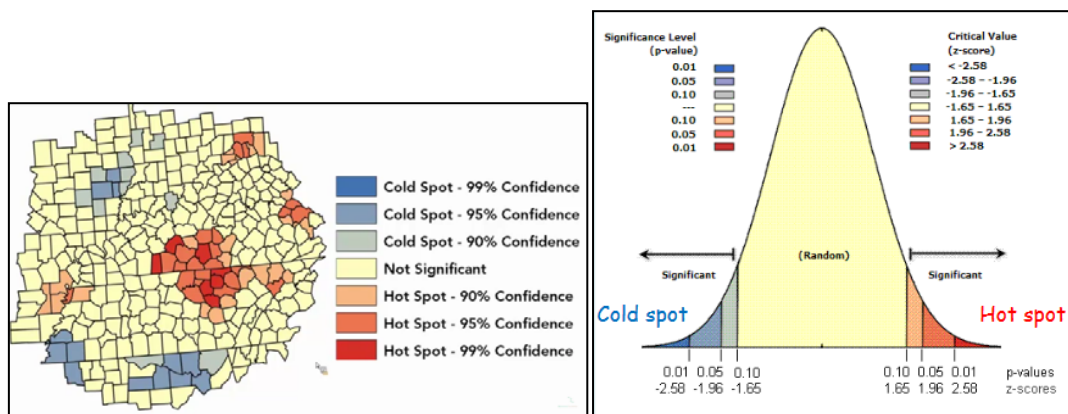


Fig. 2.31 Z score tells where features with either high or low values cluster spatially

Given a set of geo-referenced data points, the Getis–Ord G_i^* statistic identifies hot-spots of points with values higher in magnitude than one might expect by a random chance.

The G_i^* statistic measures the degree of spatial clustering of a local sample and how different it is from the expected value. It is calculated as the sum of the differences between values in the local sample and the mean, and is standardized as a z-score with a mean of zero and a standard deviation of 1.

Concentration of positive G_i^* represent clusters that are, on average, greater than the mean (Hot-spots); concentration of negative values represent clusters that are less than the mean (Cold-spots).

2.6.2.2 Cluster and Outlier Analysis mapping tool (Anselin Local Moran's I)

The Cluster and Outlier Analysis (COA) tool calculates a I index.

A positive value for I indicates that a feature has neighboring features with similarly high or low attribute values; this feature is part of a cluster. A negative value for I indicates that a feature has neighboring features with dissimilar values; this feature is an outlier. In either instance, the p-value for the feature must be small enough for the cluster or outlier to be considered statistically significant. The cluster/outlier type (COType) field distinguishes between a statistically significant cluster of high values (HH), cluster of low values (LL), outlier in which a high value is surrounded primarily by low values (HL), and outlier in which a low value is surrounded primarily by high values (LH).

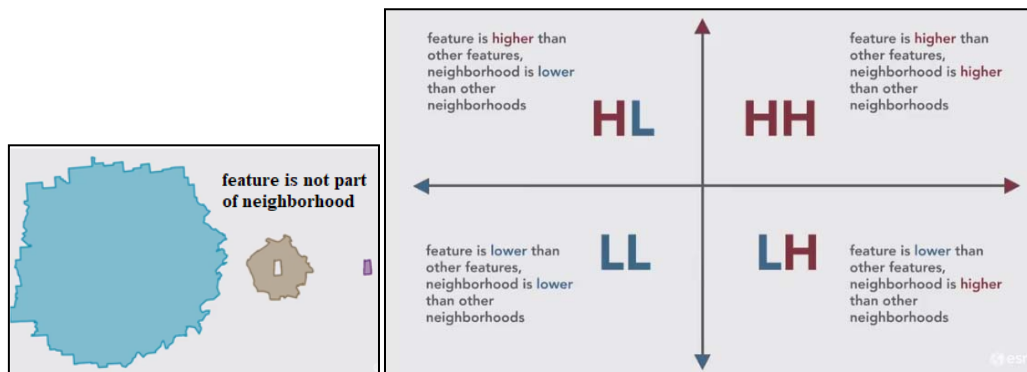


Fig. 2.32 How Cluster and Outlier(COA) tool works

A high positive Z score for a feature indicates that the surrounding features have similar values (either high values or low value). The COType field indicates HH for a statistically significant (0.05 level) cluster of high values and LL for a statistically significant (0.05 level) cluster of low values.

A low negative Z score for a feature indicates a statistically significant (0.05 level) spatial outlier. The COType field indicates if the feature has high value and is surrounded by features with low values (HL) or if the feature has a low value and is surrounded by features with high values (LH).

The input field should contain a variety of non-negative values.

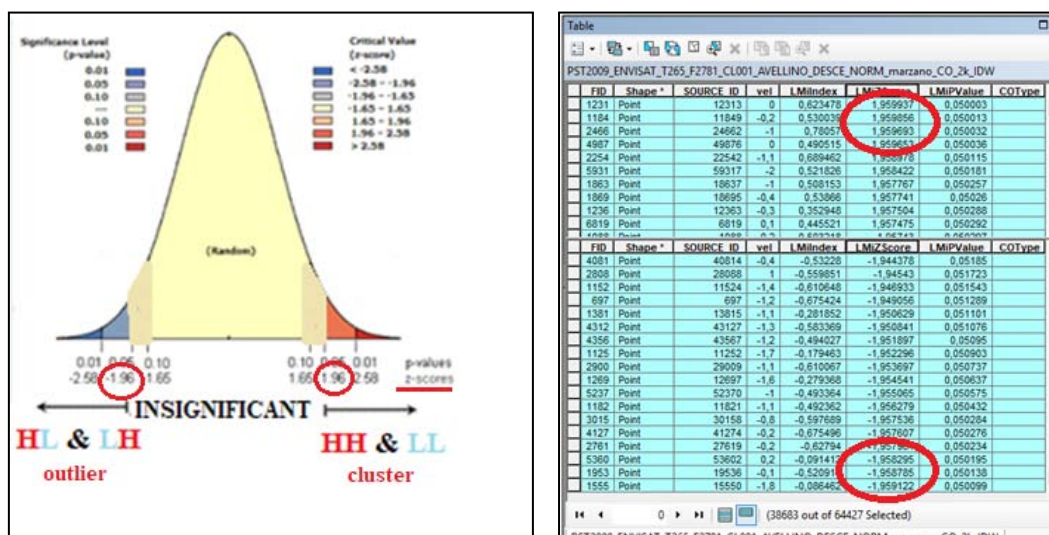


Fig. 2.33 Z score for a feature and clustering

2.7 Map interpolation: IDW method

To extract new information and meaning from the original data, usually spatial analysis is carried out with a Geographic Information System (GIS). A GIS usually provides spatial analysis tools for calculating feature statistics and carrying out geoprocessing activities as data interpolation.

There are two main groupings of interpolation techniques: deterministic and geostatistical. Deterministic interpolation techniques create surfaces from measured points, based on either the extent of similarity (Inverse Distance Weighted) or the degree of smoothing (Radial Basis Functions). Geostatistical interpolation techniques (kriging) utilize the statistical properties of the measured points. Geostatistical techniques quantify the spatial autocorrelation among measured points and account for the spatial configuration of the sample points around the prediction location.

All interpolation deterministic methods have been developed based on the theory that points closer to each other have more correlations and similarities than those farther. In IDW method, it is assumed substantially that the rate of correlations and similarities between neighbors is proportional to the distance between them that can be defined as a distance reverse function of every point from neighboring points. Interpolation predicts values for cells in a raster from a limited number of sample data points. It can be used to predict unknown values for any geographic point data.

The IDW (Inverse Distance Weighted) tool uses a method of interpolation that estimates cell values by averaging the values of sample data points in the neighborhood of each processing cell (Philip and

Watson, 18982; Watson and Philip, 1985). The closer a point is to the center of the cell being estimated, the more influence, or weight, it has in the averaging process.

Inverse distance weighted (IDW) interpolation determines cell values using a linearly weighted combination of a set of sample points. The weight is a function of inverse distance.

This method assumes that the variable being mapped decreases in influence with distance from its sampled location. If the distance is reduced and approaches 0, the relative weight of the known point increases substantially. This causes the IDW is considered an exact interpolator: the expected value at a truly sampled point will be exactly the same as the measured value. An interpolation technique that predicts a value that is identical to the measured value at a sampled location is known as an exact interpolator. An inexact interpolator predicts a value that is different from the measured value.

In this work, after the statistical operations of selection of the PS data, the IDW interpolation method is used for the generation of areal maps of average velocity ground deformation starting from PS point data.

2.8 Time series

An ordered sequence of values of a variable at equally spaced time intervals is called time series.

The usage of time series models is twofold:

- obtain an understanding of the underlying forces and structure that produced the observed data
- fit a model and proceed to forecasting, monitoring or even feedback and feedforward control.

A time series that consists of single observations recorded sequentially over equal time increments is a "univariate time series".

With a flat looking time series, without trend, where the mean, variance and autocorrelation structure do not change over time, the common assumption is that the data and the process are stationary.

Many time series display seasonality, periodic fluctuations.

There are a number of approaches to modeling time series. One approach is to decompose the time series into a trend, seasonal, and residual component. Generally the parameters of interest in PS position time series are the velocities, their associated uncertainties, and accelerations/deceleration.

In this work it is limited only to a visual inspection of a significative sample of PSs time series.

2.9 Selection, Analysis and Mapping Procedures in the various case studies

- Monte Marzano PS ascending and descending subsets have been analyzed taking into account:
 - whole native datasets, that is containing all normal and outliers PSs;
 - hot spot analysis (Getis-Ord G_i^*) applied on PSs classified as belonging to a normal frequency distribution;
 - cluster and outlier analysis (Anselin Local Moran's I) applied on PSs classified as belonging to a normal frequency distribution.

The HSA was applied, according to Perrone et al., 2013, to verify the results applying it to both datasets, ascending and descending, considering that the authors in their work used only the descending LoS mean velocity values.

They used the HSA tool to calculate the Getis-Ord G_i^* (Getis and Ord, 1992) statistics for PSs with a coherence threshold greater or equal than 0.8 (with coherence ranging from 0 to 1, Ferretti et al., 2000), in order to obtain higher quality of data. Here in it was applied on PSs classified as belonging to a normal frequency distribution.

HSA was used for identification of iso-kinematic domains and their boundaries (IKB), without allowing the evaluation of the velocity gradient across them. Iso-kinematic boundaries and domains must be compared to geological data. They can represent land sectors characterized by homogeneous kinematic behaviour and the iso-kinematic boundaries are statistical limits that bound them. Boundary geometry can be very straight or curvilinear, very narrow (less than one kilometre) with high velocity gradients or very wide with gentle gradients (Fig. 2.34).

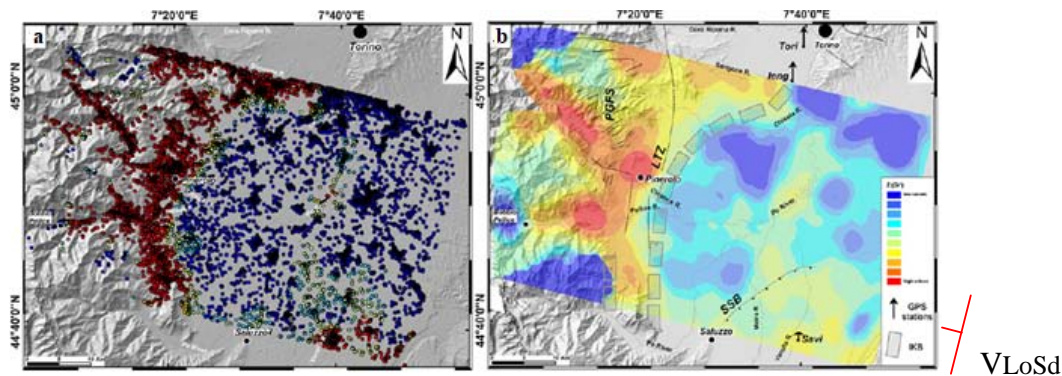


Fig. 2.34 (a) Hot Spot results calculated with $d = 2.5$ km: red and blue points represent high and low $Z(Gi^*)$ values; (b) Iso-Kinematic Map (IKM 2), expressed in high and low values of $Z(Gi^*)$, in red and blue areas, respectively. Rectangles filled with grey solid lines show the Iso-Kinematic Boundaries. (from Perrone et al., 2013 modified).

The HSA and COA provided comparable results in terms of PSs spatial clustering but, as visible in figures, better graphics with COA has made us prefer it for the subsequent interpolation processing.

They were achieved:

- a vertical V_{mean} deformation map, by IDW interpolation with cellsize of 50×50 m, about ERS (1992-2000) and ENVISAT (2003-2010) native PS datasets;
 - a vertical V_{mean} deformation map, by IDW interpolation with cellsize of 50×50 m, about ERS (1992-2000) and ENVISAT (2003-2010) with COA applied on PSs classified as belonging to a normal frequency distribution;
- Lower Volturmo Plain PS ascending and descending subsets have been analyzed taking into account:
- whole native datasets, that is containing all normal and outliers PSs;
 - cluster and outlier analysis (Anselin Local Moran's I) applied on PSs classified as belonging to a normal frequency distribution.

They were achieved:

- a vertical V_{mean} deformation map, by IDW interpolation with cellsize of 50×50 m, about ERS (1992-2000), RADARSAT (2003-2007) and ENVISAT (2003-2010) native PS datasets;
 - a vertical V_{mean} deformation map, by IDW interpolation with cellsize of 50×50 m, about ERS (1992-2000) and ENVISAT (2003-2010) with COA applied on PSs classified as belonging to a normal frequency distribution;
- Colfiorito, L'Aquila and Lunigiana case studies have been analyzed taking into account a visual inspections of a significative sample of PSs time series. In L'Aquila case study a set of IDW deformation maps were realized to show the temporal ground displacement change.

CHAPTER 3 - GEOLOGICAL FRAMEWORK

3.1 The Apennines tectonic framework

The peri-Mediterranean orogenic belts (Alps, Apennines, Carpathians, Dinarides, Albanides, Hellenides, Betic Cordillera, Rif, Maghrebides; Fig. 3.1) evolved within the framework of Africa–Eurasia major plate convergence from Late Cretaceous to Quaternary (e.g. Dewey et al., 1989; Mazzoli and Helman, 1994; Schettino and Turco, 2011, and references therein), accompanied by the motion of minor blocks such as Corsica–Sardinia (of European origin) and Adria, of African affinity (Turco et al., 2012, and references therein).

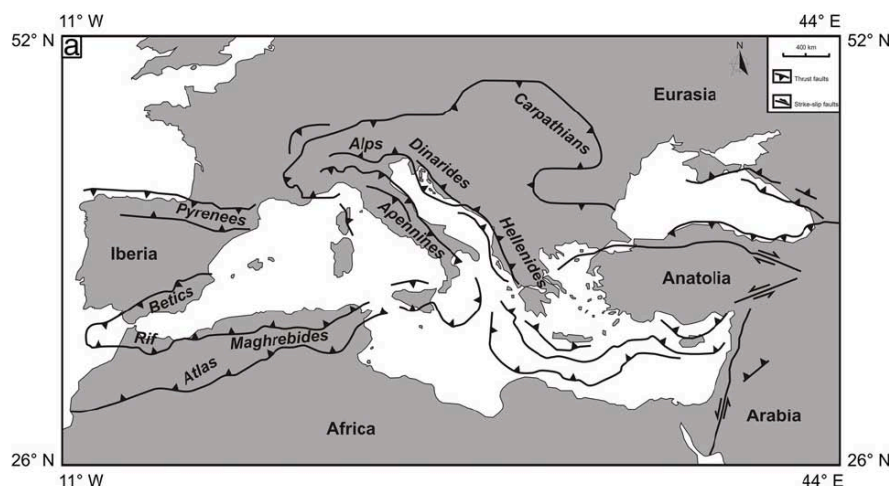


Fig. 3.1 Tectonic sketch map of the Mediterranean region, with location of the Alpine system orogenic belts (from Macchiavelli et al., 2012).

The peri-Mediterranean mountain belts are characterised by markedly curved geometries with crustal/lithospheric extension affecting the concave side of the arcs (Fig. 3.1). The coexistence of crustal shortening and extension, and the origin of the arcuate shape, has long been discussed (e.g. Andrieux et al., 1971; Bouillin, 1984; Channell et al., 1979; Edwards and Grasemann, 2009; Faccenna et al., 2004; Malinverno and Ryan, 1986). The most widely accepted interpretation, which is supported by the presence of Wadati–Benioff zones, space-time migration of volcanic arcs and magmatism and by the independence of the direction of retreat from regional plate movements, is that of roll-back, or retreat, of subduction zone formed of portions of oceanic lithosphere, which generated extensional basins (e.g., the Liguro-Provençal and Tyrrhenian basins) surrounded by curved mountain belts above the passively subducting slabs. Such processes are very well documented in the Tyrrhenian Sea–Apennines–Calabrian Arc–Sicilian Maghrebides system (e.g. Malinverno and Ryan, 1986; Kastens et al., 1988; Kastens and Masclé, 1990; Patacca et al., 1990; Doglioni et al., 1991; Patacca and Scandone, 1989, 2003; Marani et al., 2004; Rosenbaum and Lister, 2004; Carminati et al., 2010; Fig. 3.2).

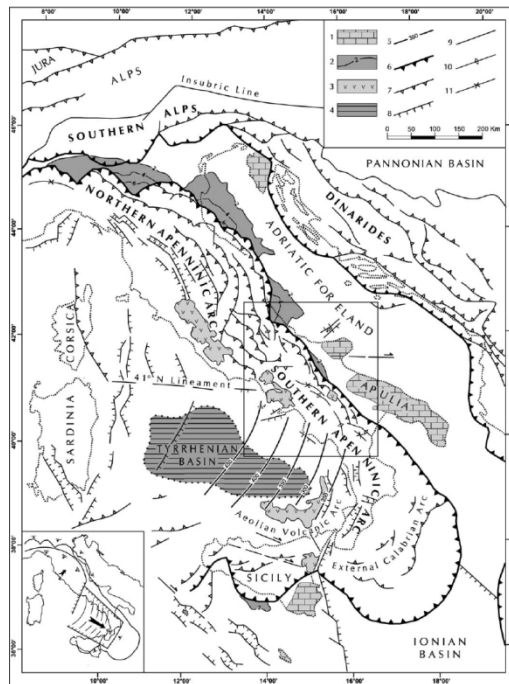


Fig. 3.2 Structural sketch of the Italian Peninsula and surrounding areas showing the northern and southern Apennines arcs. In the lower left, the present-day differential sinking of the foreland lithosphere in the northern and southern Apennines. Large arrows: directions of the last orogenic transport; small arrows: dip of the lower plate. 1) Mesozoic-Tertiary carbonates of the foreland areas. 2) Depth (in km) of the base of the Pliocene-Pleistocene deposits in the Apennine and Sicily foredeep basins. 3) Major Quaternary volcanic edifices. 4) Tyrrhenian areas floored by oceanic crust or thinned continental crust. 5) Wadati-Benioff zone in the Southern Tyrrhenian area (depths in km). 6) Front of the Maghrebides, Apennines, Southern Alps and Dinarides. 7) Other major thrusts, including the front of the Alps. 8) Normal faults. 9) High-angle faults. 10) Anticline axis. 11) Syncline axis (from Patacca and Scandone, 2003).

The Tertiary tectonic evolution of such a system involved the consumption of most of the Neo-Tethyan oceanic lithosphere originally interposed between the continental paleomargins. Subduction-accretion gave rise to the Ligurian accretionary complex (Ogniben, 1969; Knott, 1987; Bonardi et al., 1988a), whereas remnants of the overriding plate are preserved as continental crust units of the Calabrian Arc (e.g., Ciarcia et al. 2012, and references therein; Fig. 3.3).

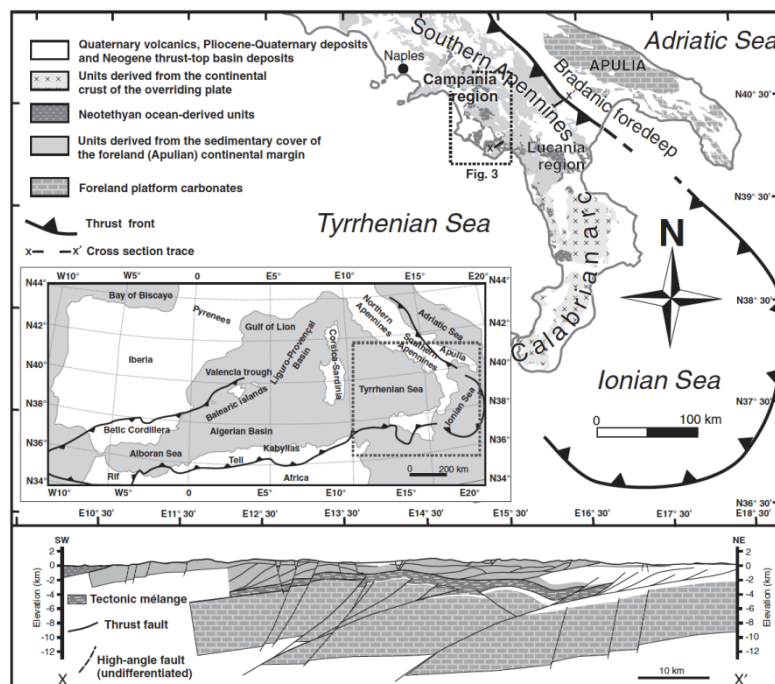


Fig. 3.3 Tectonic sketch map of southern Italy, showing location of the remnants of the continental crust in Calabria (after Ciarcia et al., 2012).

Back-arc extension and sea-floor spreading in the southern Tyrrhenian Sea occurred in Late Miocene–Quaternary times, (e.g. Sartori, 2003, and references therein). In particular, the Late Tortonian-Middle Pliocene rifting in the Tyrrhenian basin was characterised by an E-W oriented stretching direction, and initiated along the Sardinia margin to migrate eastwards (Sartori, 1990). During the Upper Miocene-Middle Pliocene extensional processes reached Tuscany, allowing post-orogenic basins to form (Elter, 1975; Barchi et al., 2003). Post-Middle Pliocene rifting was mostly confined to the southeastern portion of the basin, which was also affected by a strong Pleistocene subsidence (Sartori, 1990). Since Early Pleistocene, spreading (Savelli & Schreider, 1991) and stretching with a NW-SE orientation (Moussat et al., 1986; Sartori, 1990) are recognised within this portion of the basin (Fig. 3.4).

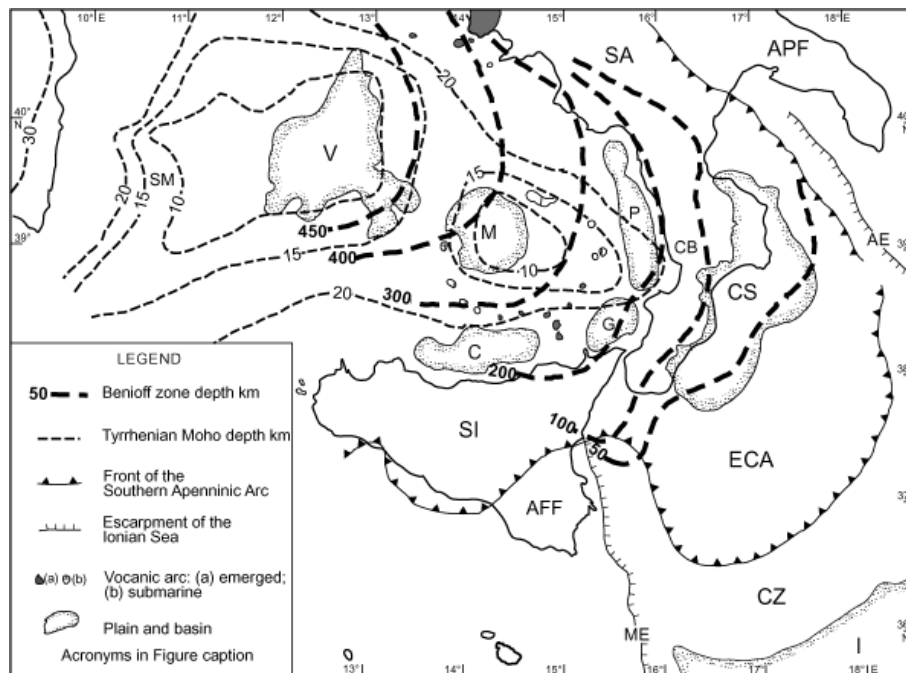


Fig. 3.4 Moho depth and Benioff zone contours in the Tyrrhenian to Ionian area. Legend: AE, Apulian escarpment; AFF, African foreland; APF, Apulian foreland; C, Cefalù basin; CS, Crotone-Spartivento basin; CZ, Cobblestone zone; ECA, External Calabria Arc; G, Gioia basin; M, Marsili basin; ME, Malta escarpment; P, Paola basin; SA, Southern Apennines; SI, Sicily; SM, Sardinia margin; V, Vavilov basin (from Sartori, 2003)

Back-arc extension in the southern Tyrrhenian basin affected the southern Apennines since Early Pleistocene times with the formation of large and thousands of m deep peri-Tyrrhenian grabens (e.g., Sartori, 1990; Savelli & Schreider, 1991). The extensional faulting of the Apennines Tyrrhenian margin were accompanied by widespread Quaternary volcanism first in Tuscany and then the Roman magmatic district (Serri et al., 2001, and references therein). In the Roman magmatic district, volcanism occurred in a first-order half-graben feature trending NW-SE (Funicello and Parotto, 1978; Faccenna et al., 1994). Quaternary spreading with a NW-SE orientation in the southern Tyrrhenian basin controlled the formation in the sothern Apennines Tyrrhenian margin, of grabens along mainly NE-SW oriented faults (Caiazzo et al., 2006 and references therein). Since the Middle Pleistocene, the peri-Tyrrhenian grabens in the northern part of southern Italy (i.e. the Garigliano and Campania plains) were affected by intense volcanism (e.g. Radicati di Brozolo et al., 1988; Brocchini et al., 2001; Rolandi et al., 2003) which, since late Quaternary times, has been active only in the volcanic centres of the Campania Plain, namely Vesuvius and Phlegrean Fields.

Roll back of the Adriatic–Apulian-Ionian foreland slab and coeval back-arc extension in the Tyrrhenian Sea resulted in significant arching of a formerly rectilinear belt (e.g. Faccenna et al., 2001, 2004; Johnston and Mazzoli, 2009; Fig. 3.2). In the Apennines, the above-described processes resulted in NE-verging thrusting. According to most interpretations, NE-directed thrusting in the Apennines and coeval SE-ward motion of the Calabria–Peloritani terrane (Bonardi et al., 2001) resulted from retreat of the composite Adriatic–Ionian slab (Malinverno and Ryan, 1986; Patacca and Sandone, 1989; Royden et al., 1987) within the general framework of NW-ward subduction beneath the Calabrian Arc. In particular, running with continuity from peninsular Italy to Sicily, the Apennines orogenic arc developed and migrated eastwards accompanying extension in the back-arc regions (Vai and Martini, 2001). In particular, the Southern Arc has migrated towards the Apulian (southern Apennines) and African (Sicily) continental

forelands; but also towards the deep marine areas off Calabria, off-scraping of the Ionian lithosphere (“oceanic foreland”) has occurred (Sartori, 2003).

The rollback process has progressively interacted with slab breakoff (Spakman and Wortel, 2004). Although various modes and timing of slab detachment beneath the Apennines have been proposed (Van der Meulen et al., 1998, 1999, 2000; Rosenbaum et al., 2008), the integration of seismic tomography evidence with robust geological data indicates that this process has become increasingly more important during the late Pliocene and Pleistocene, when the lateral migration of a slab tear within the down-going Apulian-Adriatic lithosphere, which followed a progressive SE-ward shift from c. 4 to c. 2.8 Ma, caused the formation of shallow-water to continental wedge-top basins on top of the Apennine units (Ascione et al., 2012; Mazzoli et al., 2012).

Global positioning system geodesy (D'Agostino and Selvaggi, 2004) indicates that rapid SE-ward motion of Calabria has stopped, this being consistent with reduced or negligible rates of SE-ward motion of Calabria since c. 1 Ma (Johnston and Mazzoli, 2009; Mattei et al., 2007). Slow convergence across the Africa–Eurasia plate boundary along NNW–SSE to NW–SE vectors is widely demonstrated by geodetic studies (e.g. Ward 1998). NW-oriented motion of Africa – and Adria - with respect to Europe also results in oblique convergence across most of the east–west-oriented plate boundary (Mazzoli and Helman, 1994; Di Bucci and Mazzoli, 2003). Such a convergence appears to be presently accommodated along the northern edge of Adria, as it is indicated by earthquake focal mechanisms for the Eastern Alps and related stress tensors (Montone et al. 1999, and references therein) and, in the Apennines, along a seismic belt dominated by reverse faulting offshore northern Sicily (e.g., Chiarabba et al., 2005; Billi et al., 2007) and, in the northern Apennines, by a steep blind ramp, located at around 15 to 18 km of depth in the subsurface of the Emilia foothills and adjacent Po Plain (Picotti and Pazzaglia, 2008, and references therein).

In the Apennines, E to NE directed thrusting verging towards the Adriatic-Apulian foreland ceased during the Quaternary. In particular, in the northern Apennines, E to NE verging thrust are sealed by Middle Pleistocene deposits offshore (e.g., Di Bucci and Mazzoli, 2002, and references therein), while ceasing of shortening in the southern Apennines dates back to the beginning of the Middle Pleistocene (c. 0.7 Ma; Patacca and Scandone, 2001).

Crustal shortening was followed by a final uplift involving the thrust belt and the neighbouring foredeep basin (e.g., Amato, 2000; Cinque et al., 1993; D'Agostino et al., 2001; Patacca & Scandone, 2001, 2007; Balestrieri et al., 2003; Picotti et al., 2009). A new tectonic regime was established in the chain and adjacent foothills characterized by a NE-SW oriented maximum extension (e.g., Cello et al., 1982; Cinque et al., 1993; Hippolyte et al., 1994) and by dominantly extensional faults that postdate and dissect the thrust belt (e.g. Butler et al., 2004; Caiazzo et al., 2006; Cello et al., 1982; Lavecchia et al., 1994; Calamita et al., 2000; Mirabella and Pucci, 2002; Chiaraluce et al., 2005; Mirabella et al., 2008; Ascione et al., 2013). Striking evidences of such extensional faulting are widespread, large fault-bounded intramontane basins filled with lacustrine and/or alluvial deposits, formed since the early part of the Middle Pleistocene (e.g., La Rocca & Santangelo, 1991; Ascione et al., 1992a, 1992b; Doglioni et al., 1998; Galadini, 1999; Brancaccio et al., 2000; Munno et al., 2001; Cavinato et al., 2002; Miccadei et al., 2002; D'Alessandro et al., 2003; Bosi, 2004; Galadini and Messina, 2004; Parotto et al., 2004; Moro et al., 2007; Amicucci et al., 2008; Ascione et al., 2008; Galli et al., 2010; Porreca & Mattei, 2010; 2012; Piacentini & Miccadei, 2014; Fig. 3.5).

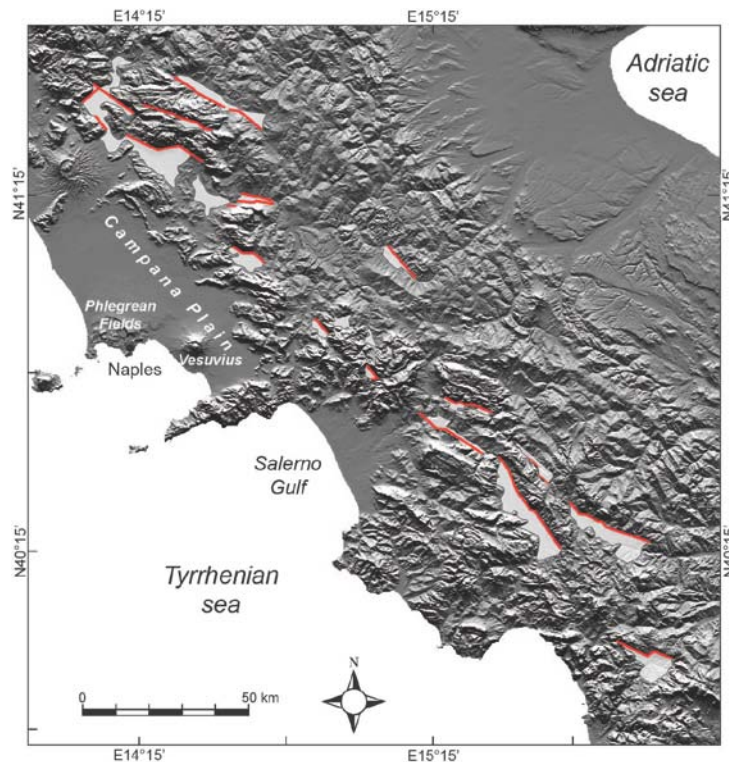


Fig. 3.5 Quaternary extensional basins of southern Italy, with indication of the generating faults

3.2 Seismotectonic framework of the Apennines

Based on available geological and geophysical information, the active tectonic behaviour of the external zones of the Apennines and adjacent foreland are characterized by a dominant NW–SE sub-horizontal compression. The related strain appears to be mainly partitioned into components of dextral strike-slip and (subordinate) reverse faulting along roughly east–west-trending structures. According to Di Bucci and Mazzoli (2003), this active deformation is an expression of the geodynamic behaviour of the Apulia–Adriatic block, which in turn finds its location within the wider framework of Africa–Europe major plate convergence. In the Po Plain area, the 2012 northern Italy earthquakes (<http://earthquake.rm.ingv.it/tdmt.php>; Ventura and Di Giovambattista, 2013) confirmed active frontal thrusting, while active tectonics in the Gargano and Tremiti areas, and focal mechanisms of the 2002 Molise earthquakes and 2013 Marche offshore earthquakes indicate that active tectonics in the Adriatic domain is mainly controlled by strike-slip crustal faults, mainly E-W oriented, dissecting the Apennine thrust belt (Di Bucci and Mazzoli, 2003; Frepoli et al., 2011; Mazzoli et al., 2014, 2015; Fig. 3.6).

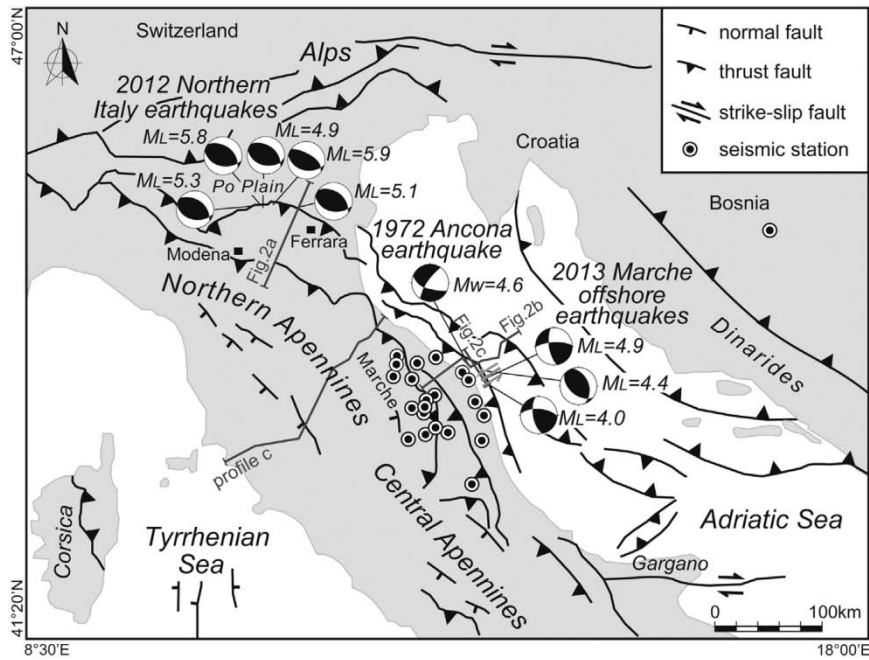


Fig. 3.6 Tectonic sketch map showing focal mechanisms for the five largest events of the 2012 northern Italy earthquakes and for the three largest events of the 2013 Marche offshore earthquakes. Grey left-lateral strike-slip fault is the seismogenic structure (Conero offshore wrench fault) interpreted by Mazzoli et al.(2014) to have generated the 2013 seismic sequence. Focal mechanism for the MW= 4.6 main shock of the 1972 Ancona earthquake (Gasparini et al., 1985; Rovida et al.,2011) is also shown, together with location of seismic stations (from Mazzoli et al., 2015).

On the other hand, a dominant NE–SW oriented extension is well established in the axial zones of the chain. Surface geology, fault-plane solutions of both strong earthquakes and background seismicity, and borehole breakouts, all indicate that normal faults control active tectonics and seismogenesis in the mountain chain (e.g. Westaway, 1992; Montone et al., 1999; Pondrelli et al., 2002, 2006; Chiarabba et al., 2005; Maggi et al., 2009; Pasquale et al., 2009; Frepoli et al., 2011; Macchiavelli et al., 2012). GPS data also show that the Apennines belt displays a distinctive NE-oriented extension (Serpelloni et al., 2005; Devoti et al., 2011; Fig. 3.7).

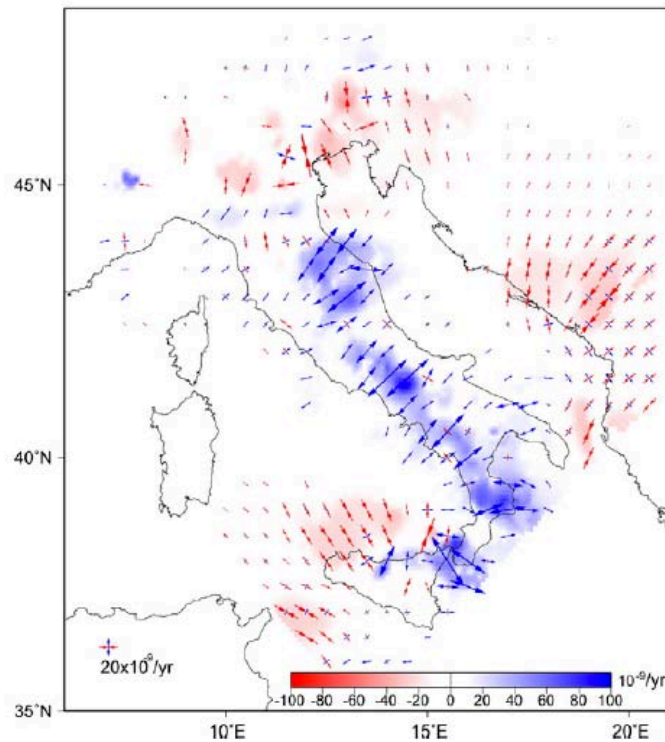


Fig. 3.7. 2D dilatation-rate map and principal strain-rate axes obtained from an interpolation of the velocity field (from Devoti et al., 2011).

At the surface, extensional processes that affect the mountain chain are expressed by widespread fault scarps, which show geomorphological or/and paleoseismological evidence of activity during the late Quaternary (e.g., Galadini et al., 1993, 1997, 1999, 2000, 2001; Pantosti et al., 1993, 1996; Michetti et al., 1995, 1996, 2000; Vittori et al., 1995; Cello et al., 1997, 2003; Galadini, 1999; Galadini and Galli, 1999, 2000; Galli et al., 2002, 2006, 2010, 2011, 2017; Galli and Galadini, 2003; Ascione et al., 2003; 2013; 2018; Cucci et al., 2004; Roberts and Michetti, 2004; Michetti et al., 2005; Caiazza et al., 2006; Moro et al., 2007; Papanikolaou and Roberts, 2007; Spina et al., 2008, 2011; Whittaker et al., 2008; Galli and Naso, 2009; Picotti et al., 2009; Di Naccio et al., 2013).

Instrumental and historical records indicate that normal faulting earthquakes occurs in a belt following the mountain belt axis, and is characterized by low to moderate magnitude events punctuated by strong earthquakes with epicentral intensities reaching X-XI MCS, and M around 7 (e.g. Boschi et al., 1997; Pondrelli et al., 2010; Scognamiglio et al., 2010; Locati et al., 2011; Serva et al., 2007; Valoroso et al., 2013; DISS Working Group, 2015; Rovida et al., 2016; Fig. 3.8; Fig. 3.9).

From north to south, the crustal seismicity shows a rotation from NW-trending alignments in the north to NNE-trending in Calabria and in the Messina strait, paralleling the rotation of the Apennines and Calabria arcs (Chiarabba et al., 2005). In the northern and southern Apennines, the NW-trending fault segments are confined within the upper 6–8 and 12–15 km of depth, respectively (Chiarabba et al., 2005; Chiarabba et al., 2009; Fig. 3.10). In the southern Apennines, the upper crustal seismic belt is 30–50 km narrow, with large earthquakes originate on ~20–40 km NW-elongated normal faults, that cut the entire upper crust down to 12–15 km depth (e.g., Bernard & Zollo, 1989; Pantosti and Valensise, 1990; Amato et al., 1992; Chiarabba et al., 2005). Background seismicity mostly occurs at the borders of the silent fault segments (Chiarabba et al., 2005).

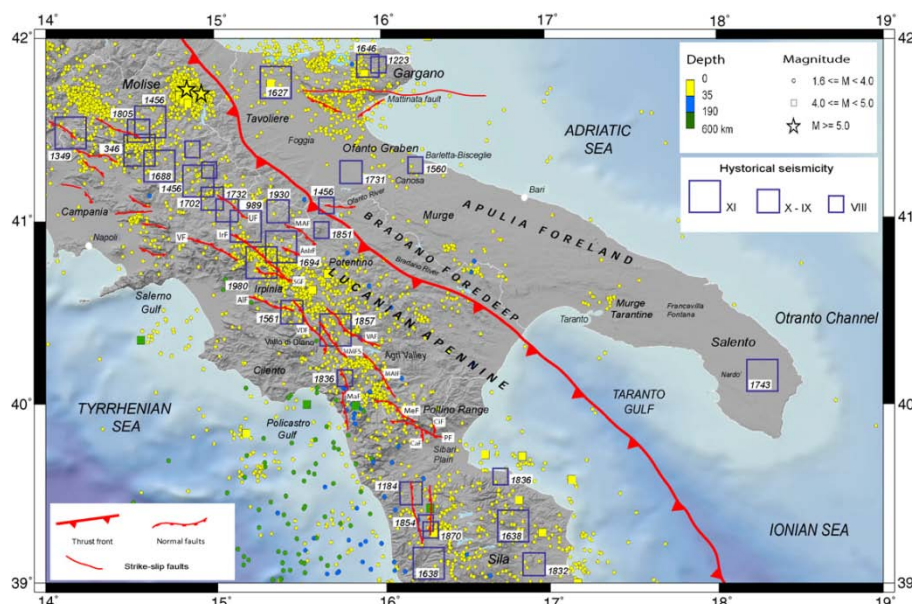


Fig. 3.8. Southern Italy historical and instrumental seismicity map. Active faults from Galadini et al. (2000). Lucanian Apennine active faults: UF, Ufita fault; MAF, Mount Mattinata–Atella fault; VF, Volturara fault; IrF, Irpinia fault; AnIrF, Antithetic Irpinia fault; SGF, San Gregorio fault; ALF, Alburni fault; VDF, Vallo di Diano fault; VAF, Val d’Agri fault; MMFS, Monti della Maddalena fault system; MALF, Monte Alpi fault; MAF, Maratea fault; MeF, Mercure fault; PF, Pollino fault; CaF, Castrovillari fault; CiF, Civita fault (from Frepoli et al., 2011).

Stemberk et al. (2018) analyzed a 3-D monitoring of strain along active faults outcropping in the central Apennines during the period 2002 – 2017 revealing that recorded fault slips correspond to the principal stress with a SW-NE orientation and slightly dipping to the SW. Fault slips is non-linear and it is affected by transient accelerations, which can last up to several months. The accelerations were induced by switching extensional and compressional stress/strain state corresponding to the principal SW-NE stress. Fault slip accelerations coincide with the periods of major seismic events that recently affected the central Apennines like the L’Aquila 2009 and Norcia 2016 earthquakes. Regarding to these two earthquakes the authors say that the recorded fault slips can be characterized as pre-seismic preceding both events.

In recent years, it has been suggested that the nucleation of normal faulting earthquakes within the framework of the active extensional stress regime can be favoured by the accumulation of pressurized CO₂-rich fluids in deep portions of the thrust belt (e.g. Miller et al., 2004; Di Luccio et al., 2010). At

depth, the coexistence of CO₂ and brine is well documented by the analysis of several wells (Inversi et al., 2013). Recently, crustal wave velocity and attenuation tomographies allowed Amoroso et al. (2017) to unravel the occurrence of brine-CO₂/CH₄ or CO₂-CH₄ mixtures at depth, underneath the epicentral area of the destructive Ms 6.9, 1980 Irpinia earthquake. According to current models, the occurrence of a deep hot source (“mantle wedge”) and the progressive dehydration of the subducted Adriatic-Apulian plate is suggested as the origin of uprising gasses (Chiarabba and Chiodini, 2013; Chiodini et al., 2013). The idea that CO₂ overpressure controls earthquake nucleation in the Apennines is based on the evidence, provided by deep boreholes, of fluids trapped at near-lithostatic pressures at depth (e.g. Chiodini and Cioni, 1989).

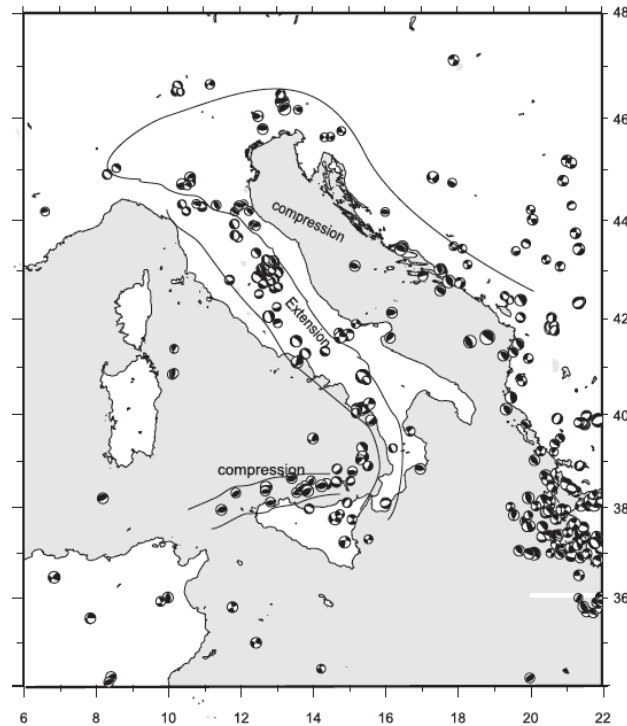


Fig. 3.9. Fault plane solutions for the $M \geq 4.5$ seismicity in the 1976-2002 time span. The extension along the Apennines belt and the compression around the Adria lithosphere and in the northern Sicily offshore are evident (from Chiarabba et al., 2005).

According to Miller et al. (2004), a sudden upward migration of CO₂ followed the two mainshocks (of magnitude 5.7 and 6.0, nine hours apart) of the 1997 Colfiorito earthquake sequence. Such mainshocks provided a transient connection between a lower zone at near-lithostatic pore pressure and crustal levels at hydrostatic pore pressure driving aftershock activity, with thousands of aftershocks that included four additional events with magnitudes between 5 and 6. Indeed, anomalously intense circulation of fluids and strong gas emissions generally follow earthquakes, especially in the northern and central Apennines (Italiano et al., 2004; Lombardi et al., 2010; Lombardi and Voltattorni, 2010).

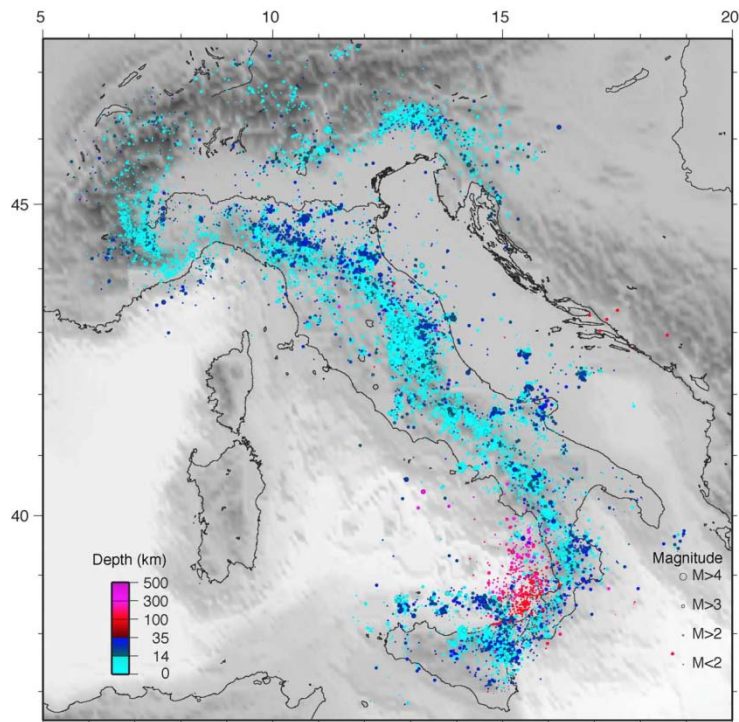
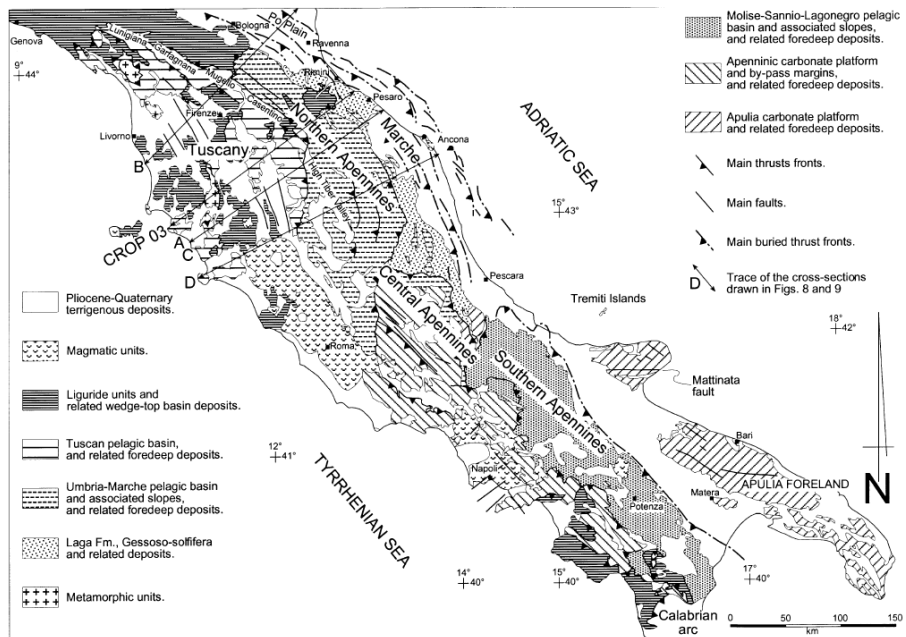


Fig. 3.10. Hypocentral distribution of about 45,000 events in the 1980-2000 time span. Colour scale, continuously varying, indicates the depth of events (blue colours for the crustal seismicity and red colours for the mantle seismicity). The different size of circles is given by the magnitude scale indicated on the lower right corner (from Chiarabba et al., 2005).

3.3 Structural setting

Although the different sectors of the Apennine chain (Fig. 3.11) chiefly result from the same regional processes, the present-day structures of the northern, central and southern parts of the thrust belt display quite variable geometries resulting in part from different styles of tectonic evolution (Mazzoli et al., 2000).



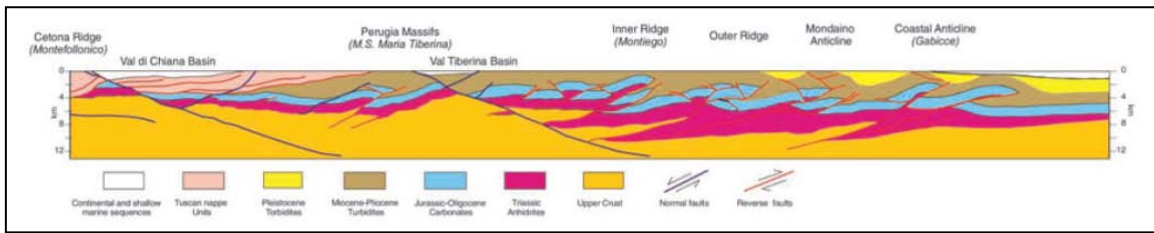


Fig. 3.11 Upper panel: Geological sketch map of peninsular Italy, from the Po Plain to the Calabrian Arc (from Di Bucci and Mazzoli, 2002), with location of the CROP 03 cross section, shown in the lower panel (from Barchi et al., 2003).

This was most probably strongly controlled, besides by the laterally varying parameters of stress, temperature, burial conditions and pore-fluid pressure, also by the original architecture of the continental paleomargin in the different areas (Mazzoli et al., 2000, and references therein). In the northern Apennines, Mesozoic rifting processes resulted in the early (middle Liassic) development of a wide basin area including fault-bounded highs and depressions (grabens/half-grabens) (e.g. Santantonio, 1993 and references therein). In the central Apennines, the basin facies above is transitional to shallow-water carbonates, whereas a further basin (Molise-Sannio) area opens to the south (Parotto and Praturlon, 1975). In southern Italy, the continental margin included a basin (Lagonegro) area, which developed since early Triassic times (e.g. Scandone, 1972; Ciarapica et al., 1990, Mazzoli, 1992), interposed between two carbonate platform domains (Mostardini and Merlini, 1986), which remained in shallow-water conditions up to Miocene times (Fig. 3.11).

3.3.1 Structure of the Northern Apennines

The northern Apennines can be divided into two broad, different structural domains: (i) the inner thrust system, which was formed in the Late Oligocene-Early Miocene (concurrently with the opening of the Liguro-Provençal Basin) and has an external front marked by the superposition of the Tuscan Nappe units on the Umbria-Marche units; an outer – Umbria-Marche - belt, which was built up since the Middle Miocene (after the Corsica rotation and concurrently with the formation of the Tyrrhenian Sea) and has an external front located in the Adriatic offshore (Barchi et al., 1998; Barchi et al., 2003) (Fig. 3.11).

The inner fold and thrust belt is composed by the stacking of several tectonic units that are, from the top: (1) The Ligurian Units, which include the Ligurian and the Subligurian Complexes. These are respectively composed of remnants of the Neo-Thetys and, in particular, of Jurassic oceanic crust and its related Jurassic-Cretaceous sedimentary cover; (2) Cretaceous-Oligocene flysch, which were thrust eastwards over the Tuscan Nappe during Late Oligocene-Early Miocene times; (3) The Tuscan Nappe, which derives from the internal Tuscan domain and includes sedimentary rocks ranging from Late Triassic evaporites to Jurassic carbonate platform, Cretaceous-Oligocene pelagic sediments and Late Oligocene-Early Miocene turbidites (Brogi and Liotta, 2005, and references therein). During the Late Oligocene-Early Miocene, the Tuscan Nappe, with the Ligurian Units at the top, were detached from the Late Triassic evaporite level and thrust over the external Tuscan domain, giving rise to the metamorphic Tuscan Nappe in the external zone.

Severe extension affected the inner belt during the Late Miocene-Middle Pliocene (in connection with the opening of the northern Tyrrhenian Sea) causing dissection of the former contractional structures, thinning of the crust and exhumation and uplift of the Apuane Alps metamorphic core complex (Elter et al., 1975; Bartolini et al., 1982; Raggi, 1985; Carmignani and Kligfield, 1990; Bernini et al., 1991; Barchi et al. 1998; Carmignani et al., 2001; Bernini and Papani, 2002; Argani et al., 2003) (Fig. 3.11). Extension is coeval with magmatism from Late Miocene (Serri et al., 1993). Middle Pliocene, southern Tuscany has been affected by rapid surface uplift (Bartolini et al., 1983; Dallmeyer and Liotta, 1998). Coeval with extension of the western sectors of the northern Apennines, thrusts were active in the Marche-Romagna area (Barchi et al., 1998). As it is shown by the CROP 03 seismic line (Barchi et al., 2003), the most significant structural feature in the upper crust of the Tuscan sector is represented by five main ENE-dipping undulate crustal scale normal faults, producing severe extension of the Tuscan crust and deeply disrupting the pre-existing compressional features. At the hanging-wall of these extensional shear zones, antithetic, high angle, west-dipping normal faults are present (Barchi et al., 1998; Boncio and Lavecchia, 2000) (Fig. 3.11). The Miocene-Pliocene, NW-SE trending intermountain basins of Tuscany are geometrically and genetically related to these shear zones (e.g., Barchi et al., 2003; Di Naccio et al., 2013). In the Late Miocene, continental to marine sediments deposited in these basins, and the Late Miocene structures and sediments were later dissected by the Pliocene-Present normal faults

(Brogi and Liotta, 2005). The low-angle normal faults include the Altotiberina Fault, which crops out west of the Tiber Basin and extends along strike up to 50 ± 60 km, deepening with a staircase trajectory to a depth of about 12 ± 14 km beneath the Umbria fold-and-thrust belt, with a total displacement of about 4 ± 5 km (Boncio and Lavecchia, 2000).

The Umbria-Marche Apennines are an arc-shaped, NE-verging, thrust-and-fold belt that involves the rocks of the sedimentary cover, which consists of Mesozoic and lower Tertiary peritidal/pelagic carbonate and marly succession, overlain by Mio-Plio-Pleistocene hemipelagic, turbiditic, and evaporitic sediments deposited in foredeep and/or wedge-top basins (e.g. De Donatis et al., 1998 and references therein) (Fig. 3.11). Underlying the sedimentary cover, the Hercynian basement is imaged in the CROP 03 deep seismic reflection profile as being faulted by SW-dipping thrusts which, within the study area, progressively uplift it from NE to SW (Pialli et al., 1998; Barchi et al., 2003). The lithological units interposed between the crystalline basement and the base of the outcropping succession (upper Triassic anhydrites and dolomites, Anidriti di Burano Fm.; Martinis and Pieri, 1964) consist of Permian red beds and Triassic continental deposits (Verrucano Formation, which crops out in Tuscany) that have been penetrated by deep wells (Anelli et al., 1994; Mazzoli et al., 2000; Mirabella et al., 2008). The sedimentary succession overlying the upper Triassic anhydrites includes lower Liassic massive platform carbonates, followed by basal cherty limestones and intercalated marls of middle Liassic to upper Jurassic age. These deposits show marked thickness and facies variability between thin condensed pelagic successions deposited on structural highs and more complete successions sedimented in deeper environments (e.g. Centamore et al., 1971; Santantonio, 1993 and references therein). Pelagic limestones and intercalated marls were mainly deposited during Cretaceous to middle Eocene times, whereas marly lithotypes are dominant in the middle Eocene to lower Miocene part of the succession (for detailed descriptions of this succession, see: Centamore and Deiana, 1986; Cresta et al., 1989). The overlying Neogene foredeep succession shows a marked sedimentary facies variability and a diachronicity from the internal to the external parts of the belt, because of the progressive foreland migration of the foredeep basin and facies differentiation within the basin (e.g. Ricci Lucchi, 1986; Menichetti et al., 1991). The most recent (Plio-Pleistocene) foredeep depocenter is located offshore in the Adriatic Sea, which represents the southward extension of the Po Basin (e.g. Pieri and Groppi, 1981; Ori et al., 1986; Argnani et al., 1991) (Fig. 3.11). Thrusts buried beneath the Adriatic Sea appear to be sealed by undeformed Middle-Upper Pleistocene deposits (e.g. Bally et al., 1986; Coward et al., 1999; Di Bucci and Mazzoli, 2002; Di Bucci et al., 2003; Tozer et al., 2006).

The late Miocene compressional structures of the Umbria-Marche region are obliquely dissected by high-angle extensional faults mostly trending N-S to NW-SE normal faults, which have been active at least since the Early or Middle Pleistocene, and bound Early/Middle Pleistocene tectonic basins filled with alluvial deposits (e.g., Blumetti et al., 1993; Calamita et al., 1994; Cello et al., 1997; Pizzi et al., 2002; Barchi et al., 2003; Galli et al., 2010).

3.3.2 Structure of the central Apennines

The central Apennines Tyrrhenian margin consists of deep graben structures, Messinian to Early Pleistocene in age, bounded by NW-SE trending faults, and by NE-SW trending transfer faults (Faccenna et al., 1994). Within the basins, volcanism related to the “Tuscany province” occurred from late Pliocene to Pleistocene in the Cimini, Tolfa and Ceriti areas, and in the Vulsini, Vico, Ernici, Sabatini and Colli Albani, with the latter ones being related to the “Roman comagmatic province” (Faccenna et al., 1994, and references therein) (Fig. 3.12).

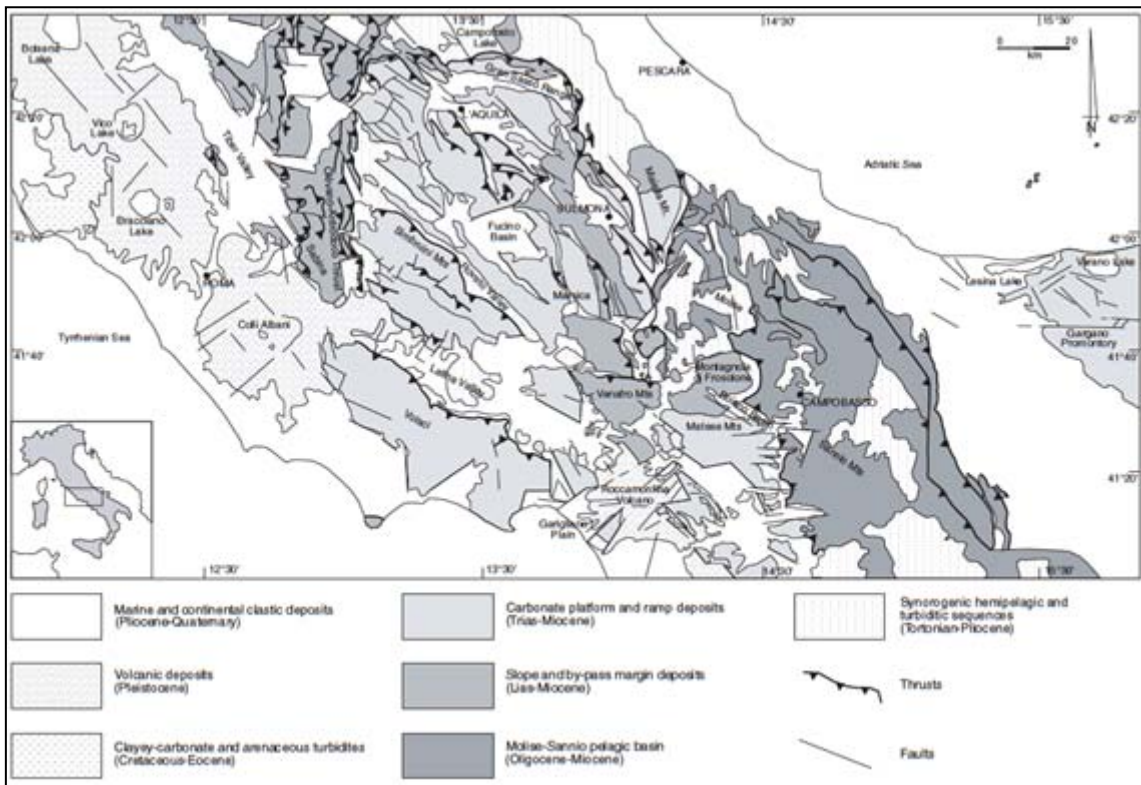


Fig. 3.12 Geological map of the central Apennines (from Mazzoli et al., 2000).

To the NE of the pery-Tyrrhenian grabens, the central Apennines fold and thrust belt is present (Fig. 3.12). It is made up of several thrust sheets progressively imbricated toward the Adriatic Sea (Accordi, 1966; Parotto and Pratlurion 1975; Bigi et al., 1990). In outcrop this region is characterised by various continental margin sedimentary successions (including carbonate platforms, by-pass margins, slopes and pelagic basins), which range in thickness from about 1000 to 5000 m (Damiani et al., 1992 and references therein). From west to east, the Sabina, Apenninic platform, Molise-Sannio and Apulian platform domains can be distinguished. The Sabina units consist of upper Triassic to Miocene sediments mainly of pelagic and slope facies, representing the southern extension of the Umbria-Marche basin (Mazzoli et al., 2000). They are arranged in at least three main N-S and NW-SE striking thrust sheets verging toward the east (Cosentino and Parotto, 1992). In the western side of this region a N-S right-lateral strike-slip fault dissects the earlier thrust structure (Alfonsi et al., 1991). The eastern tectonic boundary to this area is marked by the Olevano-Antrodoco out-of-sequence thrust (Cipollari and Cosentino, 1992) where the pelagic sediments of the Sabina region overthrust the Apenninic carbonate platform and its associated siliciclastic deposits (Parotto and Pratlurion, 1975). The Apenninic carbonate platform is formed by a shallow-water, Mesozoic carbonate succession stacked in mainly NW-SE oriented thrust sheets showing a NE transport direction (Accordi and Carbone, 1988). Along their southwestern sides, these thrust sheets are dissected by steep NW-SE trending faults. These faults bound NW-SE trending structural depressions filled with upper Miocene turbiditic deposits that are progressively younger to the NE (e.g. Cipollari and Cosentino, 1995). Structural and stratigraphic data suggest both normal (prevailing) and left-lateral strike-slip motion for these faults, with earlier transcurrent faults being reactivated as dip-slip features (Parotto and Pratlurion, 1975; Salvini, 1993; Montone and Salvini, 1993).

In the eastern Marsica region, at the eastern boundary of the Apenninic carbonate platform, the Mesozoic facies evolves from carbonate platform to Meso-Cenozoic slope facies (Colacicchi and Pratlurion, 1965; Pratlurion, 1968; Miccadei, 1993). This region is organised in a series of E to ENE verging thrusts, overprinted by N-S trending strike-slip faults (Corrado et al., 1990; Ghisetti and Vezzani, 1991; Mattei and Miccadei, 1991) (Fig. 3.12).

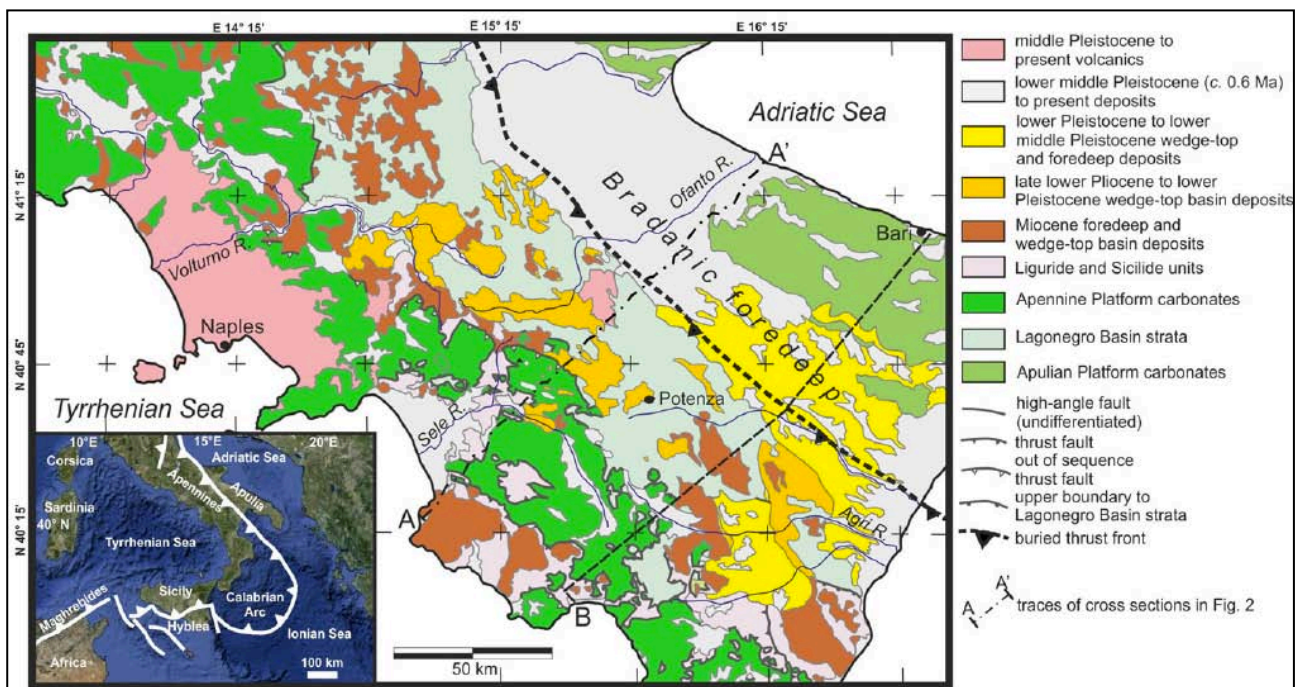
The more external Apulian carbonate platform crops out farther to the east with a predominant NNW trend of ENE-verging thrusts, offset by mainly NNW trending normal and strike-slip faults (Miccadei, 1993; Corrado et al., 1995). The carbonate platform succession consists mainly of upper Triassic-Cretaceous deposits that locally evolve upward into slope and pelagic basin facies since the Jurassic. Upward in the succession, a Langhian to Tortonian carbonate ramp unit is overlain by upper Messinian-lower Pliocene siliciclastic deposits that become progressively younger to the east (Patacca et al., 1992,

2008). Farther to the east, the Apulian carbonates, unconformably overlain by lower Pliocene hemipelagic sediments, dip under the Sannio-Molise units and under the Plio-Pleistocene foredeep deposits (Patacca et al., 1992, 2008), to crop out again in the Apulia foreland to the east. The Sannio-Molise units include Oligocene and lower Miocene pelagic basin deposits known as “Argille varicolori”. The succession evolves upward to calcarenites interfingering with marly and calcareous turbidites of Miocene age. Overlying Messinian syn-orogenic siliciclastic deposits show a more proximal facies in the Sannio units and a more distal facies in the Molise units (Tortorici, 1975; Patacca et al., 1992, 2008), indicating that these thrust sheets originated from different portions of the same basin. These units, detached from their Meso-Cenozoic substratum along the Argille varicolori level, overthrust the buried Apulian carbonates forming a N or NE vergent thrust system with widespread repetitions of the Sannio and Molise stratigraphic successions (Corrado et al., 1997).

Starting from the Late Pliocene, and mainly since the Early Pleistocene, the thrust belt has been affected by regional uplift involving also the peri-Adriatic belt (Demangeot, 1965; Dramis, 1993; D’Agostino et al., 2001; Ascione et al., 2008; Carminati & Doglioni, 2012; Faccenna et al., 2014). Coeval to uplift, extensional tectonics has affected the axial portion of the mountain belt along mainly NW-SE trending faults (Papanikolaou et al., 2005 and references therein). Such a process was accompanied by formation of lacustrine/alluvial tectonic basins within the chain (e.g., Bosi and Bertini, 1970; Bosi et al., 1995; Miccadei et al., 1998; Cavinato & De Celles, 1999; Cavinato et al., 2002; Pizzi et al., 2002; Galadini & Messina 2004; Giaccio et al., 2013).

3.3.3 Structure of the southern Apennines

Within the structure of the southern Apennines, four main regions may be distinguished: the peri-Tyrrhenian extensional margin, the southern Apennines fold and thrust belt, the Bradanic foredeep, which represents the main depozone of the Pliocene-Quaternary foreland basin system, and the Apulian promontory, which represents the orogenic foreland (Fig. 3.13).



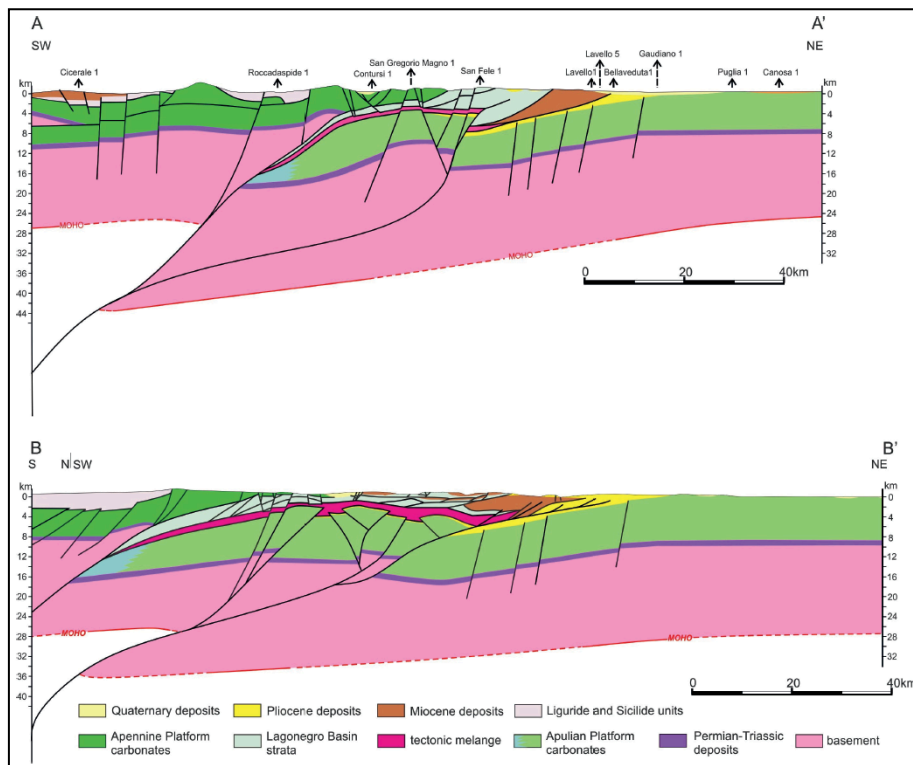


Fig. 3.13 Geological sketch map of the southern Apennines (upper panel) and cross-sections (lower panel; from Mazzoli et al., 2013).

The peri-Tyrrhenian extensional margin consists of a horst-and-graben structure along mainly NE-SW trending, SW-dipping extensional faults, which was formed starting from the Early Pleistocene (e.g., Bartole et al., 1984; Moussat et al., 1986; Mariani & Prato, 1988; Argnani et al., 1989; Sartori, 1990; Savelli & Schreider, 1991; Bruno et al., 1998, 2000; Florio et al., 1999; Milia et al., 2003; Caiazza et al., 2006; Casciello et al., 2006; Milia & Torrente, 1999, 2015 and references therein). The grabens (namely - from the N to the S - the Garigliano Plain - Gaeta Gulf, the Campania Plain, the Sele Plain - Salerno Gulf and the Policastro Gulf) are thousands of metre-deep (e.g., Ippolito et al., 1973), while uplift of the horst blocks coeval to the basin subsidence, is testified by flights of marine terraces (e.g. Caiazza et al., 2006, and references therein). In the Garigliano graben and various areas of the Campania Plain graben, volcanic edifices (Roccamonfina, and Vesuvius and Phlaegrean Fields, respectively) result from intense volcanism that occurred starting from the Middle Pleistocene (e.g. Radicati di Brozolo et al., 1988; Brocchini et al., 2001; Rolandi et al., 2003), while evidence of Early Pleistocene volcanism occur in the subsurface of the Campania Plain (ViDEPI, 2009).

The southern Apennines fold and thrust belt is NE-directed. According to studies by Mazzoli et al. (2008, 2013, and references therein), the Apennine chain consists of two main parts: the Apennine accretionary wedge and the buried Apulian Platform inversion belt (Fig. 3.13). The uppermost tectonic elements (Internal Units, Fig. 1) of the Apennine accretionary wedge north to the Calabrian Arc are represented by successions derived from the Neotethys ocean (Knott, 1987), and known as Frido, Nord-Calabrese, Sicilide and Parasicilide Units (Bonardi et al., 2004). Underneath such units, Mesozoic carbonate platform/slope and pelagic basin successions, stratigraphically covered by Neogene foredeep and wedge-top basin sediments are present (e.g., Mazzoli et al., 2008). The wedge-top basin sediments include the late Miocene Cilento Group (Pollica, San Mauro and Albidona Fms; Amore et al., 1988; Bonardi et al., 1988a; 1988b; Amore et al., 2005), which unconformably covers the Nord-Calabrese and Sicilide Units, and the Apennine Platform (Ciarcià et al., 2009). Pliocene-Pleistocene wedge-top basin deposits show ages that become younger towards the SE (Ascione et al., 2012; Fig. 3.13).

The structure of the fold and thrust belt is dominated at shallow levels by low-angle tectonic contacts separating carbonate platform/slope successions of the so-called Apennine Platform, in the hanging wall, from pelagic (Lagonegro) basin successions in the footwall (Fig. 3.13). Peritidal carbonate platform of the Apennine Platform and pelagic basin successions of the Lagonegro basin are of Triassic to Paleogene age, and are stratigraphically overlain by mid to late Miocene foredeep deposits (e.g. Scandone, 1972; D'Argenio et al., 1973; Pescatore, 1978; Mostardini and Merlini, 1986; Cello et al., 1990; Zuppetta and Mazzoli, 1997), and by late Miocene wedge-top basin deposits (Vitale and Ciarcià, 2012, and references

therein). These are completely detached from their original substratum and transported, together with detached Miocene foredeep sediments, onto the foreland carbonates of the Apulian platform. The latter consist of Mesozoic-Tertiary, 6-7 km thick shallow-water carbonates stratigraphically overlain by upper Messinian and/or Pliocene terrigenous marine deposits (e.g. Cello et al., 1989).

The shallow-water carbonates of the Apennine Platform are affected by extensional deformation related to forebulge/foredeep settings (Guerriero et al., 2010, 2011; Vitale et al., 2012), and were involved in shortening together with the underlying thick continental crust, thereby triggering the first continental collision event in the southern Apennines (Mazzoli et al., 2013; Fig. 3.13). Based on age of foredeep deposits stratigraphically overlying the carbonates, this event is ascribed to the Serravallian. According to Menardi Nougiera & Rea (2000) and Cippitelli (2007), the crystalline basement of the Apennine Platform is also involved in thrusting and occurs at relatively shallow depths (6-7 km) below the Cilento area. HP-LT metasediments of the Lungro-Verbicaro Unit (Iannace et al., 2005; Vitale et al., 2007a; Corrado et al., 2010) indicate that the distal part of the Adriatic continental margin underwent subduction – down to depths of ca. 50 km – and subsequent exhumation during the Miocene (Iannace et al., 2007; Vitale et al., 2007b).

Surface geology coupled with subsurface data point out that the Apennine accretionary wedge presently forms an allochthon overlying foreland carbonate platform strata (Apulian Platform) continuous with those exposed in the Apulian promontory to the NE (e.g., Mostardini and Merlini, 1986; Shiner et al., 2004). Buttressing of the accretionary wedge against the western margin of the Apulian Platform, wedge uplift and its final emplacement on top of the Apulian Platform carbonates are marked by exhumation recorded by apatite fission track data (cooling ages clustering around 5.5 Ma; Corrado et al., 2002, 2005; Mazzoli et al., 2008), consistent with a generalized Messinian emersion of the thrust belt (Ascione & Cinque, 1999).

The major detachment that separates the allochthon from the buried Apulian Platform carbonates is marked by a thick *mélange* zone (Mazzoli et al., 2001). Beneath the *mélange* zone, a variable thickness of Messinian evaporites and, more to the east, progressively younger Pliocene shales and arenites occur on top of the Mesozoic-Tertiary shallow-water carbonates (Patacca and Scandone, 2001, 2004; Patacca, 2007). The tectonically buried portion of the Apulian Platform, involved in the final shortening phases, is characterised by reverse-fault-related, open, long-wavelength folds that form the hydrocarbon traps for the oil discoveries (Shiner et al., 2004; Mazzoli et al., 2008, 2013). Deep-seated reverse faulting involves the basement with reactivation of pre-existing (Permo-Triassic) basement normal faults (Speranza & Chiappini, 2002; Shiner et al., 2004; Improta & Corciulo, 2006; Steckler et alii, 2008) (Fig. 3.13). The related deformation is characterized by limited horizontal displacements: the shortening of the buried Apulian Platform amounts to few tens of km at most (Menardi Nougiera and Rea, 2000; Mazzoli et al., 2000; Turrini and Rennison, 2004).

Mainly NW-SE and E-W trending extensional faults dissect the contractional structures described above, and testify to the middle Pleistocene to present-day NE-trending extensional regime active in the Apennine mountain chain, while strike-slip faulting prevails in the Apulian foreland. The former structures bound both Pleistocene intramontane basins filled with lacustrine and/or alluvial deposits (e.g., La Rocca & Santangelo, 1991; Ascione et al., 1992a, 1992b, 2013, 2018; Brancaccio et al., 2000; Munno et al., 2001; Schiattarella et al., 1991; Moro et al., 2007; Amicucci et al., 2008; Porreca and Mattei, 2010; 2012), and fault scarps of variable heights that are widespread in the region (e.g., Cinque et al., 2000; Papanikolaou and Roberts, 2007; Spina et al., 2008; Galli et al., 2006; Ascione et al., 2013, 2018, and references therein).

CHAPTER 4 - INVESTIGATION OF POST-SEISMIC GROUND DEFORMATION: THE 1980 IRPINIA EARTHQUAKE CASE STUDY

4.1 Introduction

The 1980 Irpinia earthquake was characterized by a complex source mechanism, consisting of three major sub-events at 0, 20 and 40 s, with M_w 6.9, 6.4 and 6.3 respectively (e.g. Bernard and Zollo, 1989; Westaway and Jackson, 1987; Fig. 4.1), the mainshock originating in the 8–13 km depth range (Giardini, 1993).

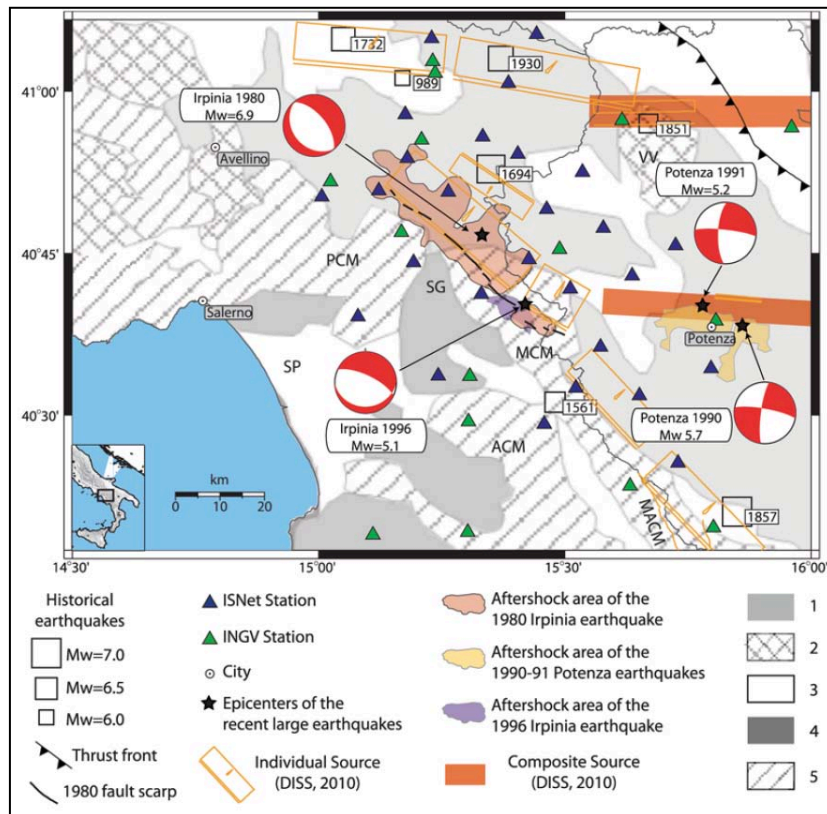


Fig. 4.1. Simplified geological map of the Campania–Lucania region integrated with seismogenic sources (DISS Working Group, 2010), locations of main historical earthquakes, focal mechanisms of large instrumental earthquakes and their aftershock zones, and locations of the ISNet (blue triangle) and INGV (green triangle) stations. Tectono-stratigraphic units are indicated in the legend as follows: (1) Molise–Sannio–Lagonegro pelagic basin and related foredeep deposits; (2) Apennine carbonate platform; (3) Apulia carbonate platform; (4) Pliocene–Quaternary terrigenous deposits; and (5) Ligurides and Sicilides. The letter designations are as follows: VV, Vulture Volcano; PCM, Picentini carbonate massif; MCM, Marzano carbonate massif; MACM, Maddalena carbonate massif; ACM, Alburno carbonate massif; SG, Sele River graben; and SP, Sele plain. (From De Matteis, 2012).

Bernard and Zollo (1989) defined at least three normal faulting ruptures on distinct fault segments: (i) the $M_s=6.9$ mainshock nucleated on the NE-dipping Mt. Marzano and Picentini Mts. segments (about 20 km long); (ii) the 20 s sub-event nucleated about 15 km southwest of the first event on a c. 20 km long normal fault; (iii) the 40 s sub-event, localized in the Ofanto basin area, was associated to a SW-dipping normal fault, antithetic to the first activated fault (Fig. 4.2a). According to Nostro et al. (1997), the 40 s sub-event might have reactivated a fault segment which ruptured during the $M_e=6.9$ (Serva, 1985), 1694 earthquake, which struck an area overlapping with that hit by the 1980 event (e.g. Porfido et al., 2002; Serva et al., 2007). Pingue and De Natale (1993) estimated an 80° SW-dip for the Ofanto fault. On the other hand, the NE-dipping fault segment responsible for the Mt. Marzano mainshock is constrained in a $53\text{--}63^\circ$ dip range by seismological data (e.g. Giardini, 1993), whereas dip values of 60° (at depth) to 70° (at surface) have been proposed by Pierdominici et al. (2011) based on breakout and log analysis of the S. Gregorio Magno 1 well. Probably due to the scarce source coverage (Cocco and Pacor, 1993), the localization and mechanism of the 20 s sub-event are largely debated. In fact, the 20 s nucleation is associated by Bernard and Zollo (1989) to a deep-seated, NE-dipping, low angle (20°) fault, and by Pantosti and Valensise (1990) to a fault plane dipping 60° to the NE. In contrast, Amoroso et al. (2005)

associate the 20 s sub-event to a SW-dipping fault antithetic to that of the mainshock (and roughly aligned with the 40 s fault; Fig. 4.2b), and suggest that it may represent a reactivation of the southernmost part of the fault activated with the 1694 earthquake.

The Mt. Marzano-Picentini Mts. fault segments and the antithetic Ofanto fault define the boundaries of both a NW-trending zone of aftershocks (which coincides with a high P-wave velocity zone; Amato and Selvaggi, 1993; Chiarabba and Amato, 1994), and of a volume affected by background microseismicity on subparallel predominantly normal faults (De Matteis et al., 2012; Fig. 4.2a).

The 1980 earthquake affected the epicentral area with widespread coseismic surface ruptures and ground deformation (detected by geodetic levelling surveys, e.g. Pingue and De Natale, 1993). Post-eventum surveys in the region recording the largest intensity (IX) reported more than 3000 ruptures, those with vertical offset showing a marked N120° main trend (Carmignani et al., 1981). Among such ruptures, the c. 2 km long, up to 50 cm high, WNW-ESE trending, NE-facing scarp formed in the PSGM basin (Mt. Difesa Ripa Rossa scarp; Bollettinari and Panizza, 1981), and the mainly NW-SE trending, NE-facing scarps in the Mt. Marzano-Piano di Pecore area (Cinque et al., 1981) were interpreted as surface faulting (Fig. 4.2d).

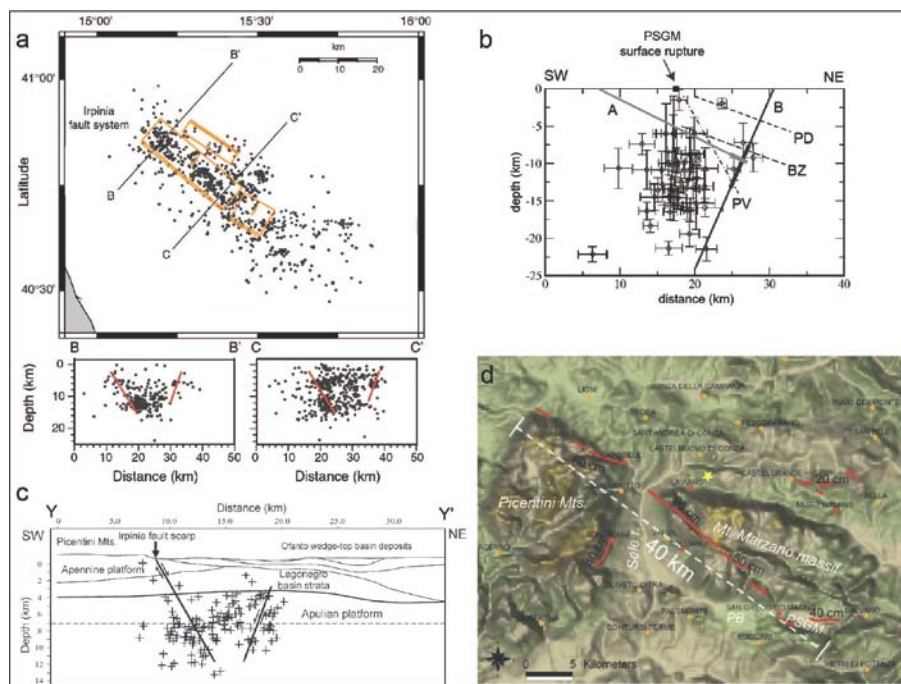


Fig. 4.2. a: Seismicity of the Irpinia region from August 2005 to April 2011 in map view (in orange, seismogenic sources from DISS working group, 2010) and in cross sections, along the profiles reported in the map (the red lines represent the projection of the fault segments of the 1980 earthquake) (from De Matteis et al., 2012, modified). b: Comparison of models for the 20 s fault, and projection of aftershocks localized on a vertical N31E cross-section cutting across the PSGM; A and B (effectively slipped area: thick line): Amoruso et al. (2005); BZ: Bernard and Zollo (1989); PD: Pingue and De Natale (1993); PV: Pantosti and Valensise (1990) (from Amoruso et al., 2005, redrawn) c: Gravity profile, and the fault segments and the aftershocks (Amato and Selvaggi, 1993) of the 1980 earthquake (from Improta et al., 2003). d: Distribution of the 1980 Irpinia earthquake coseismic surface faulting, after Bollettinari and Panizza (1981), Blumetti et al. (2002), Cinque et al. (1981), Esposito et al. (1998), Pantosti and Valensise (1990), Porfido et al. (2002) and Westway and Jacksons (1984) (from Serva et al., 2007, modified).

The latter scarps, and those affecting the SW slope of Mt. Carpineta ridge (the downthrown block being the uphill side), were interpreted by Westaway and Jackson (1984) as part of a 10 km long succession of right-stepping strands of the 1980 surface faulting, and the PSGM scarp was related to a further fault segment. Pantosti and Valensise (1990) related the coseismic faulting to three main strands (separated by gaps, i.e. the Sele valley and San Gregorio Magno gaps, with changes in strike of about 10°). Such fault strands, interpreted as part of a 38 km long, NE-dipping scarp with an average N128° strike (“Irpinia fault”), are identified with: (i) the Picentini Mts. footslope, with a N125° trend, (ii) the N135° trending Mt. Marzano-Mt. Valva scarp coupled with the N135°-N110° trending Mt. Carpineta scarp, and (iii) the N130°-N120° striking PSGM scarp (Fig. 4.2). The Mt. Marzano-Mt. Valva-Mt. Carpineta and Picentini Mts. segments have been associated with the mainshock, and the PSGM strand with the 20 s sub-event. However, Papanikolaou and Roberts (2007) suggested that the Mt. Valva-Mt. Marzano-Mt. Carpineta and the Picentini Mts. strands are part of single, continuous fault having a subdued topographic expression as

it crosses the Sele River valley, which is occupied by rocks with a low resistance to erosion. The 40 s sub-event has been later associated with c. 8 km long, up to 30 cm high, SW-facing scarps exposed between Santomenna and Muro Lucano (Blumetti et al., 2002; Fig. 4.2d).

Recently, Ascione et al. (2013) identified several fault arrays within the epicentral area of the 1980 earthquake (Fig. 4.3c). Within the structures belonging to the identified fault arrays, those developed in the area spanning from the northern Mt. Marzano massif (i.e. the Marzano fault array) to the Ofanto river valley – being characterized by a NE dip in the Mt. Marzano area and a SW dip to the NE of such a massif – are considered as the surface expression of the deep-seated graben-like structure which was activated with the 1980 earthquake (e.g., Bernard and Zollo, 1989; Pingue and De Natale, 1993; Amoroso et al., 2005). Their spatial distribution overlaps the belt affected by the 1980 earthquake aftershocks (e.g., Amato and Selvaggi, 1993), and by the present day low magnitude seismicity, which occurs on sub-parallel, predominantly normal faults (De Matteis et al., 2012; Fig. 4.1; Fig. 4.3e). A major SW dipping active fault system is identified to the SW of the earthquake epicentre, at the northern boundary of the S. Gregorio Magno – Buccino basins (Ascione et al., 2013; Fig. 4.3c). Stress inversion from surface faults and from instrumental earthquake focal mechanisms show a consistent pattern of NE-SW, roughly horizontal maximum extension (Fig. 4.3d), which is compatible with the T axis obtained from the 1980 main shock and with results of cumulative stress inversion from earthquake focal mechanism data (Fig. 4.3e). Surface structures are decoupled from the seismically active deep-seated structures, which in turn reactivate inherited basement faults (Ascione et al., 2013; Fig. 4.3b), with decoupling between deep and shallow structural levels being related to the strong rheological contrast produced by the fluid-saturated, clay-rich mélangé zone interposed between the foreland Apulian Platform carbonates and the allochthonous units, which include carbonate platform (i.e. Apennine Platform) and basin (i.e. Internal and Lagonegro) successions (Fig. 4.3b). Based on such an interpretation, the surface expression of the deep SWBF (SW Boundary Fault) is represented by the Piani di Buccino-Pantano di San Gregorio Magno fault zone (PB-PSGM), that of the CF (Central Fault) by the Mount Marzano–Mount Carpineta (MC) and Mount Ognà (Og) fault zones, and that of the NEBF (NE Boundary Fault) by the Conza (Co) and S. Fele fault strands (Fig. 4.3b and c).

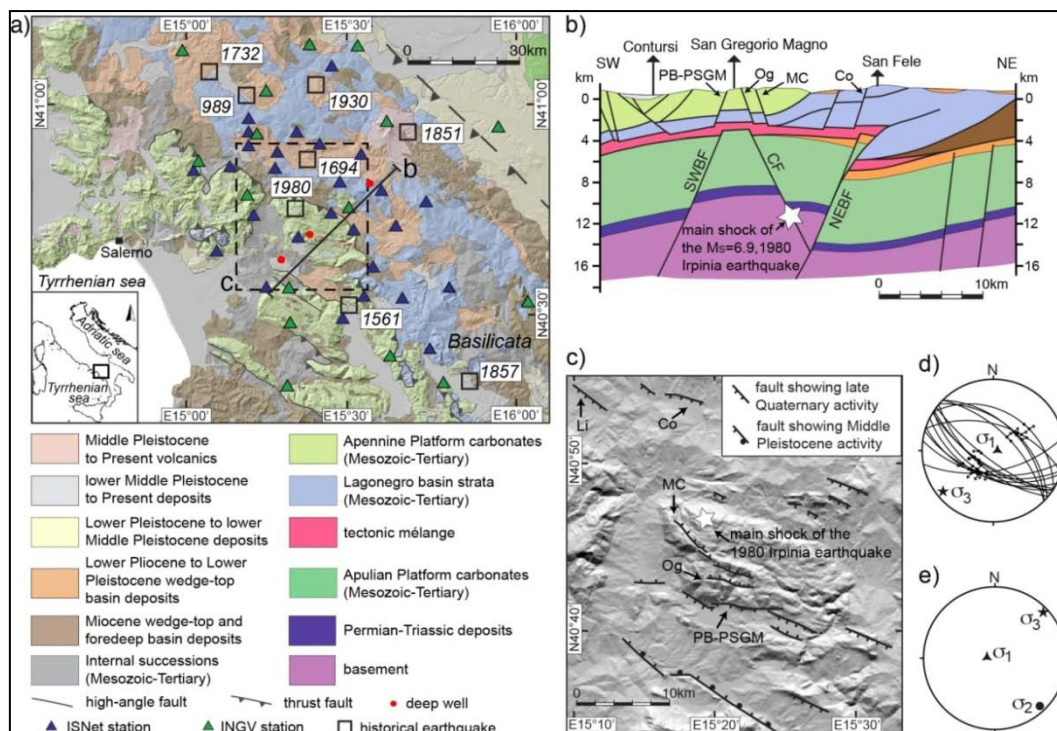


Fig. 4.3. Tectonic setting of the 1980 Irpinia earthquake. (a) Geological sketch map of the southern Apennines, showing location of seismic stations and main historical and instrumental earthquakes. (b) Cross-section (after Ascione et al., 2013). Star shows hypocentre of the Ms 6.9, 1980 Irpinia earthquake; SWBF: SW Boundary Fault; CF: Central Fault; NEBF: NE Boundary Fault. (c) Outcropping Quaternary fault arrays (after Ascione et al., 2013, modified). PB-PSGM: Piani di Buccino-Pantano di San Gregorio Magno fault zone; Og: Mount Ognà fault zone; MC: Mount Marzano–Mount Carpineta fault zone; Li: Lioni fault; Co: Conza fault. (d) Results of cumulative stress inversion from outcropping active fault segments (from Ascione et al., 2013). (e) Results of cumulative stress inversion from earthquake focal mechanism data are from De Matteis et al. (2012) (from Amoroso et al., 2014).

Galli and Peronace (2014), interpolating the data of two levelling lines, outlined the areal deformation (co-seismic subsidence) induced by the 1980 earthquake (in metres), highlighting the throw measured all along the Monte Marzano Fault System (MMFS) (Fig. 4.4)

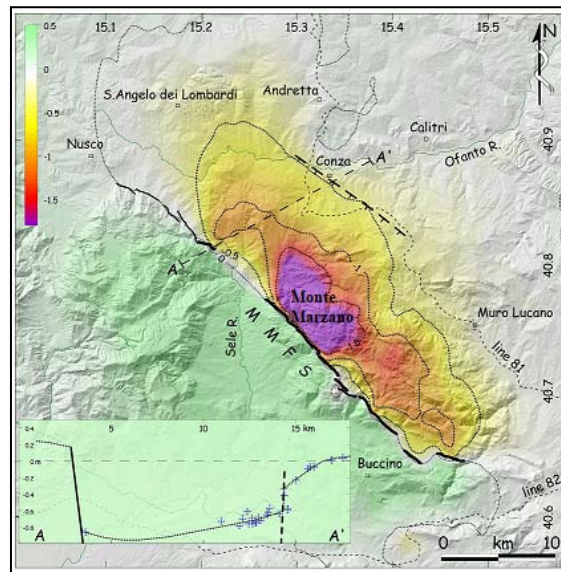


Fig. 4.4 Bold lines indicate the 1980 surface slip, according to Pantosti and Valensise (1990); in the picture is drawn the topographic profile between the master fault, the Serro Rotolo segment of MMFS, and an antithetic splay in the Conza area (dashed line NW-SE oriented in the picture) (from Galli and Peronace, 2014).

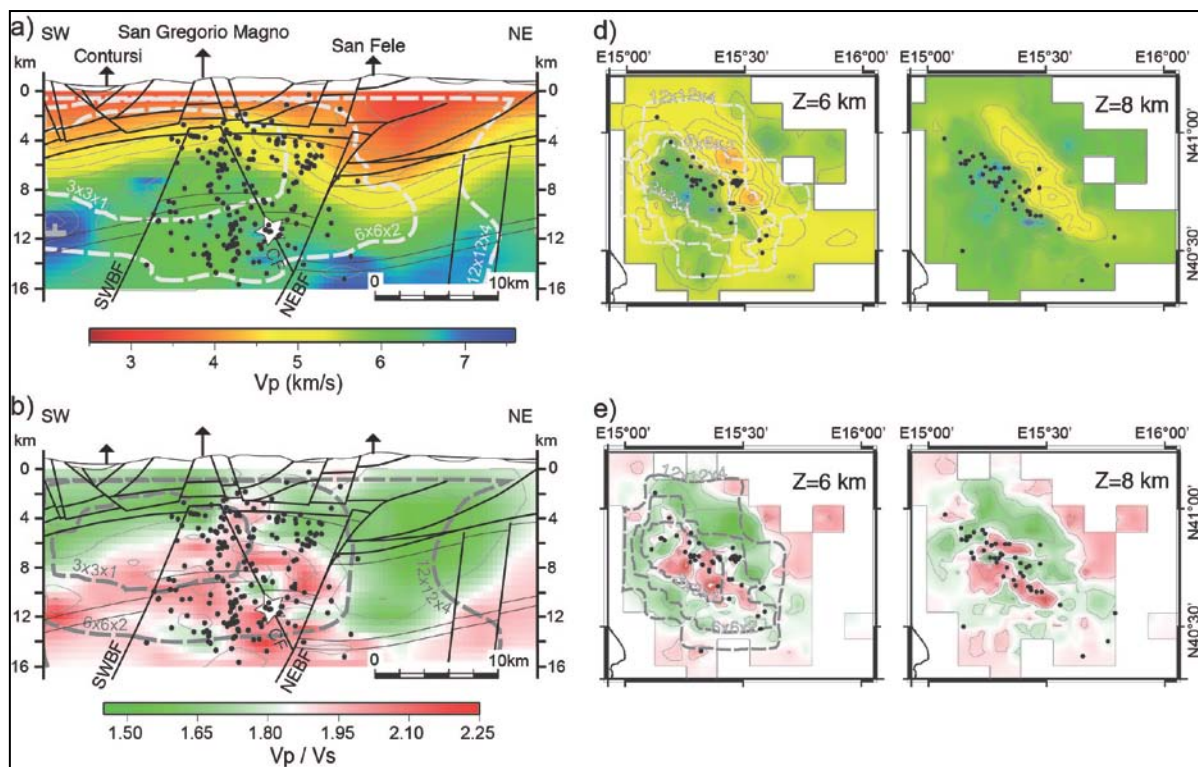


Fig 4.5. 3D tomographic model of the 1980 Irpinia earthquake region. (a) V_P velocity model and microearthquake locations projected onto the cross-section located in Fig. 1a (refer to Fig. 1b for the tectonic contacts and geological units). Grey dashed curves delimit the well-resolved regions of the model. Star shows hypocentre of the Ms 6.9, 1980 Irpinia earthquake. (b), V_P/V_S ratio for the same depth section as in (a). (d) Horizontal slice through the P-wave tomographic model at depths (Z) of 6 and 8 km. (e), Horizontal slice showing V_P/V_S ratio at depths (Z) of 6 and 8 km (from Amoroso et al., 2014, modified).

The reconstruction of the 3D P- and S-wave velocity models for the 1980 Irpinia area (Fig. 4.5), which match the geological structure, indicates a strong contribution of partial and total fluid-saturation in controlling the seismic velocities within the investigated crustal volume (Amoroso et al., 2014). This reservoir is fed by fluids rising along the major active faults and is laterally bounded by the faults

themselves, which act as barriers for cross-fault fluid flow due to the low permeability of the relatively thin cataclastic fault core (Amoroso et al., 2014).

4.2 Geological framework

Surface and subsurface (San Gregorio Magno 1 and Contursi 1 deep wells; Patacca, 2007; ViDEPI, 2010) data from the Mt. Marzano area show that the Apennine Platform carbonates are tectonically sandwiched between the underlying Lagonegro basin strata (outcropping to the N of the Mt. Marzano massif), and the overlying basinal Parasclilide unit, representing the deformed distal portion of the Apulian foreland palaeomargin (Ciarcia et al., 2009, 2012) (Fig. 4.3a).

In the study area, wedge-top basin deposits of Pliocene age (i.e. Zanclean and Piacentian; Amato et al., 1992; Ascione et al., 2012) consist of marine sediments (clays, sands and conglomerates), locally passing upwards to lacustrine and fluvial deposits, outcropping on top of the Mt. Marzano massif and in the adjacent southern (Tanagro river valley) and northern topographic lows (Fig. 4.3a). Coeval, clayey to shallow marine deposits (related to the Ofanto wedge-top basin), occupy the also northernmost part of the study area, i.e. the large Ofanto river valley.

In the Mt. Marzano area, the occurrence of a structural high of the Apulian Platform below the outcropping Apennine Platform carbonates and the underlying Lagonegro basin strata is evidenced by seismic reflection profiles and gravity data (e.g. Improta et al., 2003; Cippitelli, 2007; Mazzotti et al., 2007; Fig. 4.3b). Similarly to the structural traps of the oil fields of the Basilicata region south of our study area (Shiner et al., 2004), the Apulian Platform positive structure in the Mt. Marzano area appears to consist of a large inversion feature controlled by multiple reactivation of a major SW dipping fault of probable Triassic original age. According to this interpretation, substantial structural relief of the Apulian Platform in this area resulted from Late Pliocene to Early Pleistocene shortening and inversion, this being only weakly modified by subsequent late Quaternary extension. The top of the Apulian Platform carbonates, which is overlain by more than 600 m thick deposits including Messinian evaporites and *mélange* units (probably involving Lower Pliocene clastics), lies at 3977 m depth in the San Gregorio Magno 1 well (Patacca, 2007), whereas in the Contursi 1 well (ViDEPI, 2010;), the top of the *mélange* is found at a depth of c. 3100 m.

The fold and thrust structure is dissected by extensional faults, which control continental depocenters such as those occupying the Tanagro River valley (Ascione et al., 1992a), and the Piani di Buccino and Pantano di San Gregorio Magno basins (Ascione et al., 2003; Aiello et al., 2007). The Tanagro basin, which is occupied by several terraced alluvial units framed in the late Early Pleistocene to late Middle Pleistocene time span (Ascione et al., 1992b), formed along a major WNW-ESE striking, NE-dipping normal fault (Tanagro fault; Amicucci et al., 2008; Ascione et al., 1992b). This fault records repeated activity over the Middle Pleistocene. The formation of the Tanagro basin predates those of the Piani di Buccino and Pantano di San Gregorio Magno basins, which occurred in the Middle Pleistocene (Aiello et al., 2007), and of several minor basins within the Mt. Marzano ridge (Ascione et al., 2013).

4.3 Data analysis: construction of ground deformation maps based on PSs mean vertical velocity

In this section it is presented the procedure followed to obtain two radar PSs vertical mean velocity ground deformation maps that cover the region around the epicentral area of the 1980, 6.9 Mw, Irpinia earthquake.

The ERS 1/2 (1992 - 2000) and ENVISAT (2003 - 2010) ascending and descending PS datasets have been used to construct the maps.

4.3.1 IDW analysis of “native” PS datasets

In the first step the entire original ERS and ENVISAT PS datasets were processed. These datasets contain both normal and outlier PS data, as shown in the Tables 4.1 and 4.2.

It was applied the IDW tool (see Section 2.7), with size cell 50x50 m, to obtain two mean velocity interpolated maps, for the ascending and descending datasets. The maps were clipped around the area of interest (Fig. 4.5 and Fig. 4.6), that is around the Monte Marzano and Conza sites where they were generated, by surficial rupture process, the Monte Marzano and Conza faults (Galli and Peronace, 2014),

that is the main NE-dipping fault (responsible of mainshock, and 20-s sub-event) and the antithetic Conza fault, the SW-dipping fault responsible for 40-s sub-event.

Perimeters of the areas of interest (Fig. 4.6) were traced along the regions where the ascending and the descending original datasets and subsets are consistently overlapped, as this is a necessary condition to operate, subsequently, on the interpolated raster data and to apply the relationship (3) of Section 2.1.1. As a consequence, perimeters of analysed ERS and ENVISAT datasets are slightly different.

PS ERS original datasets	Number of PSs
ERS_T358_F819_CL003_CAPOSELE_A	38864
ERS_T358_F819_CL002_BENEVENTO_A	45672
ERS_T494_F2781_CL001_POTENZA_D	75178

Table 4.1

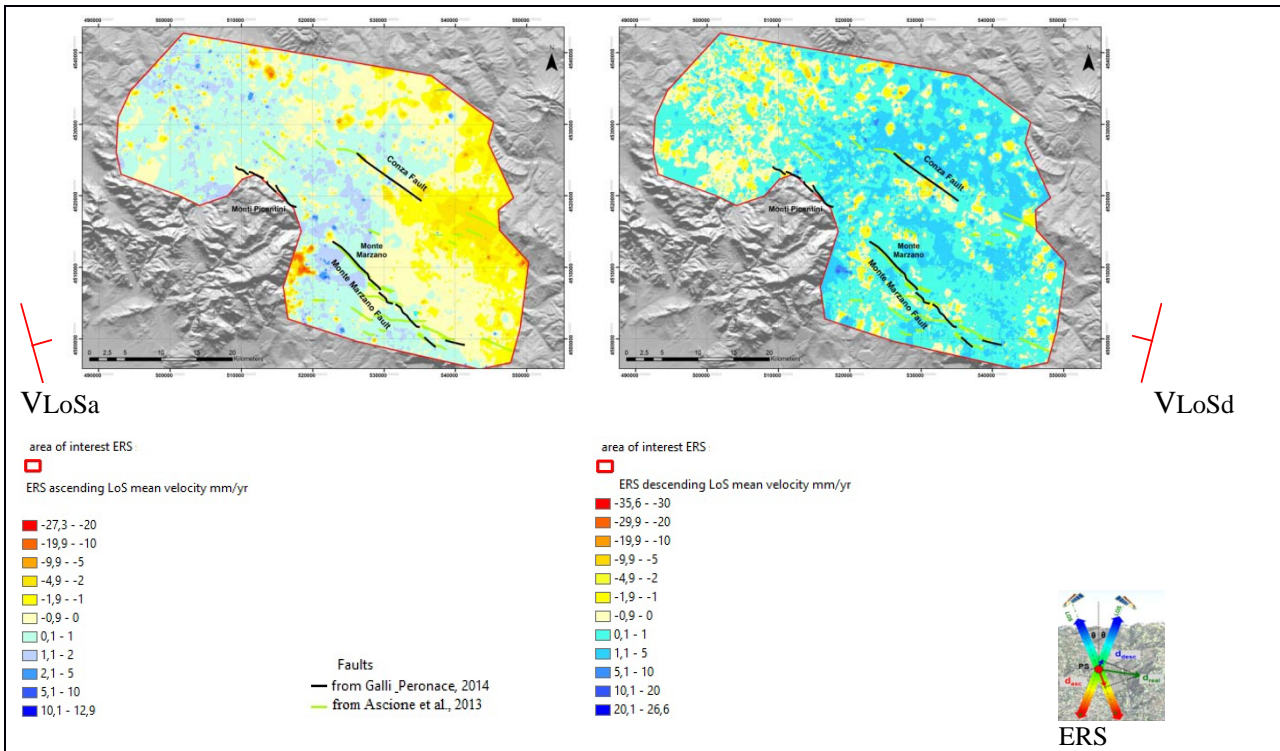


Fig. 4.6 IDW interpolation (cell 50x50 m) of ERS original PS datasets (normal + outliers) - ascending and descending mean velocity deformation maps 1992-2000

With a raster calculator tool, the vertical component of mean velocity (V_z) (Fig. 4.7) was obtained by operating with the two IDW interpolation maps in Fig. 4.6 that represent the ascending (VLoSa) and descending (VLoSd) mean velocity, or ground deformation, maps in 1992 - 2000 time span, for ERS PS "native" dataset, i.e. the dataset that includes both normal and outlier PSs.

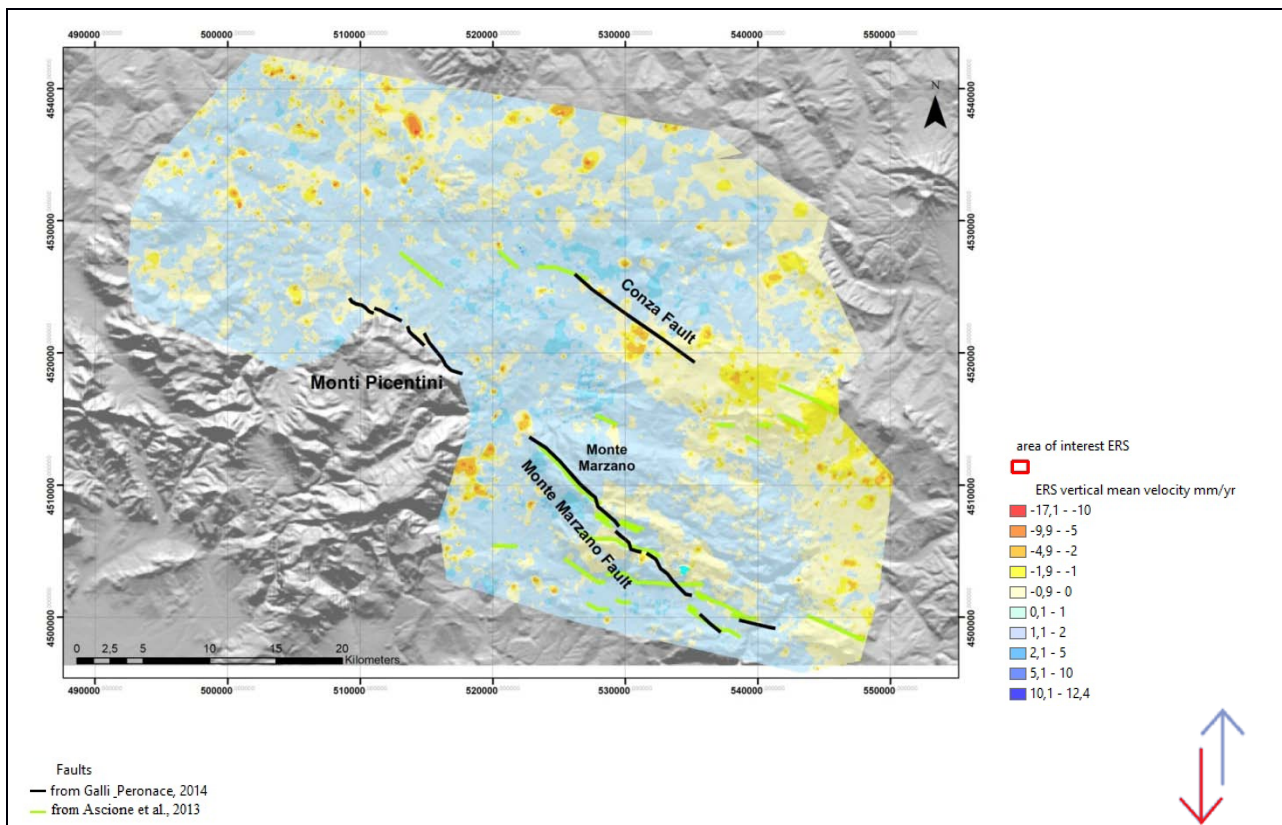


Fig. 4.7 IDW interpolation (cell 50x50 m) of ERS original PS datasets (normal + outliers) - vertical mean velocity deformation map 1992-2000

PS ENVISAT original datasets	Number of PSs
ENVISAT_T86_F816_CL001_FOGGIA_A	391518
ENVISAT_T358_F801_CL001_SALERNO_A	248986
PST2009_ENVISAT_T358_F819_CL001_BENEVENTO_A	532482
ENVISAT_T265_F2781_CL001_AVELLINO_D	463801

Table 4.2

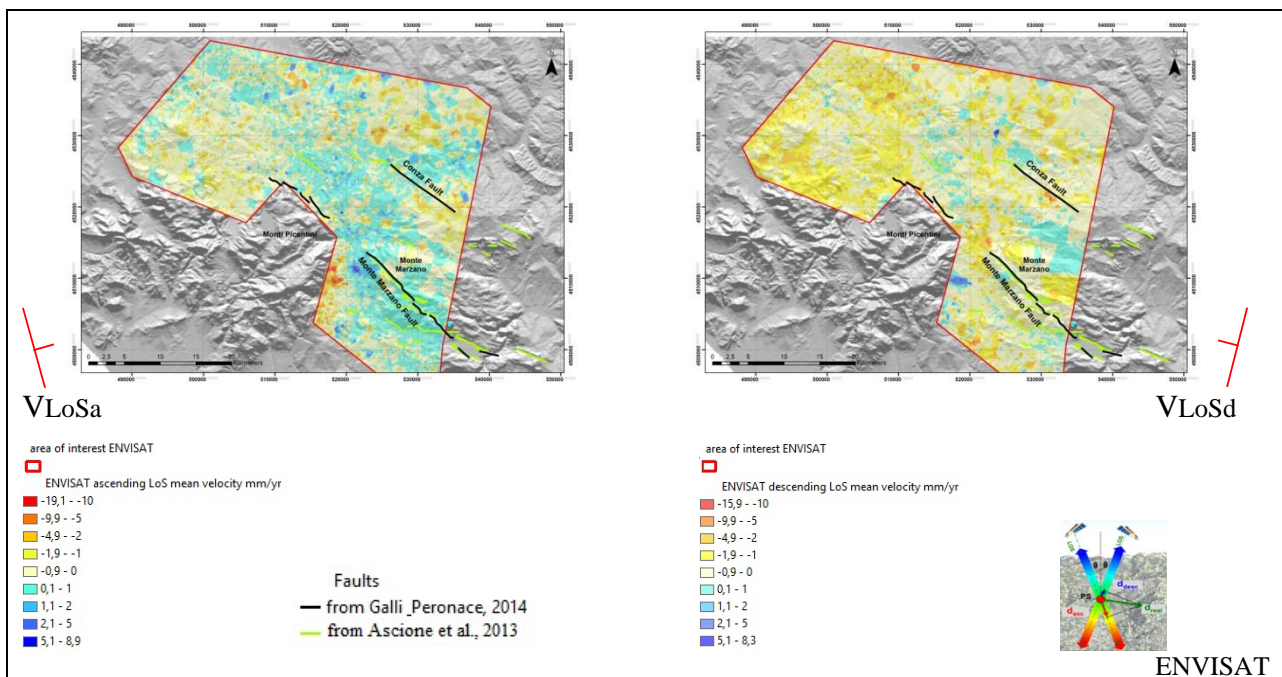


Fig. 4.8 IDW interpolation (cell 50x50 m) of ENVISAT original PS datasets (normal + outliers) - ascending and descending mean velocity deformation maps 2003 - 2010

The two IDW interpolation maps in Fig. 4.8 represent the ascending and descending mean velocity deformation maps in 2003-2010 time span and consisting of normal and outlier data. Through the same relationship (3), the vertical component of mean velocity for the ENVISAT PS original dataset is obtained too (Fig. 4.9).

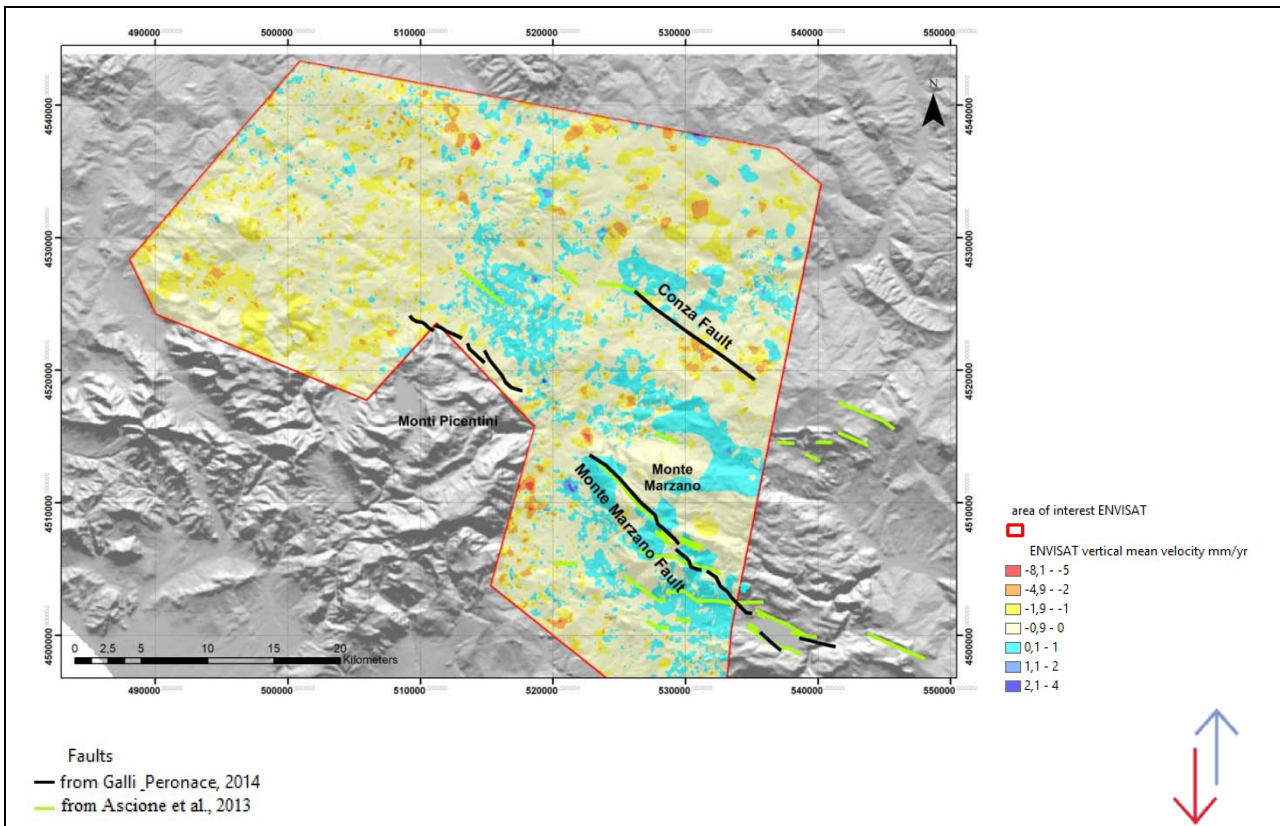


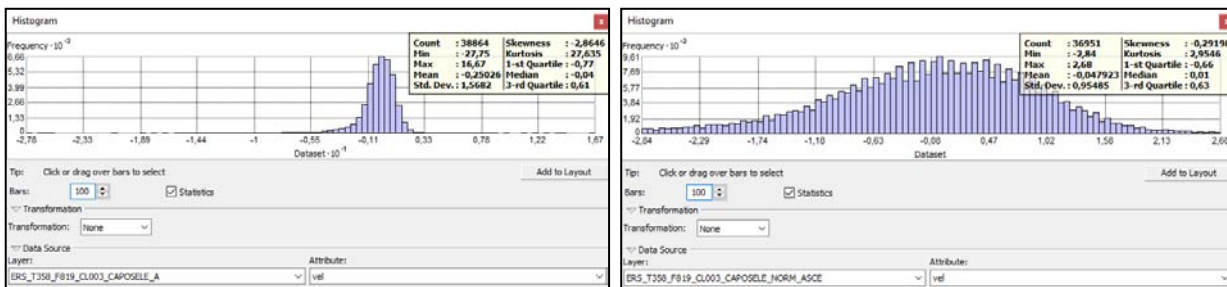
Fig. 4.9 IDW interpolation (cell 50x50 m) of ENVISAT original PS datasets (normal + outliers) - vertical mean velocity deformation map 2003 - 2010

4.3.2 Geospatial analysis: Hot Spot and Cluster and Outlier

In this case study were applied both the *Hot Spot Analysis (Getis-Ord Gi*)* and the *Cluster and Outlier Analysis (Anselin Local Moran's I)* mapping tools (Sections 6.1.1 and 6.1.2) for all PS subsets created, without applying any filter based on coherence values.

The data analysis starts with extraction of PS normal subsets (Section 6.1) from original datasets through the outliers boundaries (fence) evaluation (Fig. 4.10 and Table 4.3).

As example, in Fig. 4.10 are shown the differences between distribution histograms of the original datasets ERS_T358_F819_CL003_CAPOSELE_A and ENVISAT_T265_F2781_CL001_AVELLINO_D, that do not have a normal distributions, with the subsets extracted, called ERS_T358_F819_CL003_CAPOSELE_A_NORM and ENVISAT_T265_F2781_CL001_AVELLINO_NORM_DESCE, which instead show normal distributions.



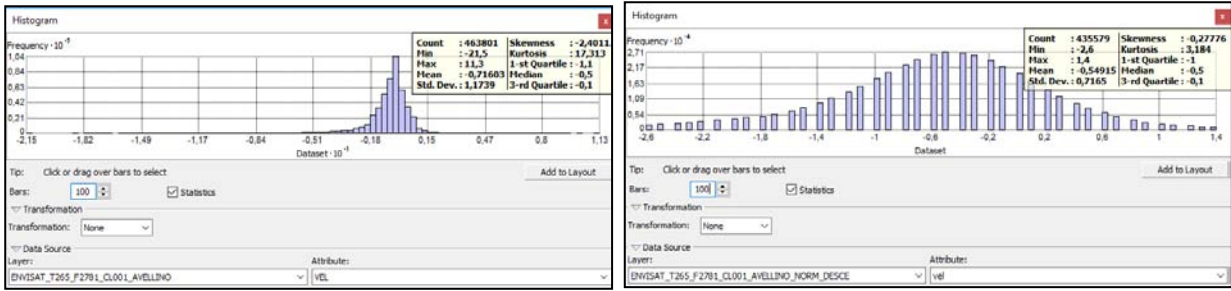


Fig. 4.10 On the left side distribution histograms of two original PS datasets; on the right side, after outliers exclusion, are obtained two PS subsets with a normal distribution called with the adding word "norm"

PS original dataset	Number of PSs	PS normal subsets	New number of PSs	PSs numeric difference
ERS_T358_F819_CL003_CAPOSELE_A	38864	ERS_T358_F819_CL003_CAPOSELE_A_NORM	36951	1913
ERS_T358_F819_CL002_BENEVENTO_A	45672	ERS_T358_F819_CL002_BENEVENTO_A_NORM	43481	2191
ERS_T494_F2781_CL001_POTENZA_D	75178	ERS_T494_F2781_CL001_POTENZA_NORM_D	69966	5212
ENVISAT_T86_F816_CL001_FOGGIA_A	391518	ENVISAT_T86_F816_CL001_FOGGIA_A_NORM	346281	45237
ENVISAT_T358_F801_CL001_SALERNO_A	248986	ENVISAT_T358_F801_CL001_SALERNO_A_NORM	226491	22495
PST2009_ENVISAT_T358_F819_CL001_BENEVENTO_A	532482	PST2009_ENVISAT_T358_F819_CL001_BENEVENTO_A_NORM	506151	26331
ENVISAT_T265_F2781_CL001_AVELLINO_D	463801	ENVISAT_T265_F2781_CL001_AVELLINO_D_NORM	435579	28222

Table 4.3 Comparison between the number of PS contained in the original datasets and those contained in the subsets obtained through the outliers exclusion process to perform statistical normal distributions of PSs (ERS light green, Envisat dark green).

Afterwards, it was performed a selection of the PSs (of both the ERS and ENVISAT datasets) falling inside the perimeter of the areas of interest,.

At this stage of the analysis, the data contained in the areas of interest will form three new subsets for the ERS data, and four new subsets for ENVISAT data, identified with the label "marzano" (Figs. from 4.11 to 4.14).

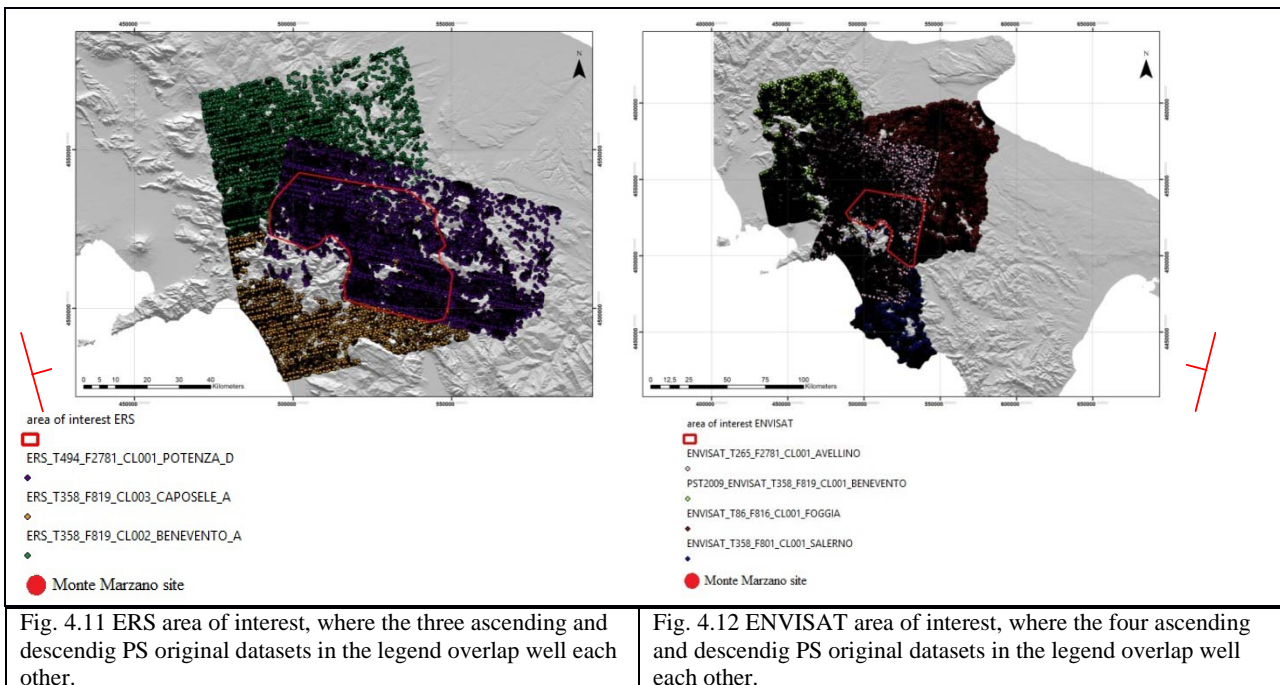
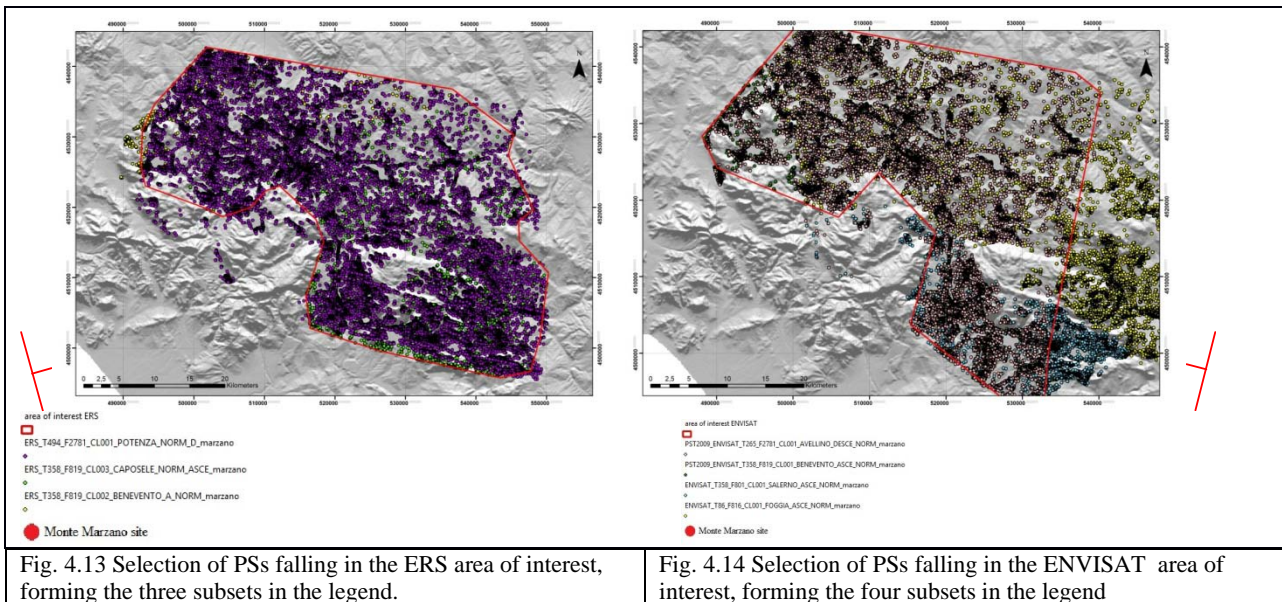


Fig. 4.11 ERS area of interest, where the three ascending and descending PS original datasets in the legend overlap well each other.

Fig. 4.12 ENVISAT area of interest, where the four ascending and descending PS original datasets in the legend overlap well each other.



The histograms in Fig. 4.15 and in Fig. 4.16 show that the three "marzano" ERS PS subsets and the four "marzano" ENVISAT PS subsets are characterised by statistic normal distributions.

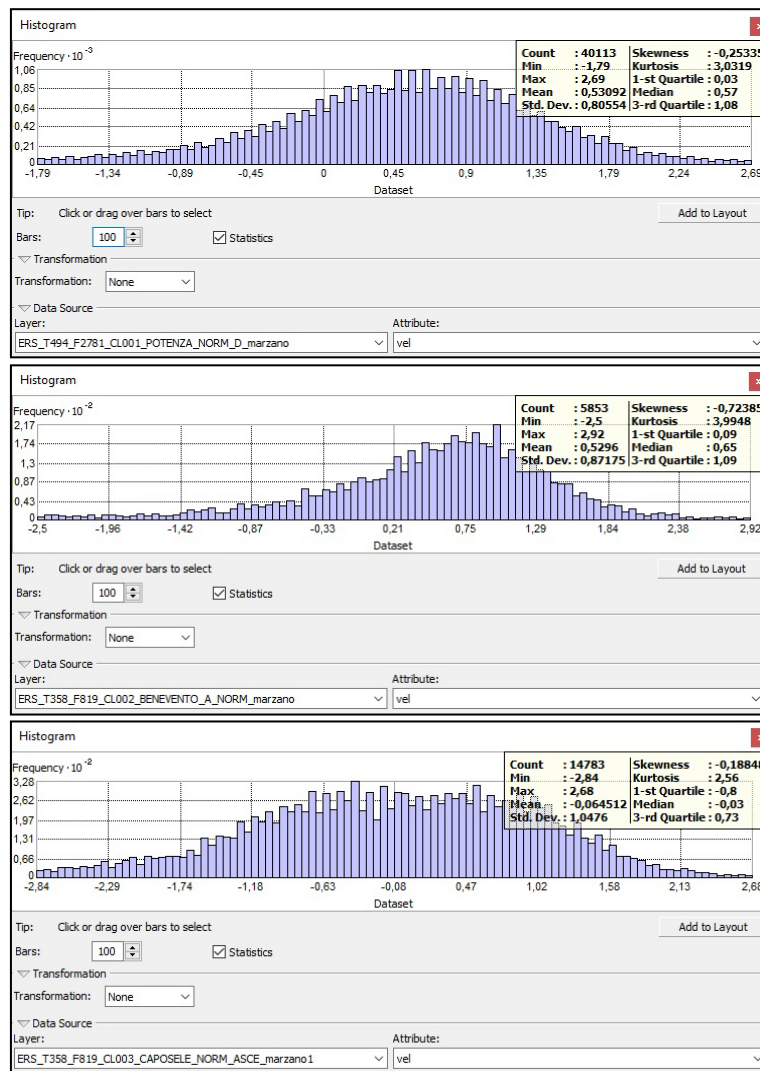


Fig. 4.14 The ERS "marzano" subsets with normal distribution

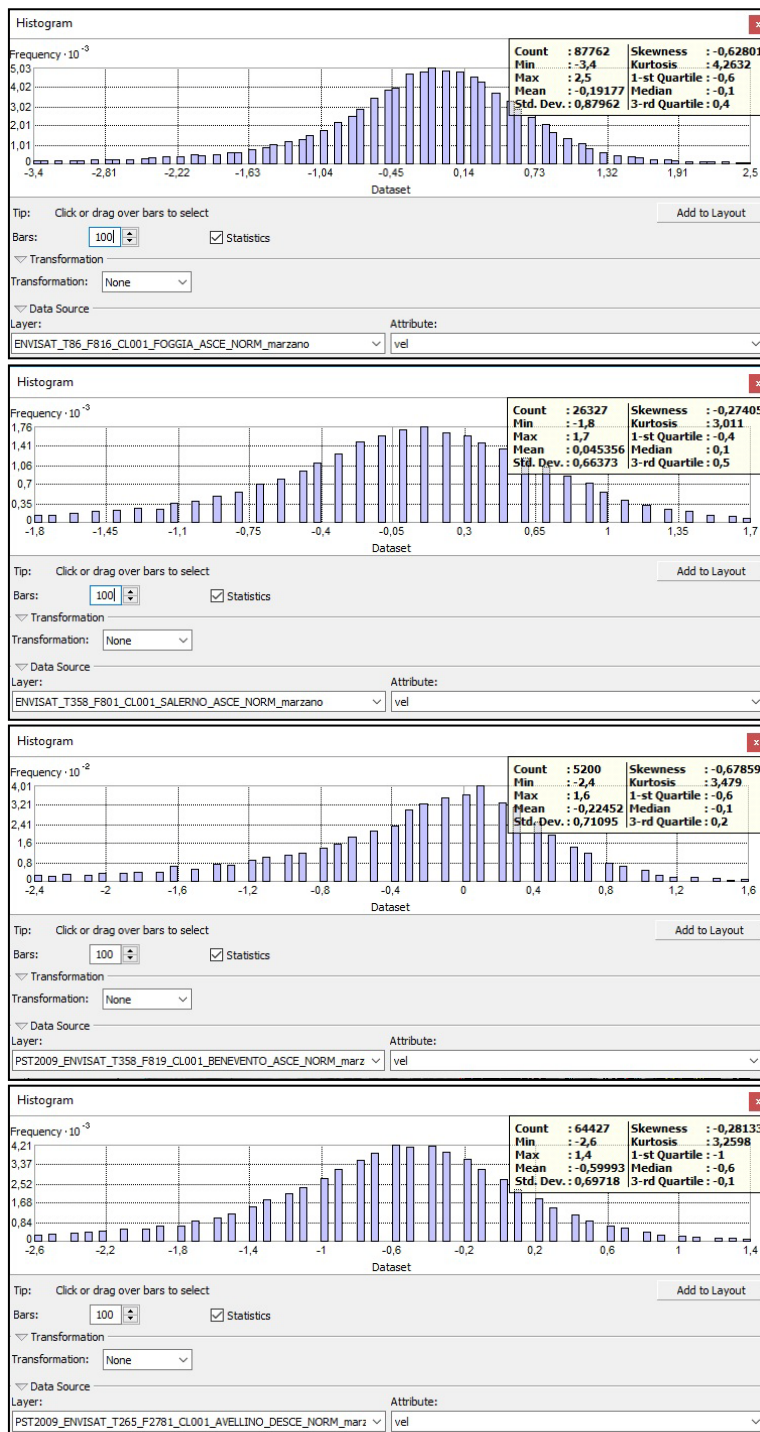


Fig. 4.15 The ENVISAT "marzano" subsets with normal distribution

Following - in part - the procedure of Perrone et al. (2013), in this case study both the *Hot Spot Analysis (Getis-Ord G_i^*)* and the *Cluster and Outlier Analysis (Anselin Local Moran's I)* mapping tools for all "marzano" were applied to the PS subsets. The subsets arising from *Hot Spot Analysis* are identified with "HS" acronym, while that ones from *Cluster and Outlier Analysis* are identified with "CO" acronym.

The mapping results are shown in Figs. from 4.17 to 4.24, for both of the used tools.

In the representation of the Hot/Cold Spot maps, the PSs classified, in the legend below (Fig. 4.16), as "not significant" (with z-score between -1.65 and 1.65) are turned off.

In the representation of the Cluster and Outlier maps, the PSs classified, in the legend below (Fig. 4.16), as "high/low outlier" (with z-score minor of -1.96 and between -1.96 and 1.96) are turned off.

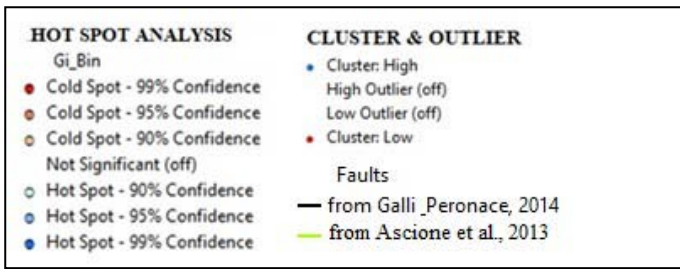


Fig. 4.16 Legend Figs. 4.17 to 4.24

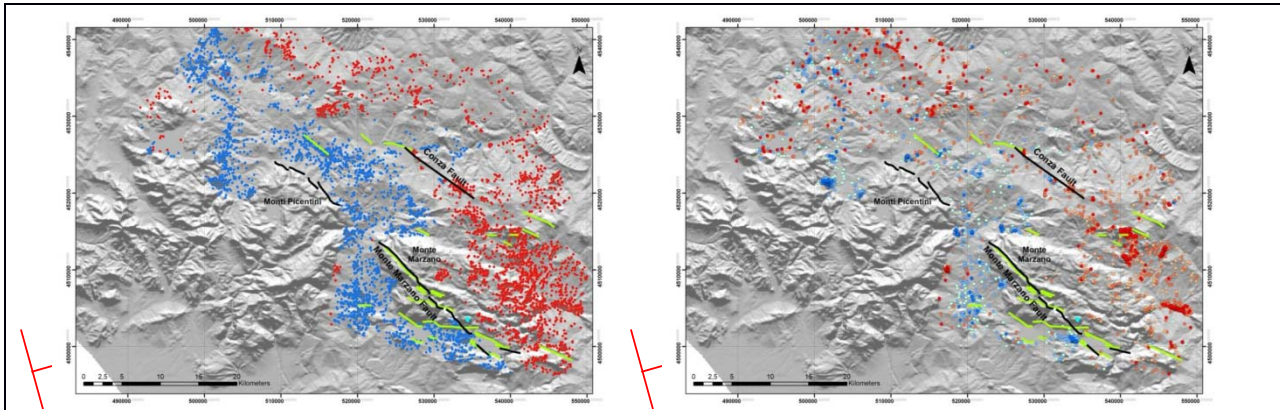


Fig. 4.17 In the map there are the following PS ascending subsets from *Cluster and Outlier Analysis* :
ERS_T358_F819_CL003_CAPOSELE_NORM_ASCE_marzano_CO_2k_IDW;
ERS_T358_F819_CL002_BENEVENTO_A_NORM_marzano_CO_2k_IDW.

Fig. 4.18 In the map there are the following PS ascending subsets from *Hot Spot Analysis* :
ERS_T358_F819_CL003_CAPOSELE_NORM_ASCE_marzano_HS_2k_IDW;
ERS_T358_F819_CL002_BENEVENTO_A_NORM_marzano_HS_2k_IDW.

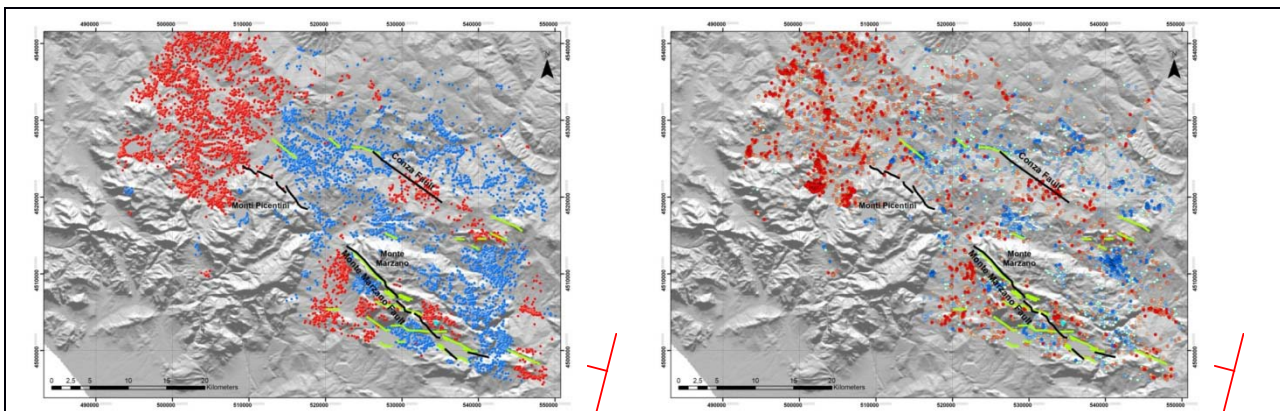


Fig. 4.19 In the map there is the following PS descending subset from *Cluster and Outlier Analysis* :
ERS_T494_F2781_CL001_POTENZA_NORM_D_marzano_CO_2k_IDW.

Fig. 4.20 In the map there is the following PS descending subset from *Hot Spot Analysis* :
ERS_T494_F2781_CL001_POTENZA_NORM_D_marzano_HS_2k_IDW.

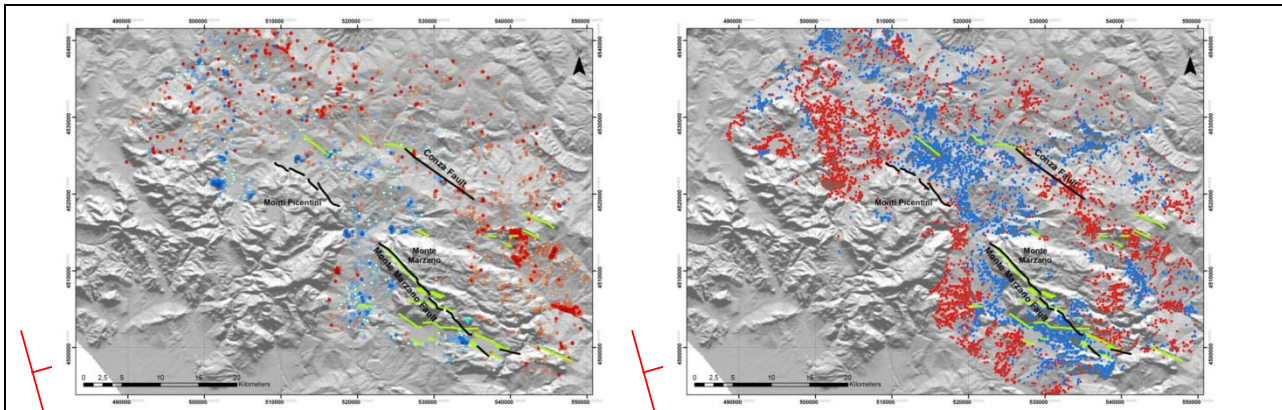


Fig. 4.21 In the map there are the following PS ascending subsets from *Hot Spot Analysis*:
 ENVISAT_T86_F816_CL001_FOGGIA_ASCE_NORM_marzано_HS_2k_IDW;
 PST2009_ENVISAT_T358_F819_CL001_BENEVENTO_ASCE_NORM_marzано_HS_2k_IDW;
 ENVISAT_T358_F801_CL001_SALERNO_ASCE_NORM_marzано_HS_2k_IDW.

Fig. 4.22 In the map there are the following PS ascending subsets from *Cluster and Outlier Analysis* :
 ENVISAT_T86_F816_CL001_FOGGIA_ASCE_NORM_marzано_CO_2k_IDW;
 PST2009_ENVISAT_T358_F819_CL001_BENEVENTO_ASCE_NORM_marzано_CO_2k_IDW;
 ENVISAT_T358_F801_CL001_SALERNO_ASCE_NORM_marzано_CO_2k_IDW.

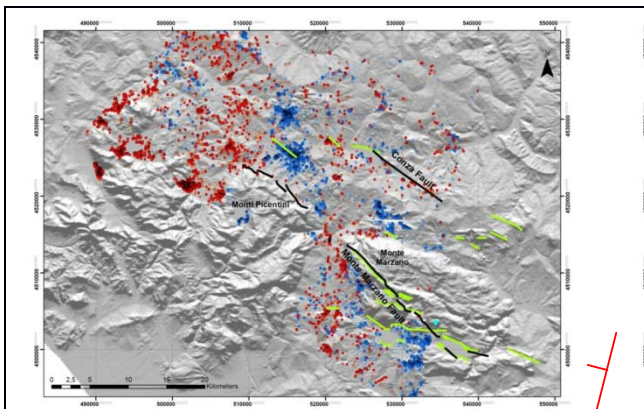


Fig. 4.23 map showing the PS descending subset from *Hot Spot Analysis* :
 PST2009_ENVISAT_T265_F2781_CL001_AVELLINO_DESCE_NORM_marzано_HS_2k_IDW.

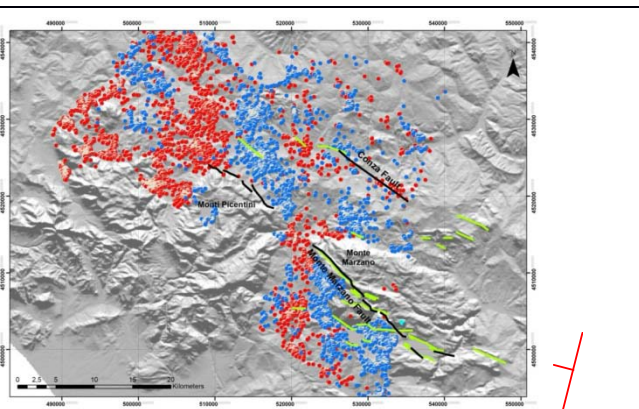


Fig. 4.24 In the map there is the following PS descending subset from *Cluster and Outlier Analysis* :
 PST2009_ENVISAT_T265_F2781_CL001_AVELLINO_DESCE_NORM_marzано_CO_2k_IDW.

In the subsets label, the word "2k", that is 2000 m, is referred to the *Threshold Distance* that is "a cutoff distance for Inverse Distance option. Features outside the specified cutoff for a target feature are ignored in analyses for that feature"; the word "IDW" is referred to the *Conceptualization of Spatial Relationships* that is "Nearby neighbouring features have a larger influence on the computations for a target feature than features that are far away".

Looking at the figures above (Figs. 4.17 to 4.24) it seems evident that:

- both mapping tools give a similar distribution of representative PSs (the red and blue points), however;
- there is a better visualization of the data in the maps deriving from the *Cluster and Outlier Analysis*. For this reason, in the following we will refer to the "CO maps".

In the "CO maps" it is possible to identify some boundaries between areas with LoS mean velocity over and under a subset mean value (the iso-kinematic boundaries and domains of Perrone et al., 2013). However, we have to consider that they are relative to one satellite point of view, while at least two LoS components are needed to obtain a two-dimensional representation.

In order to operate with a few but useful number of PSs, the further step was to remove, from the "CO" subsets, the PSs defined as "not significant", "high outlier" (HL) and "low outlier" (LH), leaving only the PSs classified as (HH) and (LL). Such a procedure allowed obtaining new and "lighter" subsets, labelled adding the letters "nout".

In the tables below (Tables 4.4 and 4.5):

- the subsets with "... CO_2k_IDW" are those obtained through *Cluster and Outlier Analysis* and they have the same number of PSs like the "... NORM_D_marzano" or "... NORM_A_marzano";
- the number of PSs in the subsets with "... CO_2k_IDW_nout" not include those classified as "not significant", "high outlier (HL)" and "low outlier (LH)".

PS ERS SUBSETS - extraction of PS HH and LL	Number of PSs
ERS_T494_F2781_CL001_POTENZA_NORM_D_marzano	40113
ERS_T494_F2781_CL001_POTENZA_NORM_D_marzano_CO_2k_IDW	40113
ERS_T494_F2781_CL001_POTENZA_NORM_D_marzano_CO_2k_IDW_nout	15702
ERS_T358_F819_CL003_CAPOSELE_NORM_ASCE_marzano	14783
ERS_T358_F819_CL003_CAPOSELE_NORM_ASCE_marzano_CO_2k_IDW	14783
ERS_T358_F819_CL003_CAPOSELE_NORM_ASCE_marzano_CO_2k_IDW_nout	8063
ERS_T358_F819_CL002_BENEVENTO_A_NORM_marzano	5853
ERS_T358_F819_CL002_BENEVENTO_A_NORM_marzano_CO_2k_IDW	5853
ERS_T358_F819_CL002_BENEVENTO_A_NORM_marzano_CO_2k_IDW_nout	1495

Table 4.4 ERS number of PSs in the subsets deriving from the selection with *Cluster and Outlier Analysis mapping tool*

PS ENVISAT SUBSETS - extraction of PS HH and LL	Number of PSs
PST2009_ENVISAT_T265_F2781_CL001_AVELLINO_DESCE_NORM_marzano	64427
PST2009_ENVISAT_T265_F2781_CL001_AVELLINO_DESCE_NORM_marzano_CO_2k_IDW	64427
PST2009_ENVISAT_T265_F2781_CL001_AVELLINO_DESCE_NORM_marzano_CO_2k_IDW_nout (only HH and LL)	23579
ENVISAT_T86_F816_CL001_FOGGIA_ASCE_NORM_marzano	87762
ENVISAT_T86_F816_CL001_FOGGIA_ASCE_NORM_marzano_CO_2k_IDW	87762
ENVISAT_T86_F816_CL001_FOGGIA_ASCE_NORM_marzano_CO_2k_IDW_nout (only HH and LL)	31085
PST2009_ENVISAT_T358_F819_CL001_BENEVENTO_ASCE_NORM_marzano	5200
PST2009_ENVISAT_T358_F819_CL001_BENEVENTO_ASCE_NORM_marzano_CO_2k_IDW	5200
PST2009_ENVISAT_T358_F819_CL001_BENEVENTO_ASCE_NORM_marzano_CO_2k_IDW_nout (only HH and LL)	1363
ENVISAT_T358_F801_CL001_SALERNO_ASCE_NORM_marzano	26327
ENVISAT_T358_F801_CL001_SALERNO_ASCE_NORM_marzano_CO_2k_IDW	26327
ENVISAT_T358_F801_CL001_SALERNO_ASCE_NORM_marzano_CO_2k_IDW_nout (only HH and LL)	9811

Table 4.5 ENVISAT number of PSs in the subsets deriving from the selection with *Cluster and Outlier Analysis mapping tool*

In the tables below (Tables 4.6 and 4.7) are reported the numbers of PSs belonging to each category derived from *Cluster and Outlier Analysis*. The PSs specified with bold style (HH and LL) are those used to construct the interpolation maps shown in the following figures (Fig. 4.26 and Fig. 4.28).

PS ERS SUBSETS - extraction of PS HH and LL	Number of PSs
ERS_T494_F2781_CL001_POTENZA_NORM_D_marzano_CO_2k_IDW	
Not Significant	21100
Cluster: High (HH)	8143
Cluster: Low (LL)	7559
High Outlier (HL)	1500
Low Outlier (LH)	1811
ERS_T358_F819_CL003_CAPOSELE_NORM_ASCE_marzano_CO_2k_IDW	
Not Significant	6116
Cluster: High (HH)	4243
Cluster: Low (LL)	3820
High Outlier (HL)	126
Low Outlier (LH)	478
ERS_T358_F819_CL002_BENEVENTO_A_NORM_marzano_CO_2k_IDW	
Not Significant	4017
Cluster: High (HH)	840
Cluster: Low (LL)	655
High Outlier (HL)	105
Low Outlier (LH)	236

Table 4.6 ERS PSs selection with *Cluster and Outlier Analysis mapping tool* . Coloured black numbers indicate PS that are not considered in the vertical mean velocity deformation maps processing

PS ENVISAT SUBSETS - extraction of PS HH and LL		Number of PSs
PST2009_ENVISAT_T265_F2781_CL001_AVELLINO_DESCE_NORM_marzano_CO_2k_IDW		
Not Significant		38683
Cluster: High (HH)		12080
Cluster: Low (LL)		11499
High Outlier (HL)		856
Low Outlier (LH)		1309
ENVISAT_T86_F816_CL001_FOGGIA_ASCE_NORM_marzano_CO_2k_IDW		
Not Significant		54212
Cluster: High (HH)		16366
Cluster: Low (LL)		14719
High Outlier (HL)		1065
Low Outlier (LH)		1400
PST2009_ENVISAT_T358_F819_CL001_BENEVENTO_ASCE_NORM_marzano_CO_2k_IDW		
Not Significant		3701
Cluster: High (HH)		716
Cluster: Low (LL)		647
High Outlier (HL)		59
Low Outlier (LH)		77
ENVISAT_T358_F801_CL001_SALERNO_ASCE_NORM_marzano_CO_2k_IDW		
Not Significant		15410
Cluster: High (HH)		4905
Cluster: Low (LL)		4906
High Outlier (HL)		618
Low Outlier (LH)		488

Table 4.7 ENVISAT PSs selection with *Cluster and Outlier Analysis mapping tool* . Coulores black numbers indicate PS that are not considered in the vertical mean velocity deformation maps processing

As an example, we can consider the two ERS and ENVISAT descending subsets, made up of PSs classified as "not significant" (nsig).

The ERS_T494_F2781_CL001_POTENZA_NORM_D_marzano_CO_2k_IDW_nsig has a normal data distribution (Fig. 4.25) and contain 21100 PSs (Table 4.6);

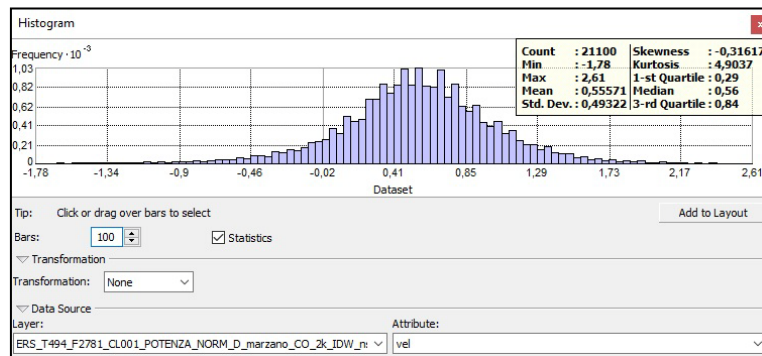


Fig. 4.25 The ERS_T494_F2781_CL001_POTENZA_NORM_D_marzano_CO_2k_IDW_nsig normal data distribution

Fig. 4.26 shows the mean velocity IDW interpolation map constructed with the above considered subset. It is almost entirely represented by the mean velocity 0 - 1 (statistic mean value 0,55). It is a flat map, without ground deformation gradient (except very local gravitational phenomena or landslide).

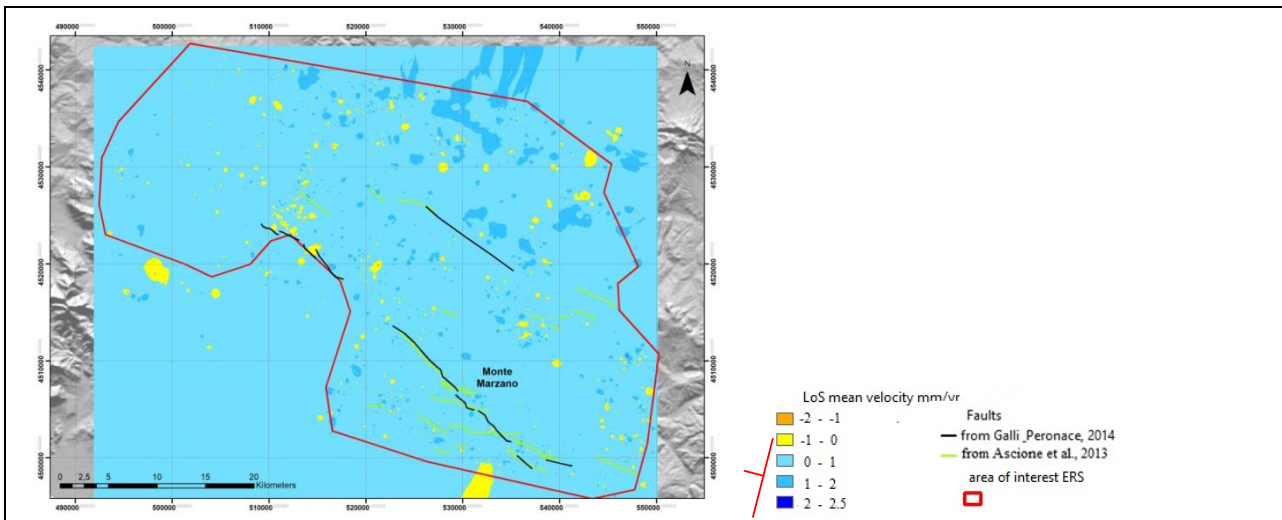


Fig. 4.26 IDW interpolation map realized with PSs classified as "not significant" in the descending subset: ERS_T494_F2781_CL001_POTENZA_NORM_D_marzano_CO_2k_IDW_nsig

In the same way, the:

PST2009_ENVISAT_T265_F2781_CL001_AVELLINO_DESCE_NORM_marzano_CO_2k_IDW_nsig subset has a normal data distribution (Fig. 4.27) with 38683 PSs (Table 4.7).

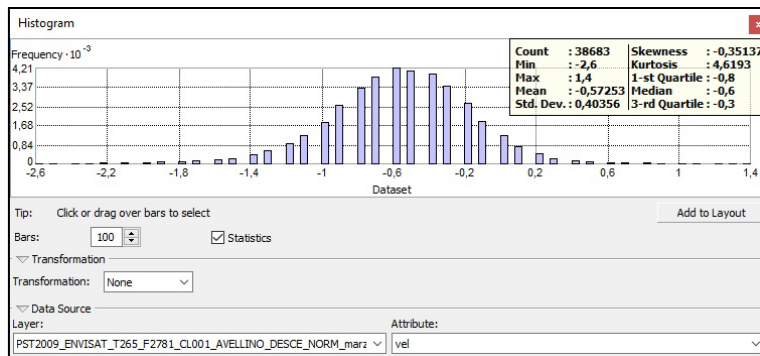


Fig. 4.27 PST2009_ENVISAT_T265_F2781_CL001_AVELLINO_DESCE_NORM_marzano_CO_2k_IDW_nsig

Fig. 4.28 shows the mean velocity IDW interpolation map constructed with the PST2009_ENVISAT_T265_F2781_CL001_AVELLINO_DESCE_NORM_marzano_CO_2k_IDW_nsig subset. It is almost entirely represented by the mean velocity -1 - 0 class (statistic mean in the subset - 0.57).

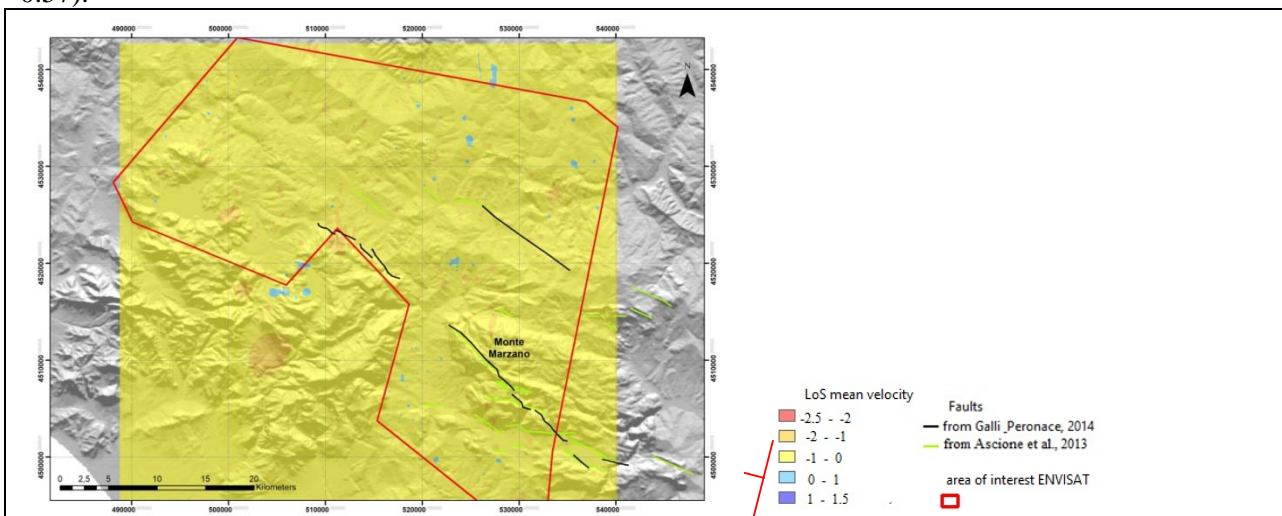


Fig. 4.28 ENVISAT descending subset - IDW interpolation map realized with PSs classified as "not significant"

Then, starting from the "... CO_2k_IDW_nout" PS subsets, applying the IDW interpolation (cell = 50x50 m) and constructing first the ascending and descending mean velocity (VLoSa and VLoSa) maps (Fig. 4.29

and Fig. 4.30), it is possible, using a raster calculator tool, to represent the vertical component of mean velocity maps, through the relationship

$$(3) \quad V_z = (V_{LoSd} + V_{LoSa})/2\cos\theta$$

applied both to the ERS and ENVISAT data (Fig. 4.31 and Fig. 4.32).

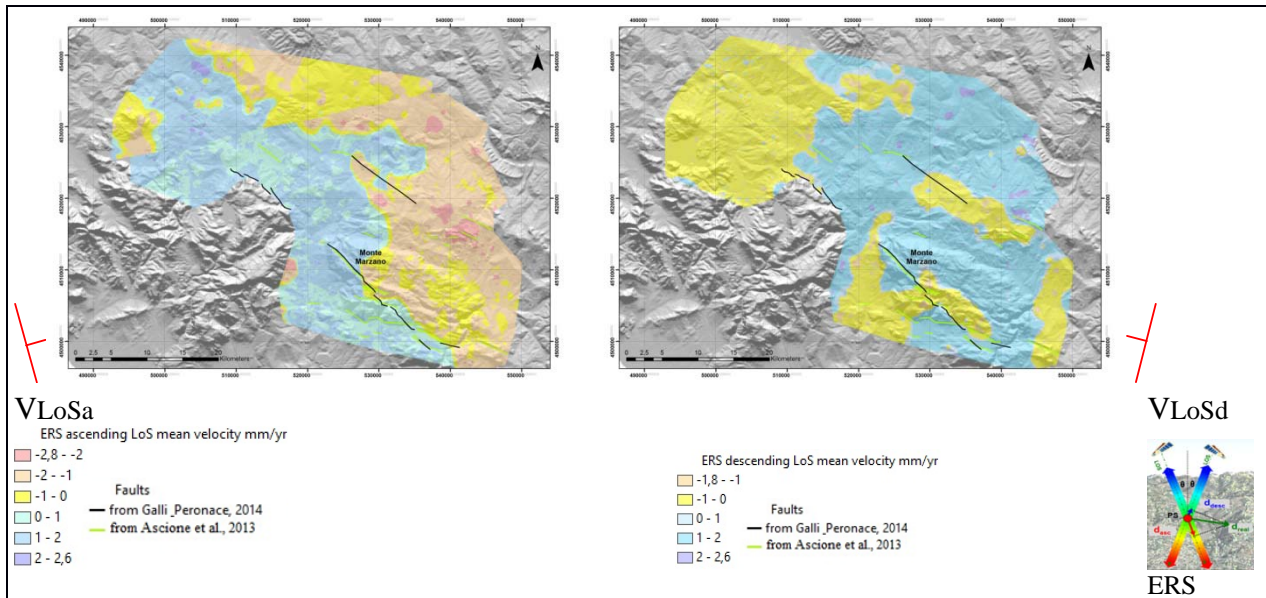


Fig. 4.29 ERS IDW interpolation map realized with PSs classified as "Cluster: High (HH)" and "Cluster: Low (LL)", ascending (left) and descending (right) subsets

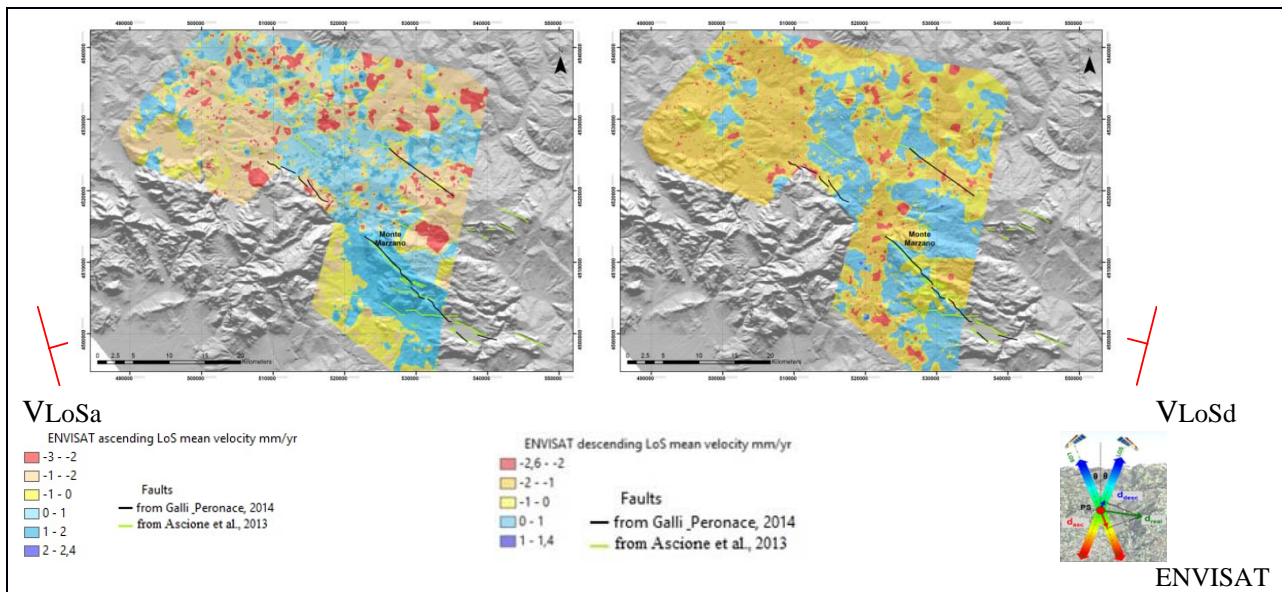


Fig. 4.30 ENVISAT IDW interpolation map realized with PSs classified as "Cluster: High (HH)" and "Cluster: Low (LL)", ascending (left) and descending (right) subsets

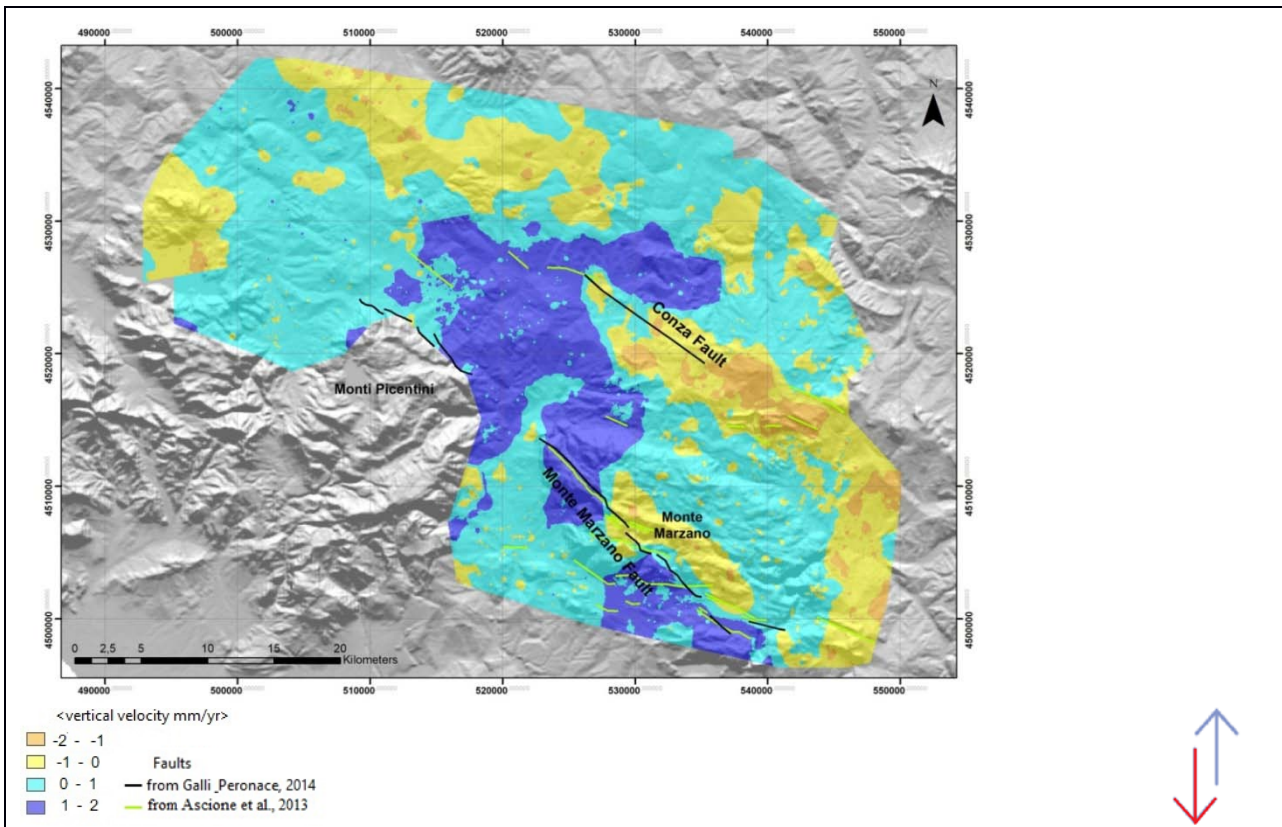


Fig. 4.31 ERS data - vertical mean velocity deformation map 1992-2000 - IDW interpolation (cell 50x50 m) - data statistical selection with *Cluster and Outlier Analysis mapping tool* considering only features HH and LL

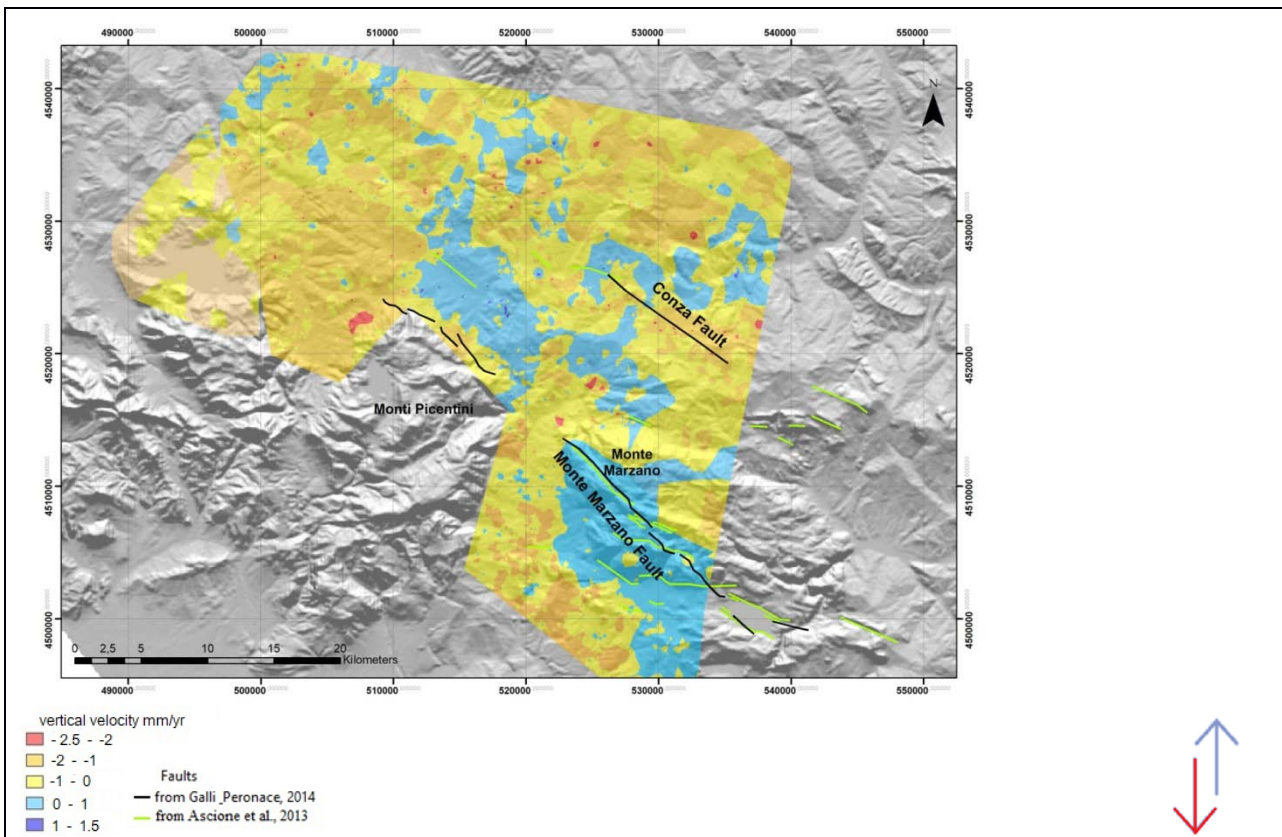


Fig. 4.32 ENVISAT data - vertical mean velocity deformation map 2003-2010 - IDW interpolation (cell 50x50 m) - data statistical selection with *Cluster and Outlier Analysis mapping tool* considering only features HH and LL (see Chapter 2)

4.4 Discussion and Concluding remarks

The maps obtained through the two types of processing here presented (for rapid comparison between them see Fig. 4.33), with one technique (i.e., IDW analysis of “native” PS datasets) requiring few steps of analysis and the other one (the one based on the Cluster and Outlier Analysis) a more complex sequence of steps, are quite similar in terms of spatial distribution of vertical (up/down) motion orientations.

Both the ERS maps show that the area of interest is for the most part slightly uplifted (0-1 mm/yr mean velocity class). However, the ERS vertical mean velocity deformation map 1992-2000, obtained with the *Cluster and Outlier Analysis mapping tool* (CO map of Fig. 4.31, also shown in the upper left corner of Fig. 4.33), shows more impressively than the map of Fig. 4.7 (upper right corner of Fig. 4.33) the presence of areas characterised by slightly higher positive velocity (1-2 mm/yr mean velocity class) in the 1992-2000 time span. These are located in the areas corresponding to: (1) the footwall block of the structure labelled Monte Marzano fault by Galli and Peronace (2014) (particularly, the northern and southern parts of such block); (2) in the the footwall block of the structure that crosses the Ofanto river valley, labelled Conza fault by Galli and Peronace (2014), and continuing southwards to San Fele (green fault trace); (3) in the central part of the sector bounded by the two structures described above, which has been identified as a major graben structure based on both seismological and levelling data (Bernard and Zollo, 1989; Pingue and De Natale, 1993).

In addition, two elongated bands, NW-SE oriented and characterised by slight subsidence (0 to -1 mm/yr or -1 to -2 mm/yr mean velocity classes), are identified in the hanging wall blocks of the Monte Marzano and the Conza - San Fele fault systems. The bands form narrow (c. 4-5 km wide) belts following the Monte Marzano and Conza - San Fele major structures. .

In the maps derived by ENVISAT PS-datasets, the area of interest is for the most part subject to subsidence (the most represented is the 0 to -1 mm/yr mean velocity class), but areas that in the ERS-based maps show uplift are still visible as slightly uplifting.

In the maps derived from the native datasets (on the right side in Fig. 4.33), localized orange or blue spots that are widespread in almost the entire analysed areas can be noticed. Comparison of spatial distribution of orange/blue spots with surface geology features shown in the schematic map of Fig. 4.3a suggests that the spots are most probably related to gravitational phenomena, which affect the shale/clay-dominated formations (e.g., Internal units and Pliocene wedge-top basin deposits) that crop out in most of the investigated region.

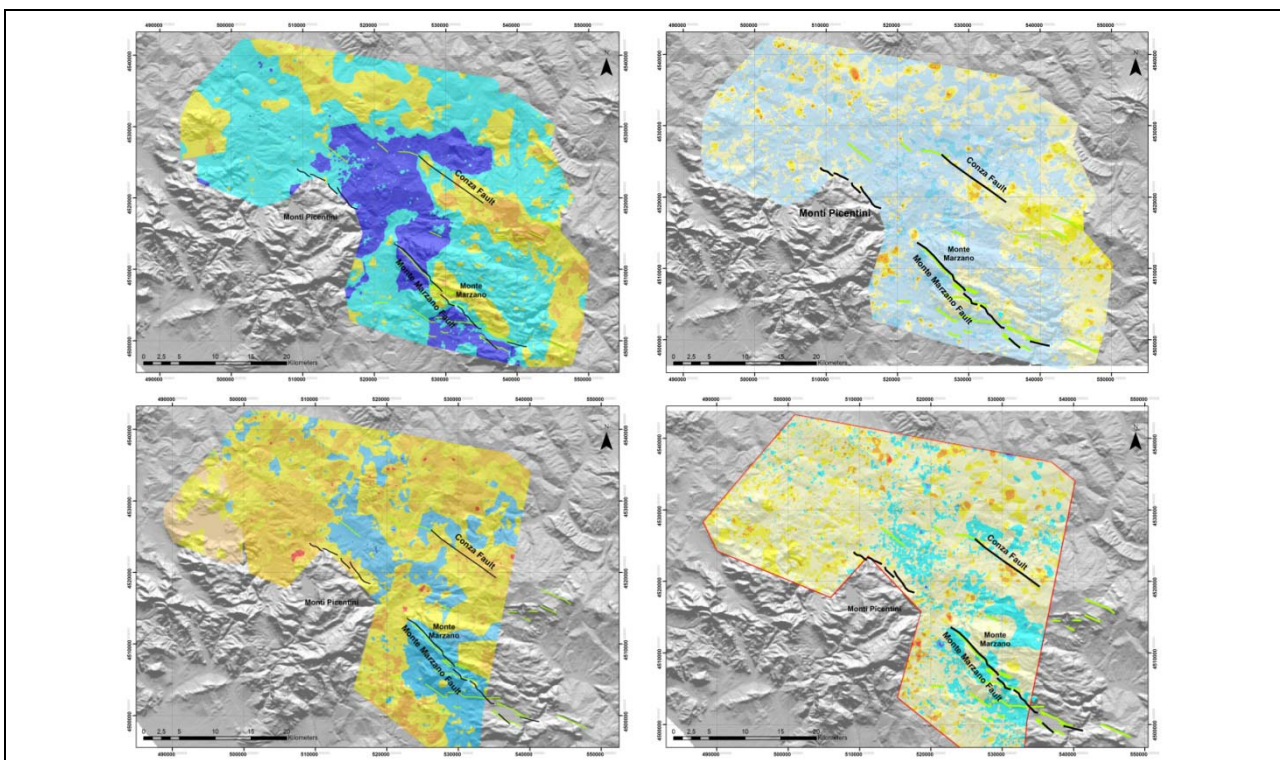


Fig. 4.33 Comparison between ERS (up) and ENVISAT (bottom) vertical mean velocity maps obtained through the IDW analysis of “native” PS datasets (maps in right side) and the *Cluster and Outlier Analysis* (maps in the left side). Upper left corner: Fig. 4.31; upper right corner: Fig. 4.7; lower left corner: Fig. 4.32; lower right corner: Fig. 4.9.

The tectonic setting of the 1980 Irpinia earthquake region is shown in Fig. 4.3. The Irpinia earthquake was characterized by a complex source mechanism, associated with at least three normal faulting ruptures on distinct fault segments (Bernard and Zollo, 1989), involving the activation of both the Central Fault (that, at the surface, is associated with the Monte Marzano fault) and the NE Boundary Fault (that, at the surface, is associated with the Conza and San Fele fault segments) shown in Fig. 4.3b.

Like Peltzer et al. (1998), we have analysed intermediate- and near-field, postseismic surface displacements following the Irpinia 1980 earthquake using processed ERS 1/2 and ENVISAT SAR data with PS-InSAR technique, covering time intervals between 1992 and 2010. The PSs interpolated maps revealed transient displacement patterns that were either not observed or only partially captured by other geodetic techniques. In particular, the PSs interpolated maps depict vertical displacements of the ground surface. Analysis of the range change maps, that cover an 18 years long time span, starts only 12 years after the 1980 earthquake.

Both the ERS and ENVISAT vertical mean velocity deformation map (Fig. 4.33) show that the footwall of the northeast dipping Monte Marzano fault has been uplifting over the analysed time span. Such a uplift is more marked during the time span covered by the ERS satellites (mean velocity of about 1-2 mm/yr). On the other hand, the hanging wall block of the Monte Marzano fault, near field of the fault itself, has been characterized by slow subsidence (in the -1 to 0 mm/yr mean velocity range). Likewise, the footwall block of south-west dipping Conza fault has been uplifting, more markedly (mean velocity of about 1-2 mm/yr) during the time span covered by the ERS surveys, while the hanging wall block was characterized by slow subsidence.

Uplift, more evident in the time span covered by the ERS surveys, characterises the sector located at the northwestern termination of both the Monte Marzano and Conza faults.

Amoroso et al. (2014), thanks to the installation of dense, high dynamic range, seismic networks operated by INGV (Istituto Nazionale di Geofisica e Vulcanologia) and AMRA (Analisi e Monitoraggio dei Rischi Ambientali) in the area struck by the 1980 Irpinia earthquake, recorded a massive waveform dataset of micro-earthquakes with magnitude larger than about 1, from August 2005 through April 2011. The researchers, by analysing VP and VS wave velocities in the upper crust of the Irpinia fault system (and the related microseismicity distribution, that appears to be confined within an uplifted block including the main normal fault rupture of the 1980 earthquake), observed in the region where intense microseismicity is located, high VP/VS and low VP×VS values, suggesting fluid accumulation within a ~15 km wide rock volume. Further studies (Amoroso et al., 2017) have provided evidence for a composition of the fluids permeating the subsurface of the 1980 Irpinia earthquake region dominated by CO₂ and brine.

At depth, high VP/VS values are located in a region that is bounded by the SWBF and the NEBF, respectively (Fig. 4.5). The projection, at the surface, of the rock volume with high VP/VS value (see Fig. 4.34) is quite consistent with the spatial distribution of the slowly uplifting sector located in the central part of the area of interest (Figs. 4.31 and 4.32) , i.e. in the central part of the area located between the Monte Marzano - Monti Picentini and Conza faults.

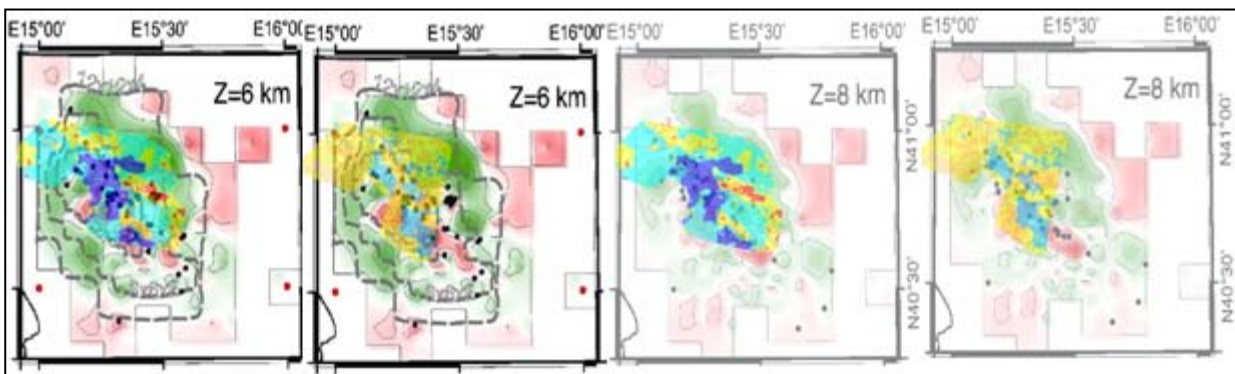


Fig. 4.34 Horizontal slice showing V_P/V_S ratio at depths (Z) of 6 and 8 km (from Amoroso et al., 2014, modified) respect to surficial SAR ground deformation. In the figures, relative to depths, on the left side there is ERS, on the right ENVISAT deformation maps.

The analysis of PS-InSAR data from the region struck by the strongest Italian earthquake of the last century, the M 6.9 1980 Irpinia earthquake, has shown that ground deformation has been affecting this area in the last tens of years.

The PS-InSAR data analysis covers a time span that ranges from 12 to 30 years after the earthquake. The analysis has shown that cumulative deformation is consistent with co-seismic deformation inferred from both seismological data (rupture mechanisms of the three main shocks, occurred in a 40 s time span; e.g., Bernard and Zollo, 1989), levelling data (e.g., Pingue and De Natale, 1993) and coseismic surface faulting (e.g., Cinque et al., 1981; Pantosti and Valensise, 1990). In addition, it is consistent with evidence of Late Quaternary – active – faults at the surface (e.g., Ascione et al., 2013; Galli et al., 2013). In particular, evidence for continuing uplift of the footwalls – and subsidence of the hanging wall blocks – of the two major faults activated with the 23th November earthquakes has been identified.

The results of PS-InSAR data show that post-seismic deformation was still occurring 30 years after the earthquake. However, the light decrease in the uplift rate from the time span surveyed by the ERS satellite to that covered by the ENVISAT could represent the effect of decay time fault creep/low energy earthquakes over decades after the earthquake, and of consequent decrease in deformation activity.

In addition, the PS-InSAR data analysis has shown that also the region in the mid part between the two main structures activated with the 1980 earthquakes is currently affected by slow uplift. Based on spatial superposition of this region with the rock volume (extending from ~ 6 km depth downwards) that has been identified as saturated of fluids, such uplift may be interpreted as the response, at the surface, to accumulation of CO₂ at depth. Comparison between the ERS- and ENVISAT-based maps shows that fluid-induced uplift has decreased in the analysed 20 years time-window, however it is not possible to assess whether such a decrease represents effective diminishing uplift (and decreasing fluid input), or a only a stage in a fluctuating long-term process.

CHAPTER 5 - INVESTIGATION OF PRE-SEISMIC GROUND DEFORMATION IN THE 1997 COLFIORITO EARTHQUAKE

5.1 Geological framework

The Umbria – Marche segment of the northern Apennines fold and thrust belt of the east-verging Neogene thrust and fold belt of Central Italy (Patacca et al., 1992; Calamita et al., 1994) (see Section 3.3.1), in the Colfiorito earthquake epicentral area, involves the rocks of the sedimentary cover, which consists of three major lithological groups that, from the top to the bottom, are: turbidites (Miocene, up to 3000 m thick), made from alternating layers of sandstones and marls; carbonates (Jurassic-Oligocene, about 2000 m thick), consisting of an early Jurassic carbonate platform (Calcare Massiccio Fm.), overlain by pelagic limestones with subordinated marly levels; and evaporites (late Triassic, 1500–2000 m thick), made from alternating layers of anhydrites and dolomites (Anidriti di Burano Fm.); these units are separated from the underlying basement by an important regional décollement (Mirabella et al., 2008; Fig. 5.1). Such a tectonic setting is suitable for trapping high-pressure fluids derived from CO₂ mantle degassing (Quattrocchi, 1999; Chiadini et al., 2000).

Calamita et al. (2000) interpret the Colfiorito seismogenic structure as a crustal thrust-ramp, inverted during the Quaternary extensional tectonics linked by high-angle normal faults reaching the surface. In the Umbria – Marche region, the east-northeast (ENE)–verging thrusts and folds dating back to the Miocene–Pliocene compressional phase are dissected by upper Pliocene–Quaternary extensional faults, mainly NNW–SSE-trending, that form fault-bounded basins (see Section 3.3.1).

Comparing the subsurface setting (reconstructed based on interpretation of seismic reflection profiles crossing the epicentral area, which constrain the subsurface geometry to a depth of about 12 km) with accurately determined earthquake locations, Mirabella et al. (2008) found that where most of the shallow seismicity of the 1997–1998 Colfiorito earthquake sequence was located entirely within the sedimentary cover and did not penetrate the underlying basement (Fig. 5.1). In particular, all earthquakes of Mw > 5 nucleated in the evaporites, the same lithologic unit where CO₂ at near-lithostatic pressure was encountered in the San Donato borehole (Miller et al., 2004; Fig. 5.2). Such a finding is explained by considering that the sedimentary cover is thick and composed of relatively strong rocks (platform carbonates and evaporites), while the upper part of the basement consists of weak phyllites and siliciclastic rocks (Mirabella et al., 2008). The effect of this weak horizon (which is also evidenced by low-Vp values measured in deep wells) has been that decoupling the sedimentary cover from the crystalline basement, where only microseismicity has been recorded (Mirabella et al., 2008). Chiaraluce et al. (2005) also showed that the main shocks of the Colfiorito sequence nucleated close to the intersections between the normal faults and the preexisting compressional/transpressional structures, which acted as lateral barriers to rupture propagation and constrained the fault size.

Chiaraluce et al. (2005) highlighted that the earthquakes distribution reflects the fault pattern mapped at the surface. In fact, the length of activated and mapped faults is quite similar (7–10 km) and the coseismic subsided region imaged by InSAR data by Stramondo et al. (1999) is located in the hanging wall of the mapped normal faults that bound the Quaternary basins. In addition, in section view there is a geometric connection between mapped normal faults and the aftershock alignments used to image fault geometry at depth, and comparison of striated fault planes and aftershock focal mechanism solutions show a strong kinematic consistency (Chiaraluce et al., 2005).

Tondi et al. (1997) had mapped in detail capable (*sensu* IAEA (1991) i.e., the subset of active faults with the potential for surface rupture, commonly associated to moderate to strong crustal earthquakes) normal faults in the region including the Colfiorito basin, also emphasizing their potential for coseismic ground displacement.

The 1997 seismic sequence left significant ground effects, which were mainly concentrated in the Colfiorito inter-mountain basin (Cello et al., 1997; Cello et al., 2000; Vittori et al., 2000).

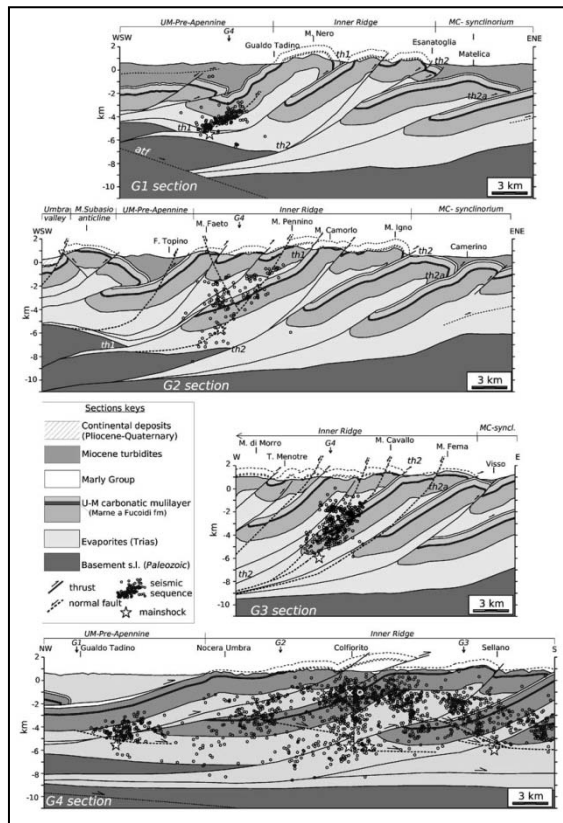


Fig. 5.1. Geological cross sections (traces in Fig. 5.2b) across the Umbria-Marche sector of the northern Apennines. G1, G2, and G3 are transversal (SW–NE) sections, and G4 is a longitudinal section (trending NW–SE). th1 and th2 are the main thrusts involving the basement (from Mirabella et al., 2008).

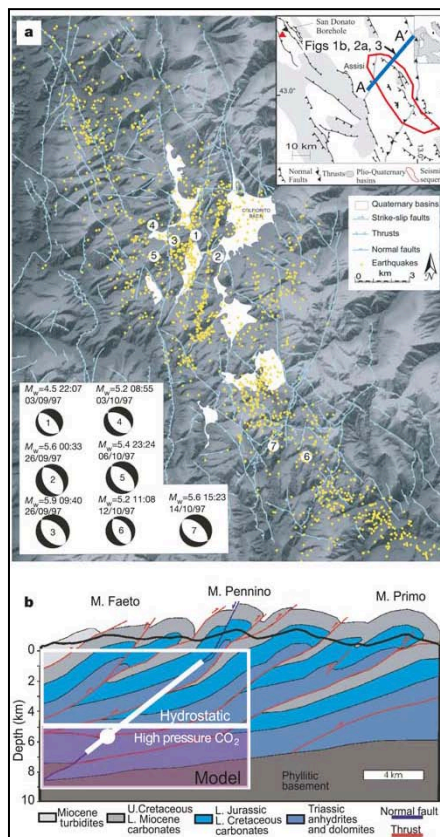


Fig. 5.2. a) Seismicity and major structures of the Colfiorito region. Near-lithostatic pore pressure (CO_2) measured in the San Donato borehole (see inset) was encountered in the evaporites and just below the seal of a sub-horizontal thrust. All $M_w > 5$ earthquakes nucleated in the evaporites. b) Geologic cross-section, with the simplified model shown superposed. U., Upper; L., Lower. (From Miller et al., 2004).

5.2 Seismotectonic and SAR remote sensing background of the 1997 Colfiorito earthquake

The 1997 Colfiorito earthquake sequence was characterized by six moderate magnitude earthquakes ($5 < M_w < 6$) (Chiaraluca et al., 2003; Fig. 5.3). The two main shocks of the sequence, with M_w 5.7 and M_w 6.0, occurred nine hours apart on September 26th 1997. The entire sequence ruptured, at depths around 7 – 8 km, adjacent and roughly parallel NW-SE trending normal fault segments dipping $40^\circ - 45^\circ$ towards the SW (Amato et al., 1998; Ekstrom et al., 1998; Chiaraluca et al., 2003; Stramondo et al., 1999; Fig. 5.4). The lateral extent of the fault segments range from 5 to 10 km and make up a broad, ~ 45 km long, NW trending fault system (Chiaraluca et al., 2003). In April 1998 the sequence migrated to the NW (Gualdo Tadino area) with a $M_w = 5.1$ event (Ciaccio et al., 2005).

At the surface, diffuse ground breaks with centimeter size throws were observed along a 10 km wide belt in the epicentral area (Basili et al., 1998; Cinti et al., 1998). The observed ground and pavement ruptures, which were associated with the largest shocks (those with M_w 5.7 and M_w 6.0), were concentrated in narrow bands that, in part, are on and near previously mapped high-angle normal faults (Cinti et al., 1998). However, based on geological investigations, modeling of expected coseismic elevation changes, and seismic data, that the surface deformation is considered not the direct result of primary rupture of faults at depth (Cinti et al., 1998).

Coseismic displacement of the two main shocks of the 1997 Colfiorito earthquake sequence has been imaged by differential interferometric (DInSAR) technique, which also allowed constraining their source mechanisms (Stramondo et al., 1999). By creating an ERS-SAR differential interferogram, Stramondo et al (1999) identified nine fringes in and around the Colfiorito basin (Fig. 5.5), corresponding to 25 cm of coseismic surface displacement, while by GPS data they estimated a maximum horizontal displacement of 14 ± 1.8 cm and a maximum subsidence of 24 ± 3 cm. Modeled maximum slip amplitudes were 47 cm for the M_w 5.7 event and 72 cm for the M_w 6.0 event, consistent with those derived from seismological data (Stramondo et al., 1999).

According to Miller et al. (2004), a sudden upward migration of CO_2 followed the two main shocks (M_w 5.7 and M_w 6.0) of the 1997 Colfiorito earthquake sequence. Such main shocks provided a transient connection between a lower zone at near-lithostatic pore pressure (CO_2 at near-lithostatic pressure was encountered in the San Donato borehole at a depth of 4.8 km about 50 km northwest of Colfiorito; Chiodini and Cioni, 1989) and an upper zone at hydrostatic pore pressure, driving aftershock activity, with thousands of aftershocks that included four additional events with magnitudes between 5 and 6. In particular, aftershocks of large earthquakes in the Colfiorito region of the northern Apennines may be driven by the coseismic release of trapped, high-pressure fluids propagating through damaged zones created by the mainshock (Miller et al., 2004).

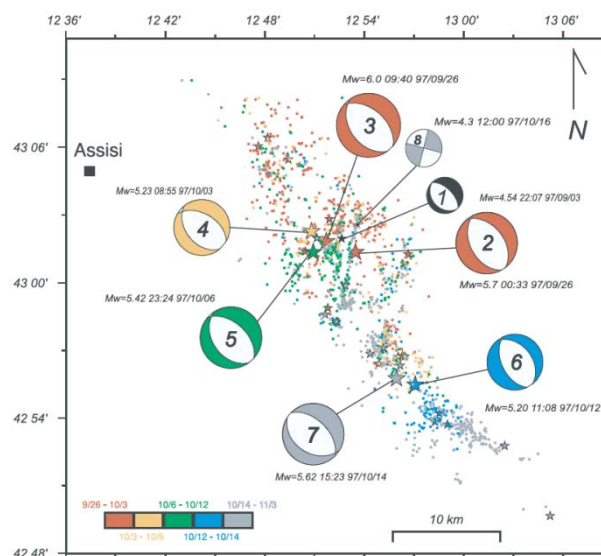


Fig. 5.3. Map view of the relocated seismicity with focal mechanisms of the main events of the Umbria-Marche 1997 seismic sequence. The epicenters are color coded by time intervals defined by the six main shocks. Numbers in the focal sphere are sequential in time (from Chiaraluca et al., 2003).

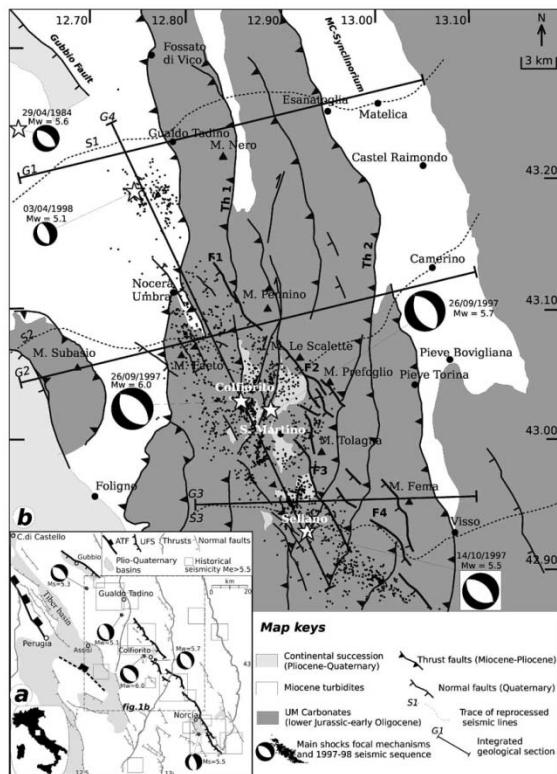


Fig. 5.4. (a) Geological sketch of the Umbria-Marche Apennines between Citta' di Castello to the NW and Norcia to the SE. The main compressional and extensional structures (ATF and UFS) of the area are drawn together with the historical seismicity ($M_e > 5.5$) and the instrumental seismicity ($M > 5.0$). (b) Geological sketch of the Umbria-Marche Apennines between Gualdo Tadino to the NW and Visso to the SE representing the Inner and Outer ridges of the region separated by the Matelica-Camerino (MC) synclinorium. The figure represents the main compressional and extensional structures, the mainshocks of the area in the last 20 years and the 1997–1998 earthquake sequence. F1, F2, F3, and F4 are the main normal fault segments. The location of the geological sections (G1, G2, and G3) are also drawn for further reference. (from Mirabella et al., 2008).

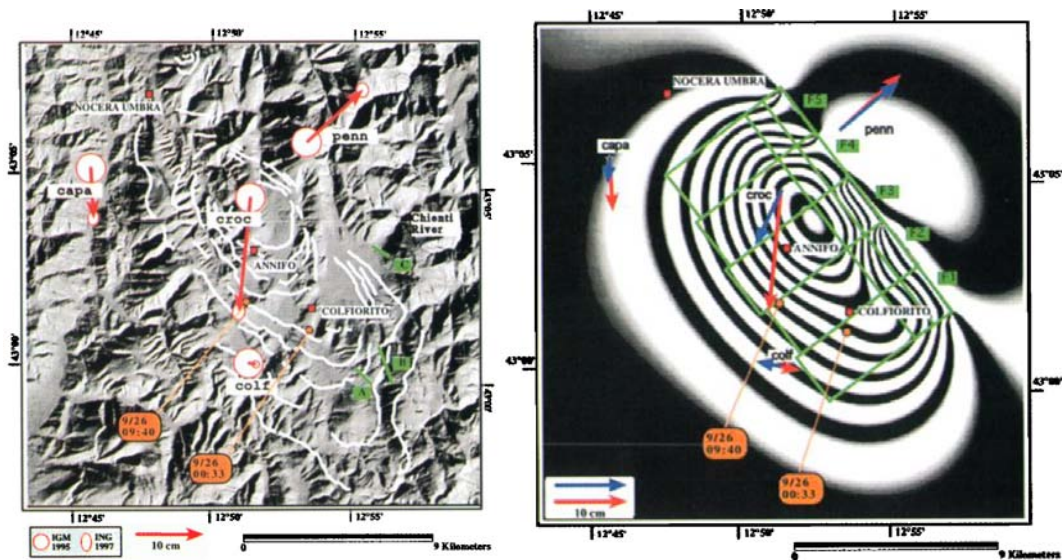


Fig. 5.5. Left: geocoded displacement contours retrieved from the interferogram. Right: synthetic interferogram and surface projection of the Colfiorito fault model. Planar displacement vectors at the GPS stations are shown by red arrows; modelled horizontal displacement vectors at the GPS stations are shown as blue arrows (from Stramondo et al., 1999).

5.3 PSs and time series analysis in Colfiorito earthquake area

The availability of about 20-year-long PS-InSAR data coverage of the Italian territory - MATTM datasets encompassing the April 1992 to December 2000 time span for ERS satellites, acquired from both the ascending and descending orbits - has allowed us to perform the analysis of ground deformation of the investigated region during a time window that predates and postdates the 1997 Colfiorito earthquake. We have analysed the ERS PSs datasets in Table 5.1.

ERS	
DESCENDING TRACK	ASCENDING TRACK
pst_ers_t79_f2748_cl002_matelica (6557 PSs)	pst_ers_t401_f858_cl004_spoletto (12261 PSs)
pst_ers_t79_f2748_cl001_gualdo (5106 PSs)	pst_ers_t401_f858_cl003_spello (28025 PSs)
pst_ers_t79_f2748_cl003_spoleto (25664 PSs)	

Table 5.1 - PS datasets used in this case study

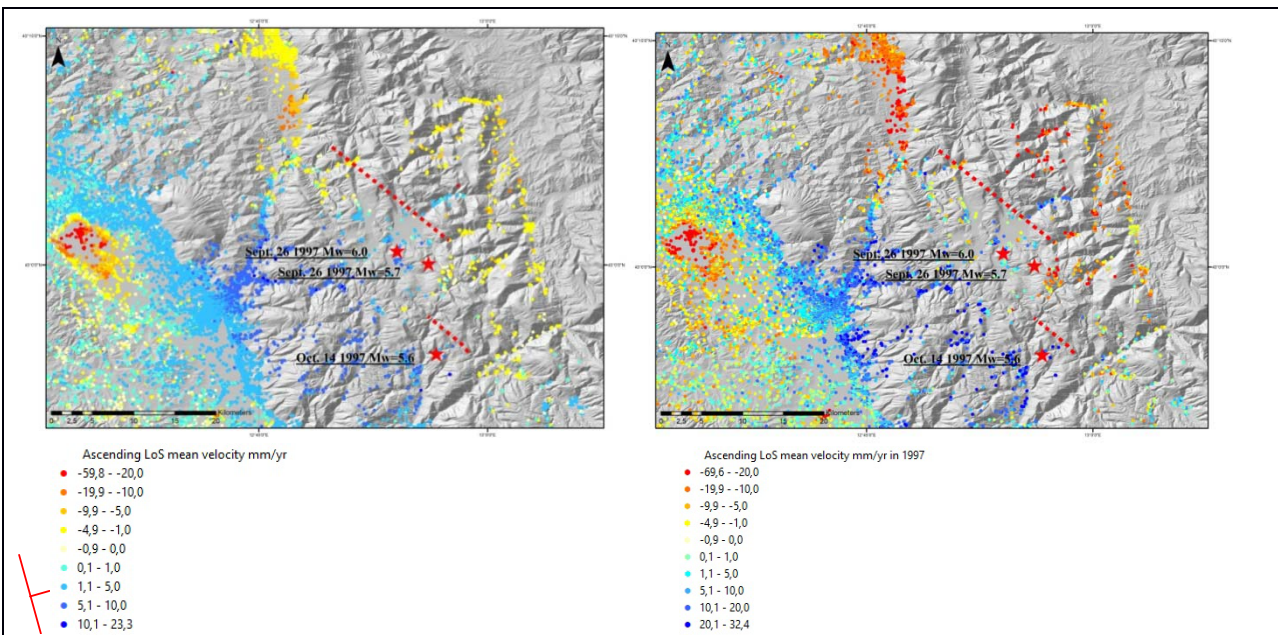


Fig. 5.6 Ascending ERS PSs datasets. Left: from 1992 to 2000. Right: only 1997. Red stars are the september-october 1997 earthquake epicenters. Red dashed lines the likely ground ruptures.

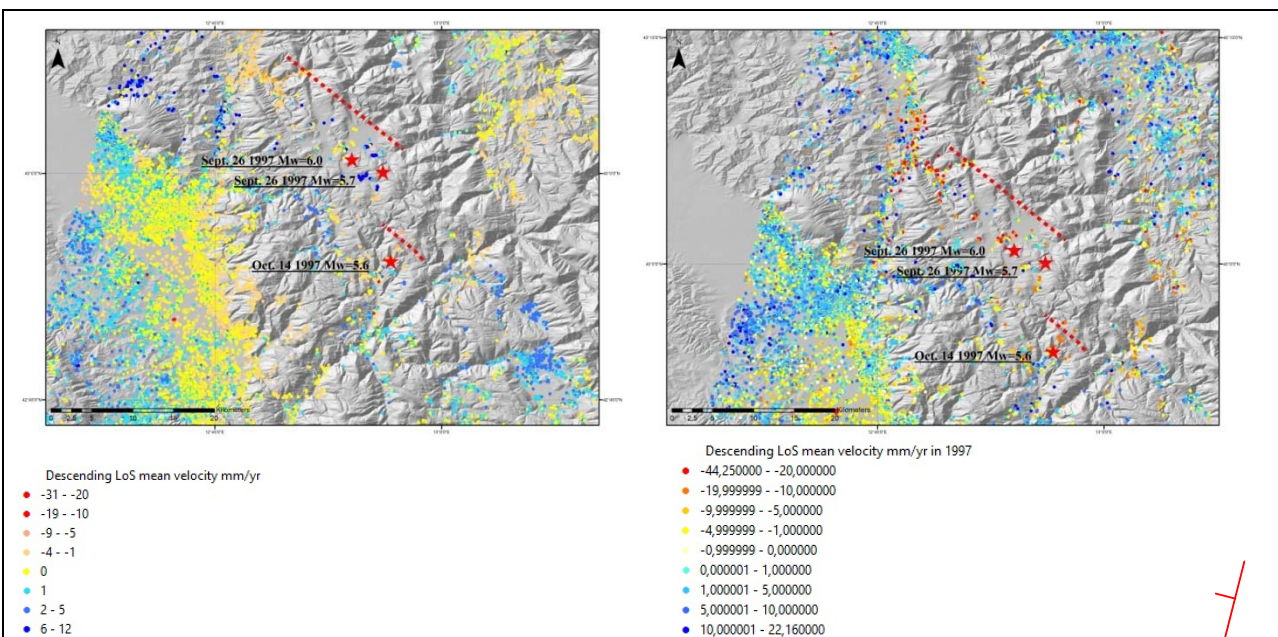


Fig. 5.7 Descending ERS PSs datasets. Left: from 1992 to 2000. Right: only 1997. Red stars are the september-october 1997 earthquake epicenters. Red dashed lines the likely ground ruptures.

As can be deduced from the Figs. 5.6 and 5.7, the area coverage of the ERS PSs on the Colfiorito epicentral area appears to be somewhat dispersed. In fact, only 235 ascending and 350 descending PSs fall down in the 160 km² wide epicentral area; this indicates a 1.5-2 PSs per km², a very low density of data in the territory. The low density is clearly connected with the scarce urbanization of the territory and therefore with the absence of adequate reflectors with respect to the radar signals emitted by the ERS 1/2 satellites. Moreover, the deformation values associated with the PSs do not seem to be consistent with the deformations (a maximum of about 25 cm) measured by Stramondo et al., 1999 (see section 5.2). In Fig. since 5.8 to 5.11 it is shown four PSs time series in the epicenter area.

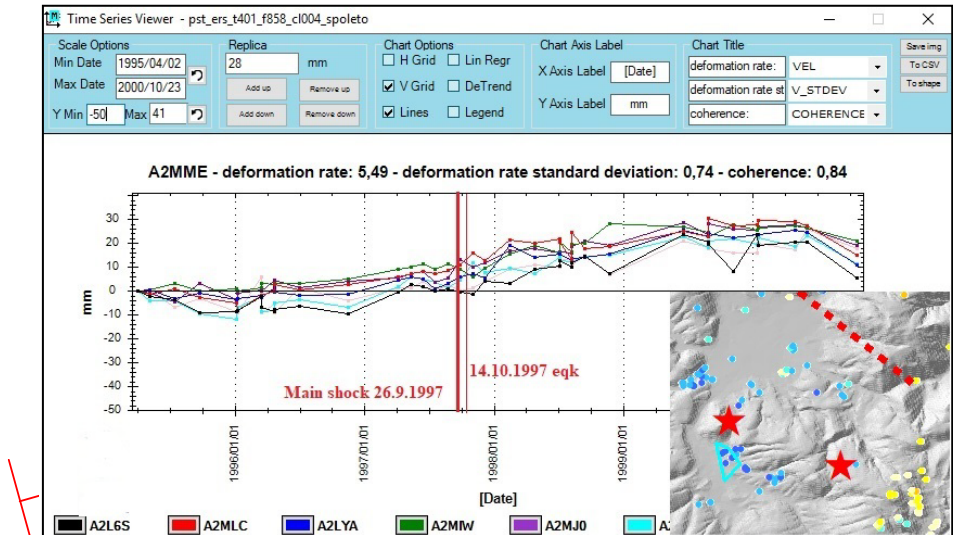


Fig. 5.8 PSs ascending time series near the epicenter area (light blue polygon)

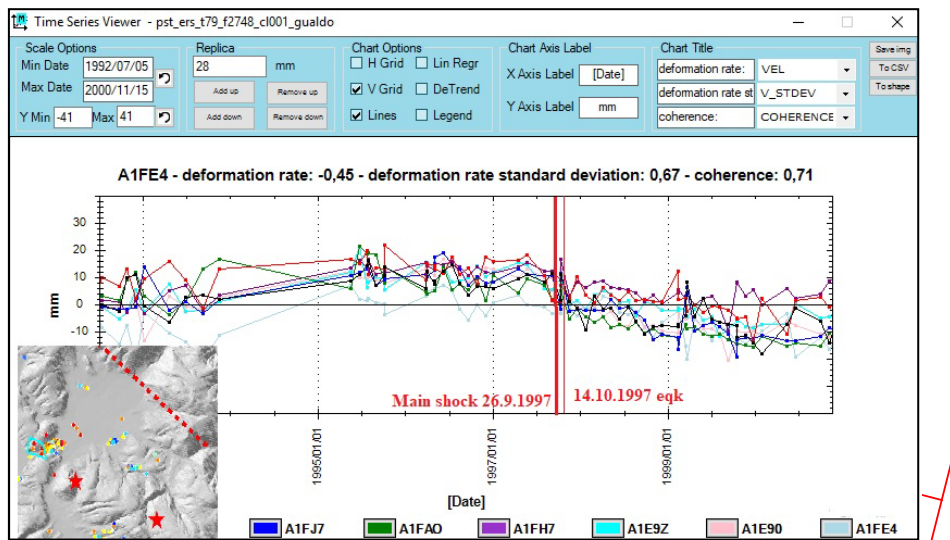


Fig. 5.9 PSs descending time series near the epicenter area (light blue polygon)

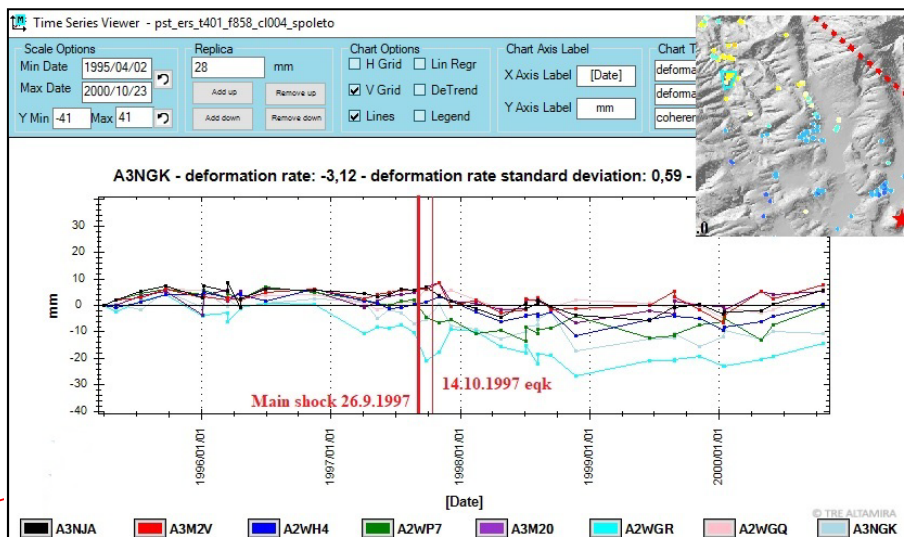


Fig. 5.10 PSs ascending time series in northern portion of epicentral area (light blue polygon)

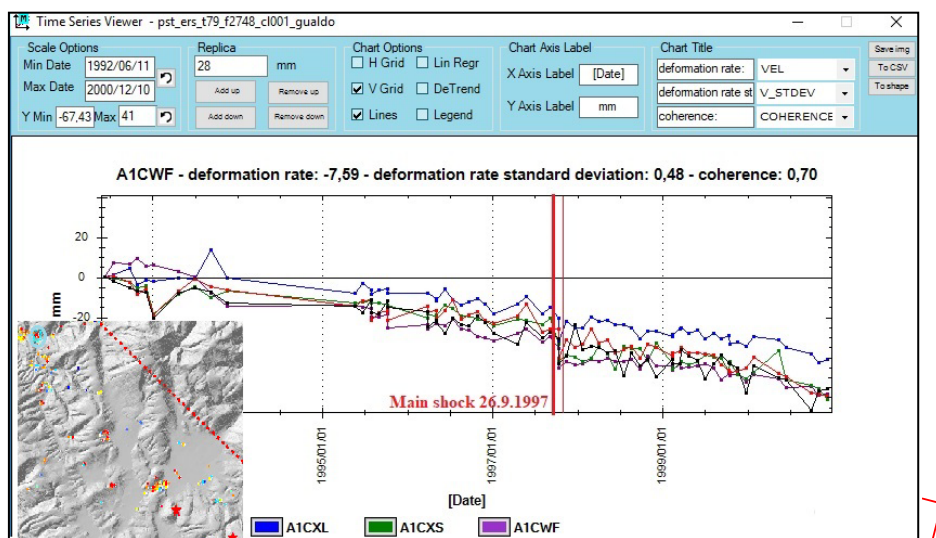


Fig. 5.11 PSs descending time series in the northern portion of epicentral area (light blue polygon)

5.4 Discussion and Concluding remarks

In Fig. 5.8 the PSs ascending time series near the epicenter don't show any signal like a step in the displacement values, in correspondence of earthquakes date; before and after the earthquakes the trend was positive, that is the PSs moved towards the satellite (to the west).

In Fig. 5.9 the PSs descending time series near the epicenter show only a weak signal like a step in the displacement values in earthquakes date; before the earthquakes the displacement trend was roughly horizontal (neither approaching to nor get away from satellite), while after it was slightly negative that is the PSs moved away from the satellite (to the west too).

Not evident pre-seismic signal seems characterize the time series near the epicenter. In the post-seismic period there was a main slightly horizontal displacement west oriented, compatible with a dip-slip normal fault segments, NW-SE trending and dipping towards the SW.

In Fig. since 5.10 the PSs ascending time series in the north of the epicentral area, show a very weak signal like a step in the displacement values in earthquakes date; before the earthquakes the displacement trend was roughly horizontal (neither approaching to nor get away from satellite), while after the trend was slightly negative, through out 1998. In 1999 and 2000 the trend turn to light positive.

In Fig. since 5.11 the PSs descending time series in the north of the epicentral area, show a very weak signal like a step in the displacement values in earthquakes date; the displacement trend was always negative, away from the satellite (to the west).

There was not evident pre-seismic signal in the northern PSs time series too. In the post-seismic period there was a mainly a very light subsident displacement west oriented, compatible with a dip-slip normal fault segments, NW-SE trending and dipping towards the SW.

CHAPTER 6 - INVESTIGATION OF PRE-SEISMIC GROUND DEFORMATION IN THE 2009 L'AQUILA EARTHQUAKE

6.1 Seismotectonic and SAR Remote Sensing background of the 2009 L'Aquila earthquake

The 6th April 2009 L'Aquila earthquake struck with strong damages the Aterno river middle valley Quaternary basin (Galli et al., 2009; Santo et al., 2014, and references therein; Fig. 6.1), in central Italy. The Mw 6.3, 6th April 2009 mainshock was preceded by foreshocks that started in October 2008 (Di Luccio et al., 2010). In the following months, many aftershocks were recorded including two strong aftershocks with Mw 5.4 and Mw 5.6 (Di Luccio et al., 2010; Papadopoulos et al., 2010; Valoroso et al., 2013). The main shock hypocentre was located at about 9 km depth along a NW-SE striking normal fault, dipping at 55°-60° (Chiarabba et al., 2009; Pondrelli et al., 2010; Scognamiglio et al., 2010). The surface expression of the structure activated with the 2009 earthquake has been associated with the Paganica - San Demetrio fault system (PSDFS, *sensu* Galli et al., 2010; Fig. 6.1), a 18-20 km long, NW-SE trending fault system composed of several, few km long segments with dextral *en-echelon* arrangement and dipping to the SW (Galli et al., 2010; 2011). The earthquake caused several ground ruptures (open cracks and fractures with vertical offsets) mainly NW-SE trending and aligned along the PSDFS but also affecting the Aterno river plain (Boncio et al., 2009; EMERGEO Working Group, 2010), some of which have been interpreted as surface faulting (Falcucci et al., 2009; Lavecchia et al., 2009). Vertical offsets of surficial fractures were mostly within 10 cm (Galli et al., 2010).

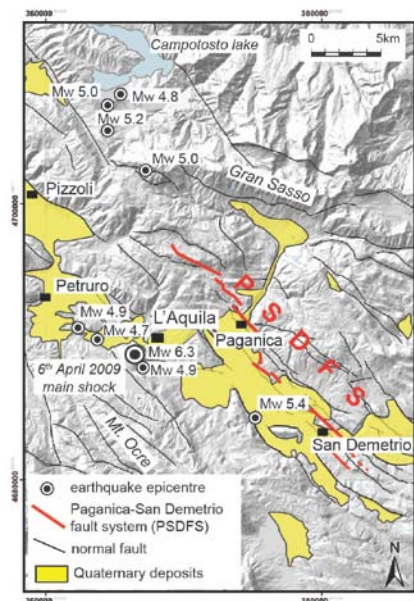


Fig. 6.1 The 2009 L'Aquila earthquake epicentre region, with location of Paganica - San Demetrio fault system (PSDFS, *sensu* Galli et al., 2010). Locations of epicentres of the Mw 6.3, 6th April 2009 main shock and of the strongest aftershocks (from the ISIDE catalogue: <http://cnt.rm.ingv.it/iside>), are also shown. The middle Aterno river valley is NW-SE trending and includes several sub-basins located from Pizzoli, in the N, to San Demetrio, in the S.

Besides the seismological and field data, a huge amount of information fundamental to the reconstruction of the 2009 L'Aquila earthquake displacement field, and to constrain the earthquake source mechanism, has been obtained by analyses of different types of remote sensing and geodetic datasets. GPS and DInSAR modelling of the co-seismic displacement field (Anzidei et al., 2009; Atzori et al., 2009; Walters et al., 2009; Papanikolaou et al., 2010) have concurred to define a 50° SW-dipping normal fault plane, geometrically consistent with both the mainshock seismogenic source and the southern segment of the PSDFS. In particular, the differential SAR interferograms (Fig. 6.2) have shown the deformation pattern generated by the fault slip, with a large sinking (~ -25 cm) of the downthrown block vs. $\sim +5$ cm in the raised block (Atzori et al., 2009; Walters et al., 2009; Papanikolaou et al., 2010). Similar values of the co-seismic deformation were estimated by GPS inversion (Cheloni et al., 2010).

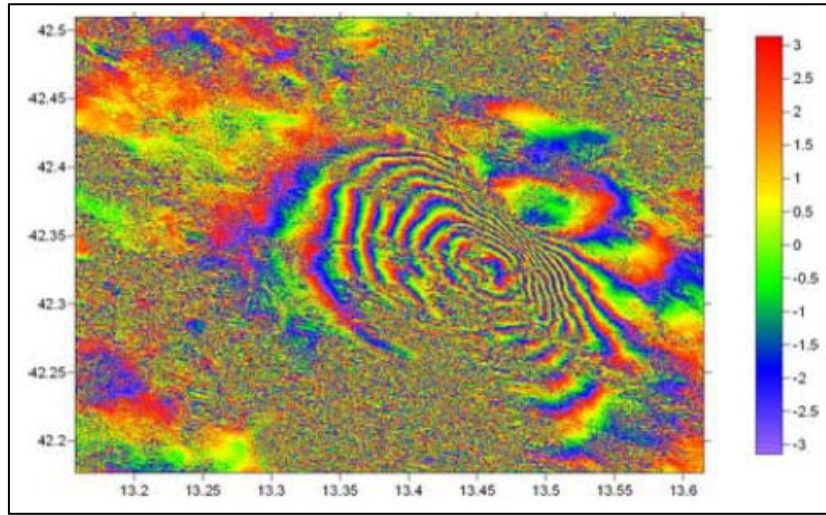


Fig. 6.2 Geocoded differential interferogram over l'Aquila region; acquisition between February and May 2009.

SAR data analysis has also allowed detection, in the region hit by the 2009 L'Aquila earthquake, of post-seismic deformation (hanging wall subsidence; Lanari et al., 2010; D'Agostino et al., 2012; Cheloni et al., 2014), while less clear is the reconstruction of the pre-seismic deformation scenario. Lanari et al. (2010) by analysis of DInSAR time series (February 2003 to October 2009) from ENVISAT ascending track data sets in the 2009 epicentre area, point out that pre-seismic surface deformation is negligible. On the other hand, by applying DInSAR processing to ALOS and ENVISAT satellites data, Atzori et al. (2013) identify a far-field pre-seismic (from 2005) deformation process in the region to the west of the mainshock epicentre. Furthermore, by analysis of multiple SAR data sets (RADARSAT, ENVISAT and COSMO-SkyMed), Moro et al. (2017) recognise in two sub-basins of the middle Aterno valley basin located to the north of the mainshock (Pizzoli and Petruo basins; Fig. 6.1), up to 15 mm of subsidence in the three years before the main shock and post-seismic uplift up to 12 mm. In both cases a relationship with seismically-induced fluctuations of the groundwater table has been hypothesised.

6.2 Materials and method

By the InSAR technique, deformations are detected as phase variations of the electromagnetic signal, through a multitemporal acquisition of SAR images, along the satellite Line of Sight (LoS; Fig. 6.3).

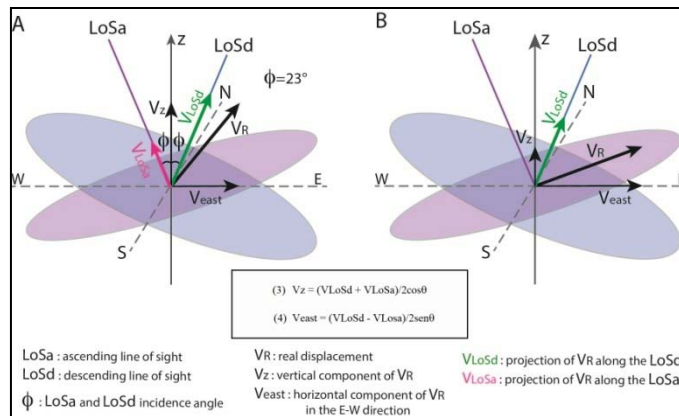


Fig. 6.3 - A: ERS and ENVISAT SAR geometry, showing LoS-oriented components of the real displacement vector (VR) along the descending and ascending satellite orbits, and in the up-down (z) and E-W planes; components of the real displacement vector (VR) oriented towards the north or south are not detected by the SAR. B: components of the real displacement vectors (VR) for PS motion occurring in a plane orthogonal to orientation of the ascending LoS, i.e., motion that is undetectable by SAR satellite in the ascending orbit, with an up-east orientation. Equations (3) and (4) are from: Lundgren et al. (2004), Manzo et al. (2006), Lanari et al. (2007), Tofani et al. (2013).

From the methodological point of view, differential interferometry is applied in terms of stacking of interferograms using SBAS (Small Baseline Subset; Berardino et al., 2002) and/or PS (Permanent Scatterer) techniques. In our work, we have used the PS-InSAR technique (Ferretti et al., 2000; 2001).

Permanent Scatterers (PSs) correspond to man-made objects (structures on the roofs of buildings, utility poles, dams, etc.) or natural (rock outcrops) reflectors characterized by stable individual electromagnetic radar phase signal over long temporal series of interferometric SAR images. The phase data from PS are used to detect topographic changes in time. The availability of about 20-year-long PS-InSAR data coverage of the Italian territory - MATTM datasets encompassing the April 1992 to December 2000 time span for ERS satellites and the November 2002 to June 2010 time span for ENVISAT satellite data, acquired from both the ascending and descending orbits - has allowed us to perform the analysis of ground deformation of the investigated region during a time window that predates and postdates the 2009 L'Aquila earthquake. We have analysed both the ERS (1991 - 2000) and ENVISAT (2003 - 2010) PS datasets (Table 6.1).

ERS	
DESCENDING TRACK	ASCENDING TRACK
pst_ers_t308_f2751_cl001_l_aquila (42573 PSs)	pst_ers_t129_f837_cl002_pineto (47650 PSs)
pst_ers_t308_f2769_cl001_sulmona (69065 PSs)	pst_ers_t129_f837_cl001_celano (126131 PSs)
ENVISAT	
DESCENDING TRACK	ASCENDING TRACK
PST2009_ENVISAT_T79_F2748_CL001_AQUILA (127089 PSs)	PST2009_ENVISAT_T401_F840_CL001_AQUILA (270047 PSs)
PST2009_ENVISAT_T308_F2751_CL001_TERAMO (341759 PSs)	PST2009_ENVISAT_T129_F837_CL001_CHIETI (308357 PSs)

Table 6.1 - PS datasets used in this case study

ERS and ENVISAT PS data from the MATTM database are high quality (coherence index ranging from 0.6 to 1. Specifically, for data in our study area the PS coherence index mean value is about 0.7, with standard deviations of PS mean velocity (in the 1991 – 2000 and 2003 – 2010 time spans) in the 0.4 to 0.5 mm/yr range, and of the deformation measurement error of ± 3 mm, respectively.

In the analysed area, centred on the L'Aquila 2009 earthquake epicentre and 340 km² wide, there are 16,700 descending track ERS PSs (55 PS/km²) and 12,000 ascending track ERS PSs (40 PS/km²), and 29,000 ENVISAT descending track PSs (95 PS/km²) and 39,000 ENVISAT ascending track PSs (130 PS/km²), respectively. The PS spatial distribution is substantially homogeneous in the analysed area.

A thoroughly visual inspection of all available, individual ERS and ENVISAT PSs time series was performed with the aim of detecting temporal changes in the ground motion oriented along both the ascending and descending LoS. Based on the results of such an inspection (Section 6.3), the ENVISAT data set was selected for the further analyses below described.

Due to the SAR acquisition geometry, it is necessary to consider ascending - descending PSs pairs in order to compose the “real” displacement in the vertical plane (z) oriented west-east (Fig. 6.3A). Such a composition may be performed using a geometrical relationship (Lundgren et al. 2004; Manzo et al., 2006; Lanari et al., 2007; Tofani et al., 2013; Fig. 6.3) linking the LoS displacement values and the LoS angle of incidence, which is $\Phi = 23^\circ$ for both ERS and ENVISAT satellites. However, PS from ascending and descending images are neither spatially coincident nor exactly synchronous. In order to homogenise the data sets from the temporal point of view, we have composed each image pair by selecting ascending-descending radar images with a time separation not larger than one month, ending with the composition of 24 radar image pairs for the 2005 – 2010 time span. Then, a GIS-aided spatial analysis was carried out in order to construct a set of raster interpolating maps of displacement values for the ascending and descending LoS, respectively. For the geospatial analysis, the Inverse Distance Weighting interpolator (IDW) statistics with 50×50 m size cell was used. The ascending and descending LoS displacement maps were constructed for different time intervals of the pre- to post-seismic time span. Individual time intervals were set based on the results of the PS time series analysis (Section 6.3.2).

The GIS-aided analysis was then applied to the construction of maps of the vertical (z, up - down) component of the “real” displacement vector, following equation (3) of Fig. 6.3.

Afterwards, we have constructed profiles along traces transversally oriented to the main structures in the study area, which synthesise the cumulative vertical displacement for each of the time intervals set based on the results of the PS time series analysis.

6.3 Results

6.3.1 ERS dataset analysis

All available descending and ascending pairs of ERS PSs time series from the 2009 L'Aquila earthquake epicentral region were analysed. The descending LoS PS time series show a periodic, seasonal signal (Fig. 6.4A) within a general sub-horizontal trend. Such a trend indicates that mean PS velocities are around 0 mm/yr with respect to the descending LoS in the 1992 – 2000 time span (Fig. 6.4A). The ascending ERS PSs time series show irregular signals, although some seasonal oscillation is still identified (Fig. 6.4B). However, as well as for the descending orbit ERS PSs time series, the general trend is sub-horizontal with a resulting LoS-oriented mean velocity around 0 mm/yr.

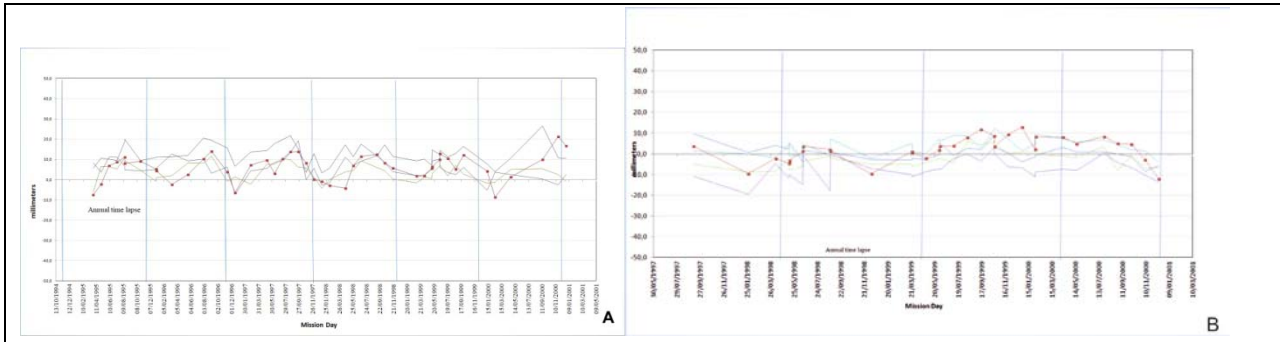


Figure 6.4 – Examples of ERS (1992 – 2000) time series of PSs from the 2009 L'Aquila earthquake epicentral region (PSDFS fault hanging wall block). A: Descending LoS time series: the general trend is sub-horizontal (mean velocity ~ 0 mm/yr), although it is evident the presence of a periodic and seasonal signal. B: Ascending LoS time series: the general trend is sub-horizontal, but the signal is quite noisy with a likely periodic and seasonal oscillation.

Since trends of both the ascending and descending time series are sub-horizontal, the composition of the single pairs of PS according with SAR geometry (Fig. 6.4) does not show substantial vertical or horizontal (E-W oriented) ground deformation all over the study region in the 1992 – 2000 time span.

6.3.2 ENVISAT dataset analysis

An in-depth visual inspection of all of the available pairs of PSs ENVISAT time series from the study region has been carried out. As for the ERS time series, the ENVISAT time series show irregular and oscillating – seasonal – signals. Such signals are the main feature of the ascending time series in the 2004 to March 2009 time span (Fig. 6.5A). In other words, no clear displacement oriented towards, or opposite to, the LoS and an almost null mean velocity (sub- horizontal trend) with respect to the ascending LoS are observed throughout the pre-seismic period in the study region. The analysis also shows that PS time series from a wide area in the middle Aterno valley to the SW of the PSDFS, image a sudden downward motion during the co- to early post-seismic period (March 2009 – May 2009; e.g., Fig. 6.5A). The final part of the PS time series records (May 2009 - June 2010) show substantial absence of ground motion oriented along the ascending LoS (Fig. 6.5A).

More complex temporal evolution, and spatial distribution, of ground motions have been detected through the analysis of PS time series from the ENVISAT descending tracks. In particular, irregular and oscillating – seasonal – signals that characterise the PS time series appear as minor features of PS motion with respect to main trends oriented along the LoS. For instance, as it is shown by the PS time series from an area close to the main shock epicentre, four main stages may be distinguished in the analysed time window (Fig. 6.5B). In a first time span (2004 to July-October 2008; Stage A in Fig. 6.5B), an upward motion oriented along the descending LoS is detected by the linear trend of the displacement. From July–October 2008 to the beginning of April 2009, the time series show a downward trend (Stage B in Fig. 6.5B). In the March-April 2009 to May-June 2009 time span, i.e., in the co-seismic to early post-seismic time span, a sudden downward motion is identified, followed by a subdued lowering from May/June 2009 to June 2010 (Stages C and D in Fig. 6.5B, respectively).

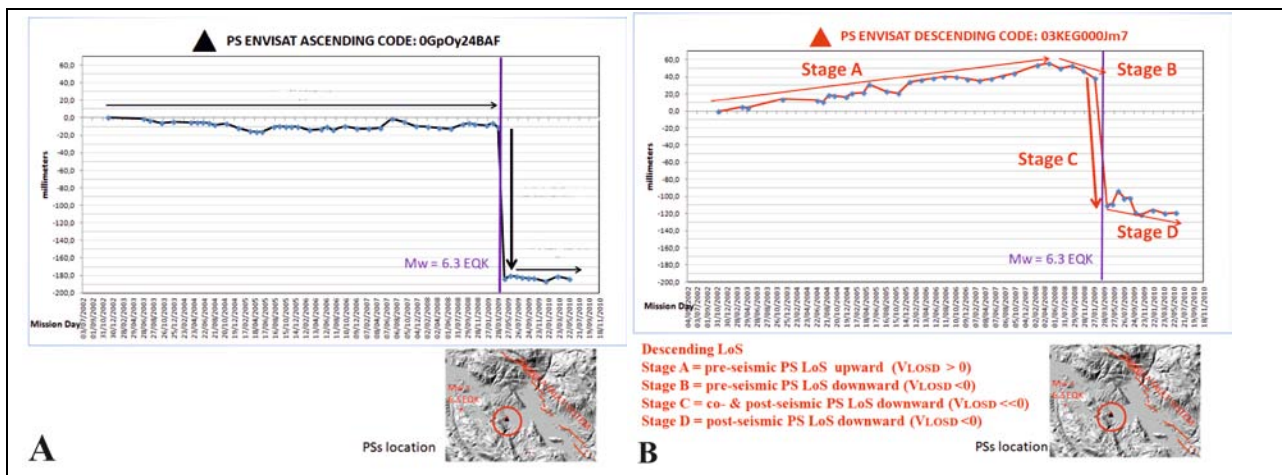


Figure 6.5 – 2003 - 2010 time series of ENVISAT PSs pair from an area close to the 2009 L’Aquila earthquake epicentre (locations in inset maps). A: Ascending LoS time series. Three stages may be distinguished: in a first stage (2004 – March 2009) the general trend is sub-horizontal (mean velocity ~ 0 mm/yr), meaning non net LoS upward or downward motion; in the short time span that includes the 2009 L’Aquila main shock (March – May 2009) a sudden downward motion is identified; in the May 2009 – June 2010 time span the general trend is sub-horizontal. B: Descending LoS time series. Four deformation stages may be distinguished in the 2004 - 2010 time span: Stage A (from 2004 to September/October 2008) corresponds to a positive (oriented upward towards the LoS) trend; Stage B (September/October 2008 – January/February 2009) corresponds to LoS downward trend; Stage C (March – May 2009) corresponds to a sudden LoS downward trend; Stage D (May 2009 – June 2010) corresponds to a slow LoS downward trend.

The different motion patterns that are detected by analysis of time series from the descending and ascending orbits find an explanation in the geometrical configurations of the two orbits (Fig. 6.3). For instance, the combination of the slow uplift/subsidence trends detected in areas to the west of the PSDFS along the descending LoS in the Stages A, B and D, with coeval apparent absence of PS motion along the ascending LoS (Fig. 6.3), may be explained by “real” PS motions occurring, with either east or west orientations, along a plane dipping at high angle with respect to the ascending LoS (Fig. 6.3B). As a result, the components of SAR-real displacement vector (i.e., displacement in an vertical, E-W oriented plane) are oriented towards up and east (Fig. 6.3B) during Stage A. Combining the two LoS-oriented motions during Stage B, the SAR-real displacement vector is oriented downwards with a westward component. The Stage C displacement inferred from PS motion along the two LoS corresponds to a vector oriented downwards (roughly vertical). The combination of the two LoS-oriented motions suggests a SAR-real displacement vector oriented downward (with a westward component) during Stage D.

The multitemporal, spatial distribution of the vertical component of PS motion in the entire study region has been analysed through the combination of both the ascending and descending displacement components. In order to select homogeneous ranges in the displacement orientation, we have separately analysed the time spans corresponding to the Stages A to D that have been distinguished by analysis of the descending PS time series (Fig. 6.5B).

The maps of Fig. 6.6 show the values of the vertical displacement cumulated during Stages A (January 2005 - September 2008) and B (September 2008 - February 2009), respectively. The map of Fig. 6.6A shows that, during Stage A, a large area covering the 2009 mainshock experienced uplift with mean values around 10 mm (the corresponding displacement along the descending LoS has a mean value of $\sim 18 \pm 6$ mm) and maximum values of ~ 25 mm. During Stage B (Fig. 6.6B), the same area that in Stage A had been uplifted underwent negative vertical displacement with mean values around 10 mm (the corresponding displacement along the descending LoS has a mean value of $\sim -14 \pm 6$ mm). The spatial distribution of the co- to early post-seismic displacement is shown in the map of Fig. 6.7, in which a sudden collapse with mean values of ~ 80 mm (and maximum values in the 180 – 200 mm range) is visible.

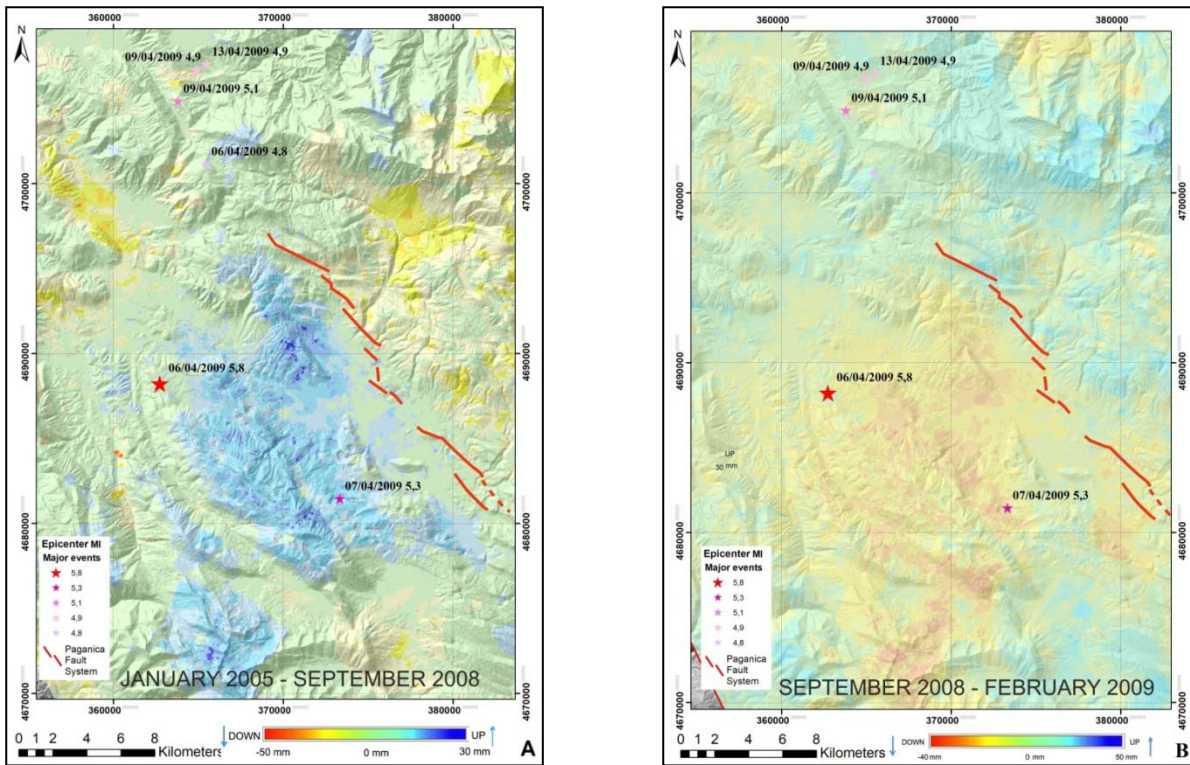


Figure 6.6 – Pre-seismic deformation pattern (IDW [50x50 m cell size] spatial interpolation) in the study region. A: Cumulative vertical (z) ground deformation during Stage A (January 2005 - September 2008); mean uplift ca. 10 mm in the PSDFS hanging wall block; the footwall block is affected by slight subsidence. B: Cumulative vertical (z) ground deformation during Stage B (September 2008 - February 2009); mean subsidence ca. 10 mm in the PSDFS hanging wall block; the footwall block shows a slight uplift.

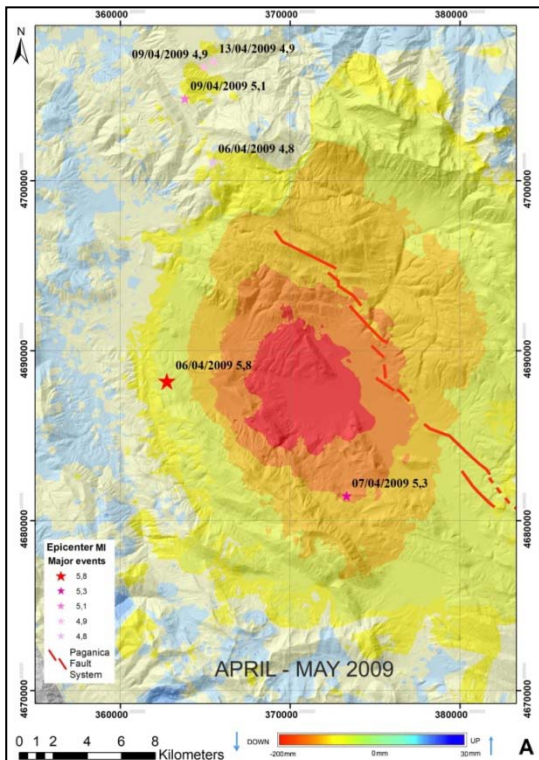


Figure 6.7 - Co- to early post-seismic deformation pattern during STAGE C (IDW [50x50 m cell size] spatial interpolation) in the study region. A: Total vertical ground deformation from February 2009 to May 2009; cumulative mean subsidence ca. 80 mm with maximum values located in the PSDFS hanging wall block.

The cross profiles of Fig. 6.8 synthesise the time-space evolution of vertical motions along a transect cut across the study region, plotted against the topographic profile. In the cross profiles, ground deformation is represented in terms of cumulative displacement summed up during Stages A to C. The displacement profiles of Fig. 6.8 show that the trace of the PSDFS falls in the highest gradient segment between the

block to the southwest, which experienced uplift during Stage A and subsidence during Stage B, and the initially lowered and then uplifted block to the northeast. A complex deformation pattern is highlighted by the bottom profile of Fig. 6.8, which shows that the area that collapsed during Stage C includes part of the elevations to the SW and NE of the middle Aterno river valley.

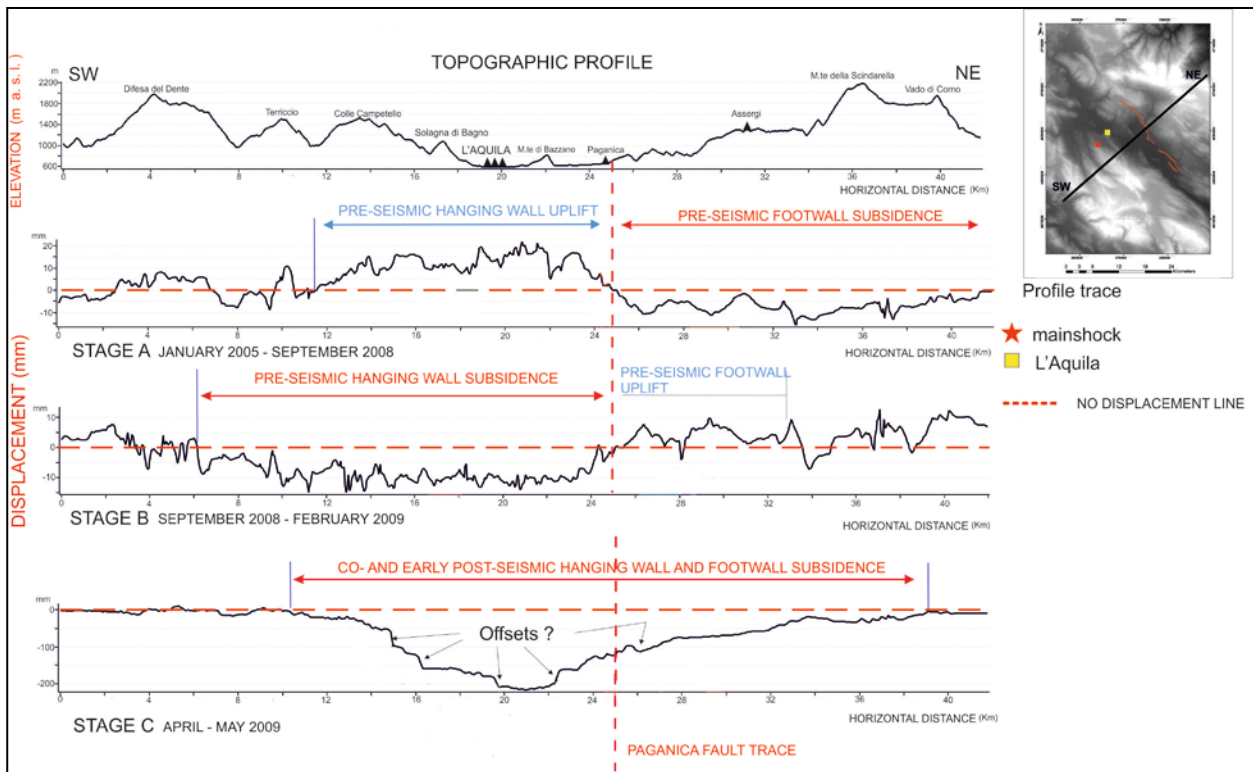


Figure 6.8 - Topographic (above) and ground deformation profiles, SW-NE oriented, constructed transverse to the Paganica segment of the PSDFS. The ground deformation profiles synthesise cumulative pre-seismic vertical displacement patterns in the pre-seismic period (STAGE A; from 2004 to September/October 2008) late pre-seismic period (STAGE B; September/October 2008 to January/February 2009) and co- to early post-seismic period (STAGE C; April to May 2009), respectively, reconstructed by processing and interpolation of PS-InSAR datasets.

6.4 Discussion and concluding remarks

The multitemporal, spatial analysis of ground deformation that we have performed through analyses of PS-InSAR datasets, provides evidence for important features of the displacements that accompanied the evolution of the 2009 seismic phenomenon occurred in the L'Aquila region during the pre- to post-seismic periods.

The analysed PS datasets bears a combination of time-variable motions, including apparent ground motion, which may be caused by atmospheric artefacts (e.g., Hanseen, 2001). Such an effect, which is very variable in time, may be considered as responsible for irregular noisy patterns (Atzori et al., 2013) such as those that characterise the time series from the ERS ascending orbit shown in Fig. 6.4B. Besides such irregular signals, short-period – seasonal – ground motions in the range of $\sim \pm 10$ mm, which are the main feature of the PS time series from the ERS descending and ascending orbits (Fig. 6.4) and of the pre- and post-seismic periods of the ascending ENVISAT PS time series (Fig. 6.5A), may be related to seasonal fluctuations in the piezometric head of the groundwater tables (Vilardo et al., 2009; Bozzano et al., 2015). Monthly-scale fluctuations characterise also the descending ENVISAT PS time series, however such a signal is subordinate, in terms of magnitude and temporal persistence, with respect to LoS oriented linear trends observed on the yearly scale time window (2003 – 2010; Fig. 6.5B).

Besides irregular and/or short period, spatially variable motions, the ERS PS time series show yearly scale sub-horizontal trends, and the combination of ascending/descending pairs has shown that no net displacement has affected the analysed region in the 1992 – 2000 time span.

A more complex scenario has been reconstructed for the narrow time window covered by the ENVISAT PS data, and in particular for the pre-seismic period. Consistent with findings by Lanari et al. (2010), data acquired from the ENVISAT ascending orbit do not show clear pre-seismic (as well as “late” post-seismic) ground displacement trends. We interpret such evidence as an effect of the geometry of the SAR

ascending orbit, which is basically unable to detect displacements within a plane at high angle (next to 90°) with respect to the ascending LoS (Section 6.3.2; Fig. 6.3B). On the other hand, the ascending dataset has provided constraints to the orientations of the pre- to post-seismic displacement vectors. The PS time series from the descending orbit and the combined (ascending plus descending) datasets have allowed detecting temporally and spatially distributed pre-seismic motions. Within the pre-seismic ground deformation frame that we have reconstructed, the PSDFS marks the boundary between blocks that experienced vertical motions with opposite orientations (Fig. 6.6). In particular, uplift, followed by subsidence, affected a large area that covers the PSDFS hanging wall block. The “early” pre-seismic uplift, which produced mean vertical displacements in the order of 10 mm, started ~ 4-5 years before the April 2009 main shock, coeval with both slow subsidence of the region to the NE that includes the PSDFS footwall block (Fig. 6.6A; Fig. 6.8), and subsidence detected by Moro et al. (2017) in the Pizzoli and Petruro sub-basins of the middle Aterno valley, to the NW of the uplifted area (Fig. 6.1; Fig. 6.6A). At ~ 6-8 month prior to the April 2009 main shock, an up-down inversion of vertical displacement affecting the blocks separated by the PSDFS is recorded (Fig. 6.9). Vertical displacements summed up during such time span were on the same order of those recorded during the former (and longer) stage.

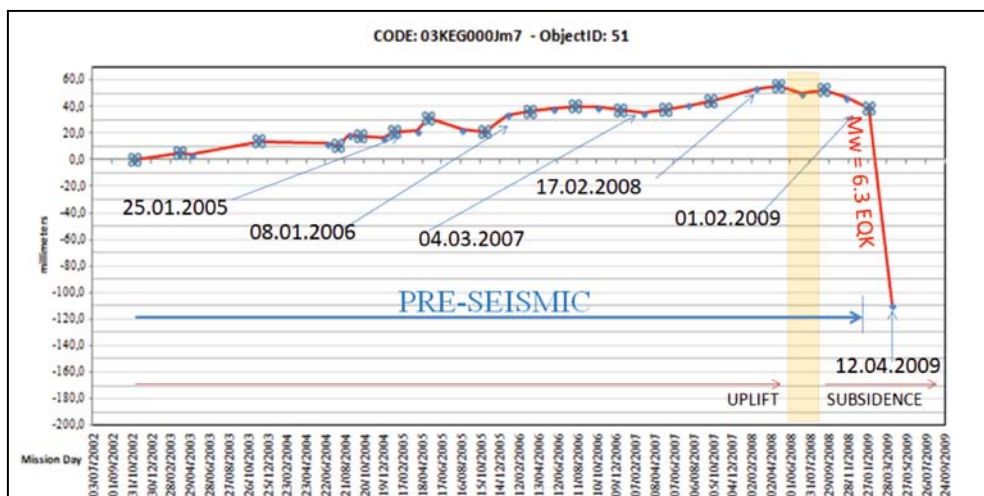


Figure 6.9 - Time intervals of about one year in which the ENVISAT satellite detected the distance of a PS along the descending LoS (LoS uplift). From the end of 2008 (8 - 6 months prior to the main shock) and the first months of 2009, the yearly uplift trend changed to subsidence.

The co- to early post-seismic vertical displacement picture is consistent with that provided by former studies based on analyses of SAR data and GPS and/or levelling data (e.g., Atzori et al., 2009; Cirella et al., 2009; Walters et al., 2009; Cheloni et al., 2010). In addition, our spatial analysis indicates that the collapsed area extends to the NE beyond the PSDFS trace (Fig. 6.6 and Fig. 6.7), and allows detecting several steps in the displacement profile (Fig. 6.8), which may suggest the occurrence of possible coseismic ruptures along the belts to the SW and NE of the area affected by maximum subsidence. The descending PS time series highlight post-seismic subsidence in the hanging wall of the PSDFS continuing at least until June 2010, consistent with evidence both provided by D’Agostino et al. (2012) based on GPS and InSAR data, and detected by Galli et al. (2010) of a few cm increase of vertical offsets of several coseismic fractures in the first months after the main shock.

The geometrical combination of the ascending and descending PS-InSAR data indicates that the displacements are not entirely vertical, but are characterised by horizontal components oriented towards either east or west (Section 6.3.2). Such evidence suggests that magnitude of “real” displacements, which in the co- to post-seismic period includes south/north-oriented components (as shown by GPS data; Cheloni et al., 2014) that are undetectable by SAR data, is larger than that evaluated with this study.

The detection by remotely sensed data of the subdued pre-seismic ground displacements that we have identified rests on a thoroughly multitemporal analysis of data by satellite image pairs. Indeed, the combined analysis of PS-InSAR datasets from both the ascending and descending orbits has been crucial to unravelling the pre-seismic behaviour of the study region.

The peculiar pre-seismic behaviour of the PSDFS hanging wall points to a relationship of the near-field surface motions with seismic phenomena. Such a relationship is also inferred from evidence that the region affected by rise followed by lowering seats on the area where the main shock and most of both

foreshocks and aftershocks (Valoroso et al., 2013) are contained, and from the chronological correlation of the up/down inversion in the pre-seismic displacements with onset of the foreshocks (October 2008; Di Luccio et al., 2010). Worthy to note, the spatial scale of such a region (which encompasses both topographic highs and lows) is independent from surface geology features, suggesting a deep-seated causative mechanism for the observed motions such as, e.g., volume changes connected to vertical/lateral fluids migration and fracturing processes at depth, with all phenomena having been documented in connection with the 2009 earthquake in the study region (e.g., Di Luccio et al., 2010; Lucente et al., 2010; Moro et al., 2017).

We suggest that pre-seismic displacements such as those that characterise the hanging wall and footwall blocks of the PSDFS may collectively represent a precursor signal of the 2009, Mw 6.3 earthquake. Our result point to the long-term (yearly scale) multitemporal InSAR data analysis as a tool crucial to the detection of ground deformation in areas struck by recent earthquakes, and to monitoring active structures.

CHAPTER 7 - INVESTIGATION OF PRE-SEISMIC GROUND DEFORMATION IN THE 2013 LUNIGIANA EARTHQUAKE

7.1 Geologic and tectonic setting

The tectonic setting of the Lunigiana–Garfagnana area is the result of extensional tectonics, started in early Pliocene, determining the formation of two NW–SE-oriented large grabens bordered by NE-dipping and SW-dipping normal faults (Elter et al., 1975; Carmignani and Kligfield, 1990; Bernini and Papani, 2002; Di Naccio et al., 2013, Eva et al., 2014). The central part of the grabens is discontinuously covered by continental deposits that recorded the progressive evolution of the two tectonic depressions from the early Pliocene to Quaternary. The Lunigiana graben extends for ~45 km along the upper Magra River valley. The Garfagnana graben is left-stepped compared to the Lunigiana graben and extends for ~27 km along the Serchio River valley, parallel to the eastern margin of the Apuane Alps metamorphic core.

The NE-dipping and SW-dipping normal faults are synthetic and antithetic splays of a major NE-dipping detachment fault (e.g., Argnani et al., 2003), which was inferred to be the northern termination of a regional-scale system of NE dipping, low-angle normal faults (Etrurian fault system in Boncio et al., 2000) extending along the entire northern Apennines (Barchi et al., 1998; Lavecchia et al., 2009).

Between the southern termination of the Lunigiana graben and the northern termination of the Garfagnana graben, there is a nearly E–W-striking, N-dipping fault zone with normal-oblique right-lateral kinematics (red line fault (k) in Fig. 7.1). This fault zone forms the northern boundary of the Apuane metamorphic core and has been interpreted as a presently active transfer fault between the Lunigiana and Garfagnana extensional grabens (north Apuane transfer fault zone in Brozzetti et al., 2007).

In Fig. 7.2 (from Stamondo et al., 2014) is shown a structural sketch of the Lunigiana and Garfagnana area with the June 21, 2013 earthquake, its focal mechanism and the 2013 sequence. The Sarzana-Equi Terme line (SL in Fig. 7.2) is equivalent to the red line fault (k) in Fig. 7.1.

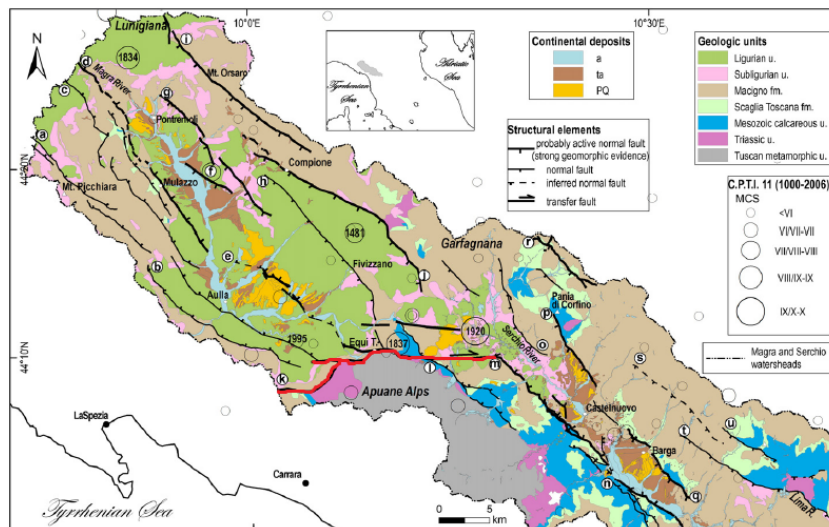


Fig. 7.1 Structural map of the Lunigiana and Garfagnana grabens showing the normal fault systems; red line k) north Apuane transfer fault zone (from Di Naccio et al., 2013, modified).

On 2013 June 21, an Mw 5.1 earthquake, 10 km depth, struck the Lunigiana area. A first focal solution for the mainshock indicates a dip-slip solution with a slight right-lateral strike-slip component. The aftershock sequence lasted for weeks, producing a large number of earthquakes. It occurred in the transfer fault zone separating the northern Lunigiana graben and the southern Garfagnana graben.

With a new INGV relocation (<https://ingvterremoti.wordpress.com/2013/08/22/ancora-attiva-la-sequenza-sismica-in-lunigiana/#comments>), the focal mechanism of the event was recalculated, showing a breaking process strike-slip type. Considering the distribution of the shocks that followed the main one and the surface deformation highlighted by the SAR data, it can be hypothesized that the fault responsible for the earthquake of M 5.2 is almost vertical and has an anti-Apennine direction (northeast-southwest).

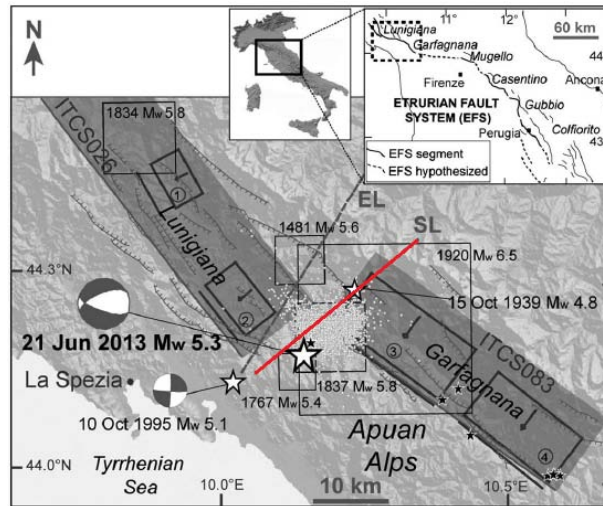


Fig. 7.2 Structural sketch of the Lunigiana and Garfagnana area with the June 21, 2013 earthquake, its focal mechanism (<http://cnt.rm.ingv.it/tdmt.html>) and the 2013 sequence. Squares: historical earthquakes having magnitude larger than 5.3; hatched lines: normal faults; dashed lines: lineaments, EL: Enza line, SL: Sarzana-Equi Terme line; dark polygon: composite seismogenic sources projection on the ground surface, black boxes: individual seismogenic sources projection onto the ground surface; black lines: up-dip projection of the seismogenic sources onto the surface 1) ITIS085-Pontremoli; 2) ITIS067-Aulla; 3) ITIS050-Garfagnana North; and 4) ITIS051: Garfagnana South; black stars: thermal springs. Inset shows the structural framework of the Etrurian Fault System. (from Stramondo et al., 2014, and references therein, modified)

Pezzo et al., 2014, applied two-pass DInSAR to measure surface displacement along the radar LoS. Only one pair, on ascending COSMO-SkyMed imagery track, had an exceptionally short temporal baseline of 1 day and a sufficient coherence for the measurements to be successful. In SAR geometry any underlying north-south displacement component is below the measurement noise level. DInSAR interferograms were generated. The displacement map derived shows a main SW-NE oriented elliptic dislocation pattern reaching a maximum value of ~ -3 cm in LoS, indicating a subsidence and/or eastward motion (Fig. 7.3).

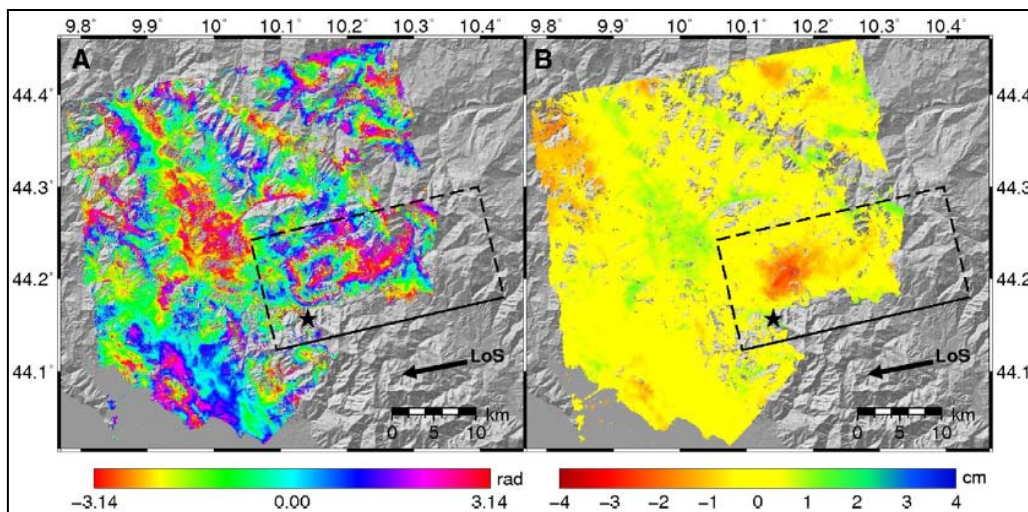


Fig. 7.3 A) and B) DInSAR ascending interferogram and displacement map derived from the interferometric pair. DInSAR deformations are positive from the ground towards the satellite. The LoS arrow shows the ground projection of the directions of positive displacement. The black rectangle represents the surface projection of the modelled fault plane, with a solid line indicating the fault trace. The black star represents the epicentre of the 2013 Jun. 21 event. (from Pezzo et al., 2014, modified).

The most reliable dislocation model achieved provides a slip distribution showing a peak value of about 30 cm, located near the mainshock hypocentre, and an overall very good correspondence with the hypocentres of the aftershocks relocated. The modelled fault plane shows a dip angle of 45° and a strike angle of 256° with an oblique mechanism, that is a main dip-slip with a slight right lateral strike-slip component.

In Stramondo et al., 2014, two differential interferograms showing the coseismic displacement have been generated using X-band and C-band data, taken from COSMO-SkyMed and RADARSAT-2 satellites, respectively. Both interferograms highlighted a clear pattern of subsidence of few cm located between the Lunigiana and Garfagnana basins. We then modeled the observed SAR deformation fields using the

Okada analytical formulation and found them to be consistent with an extensional fault plane dipping toward NW at about 50°. The integrated analysis of DInSAR, geological data, modeling, and historical seismicity suggest that the fault responsible for the June 2013 earthquake corresponds to a breached relay ramp connecting the Lunigiana and Garfagnana seismogenic sources (Fig. 7.4).

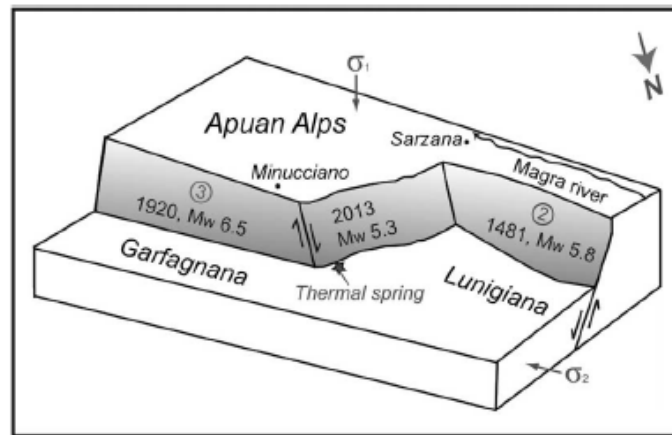


Fig. 7.4 Block diagram with the simplified fault geometry of the Lunigiana and Garfagnana areas (from Stramondo et al., 2014).

7.2 Materials and method

They were analysed the following PSs Cosmo Skymed datasets (Table 7.1) that cover the April 2011 - 2014 time span.

COSMO SKYMED	
DESCENDING TRACK	ASCENDING TRACK
PST2013_CSK_F_39_MASSA_D_CL001_MASSA (1076271 PSs)	PST2013_CSK_F_34_BARGA_A_CL001_BARGA (667071 PSs)

Table 7.1 - PS datasets used in this case study

29235 ascending and 37025 descending PSs fall down in the 100 km² wide epicentral area; this indicates a 292 ascending and 370 descending PSs per km², that is a good density of data in the territory.

The good density, in a scarce urbanized territory, is clearly connected with the power of Cosmo Skymed technology (X band radar, see Section 2.1.1).

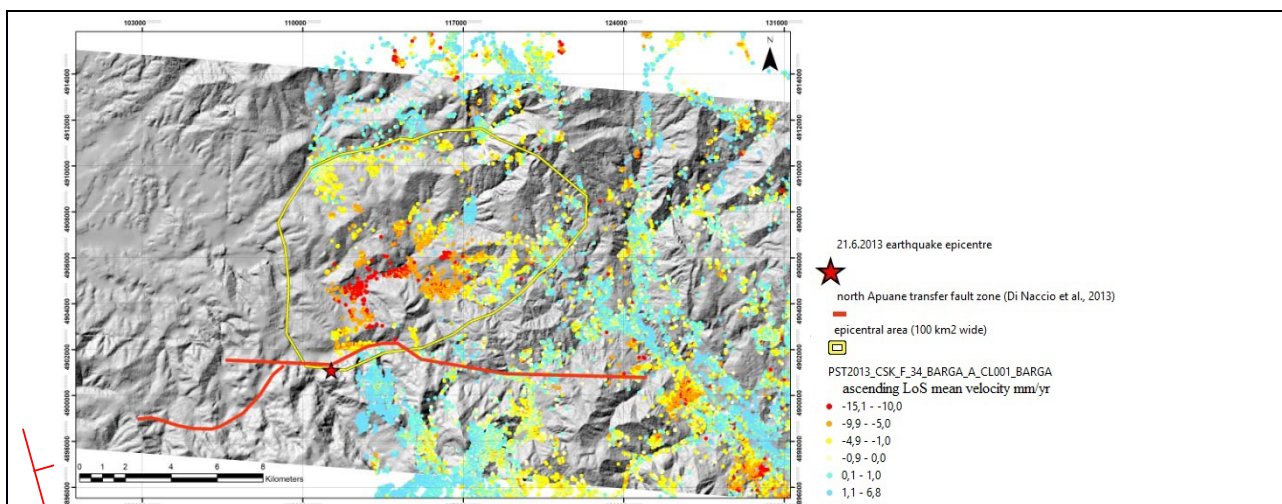


Fig. 7.5 Ascending Cosmo Skymed dataset: PSs mean velocity in the epicentral area

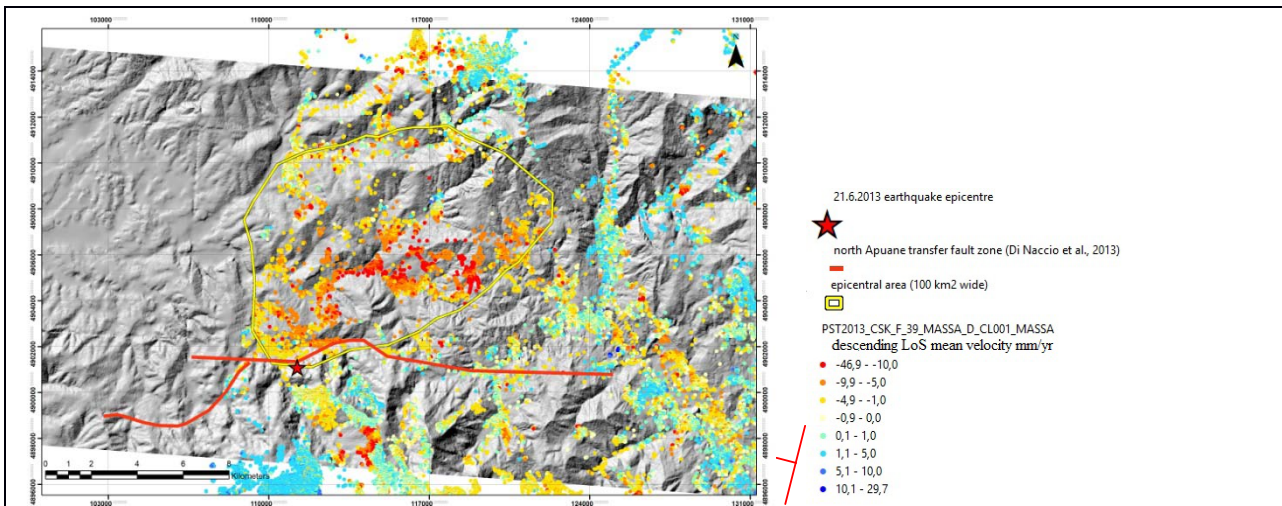


Fig. 7.6 Descending Cosmo Skymed dataset: PSs mean velocity in the epicentral area

In the present case study, if the fault was E–W striking, and N-dipping, with a little oblique right-lateral kinematics, it makes that the real displacement vector (DR) should be oriented towards North direction, more or less; if so, it would not have been there a good projection of DR on both LoSa and LoSd, that is both displacement, DLoSa and DLoSd, would have been close to zero value (Fig. 7.7). For this reason, the SAR detection could not have been satisfactory.

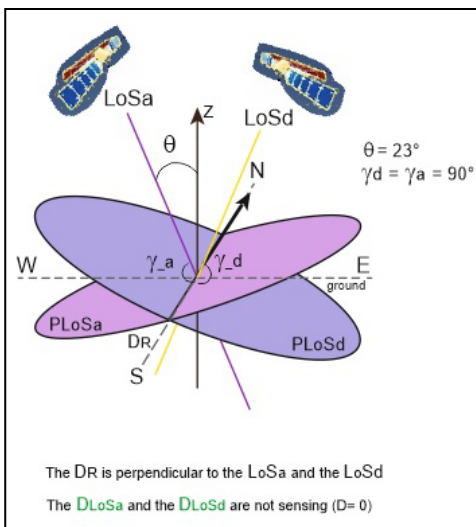


Fig. 7.7 Real displacement vector is next to a north orientation. In this case there will be no projection or a very small value on LoSa and LoSd.

7.2.1 Time series

If what was said in the previous section had been true, obviously also the time series would have had a scarce sensitivity about the possibility to identify displacements oriented approximately north-south. But in it does not seem to be that way.

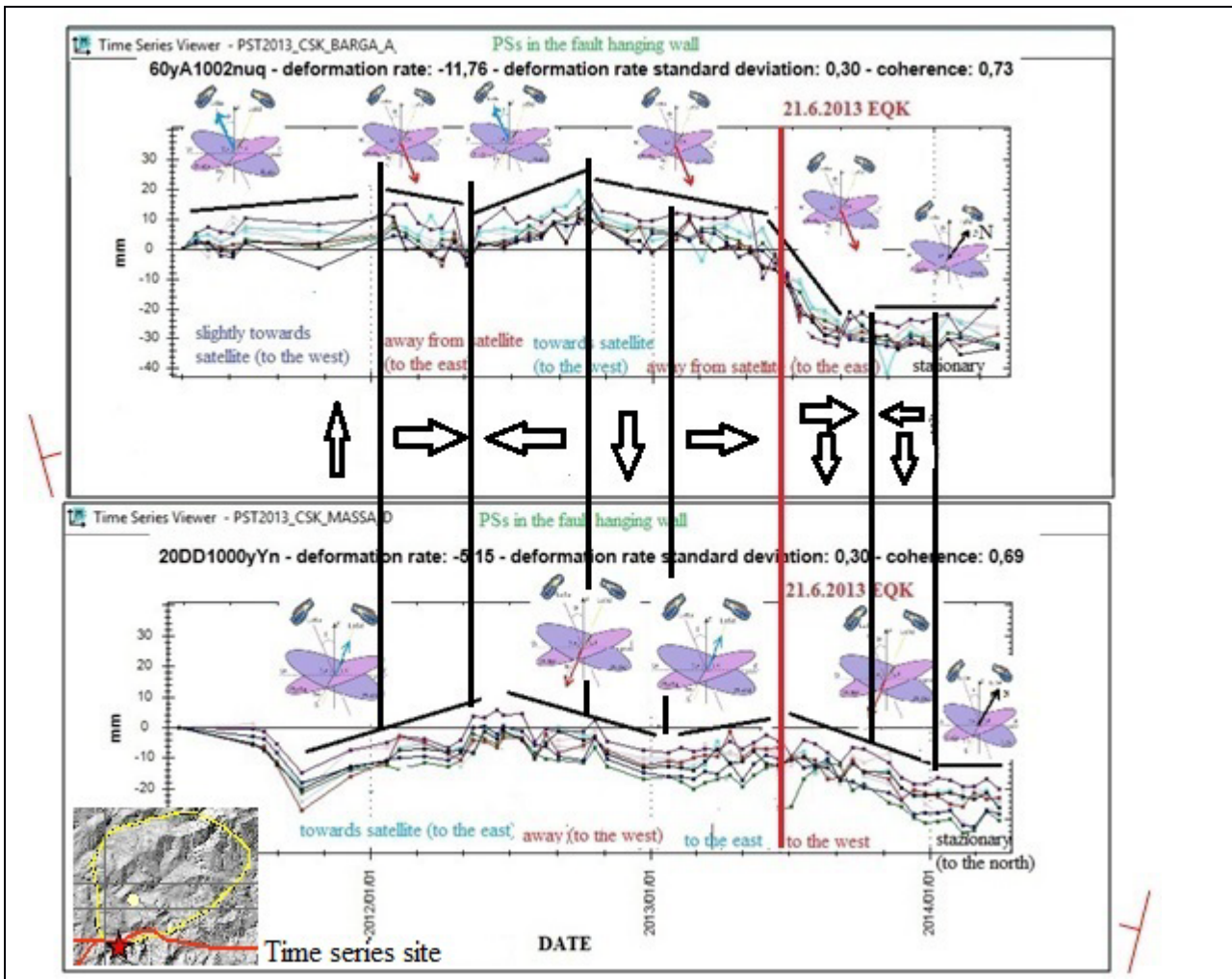


Fig. 7.8 Time series of two ascending (up) and descending (bottom) PSs next to each other (yellow point in the inset). The black arrows are the qualitative displacements, in a vertical plane E-W oriented, arising from ascending and descending LoS components as depict in the SAR geometry sketches.

In Figs. 7.8 and 7.9 it can see two example, where the first pair is next to epicenter while the second one is a little more to the north, all in the fault hanging wall. The ascending time series are quite complex with a more or less slow up and down path, like a pulse in the pre-seismic period, then a quick go down, like a jump in the earthquake time, a deceleration and a final sub-horizontal path, in co- and very early post-seismic period. The descending time series are more smooth, without evident earthquake jump, in the first case with an up and down fluctuation, in the second one with a little accelerant downward path, both before and more after the earthquake.

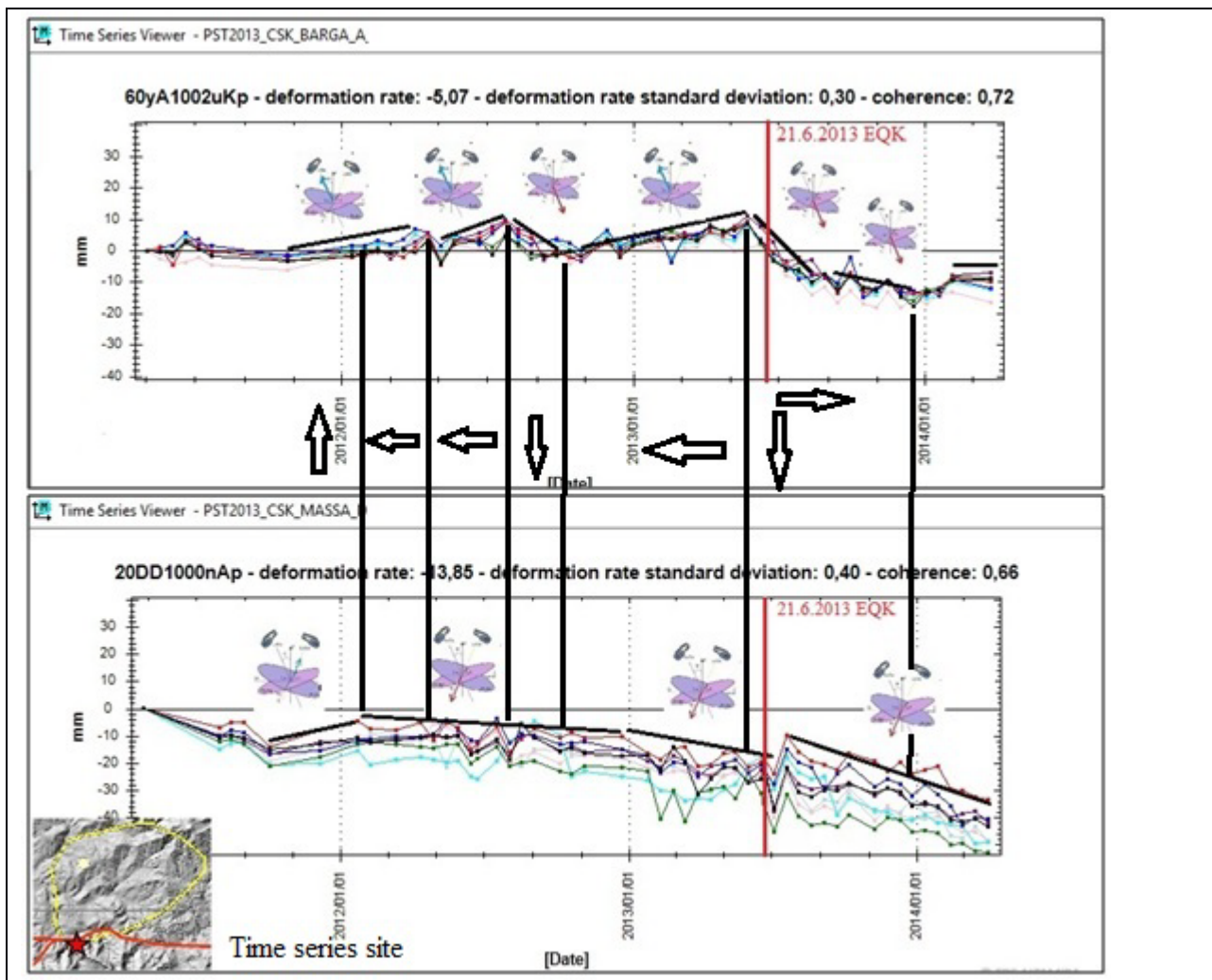


Fig. 7.9 Time series of two ascending (up) and descending (bottom) PSs next each other (yellow point in the inset). The black arrows are the qualitative displacements, in a vertical plane E-W oriented, arising from ascending and descending LoS components as depicted in the SAR geometry sketches.

7.3 Discussion and Concluding remarks

Referring to SAR acquisition geometry features (see Section 2.3.1), considering that the Cosmo Skymed SAR antenna is pointing with an incidence angle about 38° (then a little more sensitive to horizontal displacements with respect to ESA ERS/ENVISAT satellites), comparing visually the two time series pairs (Fig. 7.8 and 7.9) with each other, the qualitative resulting displacement, in a vertical plane E-W oriented, can be obtained.

It appears that the fault hanging wall displacement is mainly of a horizontal type. In the co- an early post-seismic period (the right side with respect to the vertical red line in Figs. 7.8 and 7.9) the displacement is right lateral and downward; this is in agreement with right-lateral kinematics (Atzori et al., 2014 and Stomondo et al., 2014). The pre-seismic period seems a little more complex, with vertical displacements, up or downward, left or right lateral.

The ascending time series show, much better in Fig. 7.9, a positive three pulse that grows in intensity and amplitude during the year and a half that precedes the earthquake. They do not seem to be correlated with possible seasonal variations. In 2012 there were two pulses; third pulse, the biggest one, began at the end of 2012 and grows until May 2013 when begins the right lateral shift and subsidence of fault hanging wall. Each pulse positive side, geometrically combined with the relative descending negative displacement projection, produce a pre-seismic left-lateral horizontal displacement, opposite to the co-seismic horizontal component.

Here it is suggested that pre-seismic displacements such as those that characterise the hanging wall block may represent a precursor signal of the 2013, Mw 5.3 Lunigiana earthquake.

CHAPTER 8 - INVESTIGATION OF A-SEISMIC GROUND DEFORMATION IN THE CAMPANIA PLAIN

8.1 Introduction

The present-day behaviour, in terms of vertical motions, of the Campania Plain graben is debated. Current subsidence of the Volturno river Plain has been recently assessed by the use of InSAR data (Aucelli et al., 2017; Matano et al., 2018). In these works, the Volturno Plain (the northernmost basin of the Campania Plain peri-Tyrrhenian graben) subsidence has been related to both natural and anthropic causes, with the second ones mainly related to water extraction, while the first one basically related to compaction of the uppermost (Holocene) layers of the basin fill. No data have been provided to date on the basin that extends southwards of the Canello ridge (hereinafter named Canello basin; frame 2 in Fig. 8.1).

On the other hand, low to moderate magnitude historical seismicity is recorded along the eastern boundaries of the graben, with the strongest ones being those with magnitudes 5.1 and 5.6 occurred in 1805 (Canello area) and 1466 (Nola area), respectively (Rovida et al., 2016; Fig. 8.1). Furthermore, the occurrence of scarce and low-energy seismicity in the northern part of the Volturno plain has been associated with activity of the NE–SW trending fault that bounds the plain to the NW (Luiso et al., 2018). Stratigraphy evidence from the margins of the entire Campania Plain graben points to post-MIS7 and post-MIS5 subsidence along the graben boundaries (Aprile et al., 2004; Cinque and Irollo, 2004; Santangelo et al., 2010). Evidence on Holocene vertical motions of the coastal plains of the Campania graben is not straightforward, mostly due to two main reasons. One is represented by uncertainties associated with curves of post-glacial sea-level rise along the Italian coasts (e.g., Antonioli et al., 2007), which hamper direct correlations of elevation of dated Holocene deposits buried in the plains with correlative paleo-sea level elevations. The other reason is represented by the high rate of sediment deposition, which is largely controlled by pyroclastic contribution related with strong eruptive events that, in the late Quaternary, have led to the instantaneous emplacement of deposits such as the Neapolitan Yellow Tuff, the Taurano Ignimbrite (around 10-15 m thick) or the up to 50 m thick the Campanian Ignimbrite. However, the Volturno basin coastal plain is considered as stable during the Holocene (e.g., Barra et al., 1996; Amorosi et al., 2012, 2013; Sacchi et al., 2014), while coastal plains both to the north and south of Vesuvius are considered as subsiding during the Holocene (Bellucci, 1994, 1998; Irollo et al., 2005). Irollo et al. (2005) also point to historical (post-roman) activity of the faults at the northern and southern boundaries of the Gulf of Naples graben, while activity of faults at the northern boundary of the Volturno Plain postdating the emplacement of the 39 ka old (De Vivo et al., 2001) Campanian Ignimbrite (a regional stratigraphic marker in the Campania region territory) is inferred from combined geomorphological and stratigraphical evidence (Romano et al., 1994; Cinque et al., 2000). In addition, recently published seismic stratigraphy data from the Volturno River mouth offshore (Misuraca et al., 2018), highlight the occurrence of fault displacements postdating the Last Glacial Maximum (LGM), and closely following the emplacement of the 15 ka (Deino et al., 2004) Neapolitan Yellow Tuff stratigraphical marker.

Aimed at reconstructing the overall frame of late Quaternary deformation of the Campania graben, the PS data analysis has been coupled with tectonic geomorphology analyses focused on the Volturno plain and on the Canello plain.

8.2 Geological framework

The Campania Plain is a 35 km-wide coastal plain with a flat topography and maximum elevation ranging from 35 to 50 m a.s.l. It is bounded by carbonate ridges and includes, in its central part, the volcanic districts of the Phlaegrean Fields and Vesuvius, which separate the Volturno river Plain to the north from the Sarno river Plain to the south (Fig. 8.1). The stratigraphical and geomorphological evolution of the Campania Plain has extensively been studied by several authors (e.g., Ippolito et al., 1973; Aprile & Ortolani, 1978; Brancaccio et al., 1991, 1995; Brocchini et al., 2001; Aprile et al., 2004; Putignano et al., 2007; Santangelo et al., 2017), and stratigraphical studies based on interpretation of shallow (100 m deep) wells have allowed reconstruction of the recent evolution of both the northern (Romano et al., 1994; Barra et al., 1996) and southern sectors (Cinque, 1991; Bellucci, 1994, 1998) of the Plain. However, to date, most of the knowledge on the geological history of the Campania Plain graben is inferred from subsurface data, while very little of such knowledge is based on surface geology information. This is mainly due to the widespread occurrence of very recent (late Pleistocene – Holocene)

pyroclastic/volcaniclastic deposits that blanket the Plain and its borders and – possibly – mask evidence of fault displacements.

Surface and subsurface information indicates that extensional tectonics affected the Campania Plain area since the beginning of the Early Pleistocene (Brancaccio et al., 1991; Cinque et al., 1993; Caiazza et al., 2006). Subsidence affected large portions of the Campania Plain that were downthrown below sea level, as it is inferred from the recovery of Early Pleistocene marine sediments on top of Mesozoic or Miocene rocks in deep wells (e.g., the Trecase, Castelvoturno, Villa Literno and Canello wells; Ippolito et al., 1973; Bernasconi et al., 1981, Balducci et al., 1983; Brancaccio et al., 1991; Brocchini et al., 2001; ViDEPI, 2009; Fig. 8.1).

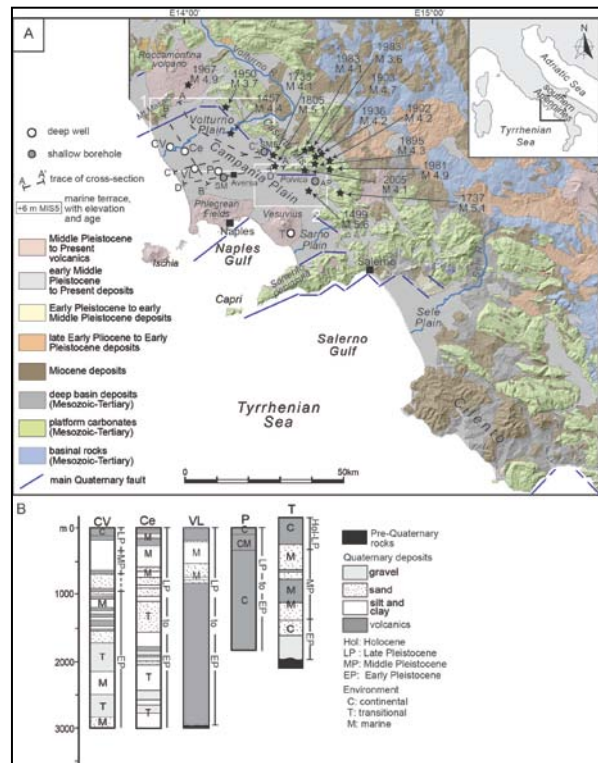


Fig. 8.1 - (A) Simplified geological map of the northern part of the southern Apennines Tyrrhenian margin, showing the coastal half-grabens analysed in this study and the main Quaternary faults at their boundaries. Location, elevation and age of uplifted marine terraces that occur in the coastal horsts are also reported (for references, see the text). Locations of deep well logs of diagram (B) and shallow boreholes SM, SME and AP are also shown. Diagram (A) also shows traces of cross sections A-A' to D-D' of Fig. 4, cross section X-X' of Fig. 2, and cross section Y-Y' of Fig. 6. (B) Logs of the main deep wells drilled onshore and offshore the Campania and Sele Plains coastal basins. CA: Cellole Aurunciwell; CV: Castelvoturno well; Ce: Canello well; VL: Villa Literno well; P: Parete well; T: Trecase well; M: Mina well; Mi: Milena well; MM: Margherita mare well; S: Sele well. Well logs are redrawn and modified from Ippolito et al. (1973), Brancaccio et al. (1991; and references therein), Brocchini et al. (2001), and ViDEPI (2009) (modified after Santangelo et al., 2017). Locations of historical earthquakes are also shown. The white frames indicate locations of the Volturno river Plain (frame 1) and of the Polvica area (frame 2).

From the Middle Pleistocene (Brancaccio et al., 1991; Hippolyte et al., 1994) strong subsidence led to the submersion of the entire Plain. During this time span (particularly, since 0.3 Ma), several explosive eruptions occurred, the source areas of which are still debated and, by some authors (Rolandi et al., 2003), related to fissures located along the basin margins. During the Late Pleistocene, volcanism affected different source areas of the Campania Plain. Onset of volcanic activity is recorded in Ischia (Gillot et al., 1982) and the Phlaegrean Fields (Rosi & Sbrana, 1987) in the first part of the Late Pleistocene, and in the late part of the Late Pleistocene in the Somma-Vesuvius area (25 ka; Brocchini et al., 2001; Di Renzo et al., 2007). In the Phlaegrean Fields area, the late part of the Late Pleistocene is marked by the major eruption of the Neapolitan Yellow Tuff, occurred at 15 ka (NYT; Deino et al., 2004).

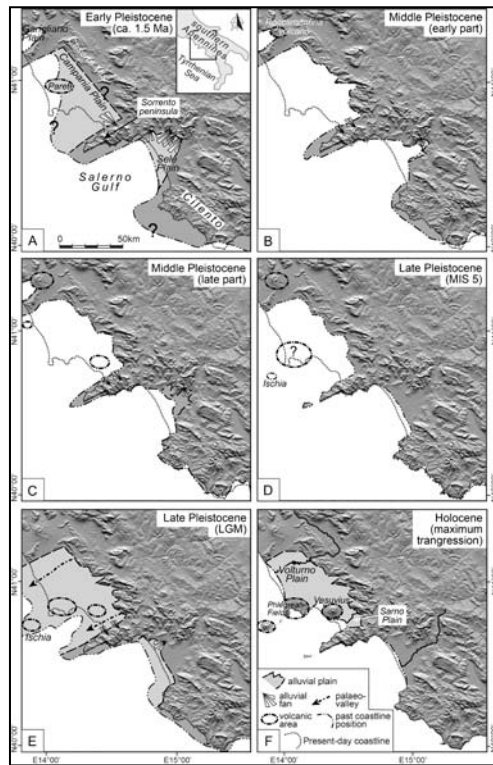


Fig. 8.2. Schematic reconstruction of different stages of the Campania and Sele Plain coastal basins long-term evolution. Past positions of the coastline are based on information on the spatial distribution of continental, marine and transitional facies sediments inferred from surface stratigraphy, geomorphological data, subsurface data from deep and shallow wells, and offshore data (from Santangelo et al., 2017).

Surface, subsurface and offshore data indicate that, as well as other peri-Tyrrhenian grabens of the southern Apennines, the large-scale structural setting of the Campania Plain consists of a major half-graben structure bounded towards the NW by a roughly NE-SW trending master fault systems located at the southeastern boundary of Mt. Massico ridge. Such a structure controls the asymmetrical - northward thickening - basin fill and lowers the carbonate successions, outcropping in the horst blocks surrounding the Plain, down to 3000 - 4000 m depths (e.g. Bartole et al., 1984; Mariani and Prato, 1988; Ascione et al., 1997; Bruno et al., 1998; Florio et al., 1999; Milia et al., 2003; Milia & Torrente, 1999, 2015 and references therein; Fig. 8.3; Fig. 8.4).

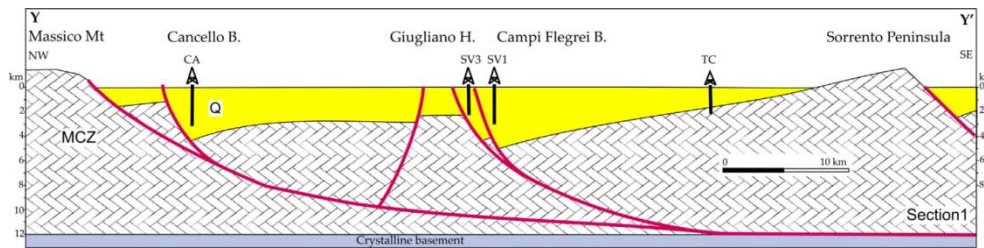


Fig. 8.3. Geological section (location in Fig. 8.4), calibrated with seismic profiles and stratigraphic logs of wells, that shows the crustal structure of the Campanian Plain characterized by NE-SW and NW-SE-trending faults. The Mesozoic-Cenozoic substrate (MCZ) is covered by Quaternary (Q) clastic deposits and volcanics. Cancellation B = Cancellation basin, Campi Flegrei B = Campi Flegrei basin, Giugliano H = Giugliano High (from Milia and Torrente, 2015).

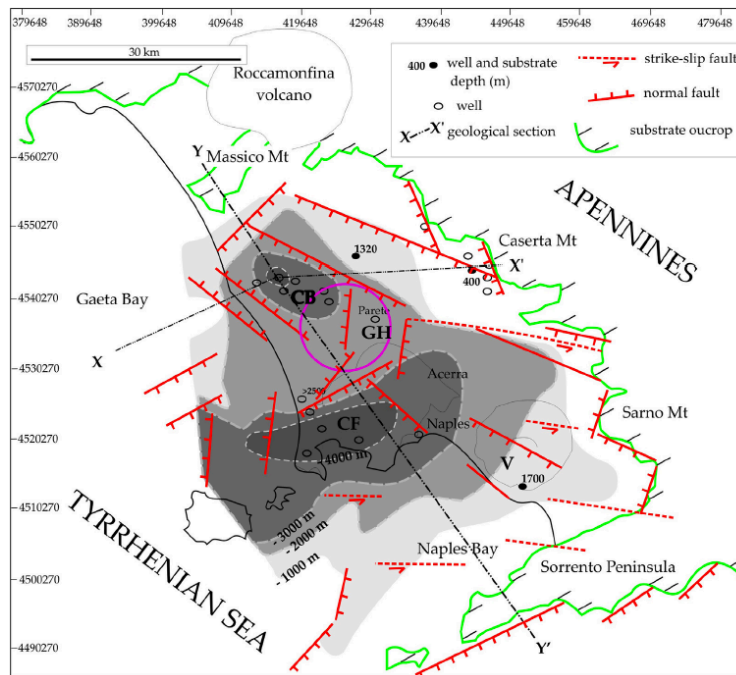


Fig. 8.4. Structure contour map of the Mesozoic-Cenozoic substrate in the Campania Plain and surrounding areas; the purple circle refers to the buried Parete volcano. CB = Cancellò Basin, CH = Giugliano High, CF = Campi Flegrei; V = Vesuvius. Contour interval is 1000 m (from Milia and Torrente, 2015).

The Campania Plain is also dissected by S and SW-dipping fault zones (e.g. Florio, 1998; Bruno et al., 2000; Casciello et al., 2006; Milia & Torrente, 2013, 2015), which define the boundaries of two major sub-basins: the Volturno Plain basin and the basin that extends between the Cancellò ridge to the north to the Lattari Mts. to the south, which includes the Vesuvius and Gulf of Naples (Fig. 8.1).

The presence of an Early Pleistocene gulf in the northern part of the Campania Plain is testified by marine and transitional (delta facies; ViDEPI, 2009) deposits drilled in the Castelvoturno and Cellose wells (Figs. 8.1 and 8.2A). Marine silts and clays, not older than the Emilian substage (1.5-1.2 Ma), have been drilled down to 2400 m depth in the Castelvoturno well (Brancaccio et al., 1991). In the central part of this coastal basin, continental volcanic deposits (mainly lavas), encountered by the Parete borehole down to 1800 m depth and by the Villa Literno well down to about 2900 m (Fig. 8.1), testify to the presence of an ancient volcanic centre, known in the literature as the Parete volcano (Fig. 8.2A; Fig. 8.4). In the Parete well, the base of the volcanic deposits has a K/Ar age of 1.8 Ma (Di Girolamo et al., 1976).

In the southern part of the Campania Plain, thick continental conglomerate deposits found in the Trecase well above the basal dolostones aged older than 1.24 Ma (Brocchini et al., 2001; Fig. 8.1), suggest a strong erosional phase following the first uplift stages, which affected the Sorrento ridge horst block during the Early Pleistocene (Caiazzo et al., 2006). According to these authors, the extensional faulting caused a strong vertical fragmentation, which led to the development, along NW-SE to N-S trending faults, of a horst-and-graben structure. Slope and alluvial sediments were then deposited along the main footslopes and in new created structural basins (i.e. Agerola basin).

The marine deposits, found in the Trecase borehole above the conglomerate layers (down to 1490 m depth) and dated 0.90 - 1.24 Ma through nannofossils (Brocchini et al., 2001), provide evidence for a strong subsidence phase, which caused the flooding of the southern part of the Campania Plain (Fig. 8.2B). In the northern part of the Plain (Volturno Plain, Castelvoturno well; Brancaccio et al., 1991) marine sands and clays, drilled between 1000 and 150 m depth, indicate the persistence of a marine environment during the early part of the Middle Pleistocene.

Surface evidence on the Middle Pleistocene marine environment is provided by paleoshorelines found in several quarries located in the Polvica area (frame 2 in Fig. 8.1). There, the identification of uplifted marine terraces in the 200 m to 50 m elevation range (Fig. 2) allows outlining the perimeter of the plain in the early stages of its formation (Ascione et al., 2016). The outcrops show a several tens of metres thick transgressive-regressive succession consisting of beach conglomerates, fossiliferous arenites and sands that rest onto wide wave-cut terraces, and pass upwards to alluvial fan and slope deposits, which are buried beneath younger alluvial fan and slope deposits. The marine-continental succession is lowered beneath the Holocene alluvial plain by a major E-W trending fault system, and is dissected by N-S and NW-SE trending oblique-slip transfer faults (Fig. 8.5 and Fig. 8.6).

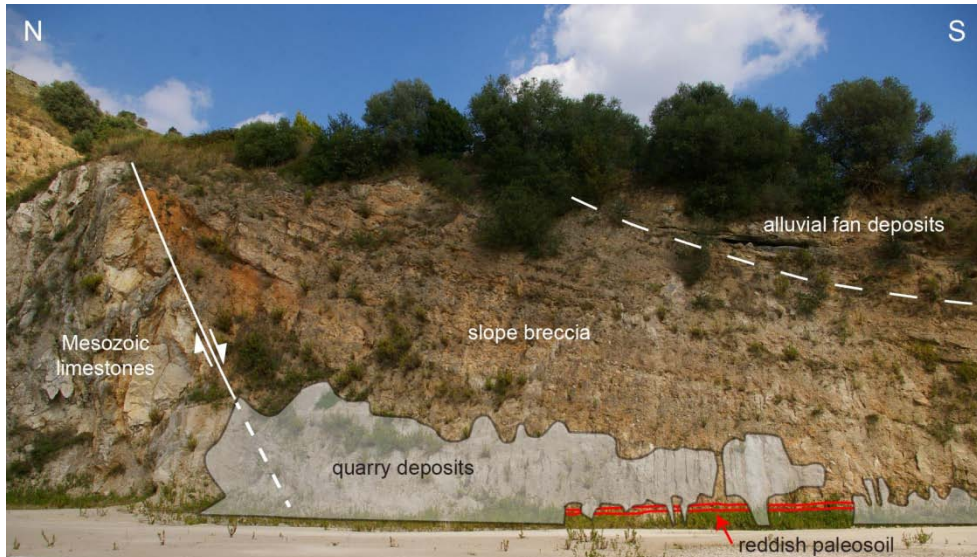


Fig. 8.5. Slope deposits offset by a roughly E-W trending fault, in the southern slope of the Mt. Fellino ridge. The slope deposits overlie shallow marine deposits (downfaulted below the ground surface) and are unconformably covered by alluvial fan deposits (from Ascione et al., 2016).



Fig. 8.6. Southern slope of the Mt. Fellino ridge: Middle Pleistocene marine sands resting on top of an abrasion platform (dashed white line) cut on the Mesozoic limestones, dissected by roughly N-S trending transfer faults (from Ascione et al., 2016).

Re-interpretation of more than 500 shallow borehole logs (30 to 200 m-deep; Romano et al., 1994) drilled in the Volturno Plain, have highlighted the presence of a widespread marine unit (Fig. 8.7, number 7) in the central and south-eastern sector of the Plain (cross sections A-A', B-B' and C-C' in Fig. 8.7). Since no borehole reaches the base of this unit, its minimum thickness was estimated to be ca. 50 m. The lower portion of this unit has been ascribed to the latest Middle Pleistocene-Late Pleistocene based on the $0.126 \pm 0.011 \text{ Ma } ^{230}\text{Th}/^{234}\text{U}$ dating of *Cladocora coespitosa* fragments (Romano et al., 1994) sampled at its top (S. Marcellino borehole, section D-D' in Fig. 8.7). It is mainly made up of silts and sands with remnants of shells, but the log data did not allow a better definition of the sedimentary environment and, consequently, of the bathymetry. The cross sections of Fig. 8.7 also show that, at the top of these marine sediments, a continental volcanic unit is present (number 5 in Fig. 8.7). Such unit, which is mainly made up of pyroclastic sands and ashes and subordinately of tuffs and lavas, reaches a maximum thickness of about 40 m in the surroundings of Aversa and San Marcellino localities (cross section D-D' in Fig. 8.7), where it also shows a dome-like shape. In this portion of the Plain, it is covered by the Campanian Ignimbrite, aged 39 ka (De Vivo et al., 2001; Fig. 8.7). Moving towards both the NW and NE of the Aversa - S. Marcellino area, the two volcanic units are separated by marine sediments mainly made up of

sands, silts and clays with fossil remains, which locally include peaty clay layers of a probable transitional environment. This unit, whose top is found at depths ranging from -30 to -10 m a.s.l., has tentatively been ascribed to MIS 3.3, on the basis of its stratigraphical position.

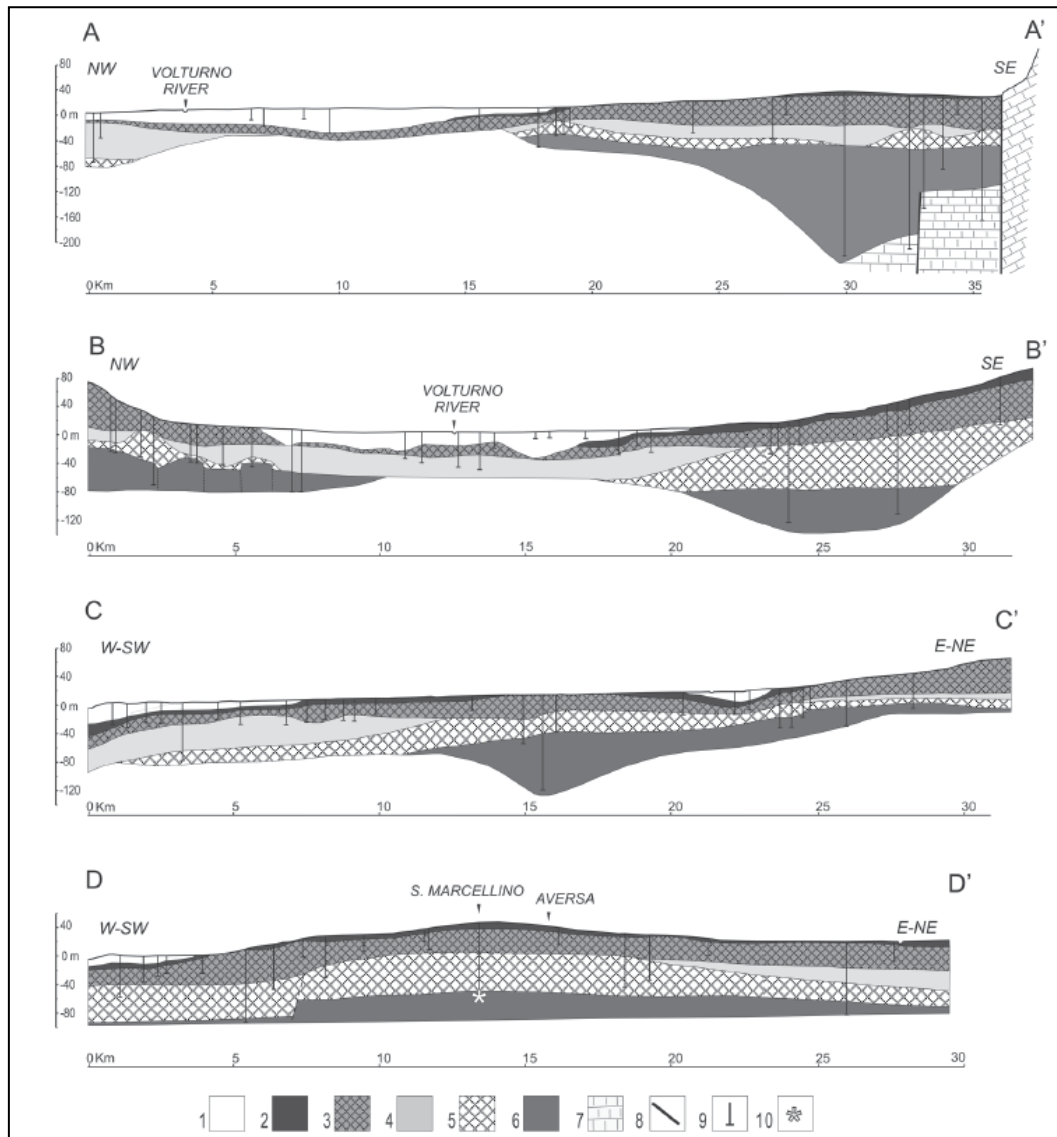


Fig. 8.7. Geological cross section of the northern portion of the Campania Plain. For location see Fig.1. 1) Holocene beach sands (a) and lagoon clays; 2) pyroclastic deposits, locally reworked (Late Pleistocene- Holocene); 3) Campanian Ignimbrite formation (CI, 39 ka); 4) marine sands and lagoon clays (Late Pleistocene, MIS 3); 5) pyroclastic and lava deposits (Late Pleistocene); 6) Canello marine and coastal sands (Late Pleistocene); 7) marine sands (late Middle Pleistocene- Late Pleistocene); 8) Tertiary flysch ; 9) Mesozoic limestones; 10) faults; 11) collected boreholes; 12) drilled boreholes; 13) dated fossiliferous layer (0.126 +/- 0.011 Ma) (Modified after Romano et al., 1994).

A 80-m deep core (SME, drilled in the area at the toe of the Caserta Mts.; Santangelo et al., 2010; Fig. 8.1) has shown that during MIS 7 (Fig. 8.2C) and MIS 5 the northeastern sector of the Campania Plain was characterised by the presence of a deep gulf with coastal lagoon systems located in its eastern flank. This palaeolandscape was affected by strong eruptive events that allowed either temporary (Aversa-San Marcellino area) or definitive (SME area) emersion of sectors of the gulf (Santangelo et al., 2017). In particular, strong volcanic activity at the end of the Middle Pleistocene is testified by the eruptive event recorded in the SME core, which is correlated with ignimbrite deposits cropping out in the eastern margin of the Campania Plain, i.e. the 157.4 ± 1 ka Taurano Ignimbrite (De Vivo et al., 2001).

Aprile et al. (2004) correlated to the Taurano Ignimbrite the pyroclastic deposits found in the subsurface of the southeastern part of the Campania Plain (both south of the Polvica ridge and present day Sarno Plain; Fig. 8.8) on top of marine sediments. The top of such sediments stands at -35 m a.s.l. and $-40 \div -50$ m a.s.l. in the subsurface of the Sarno Plain and the Mt. Fellino area (Aprile and Toccaceli, 2002) have been related to MIS 7 by Cinque and Irollo (2004).

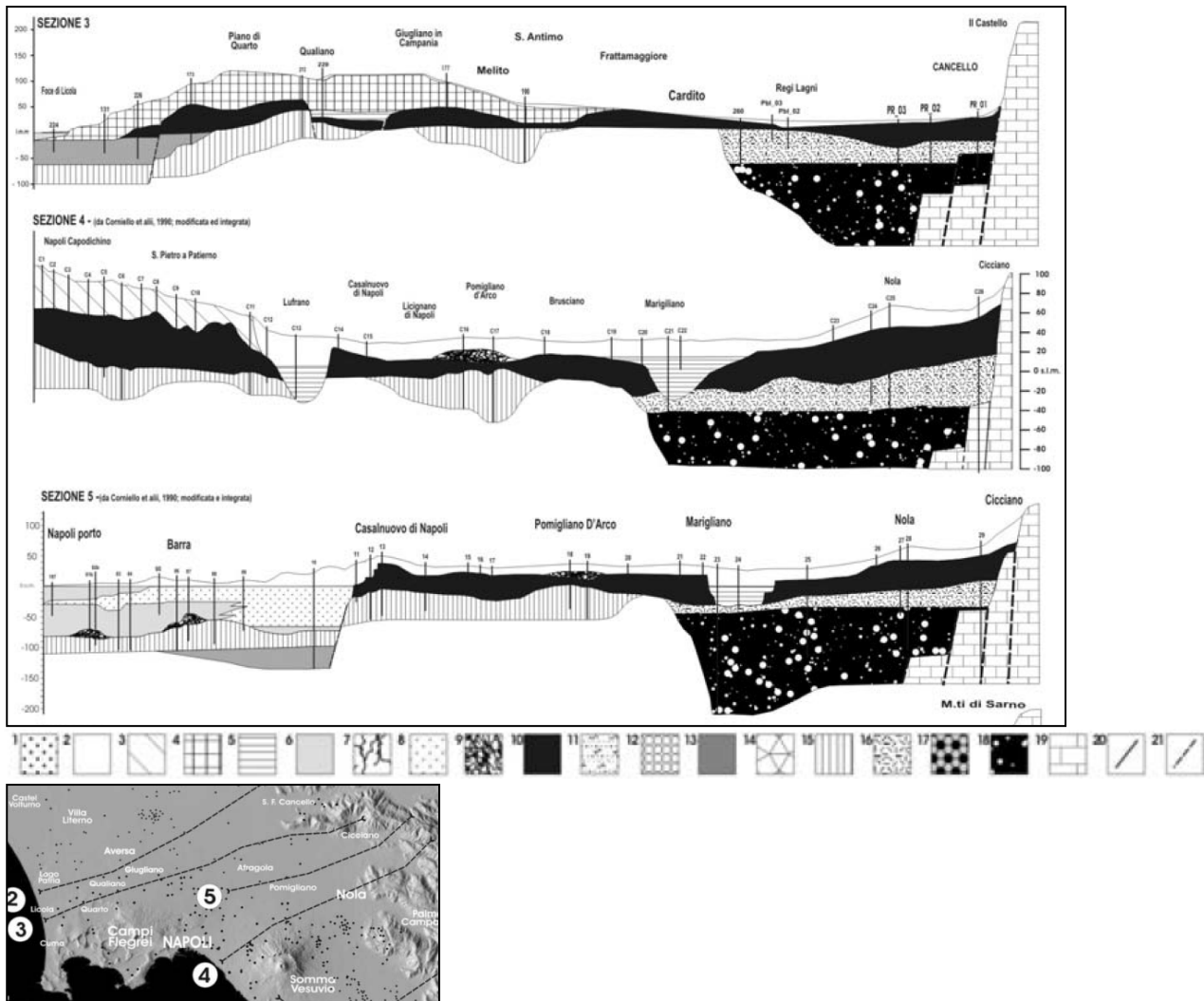


Fig. 8.8. Schematic geological sections: 1 - Present beach and eolian recent deposits; 2 - Alluvial deposits and subaerial pyroclastic products (in situ or reworked) of Pliegrean Fields and Somma-Vesuvius volcanic complex (Olocene); 3 - "Gauro" Yellow Tuff (about 10,5 ky B.P.); 4 - Neapolitan Yellow Tuff (about 12 ky B.P.); 5 - Alluvial, palustrine and lagoonal deposits of the "Versilian Complex"; 6 - Beach and shore sediments (with peat levels) of the "Versilian Complex"; 7 - Lavas and pyroclastic products of Somma-Vesuvius complex (Olocene); 8 - Alluvial deposits and subaerial pyroclastic products (in situ or reworked) post-CGT (Olocene - late Upper Pleistocene); 9 - Monte Somma lavas (late Upper Pleistocene); 10 - Campanian Grey Tuff (about 39 ky B.P.); 11 - Beach and marine deposits (late Upper Pleistocene); 12 - "Scanzano" alluvial fan deposits (Upper Pleistocene); 13 - Marine deposits (upper Pleistocene); 14 - "Gragnano" alluvial fan deposits and recent alluvial or debris cones deposits (Upper Pleistocene); 15 - Indifferenziated volcanoclastic complex (late Middle Pleistocene - Upper Pleistocene); 16 - Taurano Yellow Tuff (about 157 ky B.P.); 17 - Alluvial, lacustrine and pyroclastic deposits (late Middle Pleistocene - Upper Pleistocene); 18 - Beach and marine deposits (late Middle Pleistocene); 19 - Dolomites and limestones (Cenozoic - Mesozoic); 20 - Certain fault; 21 - Presumed fault (from Aprile et al., 2004).

These sediments indicate that also the southeastern sector of the Campania Plain, as the northern one, was entirely submerged in the late part of the Middle Pleistocene. The thick succession of sands, drilled at 365 to 700 m depths in the Trecase borehole, should be ascribed to this same time interval (Brocchini et al., 2001; Fig. 8.1). These sands rest above tephritic lavas aged 0.3 ± 0.045 Ma contending the presence of effusive centres in the south-central portion of the Campania Plain between 0.4 and 0.3 Ma.

More recent beach and transitional deposits, occurring in the subsurface of the present-day Sarno Plain, have been correlated by Barra et al. (1991) to the Last Interglacial. Such deposits (the top of which is found at -23 m a.s.l.), allow placing the Last Interglacial coastline about 13 km inland from the present-day shoreline (Barra et al., 1991; Cinque, 1991).

In the northern part of the Campania Plain, the elevation difference between the 126 ka marine deposits drilled in the S. Marcellino area (Romano et al., 1994) and basically coeval lagoon sediments of the SME core (Santangelo et al., 2010), which stand at -80 and -18 m a.s.l. respectively, suggests that different rates of subsidence have affected the eastern and central sectors of the Volturno Plain since the Last

Interglacial (Santangelo et al., 2017). The occurrence of several eruptions from 105 ka to 39 ka, when the catastrophic CI eruption occurred, is inferred from the SME core (Santangelo et al., 2010).

The Last Glacial regression (60 - 15 ka) and the Campanian Ignimbrite eruption (CI; 39 ka) represent the two main events, which have affected the palaeolandscape of the study area during the Late Pleistocene (Fig. 8.2E and 8.2F). The extremely violent explosive CI eruption (Barberi et al., 1978; Deino et al., 1994; De Vivo et al., 2001) covered the entire Campania Plain with the emplacement of pyroclastic flow deposits tens of metres thick. This unit is clearly identified in the onshore stratigraphic record all over the plain (Romano et al., 1994; Aprile et al., 2004; Fig. 8.5) and in the offshore. In the central part of the plain, the CI deposits rest on marine sands and clays related to MIS 3 (Romano et al., 1994; Fig. 8.2).

Milia and Torrente (2003) interpreted a thick seismically chaotic unit recognized in the continental shelf of the Bay of Naples as the CI. This unit, with a thickness up to 135 m, is identified in the central part of the continental shelf and its top lies between 100 and 150 m below the sea level. Both at the base and the top, it is bounded by erosional surfaces characterised by incised valleys (Milia, 2000), indicating a subaerial environment for this eruption (Milia, 1998, 2000).

These data indicate that most of the Campania Plain was located above the sea level at the moment of the CI emplacement, due to the sea level drop of the Last Glacial period (Fig. 8.2D). Data from several Authors indicate that the sea level at 37 ka was about 80 m lower than at present and reached a minimum of -120 m at about 20 ka (Bintanija et al., 2005; Siddall et al., 2005).

According to Romano et al. (1994) and Amorosi et al. (2012), deep valley incision up to 30 m occurred right after the CI deposition in the northern part of the Campania Plain. This down-cutting phase was likely enhanced by the huge thickness of unconsolidated pyroclastic material emplaced instantaneously in that area. The following, further sea-level fall occurred at the Last Glacial Maximum, caused additional river downcutting. Comparable evidence is available from the subsurface of the southeastern part of the Campania Plain, i.e. in the present-day Gulf of Naples onshore (Santangelo et al., 2017). In the northern part of this area, valley fill deposits, consisting of alluvial sediments with peat layers, occur on top of the CI (Pescatore et al., 1984; Bellucci, 1994, 1998) whereas in the southern part (present-day Sarno Plain), the top surface of the CI is dissected by a valley shaped morphology, the bottom of which stands at around 30 m below the sea level in the Pompei area (Cinque and Irollo, 2004).

Data from offshore surveys (ISPRA, 2015) allow outlining the coastline shape during the LGM (Fig. 8.2E). It was located tens of kilometres westward of the present one allowing the connection of Ischia and Capri islands to the mainland.

Re-emergence of volcanic activity at the present-day Somma-Vesuvius volcano occurred only after the CI eruption (Brocchini et al., 2001; Di Renzo et al., 2007). Magma rose along and at the intersection of linear and curved tectonic and volcano-tectonic elements. It gave rise to a number of small lava and scoria edifices termed 'lava ridges', identified on top of the C.I. by Di Vito et al. (1998). One of such tephritic centres lies above the CI deposits in the subsurface of the area around the Trecase well, as shown by a tephritic lava sequence encountered between 250 and 200 m depth (Brocchini et al., 2001). The chemical composition of the 290 - 275 m-deep fallout level of the Trecase well is comparable to that of the deposits of the Codola eruption that is aged 33 ka (Giaccio et al., 2008), and testifies to the onset of the Somma volcano activity.

The progressive growth of the Somma-Vesuvius and Phlaegrean Fields volcanic edifices, during the Late Pleistocene-Holocene, caused the final separation of the Campania Plain into two main zones: the Volturno Plain to the NW and the Sarno Plain to the SW. Combined geomorphological and stratigraphical evidence of latest Pleistocene (post-CI) or Holocene faulting is found at the boundaries of such plains (Cinque et al., 2000; Irollo et al., 2005). The latest Pleistocene - early Holocene (ca. 15–6 ka) sea-level rise promoted the rapid flooding of the lower Volturno Plain. Since ca. 6.5 ka, the turnaround from transgressive to 'regressive' (highstand) conditions marked the onset of the present Volturno River delta and the late Holocene progradation of 3–6 km of the coastal plain (Barra et al., 1996; Amorosi et al., 2013). Deceleration of the post-glacial sea-level rise is testified by middle-late Holocene prograding deposits of prodelta and delta front/strandplain facies, capped by modern alluvial, delta plain and coastal plain deposits (Amorosi et al., 2012; Sacchi et al., 2014).

8.2 Geomorphological analysis of the northern sector of the Campana Plain

An analysis of detail-scale topography of the Volturno river plain and adjacent Cancellò plain has been carried out, aimed at the identification of the erosional and depositional landforms that compose the

landscape of the plain and adjacent piedmont areas, and reconstruction of the recent (Late Pleistocene – Holocene) geomorphological evolution of the study area.

Digital topography data that have been used for the geomorphological analysis have been derived from the combination of 1x1 m LiDAR data covering the plain (made available by the Ministry of Environment - MATTM) and a 5x5 m DEM (made available by Regione Campania). The detailed topography data have allowed detection, within the smooth relief of the study area, of geomorphological features non-identified in former studies. The geomorphological analysis has been constrained by a huge amount of literature data on both surface geology and stratigraphy of the shallow subsurface (outcrop data and data from borehole and well logs up to 200 m deep; e.g., Bellucci, 1994; Romano et al., 1994; Barra et al., 1996; Aprile et al., 2004; Santangelo et al., 2010; Amoroso et al., 2012; Amoroso et al., 2013), and on preliminary results of analysis of a core (AP), drilled in the inner part of the Cancellio plain in January 2016.

The results of the geomorphological analysis have been synthesised in the geomorphological maps of Fig. 8.9 and Fig. 8.11.

8.2.1 The Volturno Plain

Fig. 8.9 shows that topography of the Volturno river plain is extremely flat. The plain extends for about 25 km reaching, in its inner part, about 20 m a.s.l., with a mean slope value of 0.8‰. The mean slope value rises to 4‰ in the innermost 5 km, i.e. in the northeastern piedmont area.

Towards the south, the Volturno plain is bounded by the north-facing slope of the dome-like hill formed in the Late Pleistocene – Holocene pyroclastics of the Phlegrean Fields (mainly the 39 ka old Campania Ignimbrite and 15 ka old Neapolitan Yellow Tuff). The piedmont areas to the NE and NW of the flattest part of the plain are formed in the deposits of the Campania Ignimbrite (about 50 m thick; Romano et al., 1994), which are covered by thin colluvial and alluvial fan deposits. Collectively, these deposits form an incised glacia rising up to about 60 m and 80 m a.s.l. along the northeastern and northwestern boundaries of the plain, respectively (Fig. 8.9).

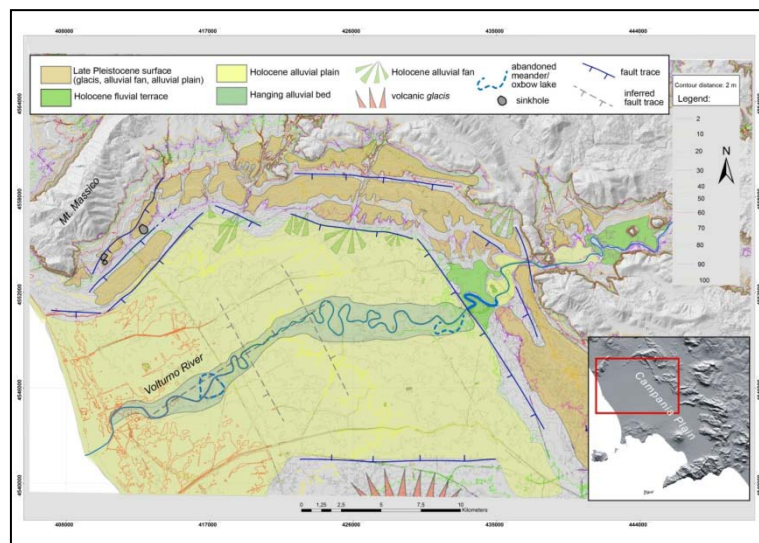


Fig. 8.9. The Volturno plain geomorphologic map (see text)

All along the plain, topography of the glacia is characterised by slope breaks. These smooth scarps, which have heights ranging from 4 to 20 m, are markedly rectilinear in plan view (Fig. 8.9). In the Mt. Massico piedmont, the scarps are NE-SW oriented, thus paralleling orientation of the major fault system that bounds the Campania plain graben to the NW (e.g., Mariani and Prato, 1988). At the northern boundary of the plain, the scarps are WNW-ESE oriented, while in the eastern part they are NW-SE oriented, thus paralleling orientation of the fault at the eastern boundary of the plain, and suggesting interpretation of the scarps affecting the glacia as fault scarps. Based on such an interpretation, in Fig. 8.9 have been mapped the traces of the inferred faults at the base of the scarps, and/or following alignments of the same scarps with rectilinear stream paths that incise the glacia.

At the northeastern boundary of the plain, the glacia is incised by the Volturno river. In this sector of the plain, the river is flanked by fluvial terraces that stand 4-5 m above the river bed, and are inset in the C.I. surface (Fig. 8.9).

The lowest ones of the scarps that bound the glacia mark the boundary of flattest area of the plain. At the toe of such scarps, several small-size alluvial fans fed by streams that dissect the glacia are identified. The flattest area of the plain coincides with the Holocene shallow marine to transitional environment and alluvial basin fill (Fig. 8.9), constructed during the coastal progradation stage that followed the maximum Holocene ingression (Romano et al., 1994; Amorosi et al., 2012). The Holocene sea-level rise, and related ingression, followed incision of the C.I. plateau, occurred during the LGM sea level fall and low-stand (Romano et al., 1994). The morphology of the eroded C.I. top surface (as reconstructed by Romano et al., 1994, and updated with data on shallow logs from the Volturno river outlet and coastal belt from Amorosi et al., 2012), is shown in Fig. 8.10, together with thickness of the post-C.I. basin fill.

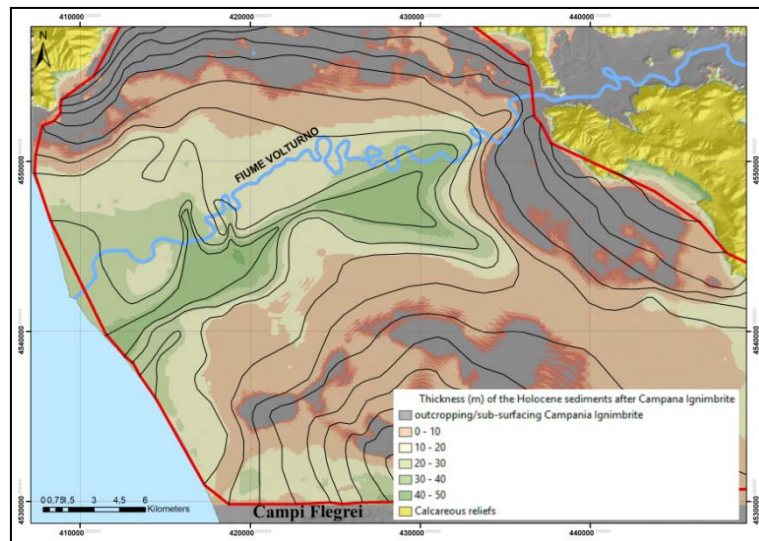


Fig. 8.10. The Volturno plain geomorphologic map (see text)

The Volturno river crosses the Holocene alluvial plain with a prevalingly meandering pattern (several abandoned meanders are also present along the active river path; Fig. 8.9). Worthy to note, the scarp at the northeastern border of the Volturno river plain marks the boundary between the sector, to the NE, in which the Volturno river crosses an incised plain, and the lower course of the river, which is characterised by an elevated alluvial bed that stands a few metres above the adjacent sector of the Holocene alluvial plain (Fig. 8.9). The abrupt change (from incision to deposition) in the Volturno river dynamics suggests identifying the area to the NE of the NW-SE trending scarp as relatively uplifted in relation to the wide area to the SW, subject to alluvial aggradation. Such an interpretation would imply differential vertical motions along the NE boundary of the alluvial plain postdating onset of Holocene filling of the Volturno river plain, i.e., in the last 5-6 ka.

A fault trace has been mapped also along the base of the dome-like hill formed in pyroclastics, at the southern boundary of the plain (Fig. 8.9) based on the straight shape of the left flank of the smooth valley that incises the dome toe.

Detail scale topography data that have been used for the geomorphological analysis allowed identification of further small-scale features of the Holocene alluvial plain. In particular, a slight elevation difference has been recognised between the sectors of the Holocene alluvial plain located in the left and right sides of the Volturno river path, with the sector in the right side resulting 1 to 2 m lower than that in the left side. Such an asymmetry could be representative of either differential accumulation rate or differential vertical motions in the sectors to the north and south of the Volturno river course.

The path of the Volturno river across the Holocene alluvial plain is marked by changes in the river pattern. In particular, the dominant meandering pattern changes to straight in the central part of the plain, accompanied by a change in width of the hanging alluvial bed (Fig. 8.9). Such changes may find explanations in the control exerted by current tectonic displacements on the river dynamics. In particular they may be indicative of two main causes, one being differential motions along structures transverse to the fluvial path, forcing changes of slope of the river path and, thus, inducing change in the pattern (e.g., Schumm et al., 2002). Alternatively, the rectilinear path may reflect vertical displacement along a NE-SW

oriented structure dissecting the plain. Such a process would have forced the river to deviate from the roughly E-W oriented path maintained in the upper part of the plain and align along the NE-SW trending structure.

8.2.2 The Cancellò Plain

The Cancellò plain develops to the south of the Cancellò – Mt. Fellino ridge. Along the ridge, undated, raised marine terraces occur. The marine terraces reach about 100 m a.s.l. in the central part of the ridge, and are downfaulted towards the west down to about 65 m a.s.l. by faults trending from about N-S to NW-SE (Ascione et al., 2016). These faults acted as transfers of a major S-dipping extensional fault system that bounds the Cancellò – Mt. Fellino ridge towards the south and lowers the marine deposits below the Cancellò plain with an offset of at least 200 m (Ascione et al., 2016). The marine deposits are even more lowered towards the axis of the Cancellò plain, as it is inferred from subsurface stratigraphy data (Aprile et al., 2004).

The topographic surface of the Cancellò plain is characterised by the presence, in the northern border, of incised alluvial fans made up of coarse grained deposits. These are overlain by less inclined younger alluvial fans that are mainly made up of loose gravels interlayered with volcanoclastic beds. The younger alluvial fans pass laterally into a quasi flat alluvial plain that stands at about 30 m a.s.l. A low-lying area, subject to ponding and occupied by marshy deposits, is identified to the south of the Cancellò ridge (Fig. 8.11).

The alluvial plain gradually rises towards the east, where a poorly inclined surface that becomes steeper towards the eastern boundary of the plain is identified. Such inclined surface consists of coalescing alluvial fans deeply indented into the eastern termination of this sector of the Campania Plain, graded towards the Cancellò plain. Outcrop data (quarry walls from the eastern of the Cancellò plain, south of Roccarainola) show that the shallow subsurface of the eastern sector of the Cancellò plain is formed, from the top, by alluvial gravels interbedded with pyroclastic layers. The alluvial deposits are characterised by braided channel facies, which typically characterise distal parts of alluvial fans. These deposits overly an eroded surface formed on the deposits of the 39 ka C.I., which are dissected by roughly E-W and N-S trending fractures and faults that, in the quarries, show subdued offsets. Analysis of topography of the Cancellò plain area has allowed identifying several Quaternary faults. Besides faults that bound the Cancellò – Mt. Fellino ridge (and dissect the marine terraces), some small rectilinear scarps (lengths ranging between 1 and 2 km), essentially E-W striking and both N- and S-facing and heights ranging between 1 and 2 m, have been identified in the eastern part of the plain (Fig. 8.11). The scarp control the drainage net at the surface and, in particular, location and shape of shallow valleys that dissect the alluvial fan/glacis and the plain.

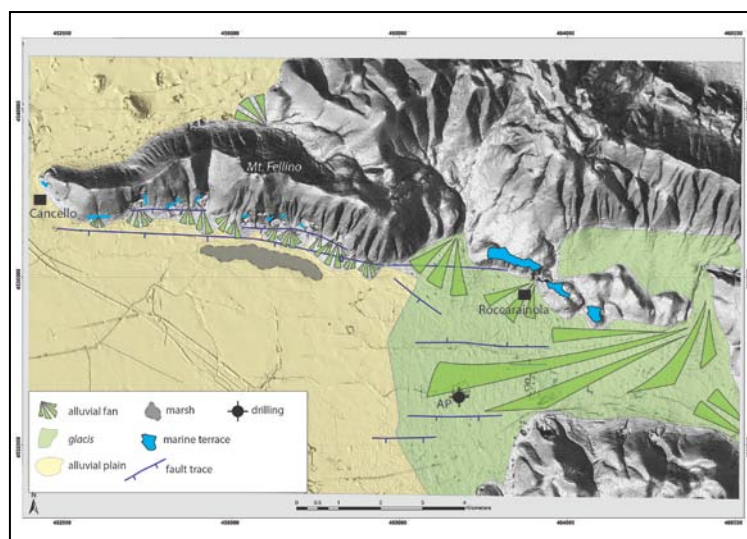


Fig. 8.11. The Cancellò plain geomorphologic map with AP core site.

Data on stratigraphy by Aprile et al. (2004) point to the presence, below the C.I., of pyroclastic deposits that are related to the 156 ka old Taurano ignimbrite, which in turns covers marine deposits. Detailed information on the subsurface of the Cancellò plain have been obtained by the AP core (Fig. 8.11). The AP core has revealed the occurrence, below the C.I. (which, in this area, is about 50 m thick), of 18 m of

deposits consisting, from the top, of alluvial pebbles, marshy silts and clays, and possibly lagoonal fossiliferous clays and silts. These deposits rest onto a 15 m thick pyroclastic unit composed of tuff fragments and sands. Preliminary results of chemical analysis of glass fragments interspersed within the pyroclastic sands point to correlation of such pyroclastic unit with the Taurano ignimbrite (Prof. P. Petrosino, personal communication). Below this ignimbrite, fossiliferous marine sands passing downwards to silts. Based on correlation of the tufaceous unit with the Taurano ignimbrite, aged 156 ka, the top of the marine succession – which stands ~35 m below the sea level – is correlated with MIS 7.

8.3 PSs vertical Vmean, ground deformation maps of Fiume Volturno Campania Plain

In this section it is presented the same procedure followed to obtain PSs vertical Vmean ground deformation maps of Monte Marzano area (Section 4.3) and it was partially followed the procedure of Perrone et al., 2013, as already explained.

They are used the ERS 1/2 (1992 - 2000) and ENVISAT (2003 - 2010) ascending and descending PS datasets, as shown in Figs 8.11 and 8.12.

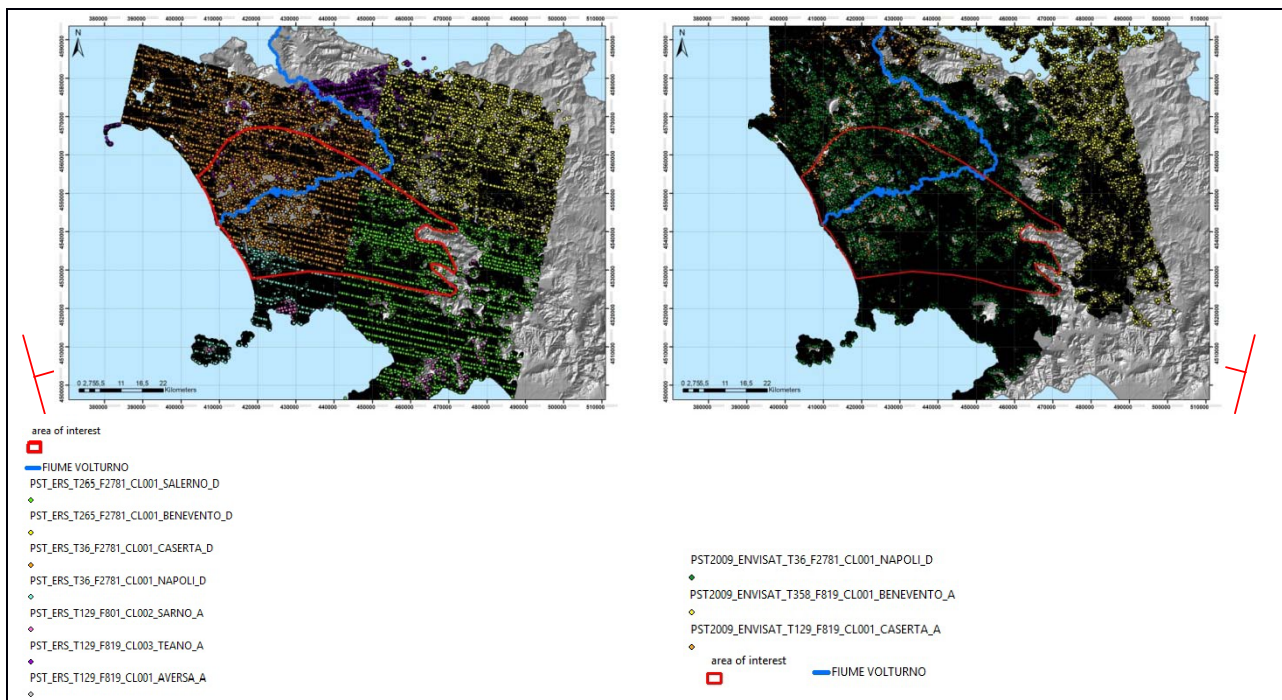
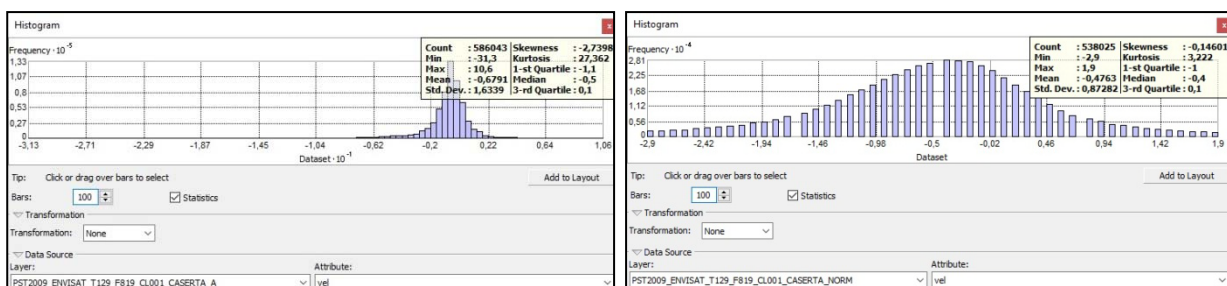


Fig. 8.11. Area of interest, where the ascending and descending PS ERS native datasets overlap each other.

Fig. 8.12. Area of interest, where the ascending and descending PS ENVISAT native datasets overlap each other.

The data analysis starts with extraction of PS normal subsets (see Section 2.1) from native datasets through the outliers boundaries (*fences*) evaluation (Fig. and Table).

In Fig. 8.13, as example, are shown the difference between distribution histograms of the native datasets PST2009_ENVISAT_T36_F2781_CL001_NAPOLI_D and PST2009_ENVISAT_T129_F819_CL001_CASERTA_A, that do not have a normal distributions, with the subsets extracted, called PST2009_ENVISAT_T36_F2781_CL001_NAPOLI_DESCE_NORM and PST2009_ENVISAT_T129_F819_CL001_CASERTA_ASCE_NORM, which instead show normal distributions.



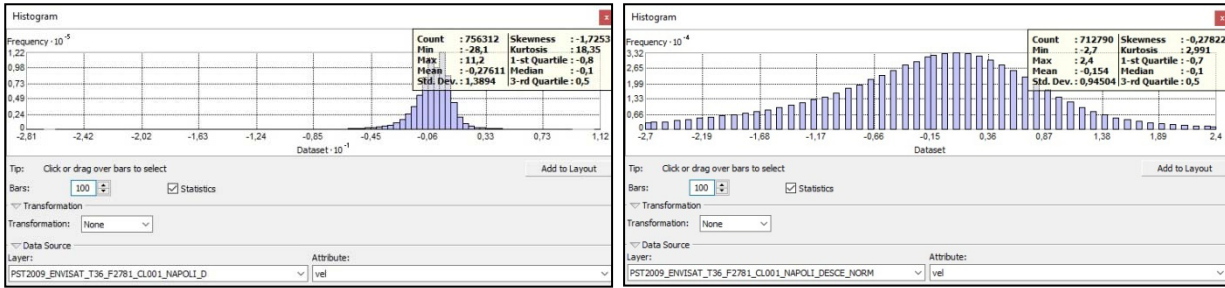


Fig. 8.13. On the left side; the frequency distributions of two native PS datasets is not normal; on the right: the same PS datasets after outliers exclusion they assume a normal frequency distributions.

PS native dataset	Number of PSs	PS normal subsets	New number of PSs	PSs numeric difference
PST_ERS_T265_F2781_CL001_SALERNO_D	154816	PST_ERS_T265_F2781_CL001_SALERNO_NORM_D	147582	7234
PST_ERS_T36_F2781_CL001_NAPOLI_D	63068	PST_ERS_T36_F2781_CL001_NAPOLI_NORM_D	57276	5792
PST_ERS_T36_F2781_CL001_CASERTA_D	127784	PST_ERS_T36_F2781_CL001_CASERTA_NORM_D	118721	9063
PST_ERS_T265_F2781_CL001_BENEVENTO_D	40666	ERS_T265_F2781_CL001_BENEVENTO_NORM_D	38294	2372
PST_ERS_T129_F801_CL002_SARNO_A	129385	PST_ERS_T129_F801_CL002_SARNO_NORM_A	120848	8537
PST_ERS_T129_F819_CL003_TEANO_A	47345	PST_ERS_T129_F819_CL003_TEANO_NORM_A	44918	2427
PST_ERS_T129_F819_CL001_AVERSA_A	119348	PST_ERS_T129_F819_CL001_AVERSA_NORM_A	110894	8454
PST2009_ENVISAT_T36_F2781_CL001_NAPOLI_D	756312	PST2009_ENVISAT_T36_F2781_CL001_NAPOLI_DESCE_NORM	712790	43522
PST2009_ENVISAT_T358_F819_CL001_BENEVENTO_A	532482	PST2009_ENVISAT_T358_F819_CL001_BENEVENTO_ASC_E_NORM	506151	26331
PST2009_ENVISAT_T129_F819_CL001_CASERTA_A	586043	PST2009_ENVISAT_T129_F819_CL001_CASERTA_ASC_E_NORM	538025	48018

Table 8.1. Comparison between the number of PS contained in the native datasets and those contained in the subsets obtained through the outliers exclusion process to realize normal statistical PS distributions (ERS light green, ENVISAT dark green).

Afterwards, it was proceeded to select the PSs inside the perimeter of the areas of interest, both for ERS that ENVISAT datasets.

At this point, the data contained in the areas of interest they will form further three new subsets for ERS data, and four new subsets for ENVISAT data, identified with the further word "pcampana_N" (Figs. 8.14 and 8.15 for ERS and Figs. 8.16 and 8.17 for ENVISAT).

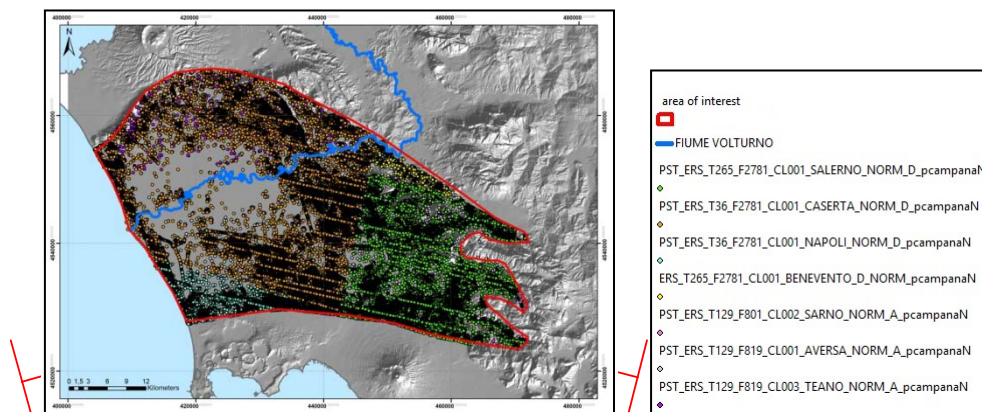


Fig. 8.14. Area of interest ERS, where the subsets in the legend overlap.

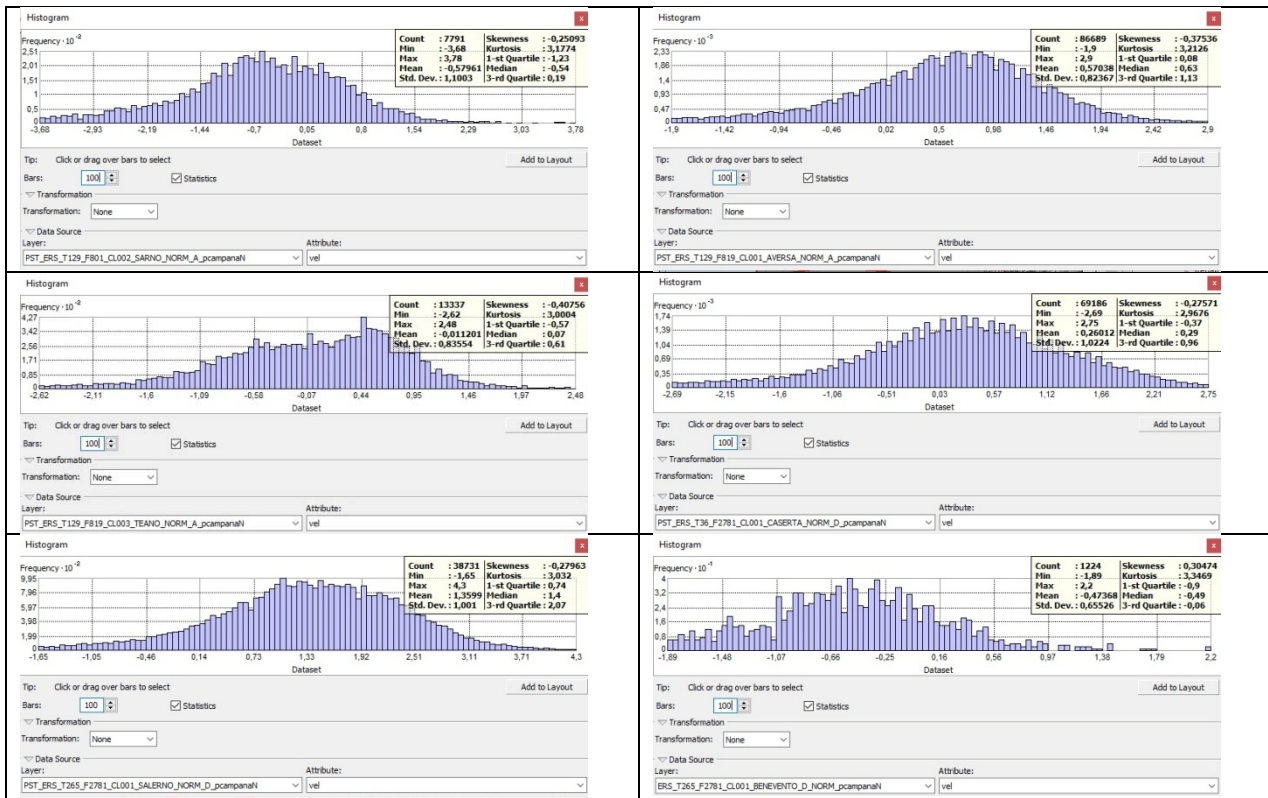


Fig. 8.15. The ERS "pcampana" subsets with normal distribution

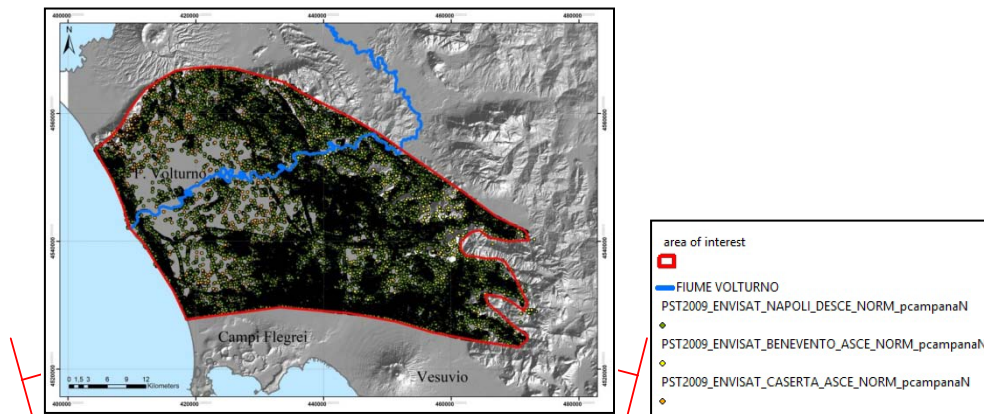


Fig. 8.16. Area of interest ENVISAT, where overlap the subsets in the legend.



Fig. 8.17. The ENVISAT "pcampana" subsets with normal distribution

In this case study we applied only the *Cluster and Outlier Analysis (Anselin Local Moran's I)* mapping tools for all ERS and ENVISAT "pcampanaN" PS subsets. The subsets arising from *Cluster and Outlier Analysis* are identified with "CO" acronym.

The mapping results are shown in Figs. from 8.18 to 8.21.

Like the Monte Marzano representation of the Cluster and Outlier maps, the PSs classified, in the legend below, as "high/low outlier" (with z-score minor of -1.96 and between -1.96 and 1.96) are turned off.

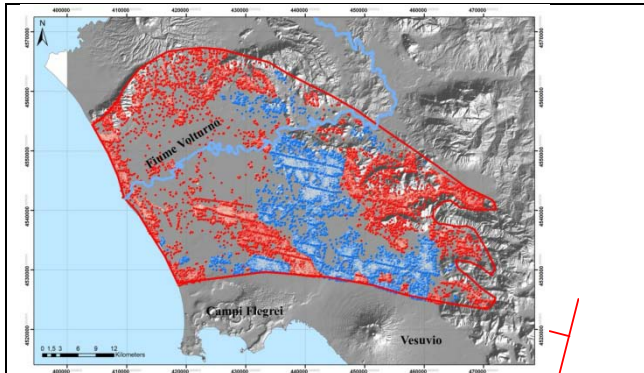


Fig. 8.18. In the map there are the following ERS descending PS subsets from *Cluster and Outlier Analysis* :
 PST_ERS_T265_F2781_CL001_SALERNO_NORM_D_pcampanaN_CO_2k_IDW
 PST_ERS_T36_F2781_CL001_CASERTA_NORM_D_pcampanaN_CO_2k_IDW
 PST_ERS_T36_F2781_CL001_NAPOLI_NORM_D_pcampanaN_CO_2k_IDW

CLUSTER & OUTLIER
 • Cluster: High
 High Outlier (off)
 Low Outlier (off)
 • Cluster: Low

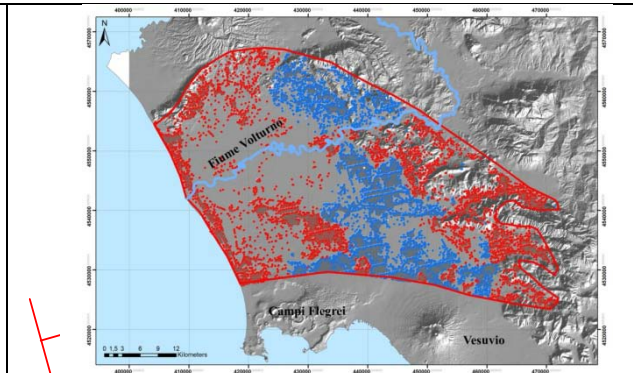


Fig. 8.19. In the map there are the following ERS ascending PS subsets from *Cluster and Outlier Analysis* :
 PST_ERS_T129_F819_CL001_AVERSA_NORM_A_pcampanaN_CO_2k_IDW
 PST_ERS_T129_F801_CL002_SARNO_NORM_A_pcampanaN_CO_2k_IDW
 PST_ERS_T129_F819_CL003_TEANO_NORM_A_pcampanaN_CO_2k_IDW

CLUSTER & OUTLIER
 • Cluster: High
 High Outlier (off)
 Low Outlier (off)
 • Cluster: Low

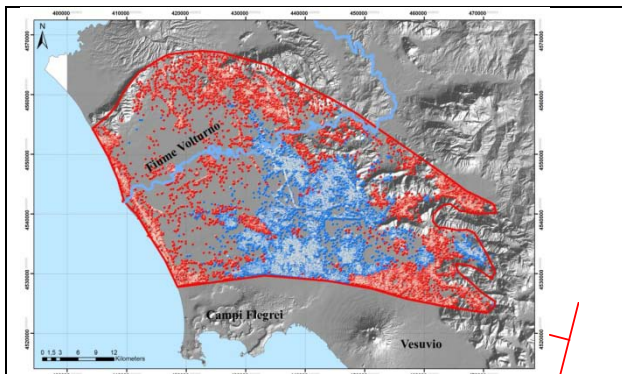


Fig. 8.20. In the map there are the following ENVISAT descending PS subsets from *Cluster and Outlier Analysis* :
 PST2009_ENVISAT_NAPOLI_DESCE_NORM_pcampanaN_CO_2k_IDW

CLUSTER & OUTLIER
 • Cluster: High
 High Outlier (off)
 Low Outlier (off)
 • Cluster: Low

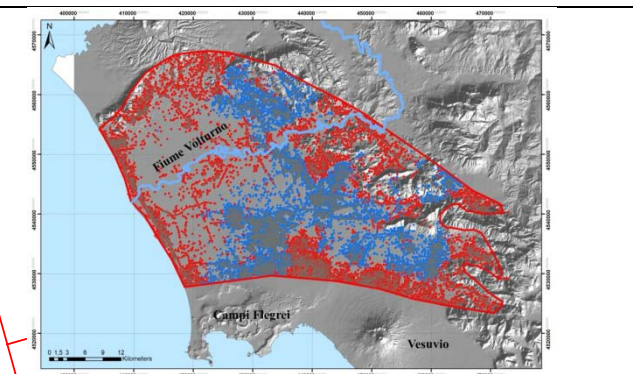


Fig. 8.21. In the map there are the following ENVISAT ascending PS subsets from *Cluster and Outlier Analysis* :
 PST2009_ENVISAT_BENEVENTO_ASCE_NORM_pcampanaN_CO_2k_IDW
 PST2009_ENVISAT_CASERTA_ASCE_NORM_pcampanaN_CO_2k_IDW

CLUSTER & OUTLIER
 • Cluster: High
 High Outlier (off)
 Low Outlier (off)
 • Cluster: Low

In the tables below there are:

- the subsets with "... CO_2k_IDW" are those obtained through *Cluster and Outlier Analysis* that have the same number of PSs like the respective "... NORM_D_pcampanaN" or "... NORM_A_pcampanaN";
- the subsets with "... CO_2k_IDW_nout" that are without those classified as "not significant", "high outlier (HL)" and "low outlier (LH)", with a very reduced number of PSs in.

PS ERS SUBSETS - extraction of PS HH and LL	Number of PSs
PST_ERS_T36_F2781_CL001_NAPOLI_NORM_D_pcampanaN	12534
PST_ERS_T36_F2781_CL001_NAPOLI_NORM_D_pcampanaN_CO_2k_IDW	12534
PST_ERS_T36_F2781_CL001_NAPOLI_NORM_D_pcampanaN_CO_2k_IDW_nout	5058
PST_ERS_T265_F2781_CL001_SALERNO_NORM_D_pcampanaN	38731
PST_ERS_T265_F2781_CL001_SALERNO_NORM_D_pcampanaN_CO_2k_IDW	38731
PST_ERS_T265_F2781_CL001_SALERNO_NORM_D_pcampanaN_CO_2k_IDW_nout	21685
PST_ERS_T36_F2781_CL001_CASERTA_NORM_D_pcampanaN	69186
PST_ERS_T36_F2781_CL001_CASERTA_NORM_D_pcampanaN_CO_2k_IDW	69186
PST_ERS_T36_F2781_CL001_CASERTA_NORM_D_pcampanaN_CO_2k_IDW_nout	37985
ERS_T265_F2781_CL001_BENEVENTO_D_NORM_pcampanaN	1224
ERS_T265_F2781_CL001_BENEVENTO_D_NORM_pcampanaN_CO_2k_IDW	1224
ERS_T265_F2781_CL001_BENEVENTO_D_NORM_pcampanaN_CO_2k_IDW_nout	275
PST_ERS_T129_F801_CL002_SARNO_NORM_A_pcampanaN	7791
PST_ERS_T129_F801_CL002_SARNO_NORM_A_pcampanaN_CO_2k_IDW	7791
PST_ERS_T129_F801_CL002_SARNO_NORM_A_pcampanaN_CO_2k_IDW_nout	4066
PST_ERS_T129_F819_CL001_AVERSA_NORM_A_pcampanaN	86689
PST_ERS_T129_F819_CL001_AVERSA_NORM_A_pcampanaN_CO_2k_IDW	86689
PST_ERS_T129_F819_CL001_AVERSA_NORM_A_pcampanaN_CO_2k_IDW_nout	45690
PST_ERS_T129_F819_CL003_TEANO_NORM_A_pcampanaN	13337
PST_ERS_T129_F819_CL003_TEANO_NORM_A_pcampanaN_CO_2k_IDW	13337
PST_ERS_T129_F819_CL003_TEANO_NORM_A_pcampanaN_CO_2k_IDW_nout	8304

Table 8.2. ERS PSs, features HH and LL selection with *Cluster and Outlier Analysis mapping tool*

PS ENVISAT SUBSETS - extraction of PS HH and LL	Number of PSs
PST2009_ENVISAT_NAPOLI_DESCE_NORM_pcampanaN	307786
PST2009_ENVISAT_NAPOLI_DESCE_NORM_pcampanaN_CO_2k_IDW	307786
PST2009_ENVISAT_NAPOLI_DESCE_NORM_pcampanaN_CO_2k_IDW_nout	157550
PST2009_ENVISAT_BENEVENTO_ASCE_NORM_pcampanaN	506151
PST2009_ENVISAT_BENEVENTO_ASCE_NORM_pcampanaN_CO_2k_IDW	506151
PST2009_ENVISAT_BENEVENTO_ASCE_NORM_pcampanaN_CO_2k_IDW_nout	85688
PST2009_ENVISAT_CASERTA_ASCE_NORM_pcampanaN	163024
PST2009_ENVISAT_CASERTA_ASCE_NORM_pcampanaN_CO_2k_IDW	163024
PST2009_ENVISAT_CASERTA_ASCE_NORM_pcampanaN_CO_2k_IDW_nout	95249

Table 8.3. ENVISAT PSs, features HH and LL selection with *Cluster and Outlier Analysis mapping tool*

In the tables below , 8.4 and 8.5, the number of PSs contained in each category derived from *Cluster and Outlier Analysis*: the PSs specified with bold style (HH and LL) are those used to realize interpolation maps in Figs. 8.26 and 8.27.;

PS ERS SUBSETS - extraction of PS HH and LL	Number of PSs
PST_ERS_T36_F2781_CL001_NAPOLI_NORM_D_pcampanaN_CO_2k_IDW	
Not Significant	5888
Cluster: High (HH)	3073
Cluster: Low (LL)	1985
High Outlier (HL)	577
Low Outlier (LH)	1011
PST_ERS_T265_F2781_CL001_SALERNO_NORM_D_pcampanaN_CO_2k_IDW	
Not Significant	12733
Cluster: High (HH)	11573
Cluster: Low (LL)	10112
High Outlier (HL)	1909
Low Outlier (LH)	2404

PST_ERS_T36_F2781_CL001_CASERTA_NORM_D_pcmpanaN_CO_2k_IDW	
Not Significant	25038
Cluster: High (HH)	19195
Cluster: Low (LL)	18790
High Outlier (HL)	3330
Low Outlier (LH)	2833
ERS_T265_F2781_CL001_BENEVENTO_D_NORM_pcmpanaN_CO_2k_IDW	
Not Significant	848
Cluster: High (HH)	133
Cluster: Low (LL)	142
High Outlier (HL)	57
Low Outlier (LH)	44
PST_ERS_T129_F801_CL002_SARNO_NORM_A_pcmpanaN_CO_2k_IDW	
Not Significant	3144
Cluster: High (HH)	2397
Cluster: Low (LL)	1669
High Outlier (HL)	147
Low Outlier (LH)	434
PST_ERS_T129_F819_CL001_AVERSA_NORM_A_pcmpanaN_CO_2k_IDW	
Not Significant	32436
Cluster: High (HH)	26438
Cluster: Low (LL)	19252
High Outlier (HL)	3043
Low Outlier (LH)	5520
PST_ERS_T129_F819_CL003_TEANO_NORM_A_pcmpanaN_CO_2k_IDW	
Not Significant	3999
Cluster: High (HH)	4722
Cluster: Low (LL)	3582
High Outlier (HL)	289
Low Outlier (LH)	745

Table 8.4. ERS PSs selection with *Cluster and Outlier Analysis mapping tool* . Coulored black numbers indicate PS that are not considered in the vertical Vmean deformation maps processing

PS ENVISAT SUBSETS - extraction of PS HH and LL	Number of PSs
PST2009_ENVISAT_NAPOLI_DESCE_NORM_pcmpanaN_CO_2k_IDW	
Not Significant	125532
Cluster: High (HH)	92690
Cluster: Low (LL)	64860
High Outlier (HL)	7677
Low Outlier (LH)	17027
PST2009_ENVISAT_BENEVENTO_ASCE_NORM_pcmpanaN_CO_2k_IDW_nout	
Not Significant	82519
Cluster: High (HH)	46034
Cluster: Low (LL)	39654
High Outlier (HL)	6164
Low Outlier (LH)	7640
PST2009_ENVISAT_CASERTA_ASCE_NORM_pcmpanaN_CO_2k_IDW	
Not Significant	54086
Cluster: High (HH)	60004
Cluster: Low (LL)	32245
High Outlier (HL)	2915
Low Outlier (LH)	10774

Table 8.5. ENVISAT PSs selection with *Cluster and Outlier Analysis mapping tool* . Red numbers indicate PS that are not considered in the vertical Vmean deformation maps processing

As an example, we consider two subsets made up of PSs classified as "not significant" (nsig). The "PST2009_ENVISAT_CASERTA_ASCE_NORM_pcampanaN_CO_2k_IDW_nsig" subset has a normal data distribution (Fig.8.22) and contains 54086 PSs (Table 8.5); The "PST_ERS_T129_F819_CL001_AVERSA_NORM_A_pcampanaN_CO_2k_IDW_nsig" subset has an almost normal data distribution (Fig. 8.23) and contain 32436 PSs (Table 8.4);

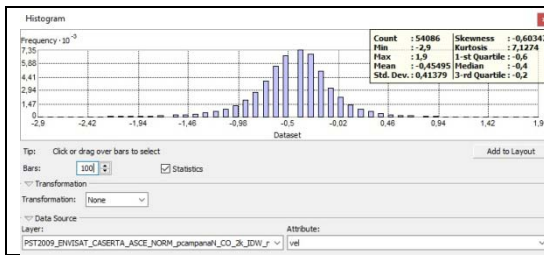


Fig. 8.22.

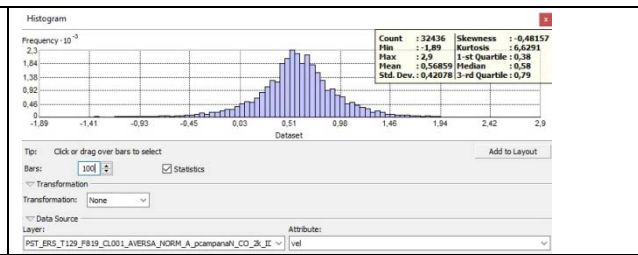


Fig. 8.23.

In Fig. 8.24 we can see the Vmean IDW interpolation map realized with the Fig. 8.22 subset. It is almost entirely represented by the the Vmean -1 - 0 class, that is the statistic mean velocity of -0,45 mm/yr in the subset.

In Fig. 8.25 we can see the Vmean IDW interpolation map realized with Fig. 8.23 subset. It is almost entirely represented by the the Vmean 0 - 1 class, that is the statistic Vmean of 0,56 mm/yr, in the subset.

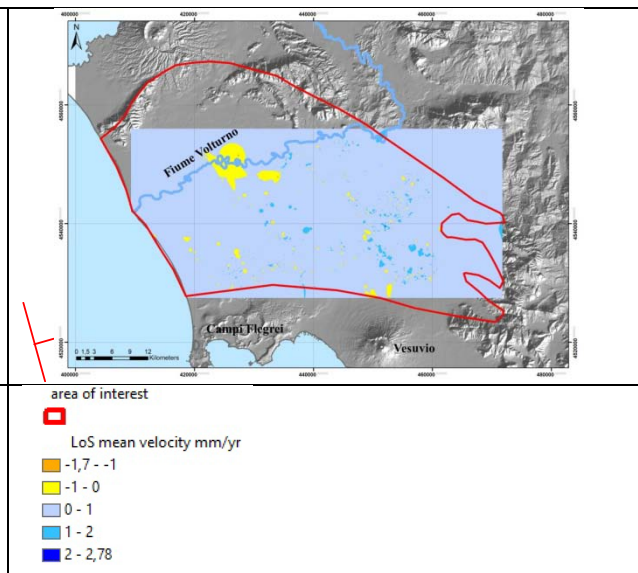
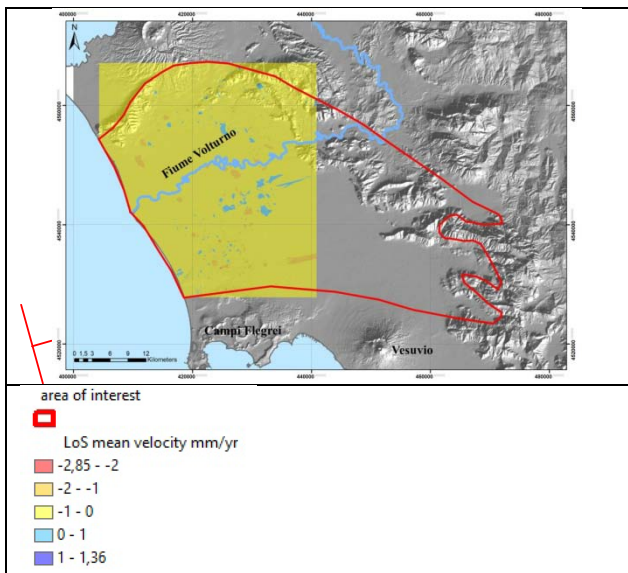


Fig. 8.24. ENVISAT ascending subset - IDW interpolation map realized with PSs classified as "not significant" (see Table 8.4)

Fig. 8.25. ERS ascending subset - IDW interpolation map realized with PSs classified as "not significant" (see Table 8.5)

Then applying the IDW interpolation (cell = 50x50 m), to the ascending and descending Vmean (VLoSa and VLoSd) it is possible obtain the maps for the native datasets consisting of normal and outlier PSs and for the "... CO_2k_IDW_nout" PS subsets (Fig.).

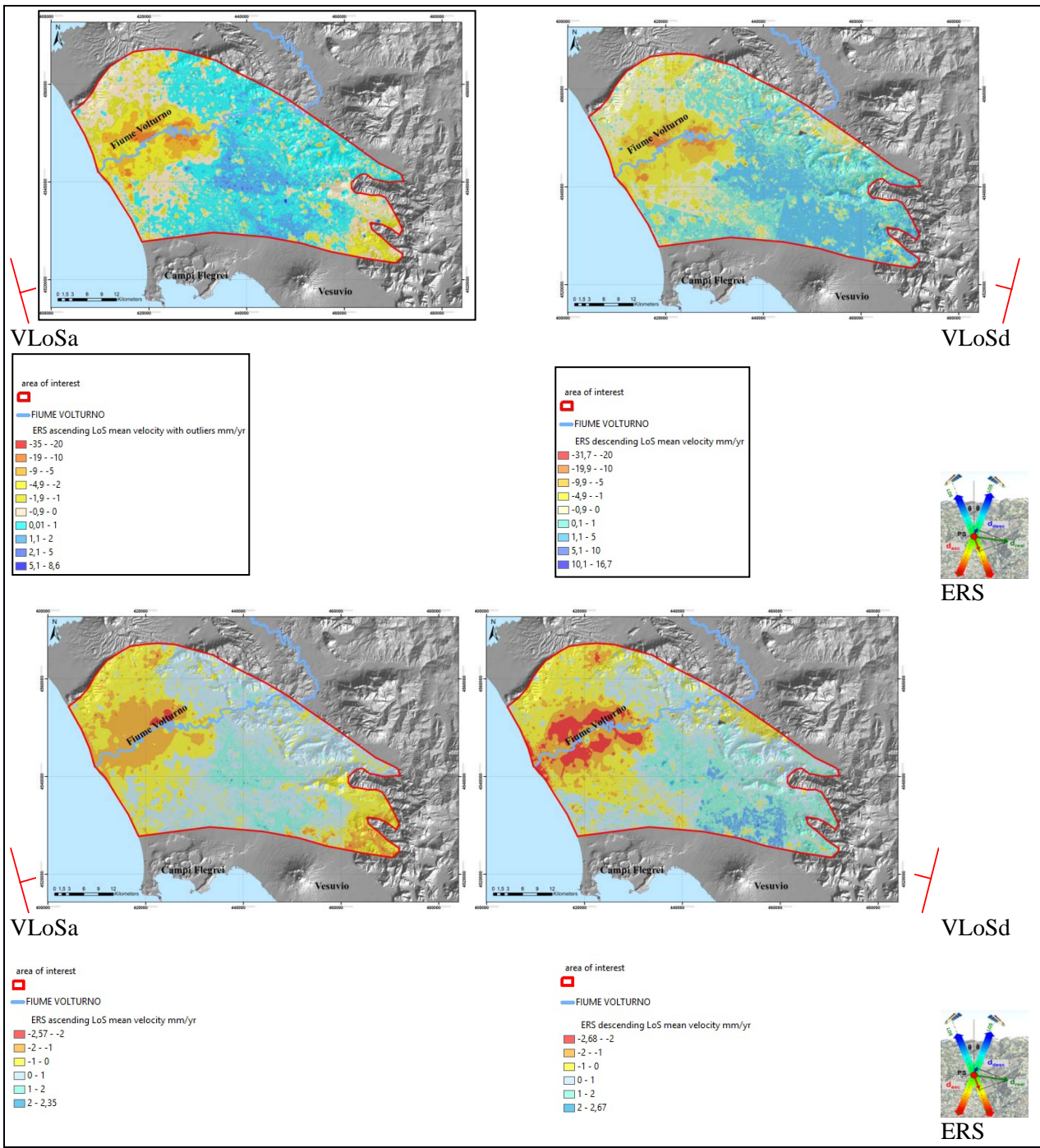


Fig. 8.26. ERS ascending and descending subsets - upper pair: IDW interpolation map realized with PSs classified as "Cluster: High (HH)" and "Cluster: Low (LL)"; lower pair, IDW interpolation map realized with native PSs datasets (normal + outlier)

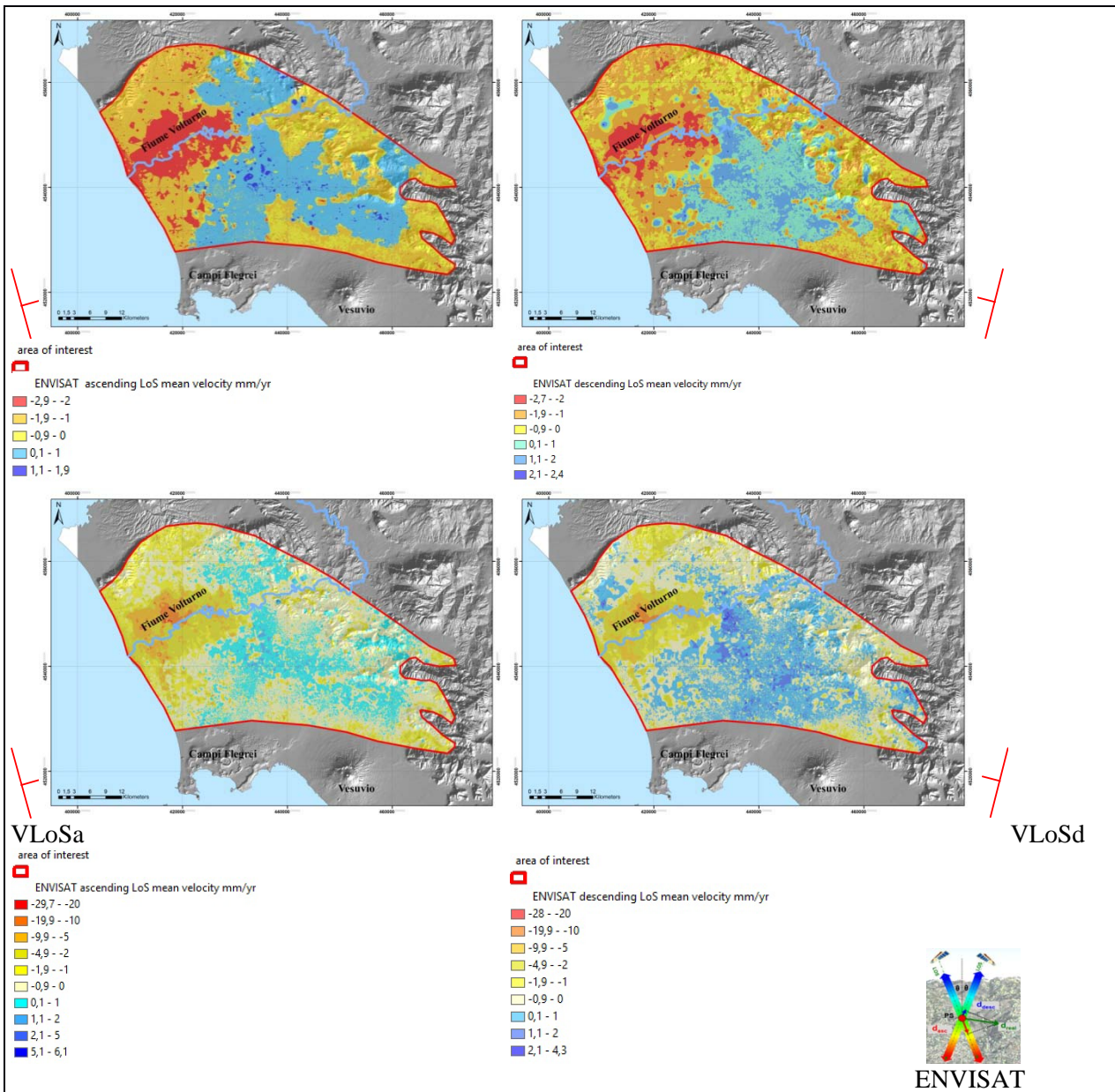


Fig. 8.27. ENVISAT ascending and descending subsets - upper pair: IDW interpolation map realized with PSs classified as "Cluster: High (HH)" and "Cluster: Low (LL)"; lower pair, IDW interpolation map realized with native PSs datasets (normal + outlier)

Using a GIS raster calculator tool, it was operated with the interpolated pairs of maps above, to represent the vertical component of V_{mean} maps, through the relationship:

$$(3) \quad V_z = (V_{LoSd} + V_{LoSa})/2\cos\theta$$

applied both to the ERS and ENVISAT datasets.

The vertical V_{mean} IDW interpolation map are represented in (Figs. from 8.28 to 8.31).

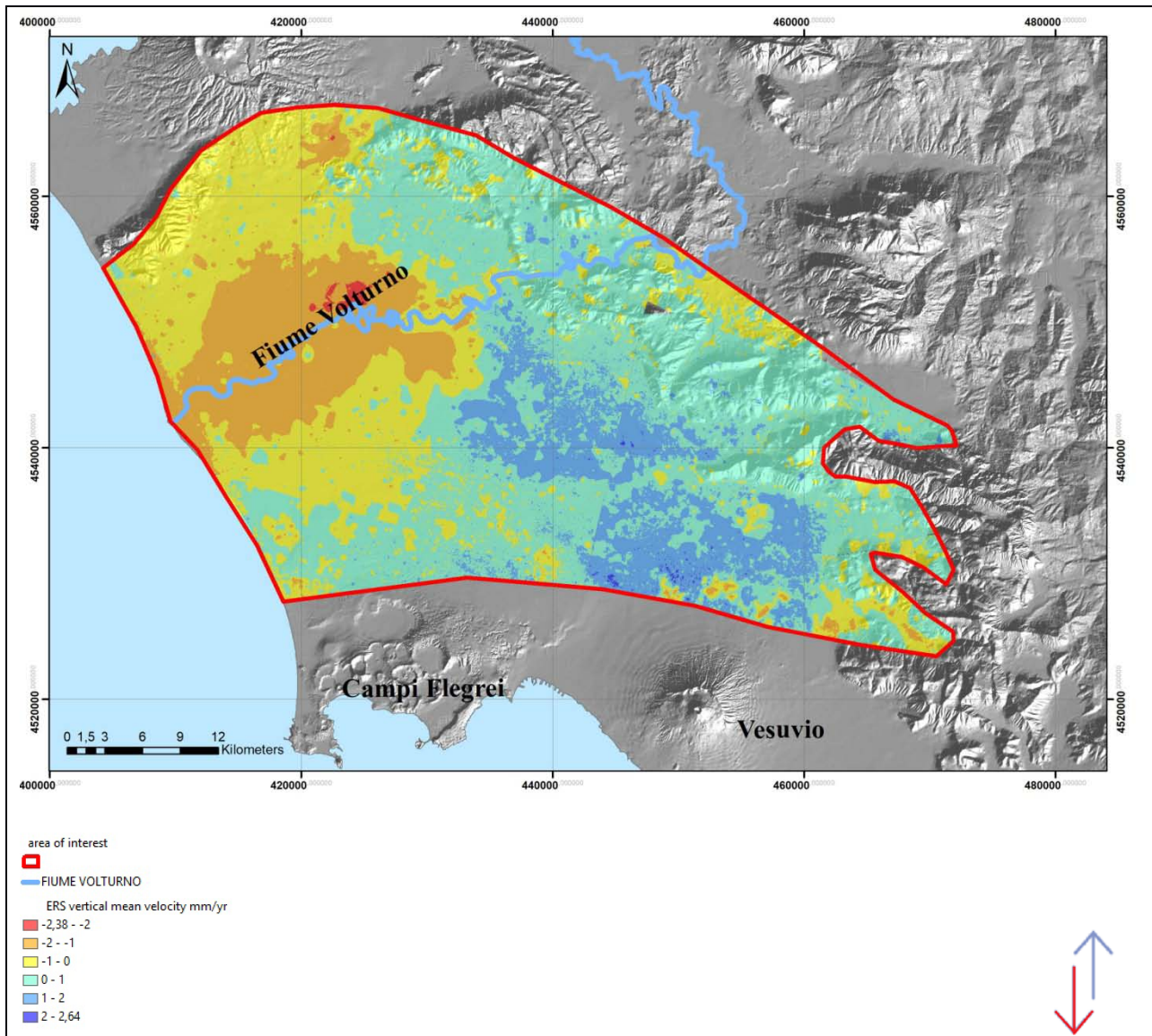


Fig. 8.28. ERS vertical Vmean IDW interpolation map realized with PSs subsets classified as "Cluster: High (HH)" and "Cluster: Low (LL)"

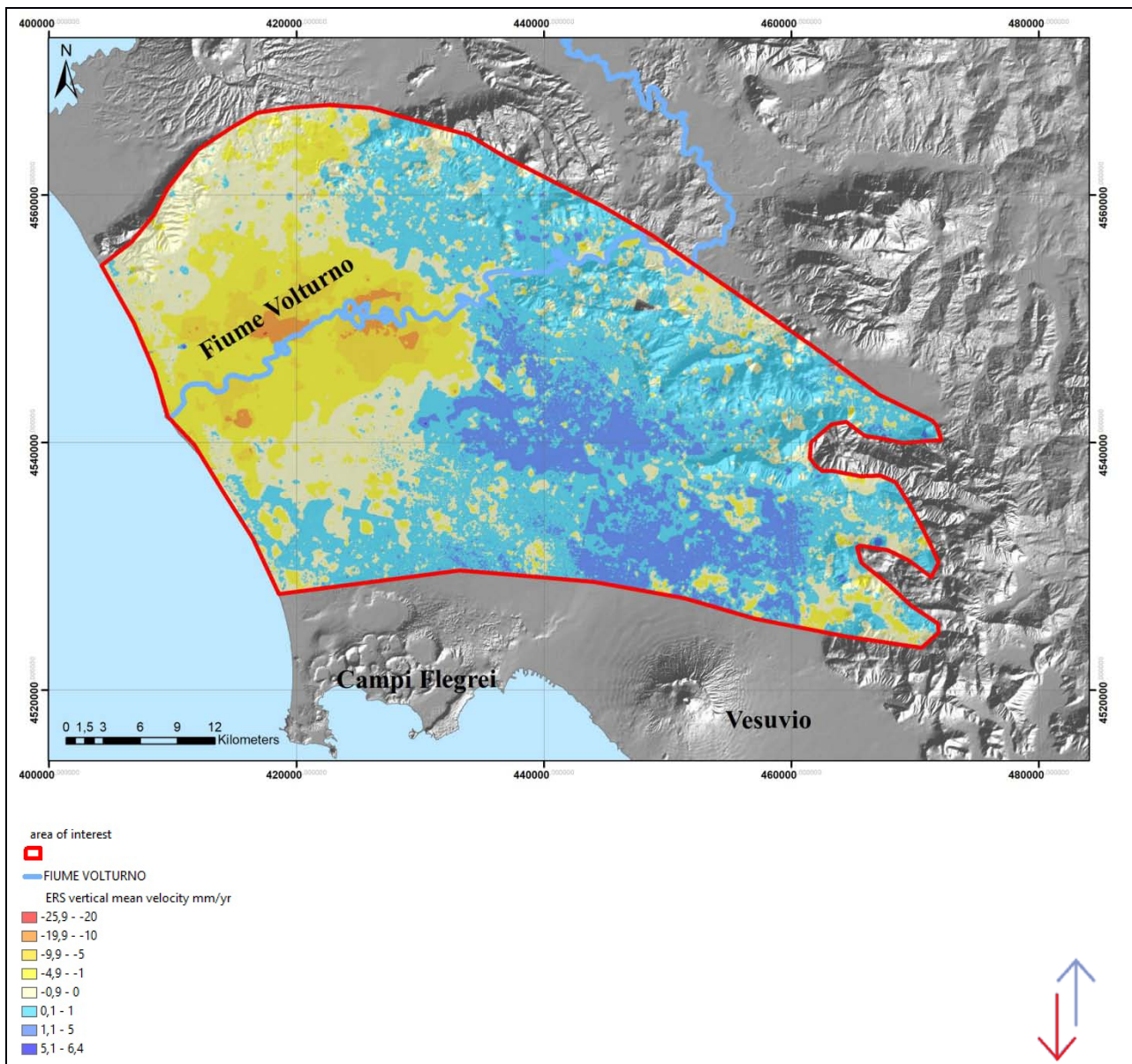


Fig. 8.29. ERS vertical Vmean IDW interpolation map realized with native PSs datasets (normal + outlier)

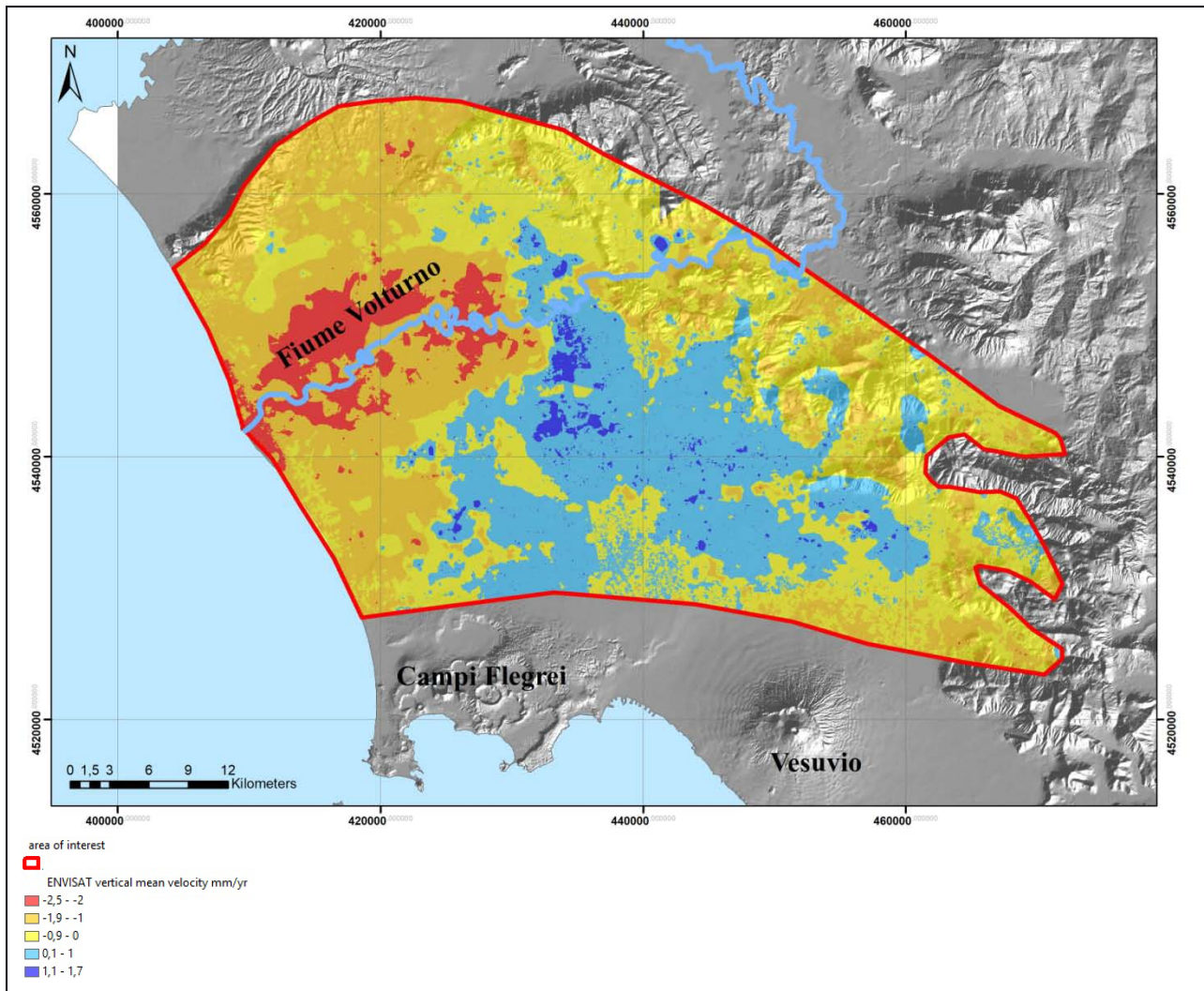


Fig. 8.30. ENVISAT vertical Vmean IDW interpolation map realized with PSs subsets classified as "Cluster: High (HH)" and "Cluster: Low (LL)"

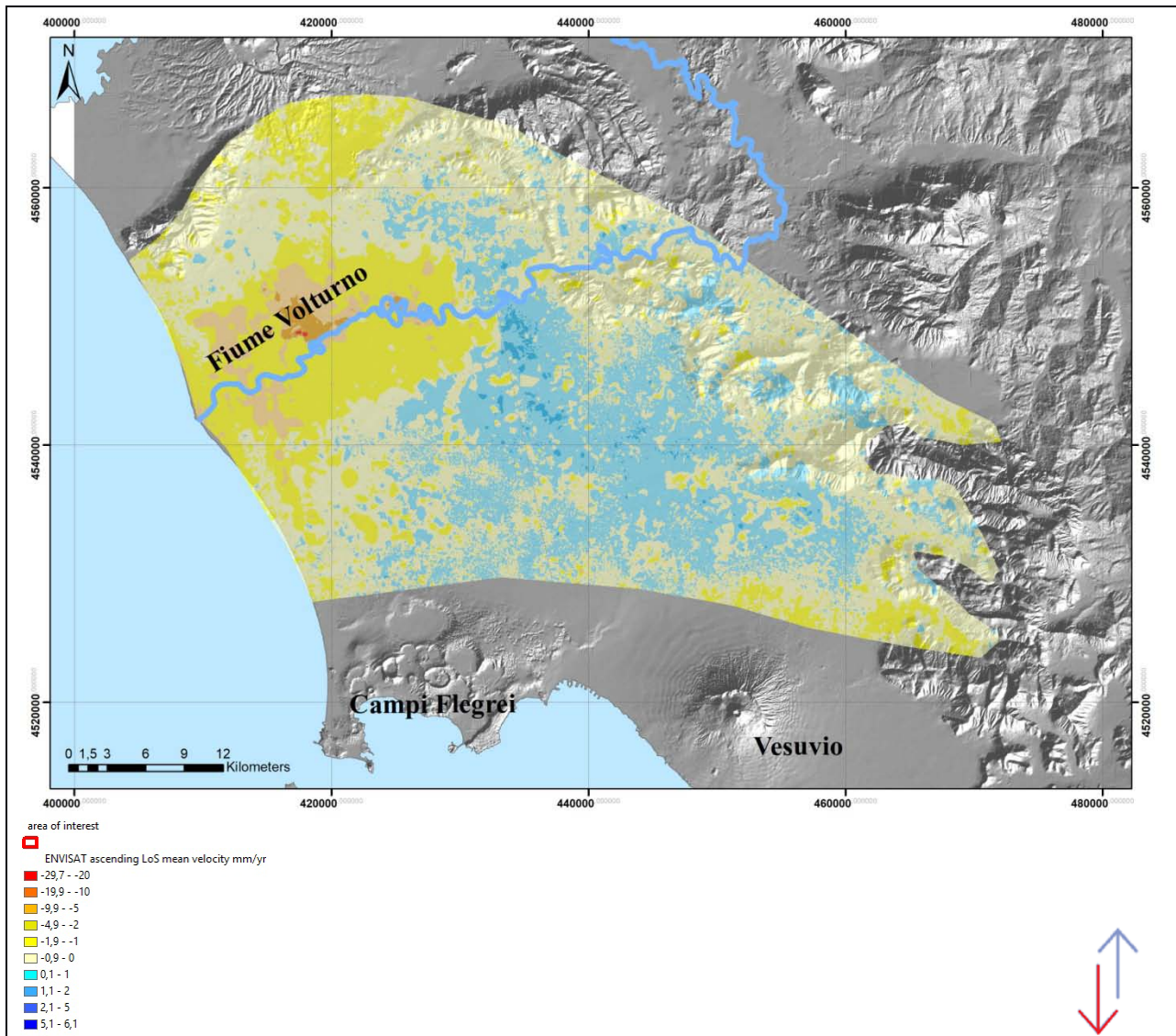


Fig. 8.31. ENVISAT vertical V_{mean} IDW interpolation map realized with native PSs datasets (normal + outlier)

8.4 ERS Time Series analysis

In this section we observe a number of four PS pairs of time series displacement from ERS descending and ascending data. The chosen PSs are very close (they are represented by a single light blue point in the map), near the Fiume Volturno, and arranged along a SSE-NNW direction, in latitude, and a WSW-ENE direction, along the straight fluvial pattern in the central part of the plain (see Sec. 8.3).

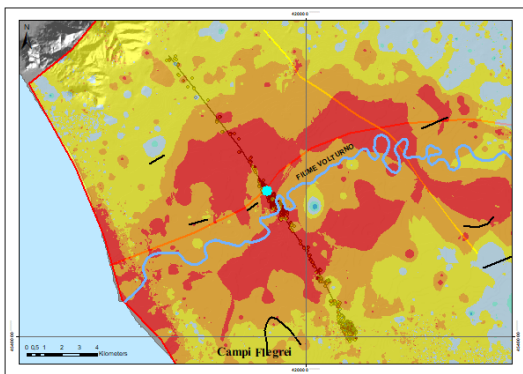


Fig. 8.32 Location (light blue point in map) of 5+5 very close PSs ERS (see the two graph below in Figs. 8.33 and 8.34) belonging to PST_ERS_T36_F2781_CL001_CASERTA_D dataset - IDW interpolation descending map realized with PSs classified as "Cluster: High (HH)" and "Cluster: Low (LL)"

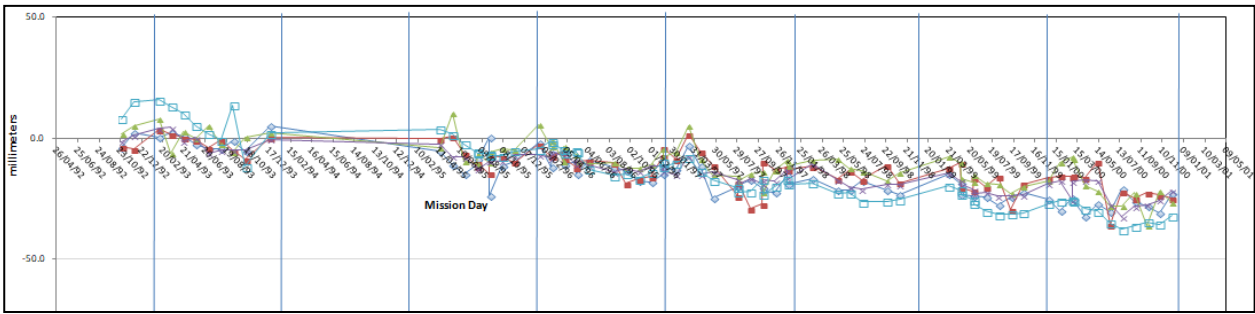


Fig. 8.33. Time series of PS belong to PST_ERS_T36_F2781_CL001_CASERTA_D outlier subset with code: BBZER

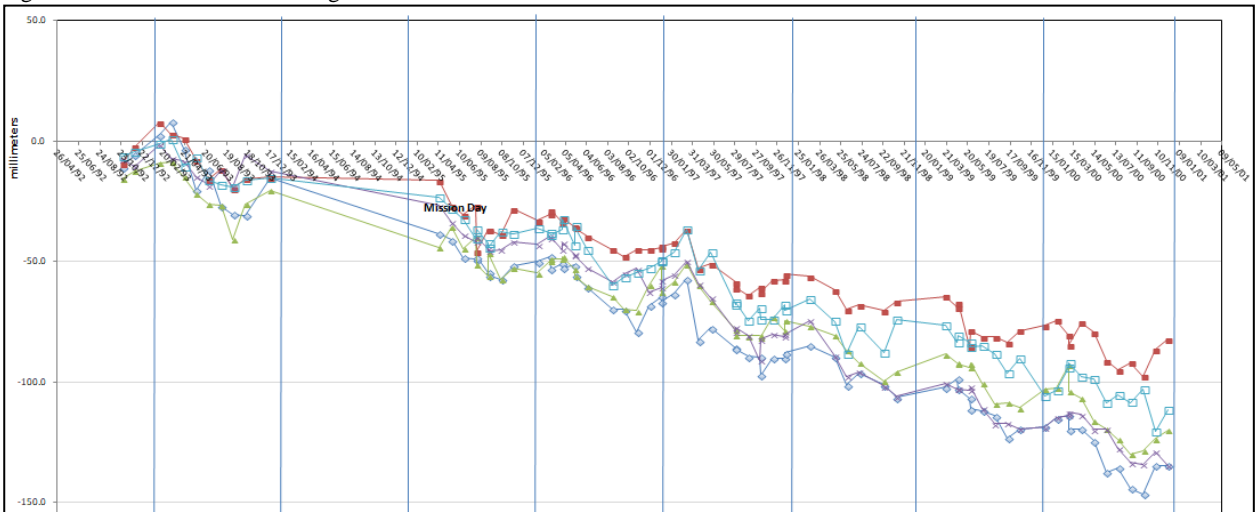


Fig. 8.34 Time series of PS belong to PST_ERS_T36_F2781_CL001_CASERTA_D outlier subset with code: BBZDG

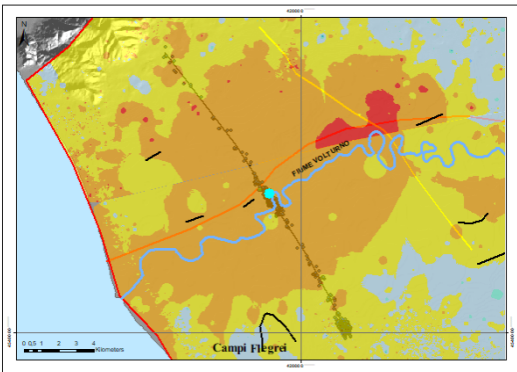


Fig. 8.35. Location (light blue point in map) of 5+5 very close PSs ERS (see the two graph below in Figs. 8.36 and 8.37) belonging to PST_ERS_T129_F819_CL001_AVERSA_A dataset, over IDW interpolation ascending map realized with PSs classified as "Cluster: High (HH)" and "Cluster: Low (LL)"

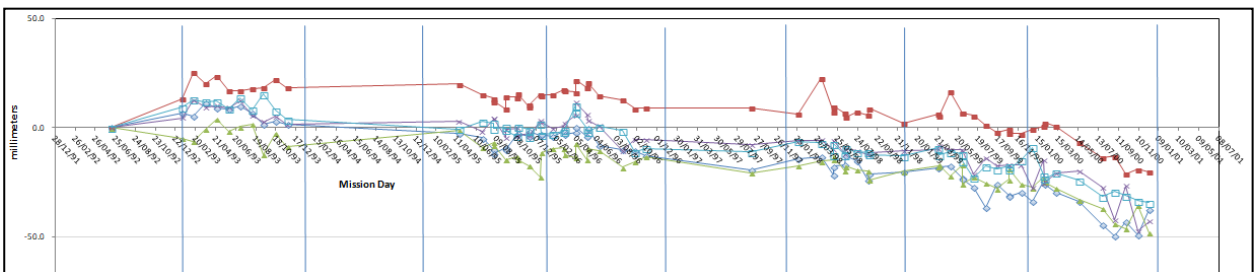


Fig. 8.36. Time series of a PS belong to PST_ERS_T129_F819_CL001_AVERSA_A outlier subset with code: BLQZQ

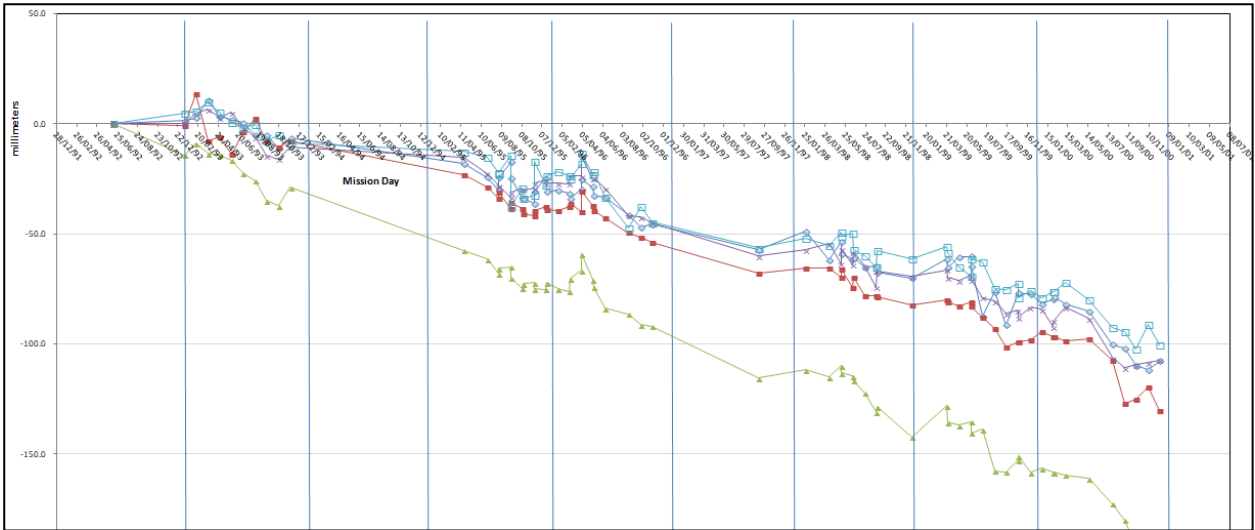


Fig. 8.37. Time series of a PS belong to PST_ERS_T129_F819_CL001_AVERSA_A outlier subset with code: BHMGW

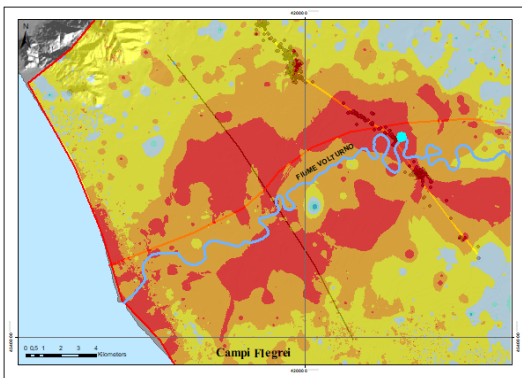


Fig. 8.38. Location (light blue point in map) of 5+5 very close PSs ERS (see the two graph belowin Figs. 8.39 and 8.40) belonging to PST_ERS_T36_F2781_CL001_CASERTA_D dataset - IDW interpolation descending map realized with PSs classified as "Cluster: High (HH)" and "Cluster: Low (LL)"

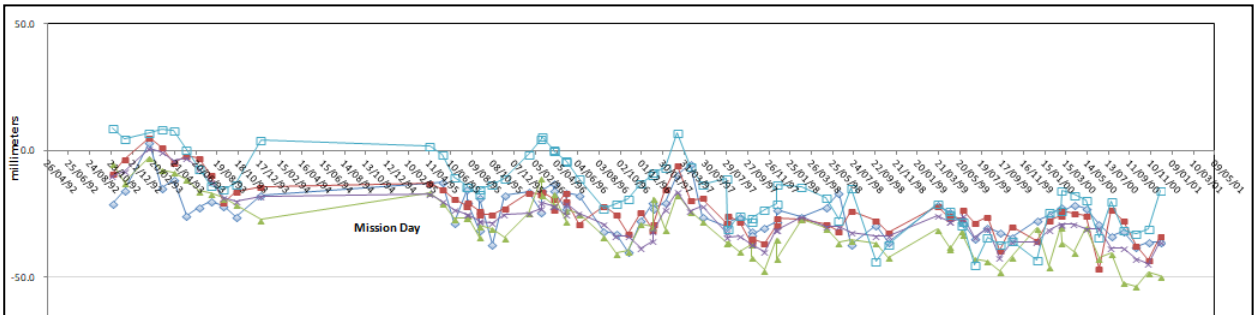


Fig. 8.39. Time series of PS belong to PST_ERS_T36_F2781_CL001_CASERTA_D outlier subset with code: A9RQ6

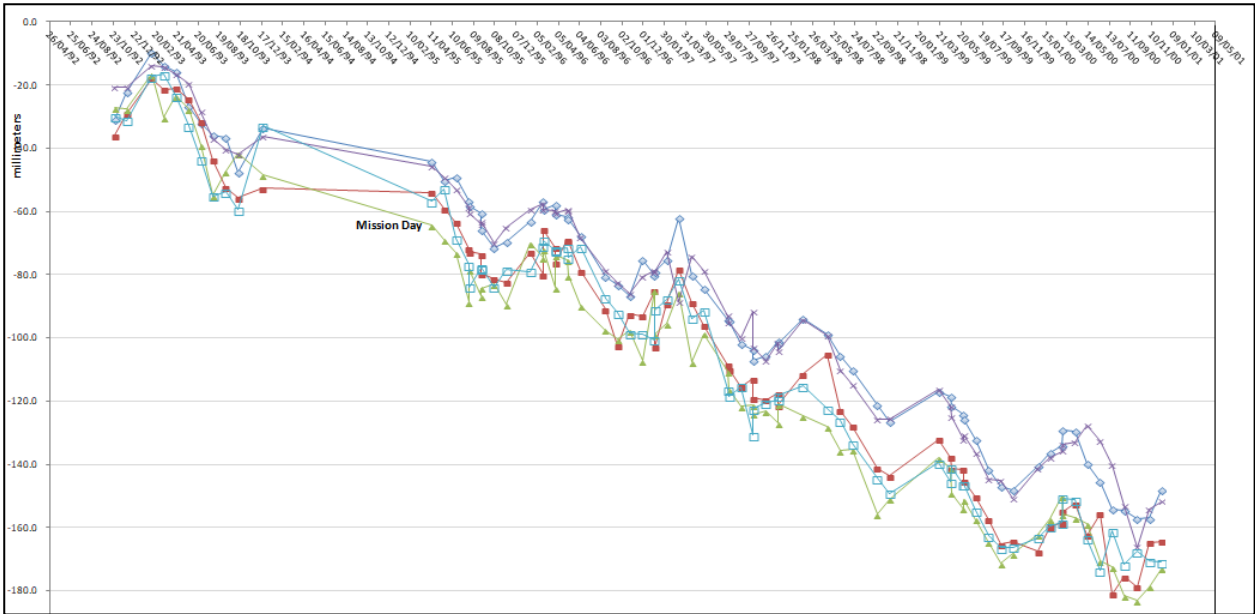


Fig. 8.40. Time series of PS belong to PST_ERS_T36_F2781_CL001_CASERTA_D outlier subset with code: A9TV2

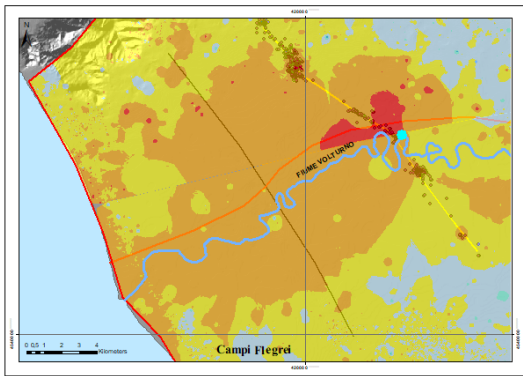


Fig. 8.41. Location (light blue point in map) of 5+5 very close PSs ERS (see the two graph below in Figs. 8.42 and 8.43) belonging to PST_ERS_T129_F819_CL001_AVERSA_A dataset - IDW interpolation ascending map realized with PSs classified as "Cluster: High (HH)" and "Cluster: Low (LL)"

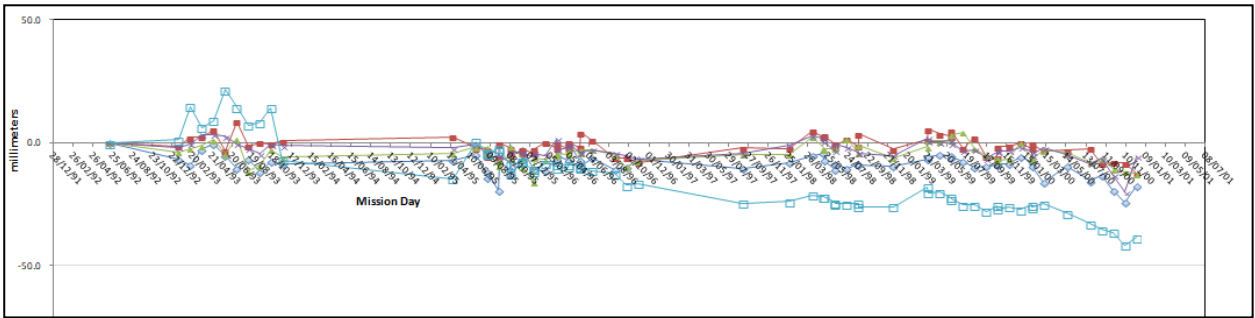


Fig. 8.42. Time series of PS belong to PST_ERS_T129_F819_CL001_AVERSA_A outlier subset with code: A2ODK

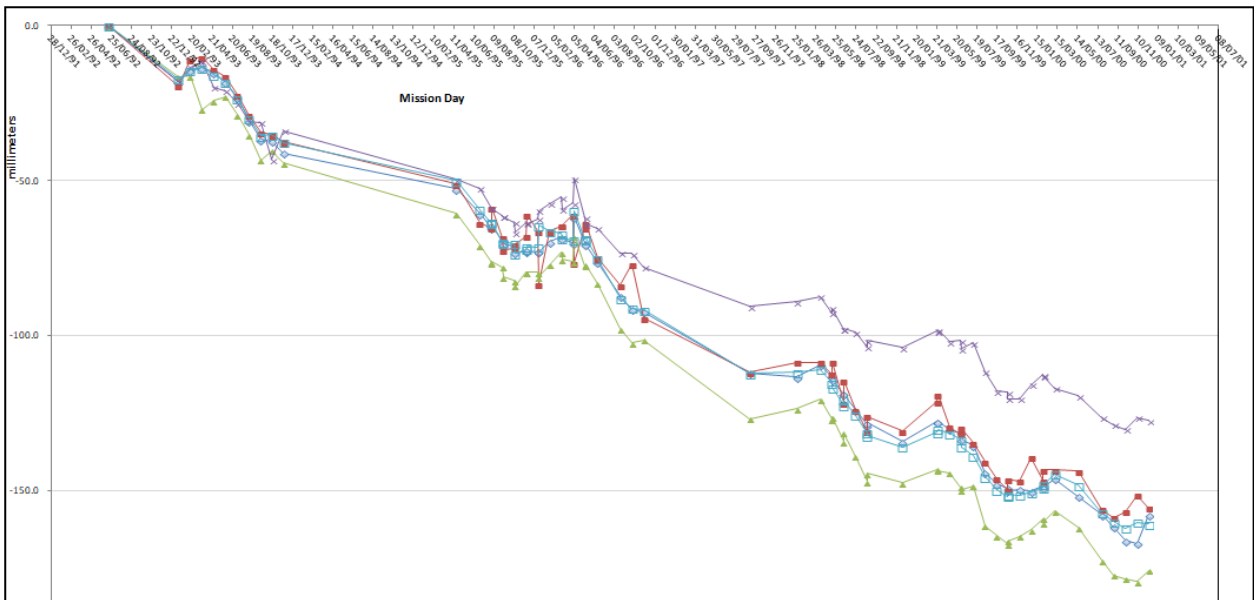


Fig. 8.43. Time series of PS belong to PST_ERS_T129_F819_CL001_AVERSA_A outlier subset with code: A8EF3

The four pairs of PSs show, in their time series, that the deformation rate, characterized by a linear trend plus a periodic seasonal fluctuation, change from very slow (sub-horizontal) to very rapid subsidence, where is, more or less, the straight fluvial pattern in the central part of the plain.

8.5 ENVISAT Time Series analysis

In this section we observe a number of four PS pairs of time series displacement from ENVISAT descending and ascending data. The chosen PSs are very close (they are represented by a single light blue point in the map), near the Fiume Volturno, and arranged along a SSE-NNW direction, in latitude, and a WSW-ENE direction, along the straight fluvial pattern in the central part of the plain (see Sec. 8.3).

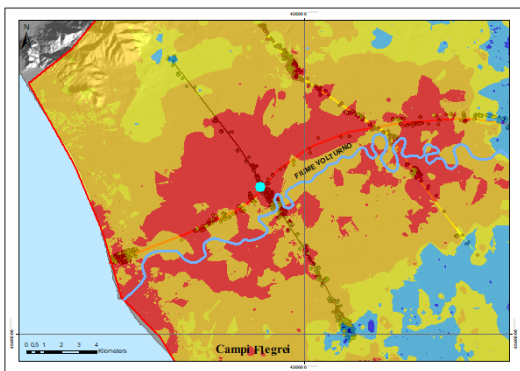


Fig. 8.44. Location (light blue point in map) of 5+5 very close PSs ERS (see the two graph below in Figs. 8.45 and 8.46) belonging to PST2009_ENVISAT_T36_F2781_CL001_NAPOLI_D dataset - IDW interpolation ascending map realized with PSs classified as "Cluster: High (HH)" and "Cluster: Low (LL)"

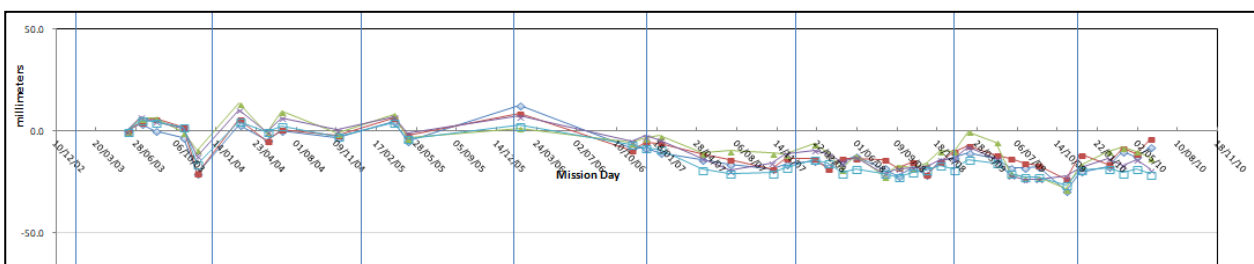


Fig. 8.45. Time series of PS belong to PST2009_ENVISAT_T36_F2781_CL001_NAPOLI_D outlier subset with code: 0004u0015S7

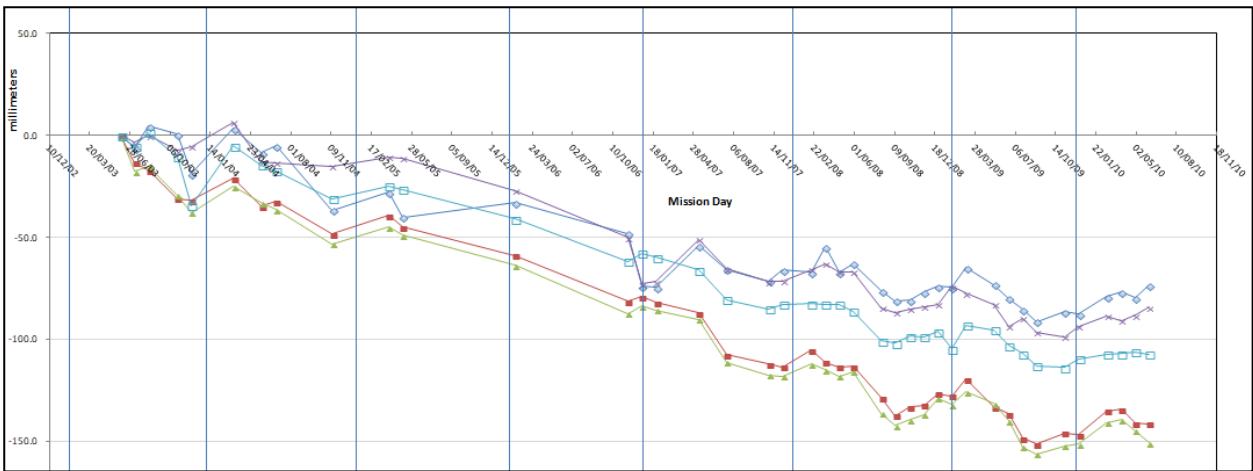


Fig. 8.46. Time series of PS belong to PST2009_ENVISAT_T36_F2781_CL001_NAPOLI_D outlier subset with code: 0004u00154h

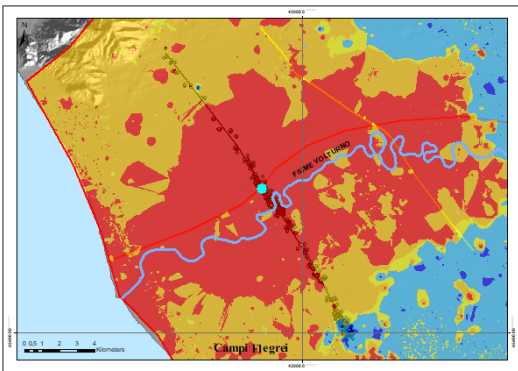


Fig. 8.47. Location (light blue point in map) of 5+5 very close PSs ERS (see the two graph below in Figs. 8.48 and 8.49) belonging to PST2009_ENVISAT_T129_F819_CL001_CASERTA_A dataset - IDW interpolation ascending map realized with PSs classified as "Cluster: High (HH)" and "Cluster: Low (LL)"

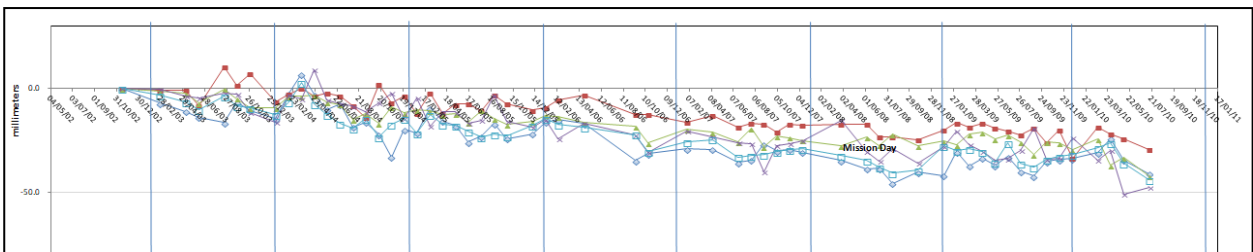


Fig. 8.48. Time series of PS belong to PST2009_ENVISAT_T129_F819_CL001_CASERTA_A outlier subset with code: 1RKiJ000yCD

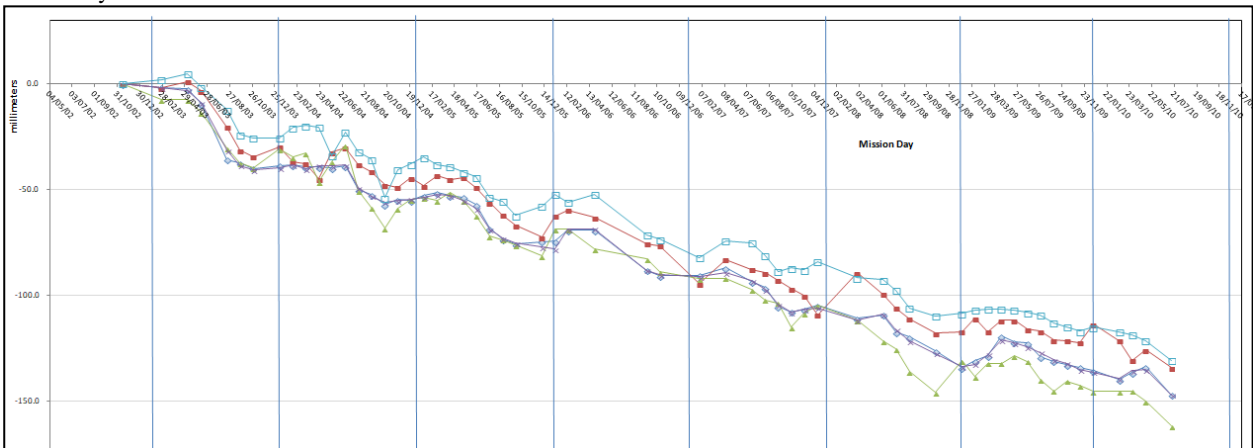


Fig. 8.49. Time series of PS belong to PST2009_ENVISAT_T129_F819_CL001_CASERTA_A outlier subset with code: 1RKiJ000yEE

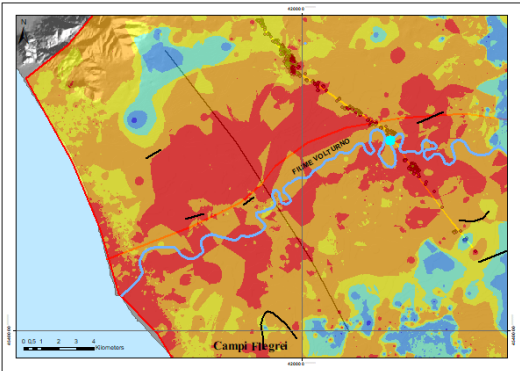


Fig. 8.50. Location (light blue point in map) of 5+5 very close PSs ERS (see the two graph below in Figs. 8.51 and 8.52) belonging to PST2009_ENVISAT_T36_F2781_CL001_NAPOLI_D dataset - IDW interpolation ascending map realized with PSs classified as "Cluster: High (HH)" and "Cluster: Low (LL)"

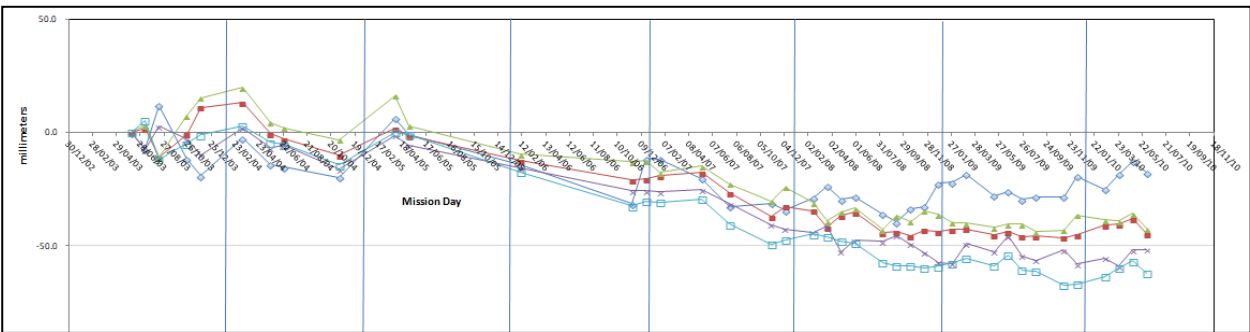


Fig. 8.51. Time series of PS belong to PST2009_ENVISAT_T36_F2781_CL001_NAPOLI_D outlier subset with code: 0004u000uRX

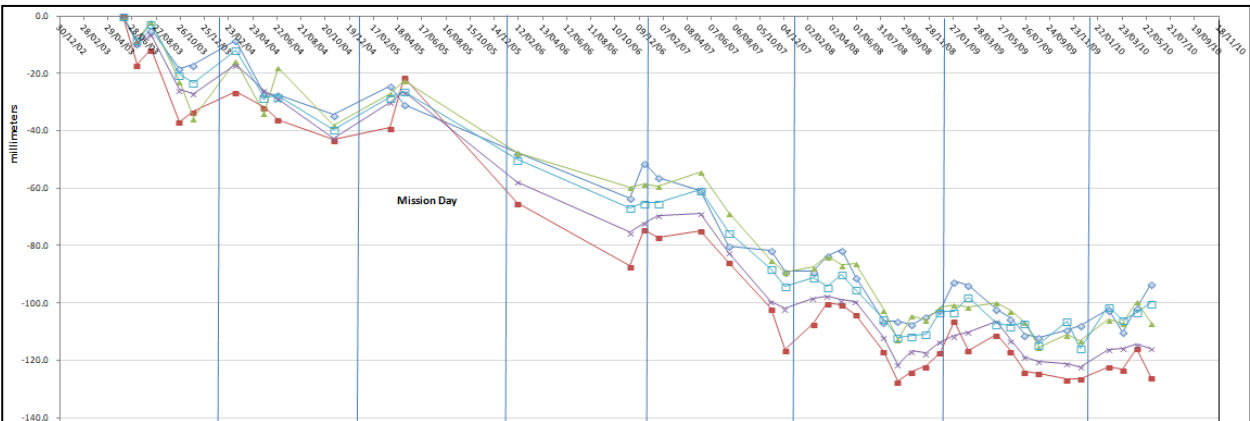


Fig. 8.52. Time series of PS belong to PST2009_ENVISAT_T36_F2781_CL001_NAPOLI_D outlier subset with code: 0004u000szP

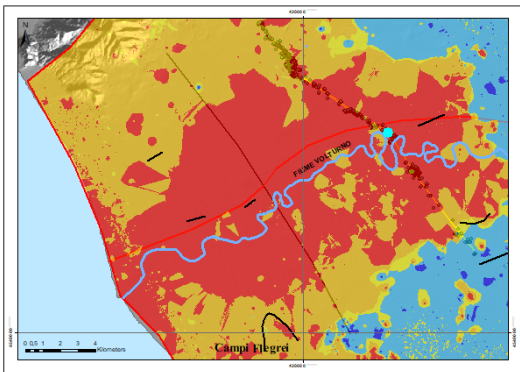


Fig. 8.53. Location (light blue point in map) of 5+5 very close PSs ERS (see the two graph below in Figs. 8.54 and 8.55) belonging to PST2009_ENVISAT_T129_F819_CL001_CASERTA_A dataset - IDW interpolation ascending map realized with PSs classified as "Cluster: High (HH)" and "Cluster: Low (LL)"

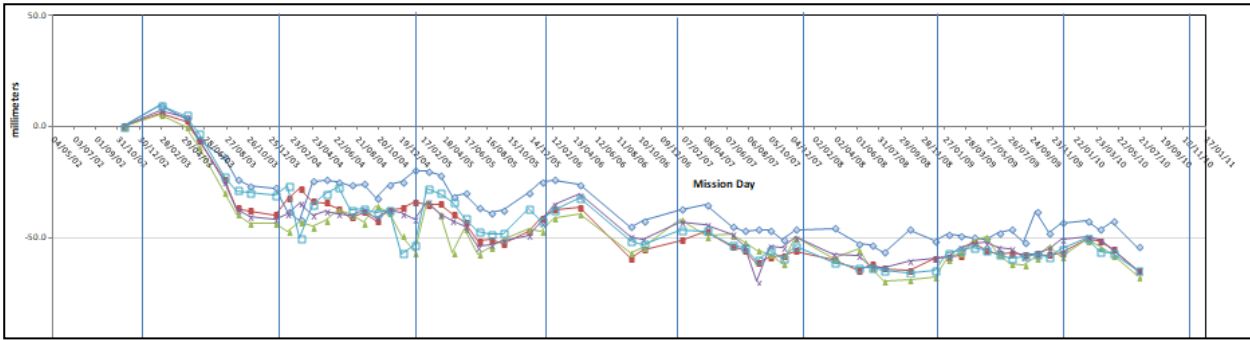


Fig. 8.54. Time series of PS belong to PST2009_ENVISAT_T129_F819_CL001_CASERTA_A outlier subset with code: IRKiJ000y1r

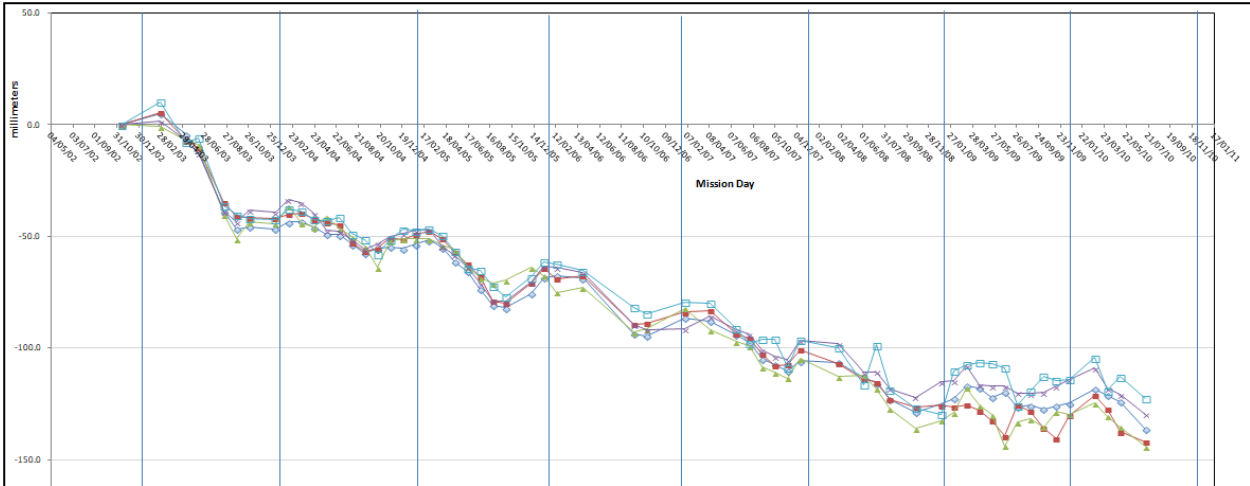


Fig. 8.55. Time series of PS belong to PST2009_ENVISAT_T129_F819_CL001_CASERTA_A outlier subset with code: IRKiJ000zD0

The four pairs of PSs show, in their time series, that the deformation rate, characterized by a linear trend plus a periodic seasonal fluctuation, change from very slow (sub-horizontal) to very rapid subsidence, where is, more or less, the straight fluvial pattern in the central part of the plain.

8.6 Discussion

The analysis of PS-InSAR data from the northern Campania plain have highlighted different behaviours, in terms of current, vertical ground deformation, of the two investigated sectors.

In particular, the geomorphological-stratigraphical analysis of the Canello plain points to the presence, still during MIS7 (i.e., c. 200 ka ago), of a marine gulf deeply indented in this part of the Campania plain eastern margin. Data from core AP (Fig. 8.11) indicate that following MIS 7, a particularly abundant pyroclastic deposition took place. Explosive volcanic activity caused sedimentation of c. 15 thick pyroclastic deposits (Taurano ignimbrite?) at 156 ka, and of the more than 50 m thick C.I. deposits at 39 ka. Abundant pyroclastic deposition was, most probably, the main factor controlling the change of the sedimentary environment from marine to transistional/continental in the area of the AP core. However, based on depth below s.l. of top of the MIS 7 deposits in the AP core, a 0.15 mm/a mean subsidence rate in the last c. 200 ka can be estimated for the inner border of the Canello plain. Consistent with evidence of slow subsidence, evidence of recent vertical motions at the northern boundary of the Canello plain is subdued. Recent (Holocene) fault activity may be inferred by evidence for ponding along the fault at the northern boundary of the plain, however no striking evidence for vertical displacement has been recognised in the more recent alluvial fans, Holocene in age, that occur across the fault itself, possibly because the rate of alluvial fan deposition exceeds the rate of faulting. On the other hand, the recognition of some 1-2 m high fault scarps in the glacia (eastern part of the plain) suggests vertical motions postdating this surface, which in the distal part (i.e., where evidence for faulting occurs) is incised by the present day drainage network, and that most probably corresponds to the depositional surface of the alluvium laid during the Last Glacial. Indeed, current alluvial fan deposition is confined in the alluvial fan bodies located close to the plain borders.

Analysis of PS-InSAR data from the Cancellò plain area and adjacent topographic highs ...shows no net vertical ground motion trend in the 1992-2010 time span. In fact, the mean velocity values in the 1992-2010 time span are very low, generally varying around 0 mm/yr (Fig. 8.56).

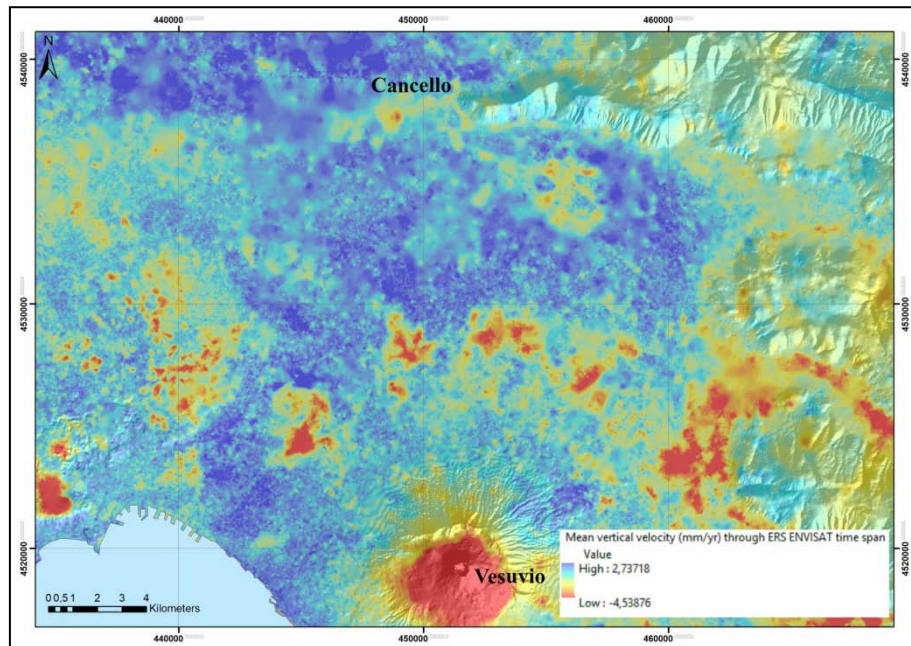


Fig. 8.56 Vertical mean velocity all along ERS - ENVISAT time span (1992-2010) in the Cancellò Plain.

The vertical velocity values obtained by geostatistical analysis of data from the topographic highs that surround the Cancellò plain are affected by the low density of PSs that are available in these areas. However, they mainly fall in a narrow range around 0 mm/yr, thus not allowing identification of a vertical motion trend. A subsiding area characterised by a “spotty” pattern is recognised in the central part of the plain. For that subsidence an anthropic contribution related to the construction of buildings and infrastructures (as it is inferred from the occurrence of rectilinear anomalous values, aligned with traces of the highways, that is visible in Fig. 8.56), and/or water extraction, may be envisaged as the major controlling factor. In general, no clear evidence of current, tectonically driven subsidence of the Cancellò graben is found in the 20 year-long time window investigated with this study. Such evidence could be related to effective absence of tectonic subsidence. Alternatively, it might be the effect of subsidence too slow to be detected by remotely sensed data. Indeed, the “geologically-estimated” mean subsidence rate evaluated for the last 200 ka (0.15 mm/yr) is very low and, assuming it as constant over the analysed time window, substantially comparable to the “around 0 mm/yr” mean velocity value estimated in most of the Cancellò plain.

PS data analysis of the Volturno plain points to a behaviour of the northern sector of the Campania plain different from that from the Cancellò plain area. It highlights a marked subsidence of the Volturno plain over the investigated time span, with vertical velocity reaching mean values between -2,0 and - 6,0 mm/yr in the 1992-2010 interval (Fig. 8.57).

Current subsidence of the Volturno river plain has been recently related to water extraction and/or compaction of the uppermost (Holocene) layers of the basin fill (Aucelli et al., 2017; Matano et al., 2018). However, the spatial distribution of the negative vertical velocity values (that covers the area bounded by rectilinear scarps) and the substantial homogeneity of estimated mean vertical velocities allow considering water extraction as possibly contributing to small-scale, localised accelerated subsidence phenomena within the wider, large-scale subsidence that has been detected. In general, most of the subsiding sector of the Volturno plain surface lacks urbanization: it is characterised by few and sparse, isolated buildings with the exception of the coastal belt, where large settlements and villages have been built in the last 40-50 yr. Worthy to note, the coastal belt is also the portion of the Volturno plain where highest negative velocity values are estimated by PS data in the 1992-2010 time span, and this suggests a correlation between fast subsidence and urbanization, pointing to an anthropic contribution to subsidence of the coastal area. Such an area is also the one in which thickness of the Holocene sediments is larger (c. 30 m) than elsewhere in the study area, as it is inferred from the post-C.I. fill of the basin (Fig. 8.57). Such an information allows identifying the coastal belt as an area prone to subsidence controlled by

compaction of fine grained Holocene sediments, which are composed by variable amounts of sands but also by silts and lagoonal clays with 1-2 m thick peat layers (Amorosi et al., 2012). Conversely, sediment compaction cannot be considered as a driving factor of subsidence recorded in the remaining part of the plain, where: (1) only sparse buildings occur; (2) thickness of the Holocene – possibly unconsolidated - sediments decreases to only 10-20 m (Fig. 8.57); (3) the fine-grained component of Holocene sediments decreases in favour of coarser alluvial sediments.

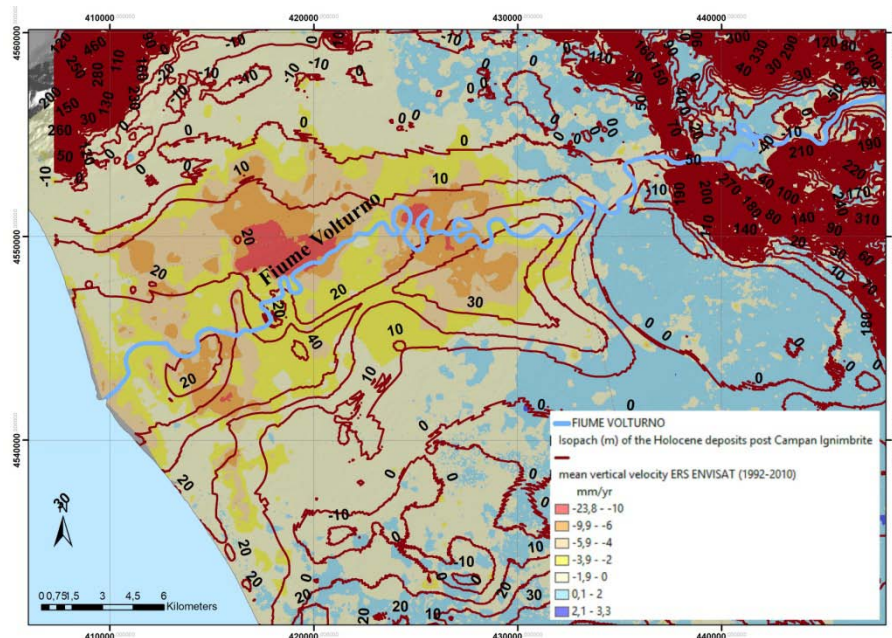


Fig. 8.57 Comparison between isopach map (brown polyline) of Holocene deposits post Campana Ignimbrite and Vertical mean velocity all along ERS - ENVISAT time span (1992-2010)

Comparison of data from the PS analysis and geomorphological analysis shows that the perimeter of the area that is subject to current negative vertical motion is defined by straight – fault – scarps formed in the C.I. deposits (and correlative alluvial fan/colluvial deposits). Such a coincidence suggests a tectonic control on current subsidence of the Volturno plain. In particular, current subsidence appears as a response to activity of: (1) the structure that has been identified – through seismic stratigraphy (e.g., Mariani and Prato, 1988)- as the master fault of the Campania Plain graben, that is to say the WSW-ENE trending faults located at the base and piedmont of Mt. Massico ridge; (2) c. E-W trending faults located at the northern edge of the plain; (3) of NW-SE trending structure at the eastern boundary of the Holocene alluvial plain. Consistent with evidence from PS-InSAR analysis, Holocene (current?) differential vertical motions along the scarp at the NE boundary of the plain are inferred from the incision/deposition dynamics of the Volturno river. Moreover, Analysis of topography of the Volturno plain has also shown evidence that the northern part of the plain (i.e., the sector to the north of the Volturno river bed) is less elevated than the southern part and has higher values of vertical velocity (-12 mm/yr; Fig. 8.57). Such evidence might suggest northward tilting of the alluvial plain, while the features of the , or differential motions between sectors within the plain . Volturno river pattern suggest the occurrence of differential vertical motions along faults transverse to the river path. Comparison with subsurface geology data, which shows the occurrence of NW-SE rectilinear steps affecting the buried C.I. top surface, suggests late Holocene subdued vertical motions along NW-SE trending faults that cross the plain.

Consistent with geomorphological evidence of Holocene displacements, seismic stratigraphy data highlight the presence of faults in the offshore the Volturno river outlet that dissect post-LGM seismic layers (Misuraca et al., 2018).

The long-term history of the Volturno plain graben points to a > 2 mm/yr mean subsidence rate in the Early Pleistocene p.p. to Present time span (i.e., in the last 1.5 Ma) of the central-western part of the plain (inferred from deep wells, e.g., Brancaccio et al., 1991). Former studies relate filling of the plain and coastal progradation to increasing aggradation (mostly due to volcanoclastic deposition) and decreasing subsidence in the Middle Pleistocene to Holocene time span (Brancaccio et al., 1991; 1995; Romano et al., 1994). However, age data from shallow wells (borehole S. Marcellino, in Romano et al., 1994;

borehole SME in Santangelo et al., 2010, and the recently drilled core AP) indicate – in the last c. 100-200 ka - faster subsidence of the central part of the Volturno plain with respect to slower subsidence (in the 0.15-0.2 mm/y range) of the northeastern boundary of the Volturno plain area (the belt mapped as glacis) and the Canello plain areas. Consistent with these long-term evaluations of subsidence, the PS SAR data point to the Canello plain and the glacis to the NE of the Volturno plain as substantially stable, and the Volturno plain as subsiding with c. 1 mm/y rate in the 1992-2010 time span.

8.7 Discussion and Concluding remarks

PS SAR data analysis of the northern Campania plain graben has allowed distinguishing the current behaviour of the Holocene alluvial plain constructed by the Volturno river from the remaining part of the plain. In particular, the piedmont belts of the Volturno river plain and the Canello plain appear as essentially stable areas, while Volturno alluvial plain is currently subject to subsidence. The tectonically-driven of the Volturno plain hypothesised with this study implies current activity of faults at the northern and eastern border of the plain. However, in the historical record no evidence of large earthquakes located in the Volturno plain is reported. This suggests that faults at the boundaries of the subsiding area might be subject to creeping and/or that vertical displacement are accomplished through scarce and low-energy seismicity along the northern border of the plain, which has been highlighted in a recently published paper (Luiso et al., 2018).

CHAPTER 9 - CONCLUDING REMARKS

The core of the study herein has been the analysis of PS SAR datasets aimed at providing new constraints to the active tectonics framework, and seismotectonics, of several regions of the Apennines. The analysed Permanent Scatterers datasets result from processing of large amounts of temporally continuous series of radar images acquired with the ERS (1992-2000), ENVISAT (2003-2010) and COSMO SKYMED (2011-2014) satellite missions.

With this study, a massive use of Permanent Scatterer datasets is applied for the first time at assessment of ground deformation of large (hundreds of km² wide) regions of Italy over the last decades, in order to unravelling their current tectonic behaviour. To date in the field of tectonics – in particular, of earthquake geology - the SAR images have been used essentially through the *DinSAR* technique (comparison between two images, acquired pre- and post-event) in order to constrain the co- and post-seismic deformation (e.g., Massonet et al., 1993; Peltzer et al., 1996, 1998; Stramondo et al., 1999; Atzori et al., 2009; Copley and Reynolds, 2014), while the approach that has been used in the case studies that are the object of the research herein is based on analyses of data that (with the exception of the Lunigiana case study) cover an about 20-year long time window. The opportunity of analysing so long, continuous SAR records has allowed detection of both coseismic displacement of moderate earthquakes (i.e., the M 6.3 2009 L'Aquila earthquake, and the M 5 2013 Lunigiana earthquake), and subdued ground displacements - and acceleration – on time scale ranging from yearly to decades.

The specific approach used in this study rests on a combination of various techniques of analysis and processing of the PS SAR datasets. In general, as the analyses that have been carried out aimed at identifying motion values with wide areal extent, a statistical filtering has been applied to PSs velocity values in order to discard from the initial, “native”, dataset fast-moving PSs that may be associated with the occurrence of local-scale phenomena (e.g., landslides, sediment compaction, water extraction, etc.). Furthermore, an in depth inspection of time series of PSs from all of the investigated areas has been carried out with the aim of identifying changing (LoS-oriented) motion trends over the analysed time windows.

A distinctive feature of this study was the estimation of vertical ground displacements. In fact, while most studies on ground deformation are based on analysis of SAR data recorded along either ascending or descending satellite orbits (thus based on LoS-oriented motions), a specific focus of this study was to obtain - starting from LoS-oriented PS velocity values - displacement values in the vertical plane oriented west-east. In order to evaluate vertical displacements, a geometrical relationship was applied to ascending - descending PSs pairs. As PS from ascending and descending tracks are neither spatially coincident nor synchronous, each image pair was obtained by selecting ascending-descending radar images with a time separation within one month. In the L'Aquila region case study, the combination of data recorded along both the ascending and descending satellite orbits has been crucial to the identification of pre-seismic ground motions, undetected in previous works that – similarly – had addressed assessment of possible pre-seismic satellite-recorded signals.

In the various case studies, different kinds of GIS-aided geostatistical analyses were used to extract and synthesise information on ground deformation through the construction of both raster maps of displacement values for the ascending and descending LoS, respectively, and maps of the vertical (z, up - down) component of the “real” displacement vector.

In the Campania plain case study, the PS SAR data analysis and processing have been integrated by detail scale geomorphological-stratigraphical analysis. Results of analyses of the two independent data sets are consistent, and point to tectonically-controlled ground displacements in a large part of the northern part of the study area (Volturno plain) during the 1992-2010 analysed time span. In particular, the integrated data sets show that the boundaries of the area affected by current subsidence follow fault scarps formed in the 39 ka old Campania Ignimbrite, while the horst blocks of such faults are substantially stable (or slightly uplifting) during the analysed time window.

Furthermore, mean rates of current subsidence and long-term (Late Pleistocene to present) mean subsidence rates are comparable, pointing to current vertical displacement assessed through the PS SAR data analysis as the expression of the recent tectonics of the analysed sectors of the Campania plain. The Campania plain substantially lacks strong historical seismicity. Such evidence suggests that the detected surface displacements result at least in part from aseismic fault activity.

The Monte Marzano case study has allowed assessment of subdued deformation along both the major structures that were activated with the Irpinia 1980 earthquake, i.e. the NE-dipping Monte Marzano fault and the SW-dipping Conza fault, respectively. Ground deformation associated with such structures

appears decreasing from the time window covered by the ERS satellites (1992-2000) to that covered by the ENVISAT (2003-2010). These data suggest that post-seismic slip of the M 6.9 has continued until 20 years after the main shock to become very weak in the following ten years. Furthermore, the PS SAR data analysis has shown that wide areas located between the Monte Marzano and Conza faults (i.e., in the one that is recognised as the graben structure bounded by those structures) show uplift in the range of 0-2 mm/yr, more evident in the period surveyed by the ERS satellites (1992-2000) and less evident in the 2003-2010 time span (ENVISAT). Such uplift might be related to the occurrence, at depth, of a fluid reservoir that has been independently identified by seismic tomography (Amoroso et al., 2014).

In depth analysis of pre-seismic periods have been carried out in three study areas, i.e. those of the 1997 Colfiorito earthquake, of the 2009 L'Aquila earthquake and of the 2013 Lunigiana earthquake.

The Colfiorito case study has not provided any significant information on possible pre-seismic ground deformation, most probably due to the PS spatial distribution in that region too much discontinuous to allow identification of both net signals from inspection of the rare and sparse PS time series, and statistically meaningful surface displacement patterns.

Both in the L'Aquila and Lunigiana case studies, ground deformation signals in the pre-seismic period have been detected from inspection of PS time series. Pre-seismic ground deformation signals detected in the Lunigiana area (which was affected by a strike-slip faulting earthquake; Eva et al., 2014, Pezzo et al., 2014, Stramondo et al., 2014) are questionable, as they are quite complex and difficult to be interpreted and framed within the local tectonic scenario.

Conversely, very clear and net pre-seismic signals have been identified in the region hit by the L'Aquila normal faulting earthquake. There, in the time span predating of some four years the 6th April 2009 main shock, ground deformation with distinct spatial patterns, and orientations, have been detected. In particular, the PS SAR analysis has shown that the hanging wall block of the Paganica fault (the surface expression of the structure activated with the main shock; e.g., Galli et al., 2010) has been subject to slow uplift and eastward horizontal motion from 2005 to September/October 2008, and then (October 2008-March 2009) subject to subsidence and westward oriented horizontal motion. Following coseismic collapse, in the early post-seismic period (April-May 2009), subsidence extended eastwards beyond the Paganica fault trace.

The region affected by opposite pre-seismic motions covers the area in which the 6th April main shock and most of both foreshocks and aftershocks (Valoroso et al., 2013) were recorded, while the inversion of the pre-seismic displacements is coeval with onset of the foreshocks (October 2008; Di Luccio et al., 2010). In addition, such a region includes both topographic highs and lows. All of such features point to a correlation of the detected motions with the seismic phenomena, and suggest a deep-seated causative mechanism, such as volume changes in response to vertical/lateral fluids migration and fracturing processes at depth, with all phenomena having been documented in connection with the 2009 earthquake in the study region (e.g., Di Luccio et al., 2010; Lucente et al., 2010; Moro et al., 2017).

Pre-seismic ground deformation that has been detected in the L'Aquila region could represent a precursor signal of the 2009, M 6.3 earthquake. Such a hypothesis should be tested, in the future, through the continuous monitoring through SAR satellites, but also high-resolution geodetic techniques, of seismically active regions worldwide aimed at detecting the possible occurrence of pre-seismic signals.

However, the results of this study point to the long-term (yearly scale) PS SAR technique as a tool crucial to the detection of ground deformation in areas struck by recent earthquakes, and to monitoring active – possibly aseismic - structures. Such knowledge may strongly support strategies addressed at territorial planning and mitigation of seismic hazard, and represent an important sustenance for actions ruled by Civil Protection. On the other hand, the results of this study highlight the importance of the existing PS database, and the importance of continuing implementing such an instrument in the future.

The advent of space-based geodetic measurements has allowed these surveys to be done more frequently, more densely, more precisely, and over larger areas of the world .

Earthquake cycle lasts on the order of 100, 200, 1000 or more years. We have just two decades of space geodesy and thus, we are trying to understand a finite process, sampling in quasi real time the surface effects of on-going structural processes via space-based geodesy by sampling just 1/10th to one 1/100th of the smallest significant unit of that process (i.e., the earthquake cycle) (Allmendinger et al., 2009).

REFERENCES

- Accordi B., 1966. La componente traslativa nella tettonica dell'Appennino laziale-abruzzese. *Geologica Romana*, 5: 355-406.
- Accordi G., Carbone F., 1988. Sequenze carbonatiche meso-cenozoiche. In: G. Accordi, F. Carbone, G. Civitelli, L. Corda, D. De Rita, D. Esu, R. Funicello, T. Kotsakis, G. Mariotti, A. Sposato (eds.), *Note illustrative alla Carta delle litofacies del Lazio-Abruzzo ed aree limitrofe*. *La Ricerca Scientifica, Quaderni*, 114 (5): 11-92.
- Achache J., Fruneau B., and Delacourt C.; 1995: Applicability of SAR Interferometry for Monitoring of Landslides. *ERS Applications, Proc. Second Int. Workshop*, 6-8 December 1995, London, p.165.
- Aiello G., Ascione A., Barra D., Munno R., Petrosino P., Russo Ermolli E., Villani F., 2007. Evolution of the late Quaternary San Gregorio Magno tectono-karstic basin (southern Italy) inferred from geomorphological, tephrostratigraphical and palaeoecological analyses: tectonic implications. *Journal of Quaternary Science*, 22(3), 233–245.
- Alfonsi L., Funicello R., Girotti O., Mattei M., Maiorani A., Preite Martinez M., Trudu C., Turi B., 1991. Structural and geochemical features of the Sabina strike-slip fault (Central Apennines). *Bollettino della Società Geologica Italiana*, 110: 217-230.
- Allmendinger R. W., Loveless J. P., Pritchard, M. E., Meade B., 2009. "From Decades to Epochs: Spanning the Gap Between Geodesy and Structural Geology of Active Mountain Belts". *Geosciences: Faculty Publications*. 19. https://scholarworks.smith.edu/geo_facpubs/19
- Amato A., 2000. Estimating Pleistocene tectonic uplift rates in South-eastern Apennines (Italy) from erosional land surfaces and marine terraces. In Slaymaker, O. (eds.) *Geomorphology, Human Activity and Global Environmental Change*, Wiley, Chichester, UK, pp. 67 – 87.
- Amato A., Cinque A., Santangelo N., Santo A., 1992. Il bordo meridionale del massiccio del Monte Marzano e la valle del Fiume Bianco: geologia e geomorfologia. *Studi Geologici Camerti, Spec. Vol.* 1992/1, 191-200.
- Amato A., Selvaggi G., 1993. Aftershock location and P-wave velocity structure in the epicentral region of the 1980 Irpinia earthquake: *Annali di Geofisica*, 36(1), 3–15.
- Amato, A., Montone P., 2007. Present-day stress field and active tectonics in southern peninsular Italy. *Geophysical Journal International*, 130(2), 519–534, <http://dx.doi.org/10.1111/j.1365-246X.1997.tb05666.x>.
- Amicucci L., Barchi M.R., Montone P., Rubiliani N., 2008. The Vallo di Diano and Auletta extensional basins in the southern Apennines (Italy): a simple model for a complex setting. *Terra Nova*, 20, 475–482.
- Amore O., Bonardi G., Ciampo G., De Capoa P., Perrone V., Sgrosso I., 1988. Relazioni tra “flysch interni” e domini appenninici: reinterpretazione delle formazioni di Pollica, San Mauro e Albidona e il problema dell'evoluzione inframiocenica delle zone esterne appenniniche. *Mem. Soc. Geol. Ital.*, 41, 285–299.
- Amore O., Bonardi G., Di Staso A., Ciampo G., De Capoa P., Morabito S., Ruggiero E., Sgrosso I., 2005. The progress of knowledge about the Miocene successions of the Southern Apennines following Selli's papers of 1957 and 1962. *Boll. Soc. Geol. Ital.*, 4, 37–44.
- Amorosi A., Molisso F., Pacifico A., Rossi V., Ruberti D., Sacchi M., Vigliotti M., 2013. The Holocene evolution of the Volturno River coastal plain (southern Italy). *J. Medit. Earth Sci. Special Issue* 7-11.
- Amorosi A., Pacifico A., Rossi V., Ruberti D., 2012. Late Quaternary incision and deposition in an active volcanic setting: The Volturno valley fill, southern Italy. *Sed. Geol.* 282, 307–320.
- Amoroso O., Ascione A., Mazzoli S., Virieux J., Zollo A., 2014. Seismic imaging of a fluid storage in the actively extending Apennine mountain belt, southern Italy. *Geophysical Research Letters*, 41, 3802-3809, doi:10.1002/2014GL060070.

- Amoroso O., Russo G., De Landro G., Zollo A., Garambois S., Mazzoli S., Parente M., Virieux J., 2017. From velocity and attenuation tomographies to rock physical modeling: inferences on fluid-driven earthquake processes at the Irpinia fault system in Southern Italy. *Geophysical Research Letters*, 44, 6752–6760, doi:10.1002/2016GL072346.
- Amoruso A., Crescentini L., Scarpa R., 2005. Faulting geometry for the complex 1980 Campania-Lucania earthquake from levelling data. *Geophysical Journal International*, 162, 156–168.
- Amoruso, A. and Crescentini, L.; 2010: Limits on earthquake nucleation and other pre-seismic phenomena from continuous strain in the near field of the 2009 L'Aquila earthquake. *Geophys. Res. Lett.*, 37, L10307, doi:10.1029/2010GL043308.
- Anelli L., Gorza M., Pieri M., Riva M., 1994. Subsurface well data in the Northern Apennines. *Memorie della Società Geologica Italiana*, 48: 461-471.
- Anselin L., 1995, Local indicators of spatial association – LISA. *Geographical Analysis* 27, 93-115.
- Anzidei M., Boschi E., Cannelli V., Devoti R., Esposito A., Galvani A., Melini D., Pietrantonio G., Riguzzi F., Sepe V. and Serpelloni E.; 2009: Coseismic deformation of the destructive April 6, 2009 L'Aquila earthquake (central Italy) from GPS data, *Geophys. Res. Lett.*, 36, L17307, doi:10.1029/2009GL039145.
- Aprile F., Ortolani F., 1978: Nuovi dati sulla struttura profonda della piana campana. *Boll. Soc. Geol. It.*, 97, 591-608.
- Aprile F., Toccaceli R.M., Sbrana A., 2004. Il ruolo dei depositi piroclastici nell'analisi cronostratigrafica dei terreni quaternari del sottosuolo della Piana Campana. *It. J. Quat. Sci.* 17, 547-554.
- Argnani A., Artoni A., Ori G.G., Roveri M., 1991. L'avanfossa centro-adriatica: Stili strutturali e sedimentazione. *Studi Geologici Camerti*, vol. spec., 1991/1: 371-381.
- Argnani A., Bortoluzzi G., Bozzani A., Canepa A., Ligi M., Palumbo V., Serracca P., Trincardi F., 1989. Sedimentary dynamics on the Eastern Tyrrhenian Margin, Italy. PS/87 Cruise report. *Giorn. Geol.* 51, s. III, 1, 165-178.
- Argnani A., Bortoluzzi G., Bozzani A., Canepa A., Ligi M., Palumbo V., Serracca P., Trincardi F., 1989. Sedimentary dynamics on the Eastern Tyrrhenian Margin, Italy. PS/87 Cruise report. *Giorn. Geol.* 51, s. III, 1, 165-178.
- Argnani A., Barbacini G., Bernini M., Camurri F., Ghielmi M., Papani G., Rizzini F., Rogledi S., Torelli L., 2003, Gravity tectonics driven by Quaternary uplift in the Northern Apennines: insights from the La Spezia-Reggio Emilia geo-transect. *Quaternary International Volumes 101–102*, 2003, Pages 13-26. [https://doi.org/10.1016/S1040-6182\(02\)00088-5](https://doi.org/10.1016/S1040-6182(02)00088-5)
- Arnaud A., Adam N., Hanssen R., Inglada J., Duro J., Closa J., Eineder M., 2003, ASAR ERS interferometric phase continuity. *IGARSS 2003*, Toulouse, France, 21–25 July, 2003
- Ascione A., Caiazzo, C., Cinque, A., 2007. Recent faulting in Southern Apennines (Italy): geomorphic evidence, spatial distribution and implications for rates of activity. *Bollettino della Società Geologica Italiana* 126, 293–305.
- Ascione A., Ciarcia, S., Di Donato, V., Mazzoli, S., Vitale S., 2012. The Pliocene-Quaternary wedge-top basins of southern Italy: an expression of propagating lateral slab tear beneath the Apennines. *Basin Research*, 24, 456–474, doi:10.1111/j.1365-2117.2011.00534.x.
- Ascione A., Cinque A., 1999. Tectonics and erosion in the long-term relief history of Southern Apennines (Italy). *Zeitschrift für Geomorphologie, Suppl.-Bd.*, 117, 1-15.

- Ascione A., Cinque A., Improta L., Villani F., 2003. Late Quaternary faulting within the Southern Apennines seismic belt: new data from Mt. Marzano area (Southern Italy). *Quaternary International*, 101–102, 27–41.
- Ascione A., Cinque A., Miccadei E., Villani F., Berti C., 2008. The Plio-Quaternary uplift of the Apennine chain: new data from the analysis of topography and river valleys in Central Italy. *Geomorphology*, 102(1), 105–118.
- Ascione A., Cinque A., Santangelo N., Tozzi, M., 1992a. Il Bacino del Vallo di Diano e la tettonica trascorrente plio-quadernaria: nuovi vincoli cronologici e cinematici. *Studi Geologici Camerti, Spec. Vol. 1992 / 1*, 201–208.
- Ascione A., Cinque A., Tozzi M., 1992b La Valle del Tanagro (Campania): una depressione strutturale ad evoluzione complessa. *Studi Geologici Camerti, Spec. Vol. 1992 / 1*, 209–219.
- Ascione A., Ciotoli G., Bigi S., Buscher J., Mazzoli S., Ruggiero L., Sciarra A., Tartarello M.C., Valente E., 2018. Assessing mantle vs. crustal sources for non-volcanic degassing along fault zones in the actively extending southern Apennines mountain belt (Italy). *Geological Society of America Bulletin*, 130 (9-10), 1697-1722, <https://doi.org/10.1130/B31869.1>
- Ascione A., Mazzoli S., Petrosino P., Valente, E., 2013. A decoupled kinematic model for active normal faults: Insights from the 1980, MS = 6.9 Irpinia earthquake, southern Italy. *Geological Society of America Bulletin*, 125, 1239–1259. doi:10.1130/B30814.1.
- Atzori S., Chiarabba C., Devoti R., Bonano M. and Lanari R.; 2013: Anomalous far-field geodetic signature related to the 2009 L'Aquila (central Italy) earthquake. *Terra Nova*, 25, 343–351, doi: 10.1111/ter.12040.
- Atzori S., Hunstad I., Chini M., Salvi S., Tolomei C., Bignami C., Stramondo S., Trasatti E., Antonioli A. and Boschi E.; 2009: Finite fault inversion of DInSAR coseismic displacement of the 2009 L'Aquila earthquake (central Italy). *Geophys. Res. Lett.*, 36, L15305, doi:10.1029/2009GL039293.
- Aucelli P.P.C., Di Paola G., Incontri P., Rizzo A., Vilardo G., Benassai G., Buonocore B., Pappone G., 2017. Coastal inundation risk assessment due to subsidence and sea level rise in a Mediterranean alluvial plain (Volturno coastal plain–southern Italy). *Estuarine, Coastal and Shelf Science*, 198, 597–609.
- Aucelli P.P.C., Di Paola G., Incontri P., Rizzo A., Vilardo G., Benassai G., Buonocore B., Pappone G., 2017. Coastal inundation risk assessment due to subsidence and sea level rise in a Mediterranean alluvial plain (Volturno coastal plain–southern Italy). *Estuarine, Coastal and Shelf Science*, 198, 597–609.
- Balducci S., Vaselli M., Verdini G., 1983. Exploration well in Ottaviano permit, Italy, Trecase 1. *European Geothermal Update 3rd Int. Sem., Munich 29 Nov-1 Dec.*, 407–418.
- Balestrieri M.L., Bernet M., Brandon M.T., Picotti V., Reiners P., Zattin M., 2003. Pliocene and Pleistocene exhumation and uplift of two key areas of the northern Apennines. *Quaternary International*, 101–102, 67–73.
- Bally A.W., Burbi L., Cooper C., Ghelardoni R., 1986. Balanced sections and seismic reflection profiles across the Central Apennines. *Memorie della Società Geologica Italiana*, 35, 257–310.
- Barberi F., Innocenti F., Lirer L., Munno R., Pescatore T., Santacroce R., 1978. The Campania Ignimbrite: a major prehistoric eruption in the neapolitan area (Italy). *Bull. Volcanol.* 41, 1, 1–22.
- Barchi M., Minelli G., Magnani B., Mazzotti A., 2003. Line CROP 03: Northern Apennines. *Mem. Descr. Carta Geol. d'It.*, 62, 127–136.
- Barchi M.R., Minelli G., Piali G., 1998. The CROP 03 profile: a synthesis of results on deep structures of the northern Apennines. *Memorie della Società Geologica Italiana*, 52, 383–400.
- Barra D., Cinque A., Gewalt M., Hurtgen C., 1991. L'ospite caldo *Sylvestra Seminis* (Bonaduce, Masoli e Pugliese, 1976) (Crustacea, Ostracoda): un possibile marker dell'ultimo interglaciale dell'area mediterranea. *Il Quaternario* 4, 2, 327–332.

- Barra D., Romano P., Santo A., Campaiola L., Roca V., Tuniz C., 1996. The Versilian transgression in the Volturno river plain (Campania, Southern Italy): Palaeoenvironmental history and chronological data. *Il Quaternario* 9, 2, 445-458.
- Bartole R., Savelli D., Tramontana M. & Wezel F.C. 1984: Structural and sedimentary features in the Tyrrhenian margin off Campania. Southern Italy. *Mar. Geol.* 55, 2/2, 163-180.
- Bartole R., Savelli D., Tramontana M. & Wezel F.C. 1984: Structural and sedimentary features in the Tyrrhenian margin off Campania. Southern Italy. *Mar. Geol.* 55, 2/2, 163-180.
- Bartolini C., Bernini M., Carloni G.C., Costantini A., Federici P.B., Gasperi G., Lazzarotto A., Marchetti G., Mazzanti R., Papani G., Pranzini G., Rau A., Sandrelli F., Vercesi P.L., Castaldini D. and Francavilla F., 1983. Carta neotettonica dell'Appennino Settentrionale. Note illustrative. *Boll. Soc. Geol. It.*, 101, 523-549.
- Bellucci F., 1994: Nuove conoscenze stratigrafiche sui depositi vulcanici del sottosuolo del settore meridionale della Piana Campana. *Boll. Soc. Geol. It.* 113, 395-420.
- Bellucci F., 1998: Nuove conoscenze stratigrafiche sui depositi effusivi ed esplosivi nel sottosuolo dell'area del Somma Vesuvio. *Boll. Soc. Geol. It.* 117, 385-405.
- Berardino P., Fornaro G., Lanari R. and Sansosti E.; 2002: A new algorithm for surface deformation monitoring based on small baseline differential SAR interferograms. *IEEE Trans. Geosci. Rem. Sens.*, 40(11), 2375-2383.
- Bernard P., Zollo A., 1989. The Irpinia (Italy) 1980 earthquake: detailed analysis of a complex normal faulting. *Journal of Geophysical Research*, 94(B-2), 1631-1648.
- Bernasconi A., Bruni P., Gorla L., Principe C. & Sbrana A. 1981: Risultati preliminari dell'esplorazione geotermica profonda nell'area vulcanica del Somma-Vesuvio. *Rend. Soc. Geol. It.* 4, 237-240.
- Bernini M., Papani G., 2002, La distensione della fossa tettonica della Lunigiana nordoccidentale (con carta geologica alla scala 1:50,000). *Boll. Soc. Geol. Ital.* 121, 313-341.
- Billi, A., Presti, D., Faccenna, C., Neri, G., Orecchio, B., 2007. Seismotectonics of the Nubia plate compressive margin in the south-Tyrrhenian region, Italy: clues for subduction inception. *Journal of Geophysical Research* 112, B08302 <http://dx.doi.org/10.1029/2006JB004837>.
- Bintanja R., van de Wal R.S.W., Oerlemans J. 2005: Modelled atmospheric temperatures and global sea levels over the past million years. *Nature* 437, 125-128.
- Blumetti A.M., Dramis F., Michetti A.M., 1993. Fault-generated mountain fronts in the central Apennines (Central Italy): Geomorphological features and seismotectonic implications. *Earth Surface Processes and Landforms*, 18(3), 203-223.
- Blumetti, A.M., Esposito, E., Ferreli, L., Michetti, A.M., Porfido, S., Serva, L. and Vittori, E., 2002, New data and reinterpretation of the November 23, 1980, M 6.9, Irpinia-Lucania earthquake (Southern Apennine) coseismic surface effects: *Studi Geologici Camerti*, 2002, 19-27.
- Bollettinari G., Panizza M., 1981. Una "faglia di superficie" presso San Gregorio Magno in occasione del sisma del 23-XI-1980: *Rendiconti della Società Geologica Italiana*, 4, 135-136.
- Bonardi G., Amore F.O., Ciampo G., De Capoa P., Micconet P., Perrone V., 1988. Il complesso Liguride *auct.*: Stato delle conoscenze e problem aperti sulla sua evoluzione pre-appenninica ed i suoi rapporti con l'Arco Calabro. *Mem. Soc. Geol. It.*, 41, 17-36.
- Bonardi G., Cavazza W., Perrone V., Rossi S., 2001. Calabria-Peloritani Terrane and Northern Ionian Sea. In: Vai, G.B., Martini, I.P. (Eds.), *Anatomy of an Orogen: The Apennines and Adjacent Mediterranean Basins*. Kluwer, Dordrecht, 287-306.

- Bonardi G., D'Argenio B., Perrone V., 1988b. Carta Geologica dell'Appennino meridionale. Mem. Soc. Geol. Ital., 41, attached map.
- Boncio P., Brozzetti F., Lavecchia G., 2000, Architecture and seismotectonics of a regional lowangle normal fault zone in central Italy. *Tectonics*, volume 19, Issue 6, Pages 1038-1055. <https://doi.org/10.1029/2000TC900023>
- Boncio, P., Pizzi, A., Brozzetti, F., Pomposo, G., Lavecchia, G., Di Naccio, D. and Ferrarini, F.; 2010: Coseismic ground deformation of the 6 April 2009 L'Aquila earthquake (central Italy, Mw 6. 3). *Geophys. Res. Lett.*, 37, L06308.
- Bosi C., Galadini F., Messina P., 1995. Stratigrafia plio-pleistocenica della conca del Fucino. *Il Quaternario*, 8(1), 83-94.
- Bosi, C., Bertini, T., 1970. Geologia della media valle dell'Aterno. *Mem. Soc. Geol. It.*, 9(4), 719-777.
- Bouillin J.-P., 1984. Nouvelle interprétation de la liaison Apennin-Maghrébides en Calabre; conséquences sur la paléogéographie téthysienne entre Gibraltar et les Alpes. *Revue de Géologie Dynamique et de Géographie Physique*, 25(5), 321–338.
- Brancaccio L., Cinque A., Romano P., Roskopf C., Russo F. & Santangelo N. 1995: L'evoluzione delle pianure costiere della Campania: geomorfologia e neotettonica. *Mem. Soc. Geogr. It.* 53, 313-337.
- Brancaccio L., Cinque A., Romano P., Roskopf C., Russo F., Santangelo N. & Santo A. 1991: Geomorphology and neotectonic evolution of a sector of the Tyrrhenian flank of the southern Apennines (region of Naples, Italy). *Zeit. fur Geom., Suppl. Bd 82*, 47-58.
- Brocchini D., Principe C., Castradori D., Laurenzi M.A., Gorla L., 2001. Quaternary evolution of the southern sector of the Campania Plain and early Somma – Vesuvius activity: insights from the Trecase 1 well. *Mineral. Petrol.* 73, 67-91.
- Broggi A., Lazzarotto A., Liotta D. (eds), 2005. Results of the CROP 18 Project. *Boll. Soc. Geol. It, Spec. Vol. 3*, 239 pp.
- Brozzetti, F., Boncio, P., Tinari, D. P., Di Naccio, D., & Torelli, L., 2007, LANFs attive e relativi meccanismi di trasferimento alla terminazione settentrionale dell'Etrurian Fault System (Lunigiana–Garfagnana, Italia). *Rendiconti della Società Geologica Italiana*, 4, 164-165.
- Bruno P.P.G., Cippitelli G., Rapolla A. 1998. Seismic study of the Mesozoic carbonate basement around Mt. Somma – Vesuvius, Italy. *J. Volcanol. Geotherm. Res.* 84, 311-322.
- Bruno P.P.G., Di Fiore V., Ventura G., 2000. Seismic study of the '41st Parallel' Fault System offshore the Campanian–Latial continental margin, Italy. *Tectonophysics* 324, 1, 37-55.
- Bürgmann R., Hilley G., Ferretti A. and Novali F.; 2006: Resolving vertical tectonics in the San Francisco Bay Area from permanent scatterer InSAR and GPS analysis. *Geology*, 34(3), 221-224.
- Butler R.W.H., Mazzoli S., Corrado S., De Donatis M., Di Bucci D., Gambini R., Naso G., Nicolai C., Scrocca D., Shiner P., Zucconi V., 2004. Applying thick-skinned tectonic models to the Apennine thrust belt of Italy: Limitations and implications. In: *Thrust Tectonics and Petroleum Systems* (Ed. by K.R. McClay). *AAPG Memoir*, 82, 647-667.
- Caiazza, C., Ascione, A., Cinque, A., 2006. Late Tertiary–Quaternary tectonics of the Southern Apennines (Italy): new evidences from the Tyrrhenian slope. *Tectonophysics*, 421, 23–51.
- Calamita F., Coltorti M., Farabollini P., Pizzi A., 1994. Le faglie normali quaternarie nella dorsale appenninica umbro-marchigiana: proposta di un modello di tettonica di inversione. *Studi Geologici Camerti*, Vol. Spec. CROP18, 211-225.

- Calamita, F., Coltorti M., Piccinini D., Pierantoni P., Pizzi A., Ripepe M., Scisciani V., Turco E., 2000. Quaternary faults and seismicity in the Umbro-Marchean Apennines (central Italy): Evidence from the 1997 Colfiorito earthquake. *J. Geodyn.*, 29, 245 – 264.
- Carmignani L., Cello G., Cerrina Feroni A., Funicello R., Klin O., Meccheri M., Patacca E., Pertusati P., Plesi G., Salvini F., Scandone P., Tortorici L., Turco E., 1981. Analisi del campo di fratturazione superficiale indotta dal terremoto Campano-Lucano del 23/11/1980. *Rendiconti della Società Geologica Italiana*, 4, 451-465.
- Carmignani L. and Kligfield R., 1990. Crustal extension in the northern Apennines: the transition from compression to extension in the Alpi Apuane core complex. *Tectonics* 9, 1275–1303
- Carminati E., Doglioni C., 2012. Alps vs. Apennines: The paradigm of a tectonically asymmetric earth. *Earth-Science Reviews*, 112, 67–96.
- Carminati E., Doglioni C., Gelabert B., Panza G., Raykova R.B., Roca E., Sabat F., Scrocca D., 2010. Evolution of the Western Mediterranean. In: Bally, A.W., Roberts, D. (Eds.), *Principles of Phanerozoic Regional Geology*, Chapter 18.4.1.
- Carnec C., Massonnet D. and King C.; 1996: Two examples of the use of SAR interferometry on displacement fields of small spatial extent. *Geophys. Res. Lett.*, 23(24), 3579-3582.
- Casciello E., Cesarano M. & Pappone G. 2006: Extensional detachment faulting on the tyrrhenian margin of the Southern Apennines contractional belt (Italy). *J. Geol. Soc. London* 163, 4, 617-629.
- Casciello E., Cesarano M. & Pappone G. 2006: Extensional detachment faulting on the Tyrrhenian margin of the Southern Apennines contractional belt (Italy). *J. Geol. Soc. London* 163, 4, 617-629.
- Cavinato G.P., Carusi C., Dall'Asta M., Miccadei E., Piacentini T., 2002. Sedimentary and tectonic evolution of Plio–Pleistocene alluvial and lacustrine deposits of Fucino Basin (central Italy). *Sedimentary Geology*, 148(1-2), 29-59.
- Cavinato G.P., De Celles P.G., 1999. Extensional basins in the tectonically bimodal central Apennines fold-thrust belt, Italy: Response to corner flow above subducting slab in retrograde motion. *Geology*, 27, 955-958.
- Cavinato G.P., Miccadei E., 1999. Plio-Pleistocene carbonate lacustrine deposits in a intramontane basin: Sulmona basins (Central Italy). In: E.H. Gierlowski-Kordesh and K.R. Kelts. “Lake basins through space and time” *A.A.P.G. Studies in Geology*, 46, 517-526.
- Cavinato G.P., Carusi C., Dall'Asta M., Miccadei E. & Piacentini T., 2002. Sedimentary and tectonic evolution of Plio-Pleistocene alluvial and lacustrine deposits of Fucino Basin (central Italy). *Sedimentary Geology* 148, 1-2, 29-59.
- Cello G., Deiana G., Ferrelì, L., Marchegiani L., Maschio L., Mazzoli S., Michetti A., Serva L., Tondi E., Vittori E., 2000. Geological constraints for earthquake faulting analysis in the Colfiorito area. *Journal of Seismology*, 4, 357–364.
- Cello G., Deiana G., Mangano P., Mazzoli S., Tondi E., Ferrelì L., Maschio L., Michetti A., Serva L., Vittori E., 1998a. Evidence for surface faulting during the September 26, 1997, Colfiorito (central Italy) earthquakes. *Journal of Earthquake Engineering*, 2, 1–22.
- Cello G., Guerra I., Tortorici L., Turco E., Scarpa R., 1982. Geometry of the neotectonic stress field in southern Italy: geological and seismological evidence. *Journal of Structural Geology*, 4, 385–393.
- Cello G., Martini N., Paltrinieri W., Tortorici L., 1989. Structural styles in the frontal zones of the southern Apennines, Italy: an example from the Molise district. *Tectonics*, 8, 753-768.
- Cello G., Mazzoli S., Tondi E., Turco E., 1997. Active tectonics in the Central Apennines and possible implications for seismic hazard analysis in peninsular Italy. *Tectonophysics* 272, 43–68.

- Cello G., Tondi E., Micarelli L., Mattioni L., 2003. Active tectonics and earthquake sources in the epicentral area of the 1857 Basilicata earthquake (southern Italy). *J. Geodyn.*, 36, 37–50.
- Centamore E., Deiana G., 1986. *Geologia delle Marche*. Studi Geologici Camerti, vol. spec., 1986/1: 1-145.
- Channell, J.E.T., D'argenio, B., Horvát, F., 1979. Adria, the African promontory, in *Mesozoic Mediterranean palaeogeography*. *Earth-Science Reviews* 15 (3), 213–292.
- Cheloni D., D'Agostino N., D'Anastasio E., Avallone A., Mantenuto S., Giuliani R., Mattone M., Calcaterra S., Gambino P., Dominici D., Radicioni F. and Fastellini G.; 2010: Coseismic and initial post-seismic slip of the 2009Mw 6.3 L'Aquila earthquake, Italy, from GPS measurements. *Geophys. J. Int.*, 181, 1539–1546.
- Cheloni D., De Novellis V., Albano M., Antonioli A., Anzidei M., Atzori S., Avallone A., Bignami C., Bonano M., Calcaterra S., Castaldo R., Casu F., Cecere G., De Luca C., Devoti R., Di Bucci D., Esposito A., Galvani A., Gambino P., Giuliani R., Lanari R., Manunta M., Manzo M., Mattone M., Montuori A., Pepe A., Pepe S., Pezzo G., Pietrantonio G., Polcari M., Riguzzi F., Salvi S., Sepe V., Serpelloni E., Solaro G., Stramondo S., Tizzani P., Tolomei C., Trasatti E., Valerio E., Zinno I. and Doglioni C.; 2017: Geodetic model of the 2016 Central Italy earthquake sequence inferred from InSAR and GPS data. *Geophys. Res. Lett.*, 44, 6778–6787, <https://doi.org/10.1002/2017GL073580>.
- Cheloni D., Giuliani R., D'Anastasio E., Atzori S., Walters R.J., Bonci L., D'Agostino N., Mattone M., Calcaterra S., Gambino P., Deninno F., Maseroli R. and Stefanelli G.; 2014: Coseismic and post-seismic slip of the 2009 L'Aquila (central Italy) MW 6.3 earthquake and implications for seismic potential along the Campotosto fault from joint inversion of high-precision levelling, InSAR and GPS data. *Tectonophysics*, 622, 168-185.
- Chiarabba C., Amato A., 1994. From tomographic images to fault heterogeneities. *Annali di Geofisica*, 37(6), 1481–1494.
- Chiarabba C., Amato A., Anselmi M., Baccheschi P., Bianchi I., Cattaneo M., Cecere G., Chiaraluce L., Ciaccio M. G., De Gori P., De Luca G., Di Bona M., Di Stefano R., Faenza L., Govoni A., Improta L., Lucente F. P., Marchetti A., Margheriti L., Mele F., Michelini A., Monachesi G., Moretti M., Pastori M., Piana Agostinetti N., Piccinini D., Roselli P., Seccia D., and Valoroso L.; 2009: The 2009 L'Aquila (central Italy) Mw 6.3 earthquake: Main shock and aftershocks. *Geophys. Res. Lett.*, 36, L18308, doi:10.1029/2009GL039627.
- Chiarabba C., Chiodini G., 2013. Continental delamination and mantle dynamics drive topography, extension and fluid discharge in the Apennines. *Geology*, 41, 715–718. doi:10.1130/G33992.1.
- Chiarabba, C., Jovane, L., Di Stefano, R., 2005. A new look to the Italian seismicity: seismotectonic inference. *Tectonophysics* 395, 251–268.
- Chiaraluce L., Ellsworth W. L., Chiarabba C., Cocco M., 2003. Imaging the complexity of an active complex normal fault system: The 1997 Colfiorito (central Italy) case study. *J. Geophys. Res.*, 108(B6), 2294, doi:10.1029/2002JB002166.
- Chiaraluce, L., Barchi M., Collettini C., Mirabella F., Pucci S., 2005. Connecting seismically active normal faults with Quaternary geological structures in a complex extensional environment: The Colfiorito 1997 case history (northern Apennines, Italy). *Tectonics*, 24, TC1002, doi:10.1029/2004TC001627.
- Chiaraluce, L., Valoroso, L., Piccinini, D., Di Stefano, R. and De Gori, P.; 2011: The anatomy of the 2009 L'Aquila normal fault system (central Italy) imaged by high resolution foreshock and aftershock locations. *J. Geophys Res.: Solid Earth*, 116, B12311, doi:10.1029/2011JB008352.
- Chiodini G., Cardellini C., Caliro S., Chiarabba C., Frondini F., 2013. Advective heat transport associated with regional Earth degassing in central Apennine (Italy). *Earth and Planetary Science Letters*, 373, 65–74, doi:10.1016/j.epsl.2013.04.009.

- Chiodini G., Cioni R., 1989. Gas geobarometry for hydrothermal systems and its application to some Italian geothermal areas. *Applied Geochemistry*, 4, 465–472, doi:10.1016/0883-2927(89)90004-8.
- Chiodini G., Frondini F., Cardellini C., Parello F., Peruzzi L., 2000. Rate of diffuse carbon dioxide Earth degassing estimated from carbon balance of regional aquifers: The case of central Apennine, Italy. *J. Geophys. Res.* 105, 8423–8434.
- Ciarapica G., Cirilli S., Martini R., Panzanelli M., Fratoni R., Salvini-Bonnard G., Zaninetti L., 1990. The Monte Facito Formation (Southern Apennines). *Bollettino della Società Geologica Italiana*, 59: 117-126.
- Ciarcia S., Mazzoli S., Vitale S., Zattin M., 2012. On the tectonic evolution of the Ligurian accretionary complex in southern Italy. *Geological Society of America Bulletin*, 123, 463-483, doi:10.1130/B30437.1.
- Ciarcia S., Vitale S., Di Staso A., Iannace A., Mazzoli S., Torre M., 2009. Stratigraphy and tectonics of an Internal Unit of the southern Apennines: implications for the geodynamic evolution of the peri-Tyrrhenian mountain belt: *Terra Nova*, 21(2), 88–96, doi:10.1111/J.1365-3121.2008.00859.X.
- Cinque A. 1991: La trasgressione versiliana nella piana del Sarno (Campania). *Geogr. Fis. Dinam. Quat.* 14, 63-71.
- Cinque A., Ascione A., Caiazzo C., 2000. Distribuzione spazio-temporale e caratterizzazione della fagliazione quaternaria in Appennino meridionale. In Galdini, F., Meletti, C., Rebez, A. (eds.), *Le ricerche del GNDT nel campo della pericolosità sismica (1996 e 1999)*. CNR-GNDT, Roma, p. 107-136.
- Cinque A., Irollo G., 2004. Il “vulcano di Pompei”: nuovi dati geomorfologici e stratigrafici. *It. J. Quat. Sci.* 17, 1, 101-116.
- Cinque A., Lambiase S., Sgrosso I., 1981. Su due faglie nell’alta valle del Sele legate al terremoto del 23.11.1980: *Rendiconti della Società Geologica Italiana*, 4, 127-129.
- Cinque, A., Patacca, E., Scandone, P., Tozzi, M., 1993. Quaternary kinematic evolution of the Southern Apennines. Relationships between surface geological features and deep lithospheric structures. *Annali di Geofisica*, 36, 249–260.
- Cipollari P., Cosentino D., 1992. La linea Olevano-Antrodoco: contributo della biostratigrafia alla sua caratterizzazione cinematica. *Studi Geologici Camerti*, vol. spec., 1991/2: 143-149.
- Cipollari P., Cosentino D., 1995. Miocene unconformities in the Central Apennines: geodynamic significance and sedimentary basin evolution. *Tectonophysics*, 252: 375-389.
- Cippitelli G., 2007. The CROP-04 seismic profile. Interpretation and structural setting of the Agropoli-Barletta Geotraverse, in Mazzotti A., Patacca E., Scandone P., eds., *CROP-04*. *Bollettino della Società Geologica Italiana*, 7, 267-281.
- Cirella A., Piatanesi A., Cocco M., Tinti E., Scognamiglio L., Michelini A., Lomax A. and Boschi E.; 2009: Rupture history of the 2009 L'Aquila (Italy) earthquake from non-linear joint inversion of strong motion and GPS data. *Geophys. Res. Lett.*, 36, L19304, <https://doi.org/10.1029/2009GL039795>.
- Cliff A. D. and J. K. Ord, 1973. *Spatial Autocorrelation*. London: Pion.
- Cocco, M. and Pacor, F., 1993, The rupture process of the 1980, Irpinia, Italy earthquake from the inversion of strong motion waveforms: *Tectonophysics*, 218, 157–177.
- Cocco, M., Chiarabba, C., Di Bona, M., Selvaggi, G., Margheriti, L., Frepoli, A., Lucente, F.P., Basili, A., Jongmans, D., Campillo, M., 1999. The April 1996 Irpinia seismic sequence: evidence for fault interaction: *Journal of Seismology*, 3, 105–117.
- Colacicchi R., Praturlon A., 1965. Stratigraphical and paleogeographical investigations on the Mesozoic shelf-edge facies in eastern Marsica (Central Apennines, Italy). *Geologica Romana*, 4: 89-118.

- Colesanti C., Ferretti A., Prati C., Rocca F., 2003, Monitoring landslides and tectonic motions with the Permanent Scatterers Technique, *Engineering Geology*, 68, 3-14
- Copley, A., and K. Reynolds (2014), Imaging topographic growth by long-lived postseismic afterslip at Sefidabeh, east Iran, *Tectonics*, 33, 330–345, doi:10.1002/2013TC003462.
- Corrado S., Aldega L., Di Leo P., Giampaolo C., Invernizzi C., Mazzoli S., Zattin M., 2005. Thermal maturity of the axial zone of the southern Apennines fold-and-thrust belt (Italy) from multiple organic and inorganic indicators. *Terra Nova*, 17, 56-65.
- Corrado S., Cosentino D., Gioia C., 1990. Sistema di retroscorrimenti nella Marsica orientale (Abruzzo, Appennino centrale). *Memorie della Società Geologica Italiana*, 45 (1): 591-603.
- Corrado S., Di Bucci D., Naso G., Butler R. W. H., 1997. Thrusting and strike-slip tectonics in the Alto Molise region (Italy): implications for the Neogene-Quaternary Evolution of the Central Apennine Orogenic System. *Journal of the Geological Society of London*, 154 (4): 679-688.
- Corrado S., Invernizzi C., Aldega L., D'Errico M., Di Leo P., Mazzoli S., Zattin M., 2010. Testing the validity of organic and inorganic thermal indicators in different tectonic settings from continental subduction to collision: the case history of the Calabria–Lucania border (Southern Apennines, Italy). *Journal of the Geological Society of London*, 167, 985–999, <http://dx.doi.org/10.1144/0016-76492009-137>.
- Corrado S., Invernizzi C., Mazzoli S., 2002. Tectonic burial and exhumation in a foreland fold and thrust belt: the Monte Alpi case history (Southern Apennines, Italy). *Geodinamica Acta*, 15, 159–177.
- Corrado S., Miccadei E., Parotto M., Salvini F., 1995. Evoluzione tettonica del settore di Montagna Grande (Appennino centrale): il contributo di nuovi dati geometrici, cinematici e paleogeotermici. *Bollettino della Società Geologica Italiana*, 115: 325-338.
- Corsini A., Farina P., Antonello G., Barbieri M., Casagli N., Coren F., Guerri L., Ronchetti F., Sterzai P. and Tarchi D., 2006: Space-borne and ground-based SAR interferometry as tools for landslide hazard management in civil protection. *Int. J. Rem. Sens.*, 27(12), 2351-2369.
- Cosentino D., Parotto M., 1992. La struttura a falde della Sabina (Appennino centrale). *Studi Geologici Camerti*, vol. spec., 1991/2: 381-387.
- Costantini M., Falco S., Malvarosa F. & Minati F., 2008, A new method for identification and analysis of persistent scatterers in series of SAR images. *Proceedings of International Geoscience and Remote Sensing Symposium*, 7-11 July 2008. Boston MA. pp. 449-452.
- Costantini M., Falco S., Malvarosa F., Minati F. & Trill F., 2009, Method of Persistent Scatterers Pairs (PSP) and High Resolution SAR Interferometry. *Proceedings of International Geoscience and Remote Sensing Symposium* 12-17 July 2009. Cape Town, South Africa.
- Costantini M., Ferretti A., Minati F., Falco S., Trillo F., Colombo D., Novali F., Malvarosa F., Mammone F., Vecchioli F., Rucci A., Fumagalli A., Allievi J., Ciminelli M.G. and Costabile S.; 2017: Analysis of surface deformations over the whole Italian territory by interferometric processing of ERS, Envisat and COSMO-SkyMed radar data. *Rem. Sens. Environ.*, 202, 250-275.
- Coward M.P., De Donatis M., Mazzoli S., Paltrinieri W., Wezel F.C., 1999. Frontal part of the northern Apennines fold and thrust belt in the Romagna-Marche area (Italy): Shallow and deep structural styles. *Tectonics*, 18, 3: 559-574.
- Cresta S., Monechi S., Parisi G., 1989. Stratigrafia del Mesozoico e Cenozoico nell'area Umbro-marchigiana. *Memorie Descrittive della Carta Geologica d'Italia*, 39: 1-182.

- Crosetto M., Crippa B., Biescas E., 2005. Early detection and in-depth analysis of deformation phenomena by radar interferometry. *Eng Geol*, 79 (1-2), pp. 81-91.
- Cucci, L., Pondrelli, S., Frepoli, A., Mariucci, M.T., Moro, M., 2004. Local pattern of stress field and seismogenic sources in the Pergola–Melandro Basin and the Agri Valley (Southern Italy). *Geophysical Journal International*, 156 (3), 575–583, doi:10.1111/j.1365-246X.2004.02161.x.
- Curlander J.C. and McDonough R. N., *Synthetic aperture radar : systems and signal processing*, 1991, New York : Wiley series in remote sensing, c1991. XVII, 647.
- D'Agostino N., Cheloni D., Fornaro G., Giuliani R. and Reale D.; 2012: Space-time distribution of afterslip following the 2009 L'Aquila earthquake. *J. Geophys. Res.*, 117, B02402.
- D'Agostino N., Jackson J.A., Dramis F., Funicello R., 2001. Interactions between mantle upwelling, drainage evolution and active normal faulting: an example from the central Apennines (Italy). *Geophysical Journal International*, 147, 475–497.
- D'Agostino N., Selvaggi G., 2004. Crustal motion along the Eurasia–Nubia plate boundary in the Calabrian Arc and Sicily and active extension in the Messina Straits from GPS measurements. *Journal of Geophysical Research*, 109, B11402 <http://dx.doi.org/10.1029/2004JB002998>.
- D'Addezio, G., Pantosti, D. and Valensise, G., 1991, Paleoearthquakes along the Irpinia fault at Pantano di San Gregorio Magno (southern Italy): *Il Quaternario*, 4(1a), 121-136.
- D'Alessandro L., Miccadei E. & Piacentini T., 2003. Morphostructural elements of central-eastern Abruzzi: contributions to the study of the role of tectonics on the morphogenesis of the Apennine chain. *Quaternary International* 101-102, 115-124.
- D'Argenio B., Pescatore T., Scandone P., 1973. Schema geologico dell'Appennino meridionale (Campania e Lucania). In: *Moderne vedute sulla Geologia dell'Appennino*. Convegno (Roma, 16-18 febbraio 1972). *Problemi attuali di Scienza e di Cultura*, Quaderno 183, Accademia Nazionale dei Lincei, Roma: 49-72.
- Dallmeyer R.D. and Liotta D., 1998. Extension, uplift of rocks and cooling ages in thinned crustal provinces: the Larderello geothermal area (inner Northern Apennines, Italy). *Geological Magazine*, 135, 193-202.
- Damiani A.V., Chiocchini M., Colacicchi R., Mariotti G., Parotto M., Passeri L., Praturlon A., 1992. Elementi litostratigrafici per una sintesi delle facies carbonatiche meso-cenozoiche dell'Appennino centrale. *Studi Geologici Camerti*, vol. spec., 1992/2: 187-213.
- De Donatis M., Invernizzi C., Landuzzi A., Mazzoli S., Potetti M., 1998. CROP 03: Structure of the Montecalvo in Foglia-Adriatic Sea segment. *Memorie della Società Geologica Italiana*, 52: 617-630.
- De Matteis R., Matrullo E., Rivera L., Stabile T.A., Pasquale G., Zollo A., 2012, Fault Delineation and Regional Stress Direction from the Analysis of Background Microseismicity in the southern Apennines, Italy: *Bulletin of the Seismological Society of America*, 102(4), 1899–1907, doi:10.1785/0120110225.
- De Vivo B., Rolandi G., Gans P.B., Calvert A., Bohron W.A., Spera F.J., Belkin H.E. 2001: New constraints on the pyroclastic eruptive history of Campania volcanic Plain (Italy). *Mineral. Petrol.* 73, 47-65.
- Deino A.L., Orsi G., Piochi M., de Vita S., 2004. The age of the Neapolitan Yellow Tuff caldera-forming eruption (Campi Flegrei caldera—Italy) assessed by $^{40}\text{Ar}/^{39}\text{Ar}$ dating method. *J. Volcanol. Geotherm. Res.*, 133, 157–170.
- Deino A.L., Southon I., Terrasi F., Campajola L., Orsi G., 1994. ^{14}C and $^{40}\text{Ar}/^{39}\text{Ar}$ dating of the Campania Ignimbrite, Phlaegrean Fields, Italy. *Abstract ICOG*, Berkeley, 77.
- Demangeot J., 1965. *Geomorphologie des Abruzzes Adriatiques*. Edition du Centre National de la Recherche Scientifique (Paris) 15, 1-403.

- Devoti R., Esposito A., Pietrantonio G., Pisani A.R., Riguzzi F., 2011. Evidence of large scale deformation patterns from GPS data in the Italian subduction boundary. *Earth and Planetary Science Letters*, 311, 230–241, <http://dx.doi.org/10.1016/j.epsl.2008.06.031>.
- Dewey J.F., Helman M.L., Turco E., Hutton D.H.W., Knott S.D., 1989. Kinematics of the Western Mediterranean. In: Coward, M.P., Dietrich, D., Park, R.G. (Eds.), *Alpine Tectonics: The Geological Society of London, Special Publication*, 45, 265–283.
- Di Bucci D., Mazzoli S., 2002. Active tectonics of the Northern Apennines and Adria geodynamics: new data and a discussion. *Journal of Geodynamics* 34 (5), 687–707.
- Di Bucci D., Mazzoli S., 2003. The October–November 2002 Molise seismic sequence (southern Italy): an expression of Adria intraplate deformation. *Journal of the Geological Society of London* 160, 503–506.
- Di Girolamo P., Nardi G., Rolandi G., Stanzione D., 1976. Occurrence of calc-alkaline two piroxenes andesites from deep boreholes in the Phlaegrean Fields. I) Petrographic and petrochemical data. *Rend. Acc. Sc. Fis. Mat. Napoli* 43, s. 4, 250-255.
- Di Luccio F., Ventura G., Di Giovambattista R., Piscini A. and Cinti F.R.; 2010: Normal faults and thrusts reactivated by deep fluids: The 6 April 2009 Mw 6.3 L'Aquila earthquake, central Italy. *J. Geophys. Res.*, 115, B06315, doi:10.1029/2009JB007190.
- Di Luccio F., Ventura G., Di Giovambattista R., Piscini A., Cinti F.R., 2010. Normal faults and thrusts reactivated by deep fluids: the 6 April 2009 Mw 6.3 L'Aquila earthquake, central Italy. *Journal of Geophysical Research: Solid Earth*, v. 115, no. B6, doi: 10.1029/1009JB007190.
- Di Martire D., Paci M., Confuorto P., Costabile S., Guastaferro F., Verta A., Calcaterra D., 2017. A nation-wide system for landslide mapping and risk management in Italy: The second Not-ordinary Plan of Environmental Remote Sensing. *International journal of applied earth observation and geoinformation*, 63, 143-157.
- Di Naccio D., Boncio P., Brozzetti F., Pazzaglia F. J., Lavecchia G., 2013, Morphotectonic analysis of the Lunigiana and Garfagnana grabens (northern Apennines, Italy): Implications for active normal faulting. *Geomorphology*, Volume 201, Pages 293-311, <https://doi.org/10.1016/j.geomorph.2013.07.003>.
- Di Renzo V., Di Vito M.A., Arienzo I., Carandente A., Civetta L., D'Antonio M., Giordano F., Orsi G. & Tonarini S. 2007. Magmatic history of Somma–Vesuvius on the basis of new geochemical and isotopic data from a deep borehole (Camaldoli della Torre). *J. Petrology* 48, 4, 753-784.
- Di Vito M., Sulpizio R., Zanchetta G. & Calderoni G. 1998: The geology of the South Western Slopes of Somma-Vesuvius, Italy as inferred by borehole stratigraphies and cores. *Acta Vulcanol.* 10, 2, 383-393.
- DISS Working Group, 2010, Database of Individual Seismogenic Sources (DISS), Version 3.1.1: A compilation of potential sources for earthquakes larger than M 5.5 in Italy and surrounding areas: <http://diss.rm.ingv.it/diss>, INGV 2010.
- Dogliani C., D'Agostino N., Mariotti G., 1998. Normal faulting vs. regional subsidence and sedimentation rate. *Marine and Petroleum Geology*, 15, 737–750.
- Dogliani C., Moretti I., Roure F., 1991. Basal lithospheric detachment, eastward mantle flow and Mediterranean geodynamics: a discussion. *Journal of Geodynamics*, 13, 47–65.
- Dramis F., 1992. Il ruolo dei sollevamenti tettonici a largo raggio nella genesi del rilievo appenninico. *Studi Geologici Camerti*, Volume Speciale 1992/1, 9–15.
- Edwards M.A., Grasemann B., 2009. Mediterranean snapshots of accelerated slab retreat: subduction instability in stalled continental collision. *Geological Society, London, Special Publications*, 311, 155–192.

- Elter P., Giglia G., Tongiorgi M., Trevisan L., 1975. Tensional and compressional areas in the recent (Tortonian to present) evolution of the Northern Apennines. *Bollettino di Geofisica Teorica ed Applicata*, 17, 3–18.
- EMERGEO Working Group; 2010: Evidence for surface rupture associated with the Mw 6.3 L'Aquila earthquake sequence of April 2009 (central Italy). *Terra Nova*, 22(1), 43-51.
- Esposito E., Gargiulo A., Iaccarino G., Porfido S., 1998. Distribuzione dei fenomeni franosi riattivati dai terremoti dell'Appennino meridionale. Censimento delle frane del terremoto del 1980, in *Proceedings, Prevention of Hydrogeological Hazards: The Role of Scientific Research*, Alba: CNR-IRPI, 409-429.
- Eva E., Solarino S., Boncio P., 2014, HypoDD relocated seismicity in northern Apennines (Italy) preceding the 2013 seismic unrest: seismotectonic implications for the Lunigiana-Garfagnana area. *Bollettino di Geofisica Teorica ed Applicata*, Vol. 55, n. 4, pp. 739-754; DOI 10.4430/bgta0131
- Faccenna C., Becker T.W., Lucente F.P., Jolivet L., Rossetti F., 2001. History of subduction and back-arc extension in the Central Mediterranean. *Geophysical Journal International*, 145, 809–820.
- Faccenna C., Funicello R., Mattei M., 1994. Late Pleistocene N-S shear zones along the Latium Tyrrhenian margin: Structural characters and volcanological implications. *Boll. Geofis. Teor. Appl.*, 36, 507 – 523.
- Faccenna C., Piromallo, C., Crespo Blanc, A., Jolivet, L., Rossetti, F., 2004. Lateral slab deformation and the origin of the arcs of the western Mediterranean. *Tectonics*, 23, TC1012 <http://dx.doi.org/10.1029/2002TC001488>.
- Falcucci E., Gori S., Peronace E., Fubelli G., Moro M., Saroli M., Giaccio B., Messina P., Naso G., Scardia G., Sposato A., Voltaggio M., Galli P. and Galadini F.; 2009: The Paganica fault and surface coseismic ruptures caused by the 6 April 2009 earthquake (L'Aquila, central Italy). *Seismol. Res. Lett.*, 80, 940-950.
- Faure Walker J.P., Roberts G.P., Cowie P.A., Papanikolaou I., Michetti A.M., Sammonds P., Wilkinson M., McCaffrey K.J.W., Phillips R.J., 2012. Relationship between topography, rates of extension and mantle dynamics in the actively extending Italian Apennines. *Earth and Planetary Science Letters*, 325–326, 76–84, <http://dx.doi.org/10.1016/j.epsl.2012.01.028>.
- Ferretti A., Prati C. and Rocca F.; 2000: Nonlinear subsidence rate estimation using permanent scatterers in differential SAR interferometry, *IEEE Transactions Geosci. Remote Sensing*, 38(5), 2202-2212.
- Ferretti A., Prati C. and Rocca F.; 2001: Permanent Scatters in SAR interferometry. *IEEE Transactions Geosci. Remote Sensing*, 39, 8–20.
- Ferretti A., Fumagalli A., Novali F., Prati C., Rocca F., Rucci A., 2011, A new algorithm for processing interferometric data-stacks: SqueeSAR. *IEEE Transactions on Geoscience and Remote Sensing*, 49: 3460-3470. doi:<http://dx.doi.org/10.1109/TGRS.2011.2124465>.
- Fielding, E. J., Blom, R. G., & Goldstein, R. M. (1998). Rapid subsidence over oil fields measured by SAR interferometry. *Geophysical Research Letters*, 25(17), 3215-3218.
- Florio G., Fedi M., Cella F. & Rapolla A. 1999: The Campanian Plain and Phlegrean Fields: structural setting from potential field data. *J. Volcanol. Geotherm. Res.* 91, 2, 361-379.
- Florio G., Fedi M., Cella F., Rapolla A., 1999. The Campanian Plain and Phlegrean Fields: structural setting from potential field data. *Journal of Volcanology and Geothermal Research*, 91, 2, 361-379.
- Frepoli A., Maggi C., Cimini G.B., Marchetti A., Chiappini M., 2011. Seismotectonic of Southern Apennines from recent passive seismic experiments. *Journal of Geodynamics*, 51, 110–124.
- Fruneau B., Achache J. and Delacourt C.; 1996: Observation and modelling of the Saint-Étienne-de-Tinée landslide using SAR interferometry. *Tectonophysics*, 265(3-4), 181-190.
- Fruneau, B., J. Achache, and C. Delacourt, 1996 Observation and modeling of the Saint-Etienne-de-Tinee landslide using SAR interferometry, *Tectonophysics*, 2,65(3-4), 181-190.

- Funiciello R., Parotto M., 1978. Il substrato sedimentario nell'area dei Colli Albani: considerazioni geodinamiche e paleogeografiche sul margine tirrenico dell'Appennino centrale, *Geol. Rom.*, 17, 233 – 287.
- Galadini F., 1999. Pleistocene changes in the central Apennine fault kinematics: a key to decipher active tectonics in central Italy. *Tectonics*, 18 (5), 877–894.
- Galadini F., Messina P., 2004. Early-Middle Pleistocene eastward migration of the Abruzzi Apennine (central Italy) extensional domain. *Journal of Geodynamics*, 37, 57-81.
- Galadini, F., Galli, P., 1999. The Holocene paleoearthquakes on the 1915 Avezzano earthquake faults (central Italy): implications for active tectonics in the central Apennines. *Tectonophysics*, 308, 143– 170.
- Galadini, F., Galli, P., 2000. Active tectonics in the Central Apennines (Italy) - input data for seismic hazard assessment. *Natural Hazards*, 22, 225–270.
- Galadini, F., Galli, P., Giraudi, C., 1997. Geological investigations of Italian earthquakes: new paleoseismological data from the Fucino Plain (Central Italy). *Journal of Geodynamics*, 24, 87–103.
- Galadini, F., Giraudi, C., Messina, P., 1999. Nuovi dati sulla tettonica tardopleistocenica dell'Alta Valle dei Sangro (Apennino Centrale): implicazioni sismotettoniche. *Il Quaternario*, 11(2), 347–356.
- Galadini, F., Meletti, C., Vittori, E., 2000. Stato delle conoscenze sulle faglie attive in Italia: elementi geologici di superficie. In: Galadini, F., Meletti, C., Rebez, A. (Eds.), *Le ricerche del GNDT nel campo della pericolosità sismica (1996–1999)*, 107–136.
- Galadini, F., Meletti, C., Vittori, E., 2001. Major active faults in Italy: available surficial data. *Netherlands Journal of Geosciences/Geologie en Mijnbouw*, 80 (3–4), 273–296.
- Galadini F., Falcucci E., Galli P., Giaccio B., Gori S., Messina P., Moro M., Saroli M., Scardia G., Sposato A., 2012, Time intervals to assess active and capable faults for engineering practices in Italy, *Engineering Geology*. doi: 10.1016/j.enggeo.2012.03.012
- Galli P., Bosi V., Piscitelli S., Giocoli A., Scionti V., 2006, Late Holocene earthquakes in southern Apennine: paleoseismology of the Caggiano fault: *International Journal of Earth Science (Geol. Rundsch.)*, doi:10.1007/s00531-005-0066-2.
- Galli P., Galadini F., 2003. Disruptive earthquakes revealed by faulted archaeological relics in Samnium (Molise, southern Italy). *Geophysical Research Letters*, 30, 5.
- Galli P., Galadini F., Moro M., Giraudi C., 2002. New paleoseismological data from the Gran Sasso d'Italia area (central Apennines). *Geophysical Research Letters*, 29, 710.1029/2001GL013292.
- Galli P., Giaccio B., and Messina P.; 2010: The 2009 central Italy earthquake seen through 0.5 Myr-long tectonic history of the L'Aquila faults system. *Quat. Sci. Rev.*, 29, 3768–3789.
- Galli P., Giaccio B., Messina P., 2010. The 2009 central Italy earthquake seen through 0.5 Myr-long tectonic history of the L'Aquila faults system. *Quat. Sci. Rev.*, 29, 3768–3789.
- Galli P., Giaccio B., Messina P., Peronace E., 2011. Paleoseismology of the L'Aquila faults (central Italy, 2009 Mw 6.3 earthquake). Clues on active fault linkage. *Geophysical Journal International*, 187, 1119-1134, doi: 10.1111/j.1365-246X.2011.05233.x.
- Galli P., Giaccio B., Messina P., Peronace E., Amato V., Naso J.A., Nomade S., Pereira A., Piscitelli S., Bellanova J., Billi A., Blamart D., Galderisi A., Giocoli A., Stabile T., Thil F., 2017. Middle to Late Pleistocene activity of the northern Matese fault system (southern Apennines, Italy). *Tectonophysics*, 699, 61-81.
- Galli P., Naso J.A., 2009. Unmasking the 1349 earthquake source (southern Italy): paleoseismological and archaeoseismological indications from the Aequae Iuliae fault: *Journal of Structural Geology*, 31, 128–149, doi:10.1016/j.jsg.2008.09.007.

- Gasparini C., Iannaccone G., Scarpa R., 1985. Fault-plane solutions and seismicity of the Italian peninsula. *Tectonophysics* 117, 59–78.
- Getis A., Ord J. K., 1992, The Analysis of Spatial Association by Use of Distance Statistics. *Geographical Analysis*, Vol. 24, No. 3, <https://doi.org/10.1111/j.1538-4632.1992.tb00261.x>
- Ghisetti F., Vezzani L., 1991. Thrust belt development in the Central Apennines (Italy): northward polarity of thrusting and out-of-sequence deformation in the Gran Sasso chain. *Tectonics*, 10: 904-919.
- Giaccio B., Castorina F., Nomade S., Scardia G., Voltaggio M., Sagnotti L., 2013. Revised chronology of the Sulmona lacustrine succession, central Italy. *Journal of Quaternary Science*, 28(6), 545-551.
- Giaccio B., Isaia R., Fedele F.G., Di Canzio E., Hoffecker J., Ronchitelli A., Sinitsyng A.A., Anikovichg M., Lisitsyng S.N. & Popov V.V. 2008: The Campanian Ignimbrite and Codola tephra layers: two temporal/stratigraphic markers for the Early Upper Palaeolithic in southern Italy and eastern Europe. *J. Volcanol. Geotherm. Res.* 177, 1, 208-226.
- Giardini D., 1993. Teleseismic observation of the November 23 1980, Irpinia earthquake. *Annali di Geofisica*, 36(1), 17-25.
- Gillot P.Y., Chiesa S., Pasquaré G. & Vezzoli L. 1982: <33,000 yr K/Ar dating of the volcanotectonic horst of the Isle of Ischia, Gulf of Naples. *Nature* 299, 242-245.
- Gruppo di Lavoro CPTI, 1999. Catalogo Parametrico dei Terremoti Italiani. ING, GNDT, SGA, SSN, Bologna.
- Guerriero V., Iannace A., Mazzoli S., Parente M., Vitale S., Giorgioni M., 2010. Quantifying uncertainties in multi-scale studies of fractured reservoir analogues: Implemented statistical analysis of scan line data in carbonate rocks. *Journal of Structural Geology*, 32, 1271-1278, doi:10.1016/J.JSG.2009.04.016.
- Guerriero V., Vitale S., Ciarcia S. & Mazzoli S. (2011) - Improved statistical multi-scale analysis of fractured reservoir analogues. *Tectonophysics*, 504, 14-24, doi:10.1016/J.TECTO.2011.01.003.
- Gütting R. H., 1994, An Introduction to Spatial Database Systems, *VLDB Journal*, Vol. 3, No. 4, October 1994.
- Hansen R.F.; 2001: Radar interferometry: data interpretation and error analysis, Kluwer Academic Publishers, pp. 1-308.
- Hippolyte J.C., Angelier J. & Roure F. 1994: A major geodynamic change revealed by Quaternary stress pattern in the Southern Apennines. *Tectonophysics* 230, 199-210.
- Hippolyte, J.-C., Angelier, J., Roure, F., 1994. A major geodynamic change revealed by Quaternary stress patterns in the Southern Apennines (Italy). *Tectonophysics*, 230, 199–210.
- Hooper A., Zebker H., Segall P. and Kampes. B., 2004, A new method for measuring deformation on volcanoes and other natural terrains using InSAR persistent Scatterers, *Geophysical Research Letters*, Vol. 31.
- IAEA, 1991. Earthquakes and associated topics in relation to nuclear power plant siting. A safety guide. Safety Series, International Atomic Energy Agency, Vienna. 50-SG-S1 (Rev. 1), 60 pp
- Iannace A., Bonardi G., D'Errico M., Mazzoli S., Perrone V., Vitale S., 2005. Structural setting and tectonic evolution of the Apennine Units of northern Calabria. *Comptes Rendus -Geoscience*, 337, 1541–1550.
- Iannace A., Vitale S., D'Errico M., Mazzoli S., Di Staso A., Macaione E., Messina A., Reddy S.M., Somma R., Zamparelli V., Zattin M., Bonardi G., 2007. The carbonate tectonic units of northern Calabria (Italy): A record of Apulian paleomargin evolution and Miocene convergence, continental crust subduction, and exhumation of HP-LT rocks. *Journal of the Geological Society of London*, 164, 1165–1186.
- Improta L., Bonagura M., Capuano P. Iannaccone G., 2003. An integrated geophysical investigation of the upper crust in the epicentral area of the 1980, Ms=6.9 Irpinia earthquake (Southern Italy). *Tectonophysics*, 361, 139–169.

- Improta L., Corciulo M., 2006. Controlled source nonlinear tomography: A powerful tool to constrain tectonic models of the Southern Apennines orogenic wedge, Italy. *Geology*, 34, 941-944.
- Inversi B., Scrocca D., Montegrossi G., Livani M., Petracchini L., Brandano M., Brillì M., Giustini F., Recanati R., Gola G., 2013. 3D geological modelling of a fractured carbonate reservoir for the study of medium enthalpy geothermal resource in the Southern Apennines (Campania Region, Italy). *Proceedings European Geothermal Congress, Pisa, Italy*.
- Ippolito F., Ortolani F. & Russo M. 1973: Struttura marginale tirrenica dell'Appennino campano: reinterpretazione di dati di antiche ricerche di idrocarburi. *Mem. Soc. Geol. It.* 12, 227-250.
- Ippolito F., Ortolani F., Russo M., 1973. Struttura marginale tirrenica dell'Appennino campano: reinterpretazione dei dati di antiche ricerche di idrocarburi. *Memorie della Società Geologica Italiana*, 12, 227-250.
- Irollo G., Ascione A. & Cinque A. 2005: Segnalazione di attività olocenica lungo due fault zones dell'hinterland del Golfo di Napoli. *Atti 24° Convegno Nazionale GNGTS, Roma 15-17 nov. 2005*, 17-21.
- Italiano F., Martinelli G., Rizzo A., 2004. Geochemical evidence of seismogenic-induced anomalies in the dissolved gases of thermal waters. A case study of Umbria (Central Apennines, Italy) both during and after the 1997-1998 seismic swarm. *Geochemistry, Geophysics, Geosystems*, 5, doi:10.1029/2004GC000720.
- Johnston S.T., Mazzoli S., 2009. The Calabrian Orocline: buckling of a previously more linear orogen. In: Murphy, J.B., Keppie, J.D., Hynes, A.J. (Eds.), *Ancient Orogens and Modern Analogues*. Geological Society of London, Special Publications 327, 113–125, [http://dx.doi.org/10.1144/SP327.70305-8719/09/\\$15.00](http://dx.doi.org/10.1144/SP327.70305-8719/09/$15.00).
- Jordan T.H., Chen Y.T., Gasparini P., Madariaga R., Main I., Marzocchi W., Papadopoulos G., Sobolev G., Yamaoka K. and Zschau J.; 2011: Operational Earthquake Forecasting; State of Knowledge and Guidelines for Utilization. *Ann. Geophys.*, 54, 4.
- Kastens, K., Mascle, J., Auroux, C., et al., 1988. ODP Leg 107 in the Tyrrhenian Sea: insights into passive margin and back-arc basin evolution. *Geological Society of America Bulletin* 100, 1140–1156.
- Kastens, K.A., Mascle, J., 1990. The geological evolution of the Tyrrhenian Sea: an introduction to the scientific results of ODP Leg 107. In: Kastens, K.A., Mascle, J., et al. (Eds.), *Proceedings of the Ocean Drilling Program, Scientific Results 107*, 3–26, (College Station, TX - Ocean Drilling Program).
- Kimura H. and Yamaguchi Y.; 2000: Detection of landslide areas using satellite radar interferometry. *Photogram. Eng. Rem. Sens.*, 66(3), 337-344.
- Knott S.D., 1987. The Liguride Complex of Southern Italy a Cretaceous to Paleogene accretionary wedge. *Tectonophysics*, 142: 217-226.
- La Rocca, S. Santangelo, N., 1991, Nuovi dati sulla stratigrafia e sull'evoluzione geomorfologica del bacino lacustre pleistocenico del fiume Noce (Basilicata): *Geografia Fisica e Dinamica Quaternaria*, 14(2), 229-242.
- Lanari R., Berardino P., Bonano M., Casu F., Manconi A., Manunta M., Manzo M., Pepe A., Pepe S., Sansosti E., Solaro G., Tizzani P. and Zeni G.; 2010: Surface displacements associated with the L'Aquila 2009 Mw 6.3 earthquake (central Italy): New evidence from SBAS-DInSAR time series analysis. *Geophys. Res. Lett.*, 37, L20309.
- Lanari R., Casu F., Manzo M., Zeni G., Berardino P., Manunta M. and Pepe A.; 2007: An Overview of the Small BAseline Subset Algorithm: A DInSAR Technique for Surface Deformation Analysis. In: Wolf D., Fernández J. (eds) *Deformation and Gravity Change: Indicators of Isostasy, Tectonics, Volcanism, and Climate Change*. Pageoph Topical Volumes. Birkhäuser Basel.

- Lavecchia G., Boncio P., Brozzetti F., de Nardis R., di Naccio D., Ferrarini F., Pizzi A. and Pomposo G.; 2009: The April 2009 L'Aquila (central Italy) seismic sequence (Mw 6.3): a preliminary seismotectonic picture. In: *Recent Progress on Earthquake Geology*, Nova Science Publishers, Inc.
- Lavecchia, G., Brozzetti F., Barchi M., Keller J., Menichetti M., 1994. Seismotectonic zoning in east-central Italy deduced from the analysis of the Neogene to present deformations and related stress fields. *Geol. Soc. Am. Bull.*, 106, 1107 – 1120.
- Locati M., Camassi R., Stucchi, M. (eds.), 2011, DBMI11, the 2011 version of the Italian Macroseismic Database. Milano, Bologna, <http://emidius.mi.ingv.it/DBMI11>.
- Lombardi A.M., Cocco M., Marzocchi W., 2010. On the Increase of Background Seismicity Rate during the 1997–1998 Umbria-Marche, Central Italy, Sequence: Apparent Variation or Fluid-Driven Triggering?. *Bulletin of the Seismological Society of America*, 100, 1138–1152.
- Lombardi S., Voltattorni N., 2010. Rn, He and CO₂ soil gas geochemistry for the study of active and inactive faults: *Applied Geochemistry*, 25, 1206–1220.
- Lucente F.P., De Gori P., Margheriti L., Piccinini D., Di Bona M., Chiarabba C. and Piana Agostinetti N.; 2010: Temporal variation of seismic velocity and anisotropy before the 2009 Mw 6.3 L'Aquila earthquake, Italy. *Geology*, 38(11), 1015-1018, doi:10.1130/G31463.1.
- Luiso P., Paoletti V., Nappi R., La Manna M., Cella F., Gaudiosi G., Fedi M., Iorio M., 2018. A multidisciplinary approach to characterize the geometry of active faults: the example of Mt. Massico, Southern Italy. *Geophysical Journal International*, 213(3), 1673-1681.
- Lundgren P., Casu F., Manzo M., Pepe A., Berardino P., Sansosti E. and Lanari R.; 2004: Gravity and magma induced spreading of Mount Etna volcano revealed by satellite radar interferometry, *Geophys. Res. Lett.*, 31, L04602.
- Machette M.N., (2000), Active, capable, and potentially active faults - a paleoseismic perspective. *Journal of Geodynamics*, 29, 387-392.
- Macchiavelli, C., Mazzoli S., Megna A., Saggese F., Santini S., Vitale S., 2012. Applying the multiple inverse method to the analysis of earthquake focal mechanism data: new insights into the active stress field of Italy and surrounding regions. *Tectonophysics* 580, 124–149.
- Maggi C., Frepoli A., Cimini G.B., Console R. and Chiappini R., 2009. Recent seismicity and crustal stress field in the Lucanian Apennines and surrounding areas (Southern Italy). *Seismotectonic implications*. *Tectonophysics*, 463, 130–144.
- Malinverno A., Ryan W.B.F., 1986. Extension in the Tyrrhenian Sea and shortening in the Apennines as a result of arc migration driven by sinking of the lithosphere. *Tectonics*, 5, 227–245.
- Manzo M., Ricciardi G.P., Casua F., Ventura G., Zeni G., Borgström S., Berardino P., Del Gaudio C. and Lanari R.; 2006: Surface deformation analysis in the Ischia Island (Italy) based on spaceborne radar interferometry. *J. Volcanol. Geother. Res.*, 151(4), 399-416.
- Mariani M. & Prato R. 1988: I bacini neogenici costieri del margine tirrenico: approccio sismico-stratigrafico. *Mem. Soc. Geol. It.* 41, 519-531.
- Mariani M., Prato R., 1988. I bacini neogenici costieri del margine tirrenico: approccio sismico-stratigrafico. *Mem. Soc. Geol. It.* 41, 519-531.
- Massonnet D. and Rabaute T.; 1993: Radar interferometry: limits and potential. *IEEE Trans. Geosci. Remote Sensing*, 31, 455–464.

- Massonnet D., Feigl K., Rossi M. and Adragna F., 1994, Radar interferometric mapping of deformation in the year after the Landers earthquake. *Nature* volume 369, pages 227–230
- Massonnet D., Holzer T., Vadon H. (1997). Land subsidence caused by the East Mesa geothermal field, California, observed using SAR interferometry. *Geophysical research letters*, 24(8), 901-904.
- Massonnet K.F., Rossi M., Adragna F., 1994. Radar interferometric mapping of deformation in the year after the Landers earthquake. *Nature*, 369, 227–230.
- Mattei M., Miccadei E., 1991. Strike-slip tectonics between the Marsica Range and the Molisan Basin in the Sangro Valley (Abruzzo, Central Italy). *Bollettino della Società Geologica Italiana*, 110: 737-745.
- Mattei, M., Cifelli, F., D'Agostino, N., 2007. The evolution of the Calabrian Arc: evidence from paleomagnetic and GPS observations. *Earth and Planetary Science Letters*, 263 (3–4), 259–274.
- Mazzoli S., 1992. Structural analysis of the Mesozoic Lagonegro Units in SW Lucania (Southern Italian Apennines). *Studi Geologici Camerti*, 12: 117-146.
- Mazzoli S., Ascione A., Candela S., Iannace A., Megna A., Santini S., Vitale S., 2013, Subduction and continental collision events in the southern Apennines: constraints from two crustal cross-sections. *Rendiconti Online della Società Geologica Italiana*, 25, 78-84.
- Mazzoli S., Barkham S., Cello G., Gambini R., Mattioni L., Shiner P., Tondi E., 2001. Reconstruction of continental margin architecture deformed by the contraction of the Lagonegro Basin, southern Apennines, Italy. *Journal of the Geological Society*, 158, 309-319.
- Mazzoli S., Corrado S., De Donatis M., Scrocca D., Butler R.W.H., Di Bucci D., Naso G., Nicolai C., Zucconi V., 2000. Time and space variability of “thin-skinned” and “thick-skinned” thrust tectonics in the Apennines (Italy). *Rend. Lincei, Scienze Fisiche e Naturali*, 11 (serie 9), 5-39.
- Mazzoli S., D’Errico M., Aldega L., Corrado S., Invernizzi C., Shiner P., Zattin M., 2008. Tectonic burial and ‘young’ (< 10 Ma) exhumation in the southern Apennines fold and thrust belt (Italy). *Geology*, 36, 243–246.
- Mazzoli S., Helman, M., 1994. Neogene patterns of relative plate motion for Africa–Europe: some implications for recent central Mediterranean tectonics. *Geologische Rundschau*, 83, 464–468.
- Mazzoli S., Macchiavelli C., Ascione A., 2014. The 2013 Marche offshore earthquakes: new insights into the active tectonic setting of the outer northern Apennines. *Journal of the Geological Society*, 171, 457-460, doi: 10.1144/jgs2013-091
- Mazzoli S., Santini S., Macchiavelli C., Ascione A., 2015. Active tectonics of the outer northern Apennines: Adriatic vs. Po Plain seismicity and stress fields. *Journal of Geodynamics*, 84, 62-76, doi: 10.1016/j.jog.2014.10.002
- Mazzoli S., Szaniawski R., Mittiga F., Ascione A., Capalbo A., 2012. Tectonic evolution of Pliocene-Pleistocene wedge-top basins of the southern Apennines: new constraints from magnetic fabric analysis. *Canadian Journal of Earth Sciences*, 49, 492-509, doi:10.1139/E11-067.
- Mazzotti A., Stucchi E., Fradelizio G.L., Zanzi L., Scandone P., 2007. Re-processing of the CROP-04 seismic data: *Bollettino della Società Geologica Italiana*, 7, 141-153.
- Meisina C., Zucca F., Fossati D., Ceriani M. and Allievi J.; 2006: Ground deformation monitoring by using the Permanent Scatterers Technique: The example of the Oltrepo Pavese (Lombardia, Italy). *Eng. Geol.*, 88(3-4), 240-259.
- Mele F. and Amato A.; 2014: <https://ingvterremoti.wordpress.com/2014/11/09/linizio-e-la-fine-della-sequenza-sismica-dellaquila/>, INGV-CNT.

- Menardi Noguera A., Rea G., 2000. Deep structure of the Campanian-Lucanian Arc (southern Apennines). *Tectonophysics*, 324, 239-265.
- Menichetti M., De Feyter A.J., Corsi M., 1991. CROP 03 - Il tratto Val Tiberina - Mare Adriatico: Sezione geologica e caratterizzazione tettonico-sedimentaria delle avansosse della zona Umbria-Marchigiano-Romagnola. *Studi Geologici Camerti*, vol. spec., 1991/1: 279-293.
- Miccadei E., 1993. La Geologia dell'area dell'Alto Sagittario-Alto Sangro. *Geologica Romana*, 29: 463-494.
- Miccadei E., Parotto M., Piacentini T., 1998. Assetto geologico-strutturale dei Monti della Conca Subequana (Appennino abruzzese, Italia centrale). *Geologica Romana*, 34, 31-50.
- Miccadei, E., Piacentini, T., Barberi, R., 2002. Uplift and local tectonic subsidence in the evolution of intermontane basins: the example of the Sulmona basin (central Apennines, Italy). *Studi Geologici Camerti*, 119–133.
- Michetti A.M., Brunamonte F., Serva L., Vittori E., 1996. Trench investigations of the 1915 Fucino earthquake fault scarps (Abruzzo, Central Italy): geological evidence of large historical events. *Journal of Geophysical Research* 101, 5921–5936.
- Michetti A.M., Brunamonte F., Serva L., Whitney R.A., 1995. Seismic hazard assessment from paleoseismological evidence in the Rieti Region (Central Italy). In: Serva, L., Slemmons, D.B. (Eds.), "Perspectives in Paleoseismology", Association of Engineering Geologists Bulletin, Special Publication No. 6, pp. 63–82.
- Michetti, A.M., Serva, L. Vittori, E., 2000. ITHACA Italy Hazard from Capable Faults: a database of active faults of the Italian onshore territory. CD-Rom and explicative notes, ANPA.
- Milia A. 1998: Le unità piroclastiche tardo-quadernarie nel Golfo di Napoli. *Geogr. Fis. Din. Quat.* 21, 147–153.
- Milia A. 2000: The Dohrn Canyon formation: a response to the eustatic fall and tectonic uplift of the outer shelf (Eastern Tyrrhenian Sea margin, Italy). *Geo-Mar. Lett.* 20, 101-108.
- Milia A., Torrente M.M. 1999: Tectonics and stratigraphic architecture of a peri-Tyrrhenian half-graben (Bay of Naples, Italy). *Tectonophysics* 315, 301-318.
- Milia A., Torrente M.M., 2015. Tectono-stratigraphic signature of a rapid multistage subsiding rift basin in the Tyrrhenian-Apennine hinge zone (Italy): A possible interaction of upper plate with subducting slab. *J. Geodynamics*, 86, 42-60.
- Milia A., Torrente M.M., Massa B., Iannace P., 2013. Progressive changes in rifting directions in the Campania margin (Italy): New constrains for the Tyrrhenian Sea opening. *Global Planet. Ch.* 109, 3-17.
- Milia A., Torrente M.M., Russo M., Zuppetta A. 2003. Tectonics and crustal structure of the Campania continental margin: relationships with volcanism. *Mineralogy and Petrology*, 79, 33-47.
- Miller S.A., Colletti C., Chiaraluce L., Cocco M., Barchi M., Kaus B.J., 2004. Aftershocks driven by a high-pressure CO₂ source at depth. *Nature*, 427, 724–727.
- Mirabella F., Barchi M., Lupattelli A., Stucchi E., Ciaccio M.G., 2008. Insights on the seismogenic layer thickness from the upper crust structure of the Umbria-Marche Apennines (central Italy). *Tectonics*, 27, TC1010, doi:10.1029/2007TC002134
- Mirabella F., Pucci S., 2002. Integration of geological and geophysical data along a section crossing the region of the 1997 – 98 Umbria-Marche earthquake (Italy). *Boll. Soc. Geol. Ital.*, Vol. Spec. 1, 891 – 900.
- Misuraca M., Budillon F., Tonielli R., Di Martino G., Innangi S., Ferraro L., 2018. Coastal evolution, hydrothermal migration pathways and soft deformation along the Campania continental shelf (southern Tyrrhenian Sea): Insights from high-resolution seismic profiles. *Geosciences*, 8(4), 121, doi:10.3390/geosciences8040121
- Montone P., Amato A., Pondrelli S. 1999. Active Stress Map of Italy. *Journal of Geophysical Research*, 140 (B11), 25595–25610.

- Montone P., Salvini F., 1993. Geologia strutturale dei rilievi tra Colli di Monte Bove (Carsoli) e Tagliacozzo, Abruzzo. *Geologica Romana*, 29: 15-29.
- Mora, O., et al., 2003, Linear and nonlinear terrain deformation maps from a reduced set of interferometric SAR images, *IEEE Trans. Geosci. Remote Sensing*, Vol. 41, 2243-2253.
- Moro M., Amicucci L., Cinti F.R., Doumaza F., Montone P., Pierdominici S., Saroli M., Stramondo S., Di Fiore B., 2007. Surface evidence of active tectonics along the Pergola-Melandro fault: A critical issue for the seismogenic potential of the southern Apennines, Italy. *Journal of Geodynamics*, 44, 19–32.
- Moro M., Saroli M., Stramondo S., Bignami C., Albano M., Falcucci E., Gori S., Doglioni C., Polcari M., Tallini M., Macerola L., Novali F., Costantini M., Malvarosa F. and Wegmüller U.; 2017: New insights into earthquake precursors from InSAR. *Nature Sci. Rep.*, 7, 12035.
- Mostardini F., Merlini S., 1986. Appennino centro-meridionale. Sezioni geologiche e proposta di modello strutturale. *Mem. Soc. Geol. It.*, 35, 177-202.
- Moussat E., Rehault J.P. & Fabbri A. 1986: Rifting et évolution tectono-sédimentaire du Bassin Tyrrhénien au cours du Neogene et du Quaternaire. *Giorn. Geol.* 48, s. 3, 1/2, 41-62.
- Moussat E., Rehault J.P., Fabbri A., 1986. Rifting et évolution tectono-sédimentaire du Bassin Tyrrhénien au cours du Neogene et du Quaternaire. *Giorn. Geol.* 48, s. 3, 1/2, 41-62.
- Munno, R., Petrosino, P., Romano, P., Russo Ermolli, E., 2001. A late middle Pleistocene climatic cycle in southern Italy inferred from pollen analysis and tephrostratigraphy of the Acerno Lacustrine succession: *Géographie Physique Quaternaire*, 55(1), 87–99.
- Nostro C., Cocco M., Belardinelli M.E., 1997. Static stress change in extensional regimes: an application to southern Apennines (Italy). *Journal of Geophysical Research*, v. 87, p. 234–248.
- Ogniben L., 1969. Schema introduttivo alla geologia del confine calabro-lucano. *Memorie della Società Geologica Italiana*, 8: 453-763.
- Ori G.G., Roveri M., Vannoni F., 1986. Plio-Pleistocene sedimentation in the Apenninic foredeep (central Adriatic Sea, Italy). In: P.A. Allen, P. Homewood (eds.), *Foreland Basins*. International Association of Sedimentologists Special Publication, 8: 183-198.
- Ouzounov D., Pulinets S., Hattori K., Taylor P. (eds.), 2018. *Pre-Earthquake Processes: A Multidisciplinary Approach to Earthquake Prediction Studies*. :Geophysical Monograph Series, American Geophysical Union.
- Pantosti D., D'Addezio G., Cinti F., 1996. Paleoseismicity of the Ovindoli–Pezza fault, central Apennines, Italy: a history including a large, previously unrecorded earthquake in the Middle Ages (860–1300 A.D.). *Journal of Geophysical Research*, 101, 5937–5960.
- Pantosti D., Schwartz D.P., Valensise G., 1993. Paleoseismology along the 1980 surface rupture of the Irpinia Fault: implications for earthquake recurrence in the Southern Apennines, Italy. *Journal of Geophysical Research*, 98, 6561–6577.
- Pantosti D., Valensise G., 1990. Faulting mechanism complexity of the November 23, 1980, Campania-Lucania earthquake inferred from surface observations: *Journal of Geophysical Research*, 95(B-10), 15319–15341.
- Papadopoulos G.A., Charalampakis M., Fokaefs A. and Minadakis G.; 2010: Strong foreshock signal preceding the L'Aquila (Italy) earthquake (Mw 6.3) of 6 April 2009. *Nat. Hazards Earth Syst. Sci.*, 10, 19-24.
- Papanikolaou I.D., Fomelis M., Parcharidis I., Lekkas E.L. and Fountoulis I.G.; 2010: Deformation pattern of the 6 and 7 April 2009, MW=6.3 and MW=5.6 earthquakes in L'Aquila (Central Italy) revealed by ground and space based observations. *Nat. Hazards Earth Syst. Sci.*, 10(1), 73.

- Papanikolaou I.D., Roberts G.P., 2007. Geometry, kinematics and deformation rates along the active normal fault system in the southern Apennines: implications for fault growth. *Journal of Structural Geology*, 29, 166–188.
- Papanikolaou, I.D., Roberts, G.P., Michetti, A.M., 2005. Fault scarps and deformation rates in Lazio–Abruzzo, Central Italy: Comparison between geological fault slip-rate and GPS data. *Tectonophysics*, 408(1-4), 147-176.
- Parotto M., Praturlon A., 1975. Geological summary of Central Apennines. *La Ricerca Scientifica, Quaderni*, C.N.R., 90: 257-311.
- Parotto M., Cavinato G.P., Miccadei E. & Tozzi M., 2004. Line CROP 11: Central Apennines. *Memorie Descrittive della Carta Geologica d'Italia* 62, 145-153.
- Patacca E., 2007. Stratigraphic constraints on the CROP-04 seismic line interpretation: San Fele 1, Monte Foi 1 and San Gregorio Magno 1 wells (Southern Apennines, Italy), in Mazzotti, A., Patacca, E. and Scandone, P., eds., CROP-04. *Bollettino della Società Geologica Italiana*, 7, 185-239.
- Patacca E., 2007. Stratigraphic constraints on the CROP-04 seismic line interpretation: San Fele 1, Monte Foi 1 and San Gregorio Magno 1 wells (Southern Apennines, Italy), in Mazzotti, A., Patacca, E. and Scandone, P., eds., CROP-04: *Bollettino della Società Geologica Italiana*, 7, 185-239.
- Patacca E., Scandone P., 1989. Post-Tortonian mountain building in the Apennines. The role of the passive sinking of a relict lithospheric slab. In: *The lithosphere in Italy. Advances in Earth Science Research* (Ed. by A., Boriani, M., Bonafede, G.B., Piccardo and G.B., Vai). *Atti Accad. Naz. Lincei*, Roma, 80, 157-176.
- Patacca E., Scandone P., 2001. Late thrust propagation and sedimentary response in the thrust-belt–foredeep system of the Southern Apennines (Pliocene-Pleistocene). in Vai, G.B. and Martini, I.P., eds., *Anatomy of an Orogen: the Apennines and Adjacent Mediterranean Basins: Dordrecht, Kluwer Academic Publishers*, p. 401-440.
- Patacca E., Scandone P., 2004. The Plio-Pleistocene thrust belt-foredeep system in the southern Apennines and Sicily (Italy). *Geology of Italy. Special Volume of the Italian Geological Society for the IGC, 32, Florence-2004* (Ed. by U. Crescenti, S. D'Offizi, S. Merlini and R. Sacchi), 93-129. *Società Geologica Italiana*, Roma.
- Patacca E., Scandone P., 2007. Constraints on the interpretation of the CROP-04 seismic line derived from Plio-Pleistocene foredeep and thrust-sheet-top deposits (Southern Apennines, Italy). CROP-04 (Edited by A. Mazzotti, E. Patacca & P. Scandone). *Boll. Soc. Geol. It., Special Issue*, 7, 241-256.
- Patacca E., Scandone P., Bellatalla M., Perilli N., Santini U., 1992. La zona di giunzione tra l'arco appenninico settentrionale e l'arco appenninico meridionale nell'Abruzzo e nel Molise. *Studi Geologici Camerti*, vol. spec., 1991/2: 417-441.
- Patacca E., Scandone P., Di Luzio E., Cavinato G.P., Parotto M., 2008. Structural architecture of the Central Apennines. Interpretation of the CROP 11 seismic profile from the adriatic coast to the orographic divide. *Tectonics*, 27, TC3007.
- Patacca, E., Sartori, R., Scandone, P., 1990. Tyrrhenian basin and Apenninic arcs: kinematic relations since late Tortonian times. *Mem. Soc. Geol. Ital.* 45, 425– 451.
- Peltzer G., Rosen P., Rogez F., Hudnut K., 1996, Postseismic Rebound in Fault Step-Overs Caused by Pore Fluid Flow. *Science*, Vol. 273, Issue 5279, pp. 1202-1204, DOI: 10.1126/science.273.5279.1202
- Peltzer G., Rosen P., Rogez F., Hudnut K., 1998, Poroelastic rebound along the Landers 1992 earthquake surface rupture. *Journal of Geophysical Research, Solid Earth*, Volume103, IssueB12, Pages 30131-30145, <https://doi.org/10.1029/98JB02302>
- Pescatore T., 1978. Evoluzione tettonica del Bacino Irpino (Italia meridionale) durante il Miocene. *Bollettino della Società Geologica Italiana*, 97: 783-805.

- Pescatore T., Diplomatico G., Senatore M.R., Tramutoli M. & Mirabile L. 1984: Contributi allo studio del Golfo di Pozzuoli. *Mem Soc. Geol. It.* 27, 133-149.
- Pezzo G., Merryman Boncori J. P., Atzori S., Piccinini D., Antonioli A., Salvi S., 2014, The 2013 Lunigiana (Central Italy) earthquake: Seismic source analysis from DInSAR and seismological data, and geodynamical implications for the northern Apennines. *Tectonophysics* 636 (2014) 315–324.
- Philip G. M. and Watson D. F., 1982, A Precise Method for Determining Contoured Surfaces. *Australian Petroleum Exploration Association Journal* 22: 205–212.
- Piacentini T. & Miccadei E., 2014. The role of drainage systems and intermontane basins in the Quaternary landscape of the Central Apennines chain (Italy). *Special Issue: Intermontane Basins: Quaternary morphoevolution of Central-Southern Italy*, Aucelli P.P.C., Della Seta M., Giano S.I., Schiattarella M. Eds. *Rendiconti Lincei - Scienze Fisiche e Naturali* 25, 2, 139-150. DOI:10.1007/s12210-014-0312-2.
- Pialli G., Barchi M., Minelli G. (eds.), 1998. Results of the CROP 03 deep seismic reflection profile. *Memorie della Società Geologica Italiana*, 52.
- Picotti V., Pazzaglia F.J., 2008. A new active tectonic model for the construction of the Northern Apennines mountain front near Bologna (Italy). *Journal of Geophysical Research* 113, B08412, doi:10.1029/2007JB005307.
- Picotti V., Ponza A., Pazzaglia F.J., 2009. Topographic expression of active faults in the foothills of the Northern Apennines. *Tectonophysics*, 474, 285–294.
- Pierdominici S., Mariucci M.T., Montone P., 2011. A study to constrain the geometry of an active fault in southern Italy through borehole breakouts and downhole logs. *Journal of Geodynamics*, 52 (3-4), 279-289.
- Pieri M., Groppi G., 1981. Subsurface geological structure of the Po Plain. *Pubbl. 414 P.F. Geodinamica, C.N.R.*, 23 pp.
- Pingue F., De Natale G., 1993. Fault mechanism of the 40 s subevent of the 1980 Irpinia (Southern Italy) earthquake from leveling data. *Geophysical Research Letters*, 20, 911-914.
- Pizzi A., Calamita F., Coltorti M., Pieruccini P., 2002. Quaternary normal faults, intramontane basins and seismicity in the Umbria-Marche-Abruzzi Apennine Ridge (Italy): contribution of neotectonic analysis to seismic hazard assessment. *Boll. Soc. Geol. It., Spec. Publ*, 1(31), 923-929.
- Pondrelli S., Salimbeni S., Morelli A., Ekström G., Olivieri M. and Boschi E.; 2010: Seismic moment tensors of the April 2009, L'Aquila (Central Italy), earthquake sequence. *Geophys. J. Int.*, 180(1), 238–242.
- Pondrelli, S., Morelli, A., Ekstrfm, G., Mazza, S., Boschi, E., Dziewonski, A.M., 2002. European–Mediterranean regional centroid-moment tensors: 1997–2000. *Phys. Earth Planet. Inter.*, 130, 71–101.
- Pondrelli, S., Salimbeni, S., Ekström, G., Morelli, A., Gasperini, P. and Vannucci, G., 2006, The Italian CMT dataset from 1977 to the present: *Physical Earth Planetary International*, 159 (3–4), 286–303.
- Porfido S., Esposito E., Michetti A.M., Blumetti A.M., Vittori E., Tranfaglia G., Guerrieri L., Ferrelì L., Serva L., 2002. The geological evidence for earthquakes induced effects in the Southern Apennines (Italy): Surveys in *Geophysics*, 23, 529–562.
- Porreca, M. and Mattei, M., 2010, Tectonic and environmental evolution of Quaternary intramontane basins in Southern Apennines (Italy): insights from palaeomagnetic and rock magnetic investigations. *Geophysical Journal International*, 182, 682–698.
- Porreca, M. and Mattei, M., 2012, AMS fabric and tectonic evolution of Quaternary intramontane extensional basins in the Picentini Mountains (southern Apennines, Italy). *International Journal of Earth Science (Geol. Rundsch.)*, 101, 863–877.

- Prati C., Ferretti A. and Perissin D.; 2010: Recent advances on surface ground deformation measurement by means of repeated space-borne SAR observations. *J. Geodyn.*, 49(3-4), 161-170
- Praturlon A., 1968. Note Illustrative della Carta Geologica d'Italia alla scala 1:100.000 - Foglio 152 Sora. Servizio Geologico d'Italia: 1-76.
- Putignano M.L., Ruberti D., Tescione M. & Vigliotti M. 2007: Evoluzione tardo quaternaria del margine casertano della Piana Campana (Italia meridionale). *Boll. Soc. Geol. It.* 126, 1, 11-24.
- Quattrocchi F., 1999. In search of evidence of deep fluid discharges and pore pressure evolution in the crust to explain the seismicity style of the Umbria-Marche, 1997–1998 seismic sequence (Central Italy). *Ann. Geophys.* 42, 609–636.
- Radicati di Brozolo F., Di Girolamo P., Turi B. & Oddone M., 1988: ^{40}Ar - ^{39}Ar and K-Ar dating of K-rich rocks from the Roccamonfina Volcano, Roman Comagmatic Region, Italy. *Geochim. Cosmochim. Acta* 52, 1435-1441.
- Ricci Lucchi F., 1986. The Oligocene to Recent foreland basins of the northern Apennines. In: P.A. Allen, P. Homewood (eds.), *Foreland Basins*. International Association of Sedimentologists, Special Publication, 8: 105-139.
- Roberts G.P., Michetti A.M., 2004. Spatial and temporal variations in growth rates along active normal fault systems: an example from The Lazio–Abruzzo Apennines, central Italy. *Journal of Structural Geology*, 26, 339–376.
- Rolandi G., Bellucci F., Heizler M.T., Belkin H.E., De Vivo B., 2003. Tectonic controls on the genesis of ignimbrites from the Campania volcanic zone, southern Italy. *Mineral. Petrol.* 79, 3-31.
- Romano P., Santo A. & Voltaggio M. 1994: L'evoluzione geomorfologica della pianura del F. Volturno (Campania) durante il tardo Quaternario (Pleistocene medio-superiore - Olocene). *Il Quaternario* 7, 1, 41-56.
- Rosi M. & Sbrana A. 1987: Phlegrean Fields. *Quaderni de "La Ricerca Scientifica"*, CNR Roma 114, 9, 175 pp.
- Rovida, A., Locati, M., Camassi, R., Lolli, B., and Gasperini, P., 2016, CPTI15, the 2015 version of the Parametric Catalogue of Italian Earthquakes. Istituto Nazionale di Geofisica e Vulcanologia, <http://doi.org/10.6092/INGV.IT-CPTI15>.
- Royden L.H., Patacca E., Scandone P., 1987. Segmentation and configuration of subducted lithosphere in Italy: an important control on thrust-belt and foredeep-basin evolution. *Geology*, 15: 714-717.
- Sacchi M., Infuso S. & Marsella E. 1994: Late Pliocene–Early Pleistocene compressional tectonics in offshore Campania (eastern Tyrrhenian margin). *Boll. Geof. Teor. Appl.* 26, 141/144, 469-482.
- Sacchi M., Molisso F., Pacifico A., Vigliotti M., Sabbarese C. & Ruberti, D. 2014: Late-Holocene to recent evolution of Lake Patria, South Italy: An example of a coastal lagoon within a Mediterranean delta system. *Glob. Planet. Ch.* 117, 9–27.
- Salvini F., 1993. Block tectonics in thin-skin style-deformed regions: examples from structural data in Central Apennines. In: E. Boschi (ed.), *Modes of crustal deformation: from brittle upper crust through detachments to the ductile lower crust*. *Annali di Geofisica*, Special Issue: 97-107.
- Santangelo N., 1991. Evoluzione geomorfologia e stratigrafica di alcuni bacini lacustri del confine campano-lucano (Italia Meridionale) (Tesi di Dottorato, III Ciclo). Napoli, Università Federico II, 109 p.
- Santangelo N., Ciampo G., Di Donato V., Esposito P., Petrosino P., Romano P., Russo Ermolli E., Santo A., Toscano F., Villa I. 2010: Late Quaternary buried lagoons in the northern Campania plain (southern Italy): evolution of a coastal system under the influence of volcano-tectonics and eustatism. *It. J. Geosci.* 129, 1, 156-175.

- Santangelo N., Romano P., Ascione A., Russo Ermolli E., 2017. Quaternary evolution of the Southern Apennines coastal plains: a review. *Geologica Carpathica*, 68, 1, 43–56. doi: 10.1515/geoca-2017-0004
- Santantonio M., 1993. Facies associations and evolution of pelagic carbonate platform/basin systems. Examples from the Italian Jurassic. *Sedimentology*, 40: 1039-1067.
- Santo A., Ascione A., Di Crescenzo G., Miccadei E., Piacentini T. and Valente E.; 2014: Tectonic-geomorphological map of the middle Aterno River valley (Abruzzo, Central Italy), *J. Maps*, 10(3), 365-378.
- Sartori R., 1990. The main results of ODP Leg 107 in the frame of Neogene to Recent geology of the PeriTyrrhenian areas. In: A. Kastens & K.J. Mascle, et al. (Eds.): *Proceedings of ODP, Scientific Results*, 107, College Station, TX (Ocean Drilling Program), 715-730.
- Sartori R., 2003. From seafloor to deep mantle: architecture of the Tyrrhenian backarc basin. In: Marani, M., Gamberi, F., Bonatti, E. (Eds.), *Memorie Descrittive Della Carta Geologica d'Italia*, 64, 194 pp.
- Savage J. C., Svarc J. L., 1997, Postseismic deformation associated with the 1992 $M_w=7.3$ Landers earthquake, southern California. *Journal of Geophysical Research*, Volume 102, Issue B4, Pages 7565-7577. <https://doi.org/10.1029/97JB00210>
- Savelli C., Schreider A.A., 1991. The opening processes in the deep Tyrrhenian basins of Marsili and Vavilov, as deduced from magnetic and chronological evidence of their igneous crust. *Tectonophysics* 190, 119-131.
- Scandone P., 1972. Studi di geologia lucana: carta dei terreni della serie calcareo-silico-marnosa e note illustrative. *Bollettino della Società dei Naturalisti in Napoli*, 81, 225-300.
- Schettino A., Turco E., 2011. Tectonic history of the western Tethys since the Late Triassic. *Geological Society of America Bulletin*, 123, 89-105.
- Schiattarella M., Torrente M.M., Russo F., 1994. Analisi strutturale ed osservazioni morfostratigrafiche nel bacino del Mercure (confine calabro-lucano). *Il Quaternario*, 7, 613-626.
- Schumm S.A., Dumont, J.F., Holbrook, J.M., 2002. *Active tectonics and alluvial rivers*. Cambridge University Press.
- Scognamiglio, L., E. Tinti, A. Michelini, D.S. Dreger, A. Cirella, M. Cocco, S. Mazza and A. Piatanesi; 2010: Fast determination of moment tensors and rupture history: What has been learned from the 6 April 2009 L'Aquila earthquake sequence. *Seismol. Res. Lett.*, 81, 892–906, doi:10.1785/gssrl.81.6.892.
- Serpelloni, E., Anzidei, M., Baldi, P., Casula, G., Galvini, A., 2005. Crustal velocity and strain rate fields in Italy and surrounding regions: new results from the analysis of 22 permanent and non-permanent GPS networks. *Geophysical Journal International*, 161, 861–880.
- Serva, L., 1985, The earthquake of September 8, 1694 in Campania–Lucania: Atlas of Iseismal Maps of Italian Earthquakes, vol. 2A. CNR-PFG.
- Serva, L., Esposito, E., Guerrieri, L., Porfido, S., Vittori, E. and Comerci, V., 2007, Environmental effects from five historical earthquakes in southern Apennines (Italy) and macroseismic intensity assessment: Contribution to INQUA EEE Scale Project: *Quaternary International*, 173–174, 30–44.
- Shiner P., Beccacini A., Mazzoli S., 2004. Thin-skinned versus thick-skinned structural models for Apulian Carbonate Reservoirs: constraints from the Val D'Agri Fields: *Marine and Petroleum Geology*, 21, 805-827.
- Siddall M., Rohling E.J., Almogi-Labin A., Hemleben Ch., Melschner D., Schmelzer I., Smeed, D.A. 2003. Sea-level fluctuations during the last glacial cycle. *Nature* 423, 853–858.
- Spakman W., Wortel M.J.R., 2004. A tomographic view on western Mediterranean geodynamics. In: W. Cavazza, F.M. Roure, W. Spakman, G.M. Stampfli and P.A. Ziegler (eds.) *The TRANSMED Atlas - the Mediterranean Region from Crust to Mantle*, pp. 31-52. SpringerVerlag, Berlin.

- Speranza F., Chiappini M., 2002 Thick-skinned tectonics in the external Apennines, Italy: New evidence from magnetic anomaly analysis. *Journal of Geophysical Research*, 107, 2290.
- Spina V., Tondi E., Galli P., Mazzoli S., 2011. Complex basin development in a wrench-dominated back-arc area: Tectonic evolution of the Crati Basin, Calabria, Italy. *Journal of Geodynamics*, 51, 90-109, doi:10.1016/J.JOG.2010.05.003.
- Spina V., Tondi E., Galli P., Mazzoli S., Cello G., 2008. Quaternary fault segmentation and interaction in the epicentral area of the 1561 earthquake (Mw=6.4), Vallo di Diano, southern Apennines, Italy. *Tectonophysics*, 453, 233-245, doi:10.1016/J.TECTO.2007.06.012.
- Steckler M.S., Piana Agostinetti, N., Wilson C.K., Roselli P., Seeber L., Amato A., Lerner-Lam A., 2008. Crustal structure in the Southern Apennines from teleseismic receiver functions. *Geology*, 36 (2), 155–158.
- Stemberk J., Dal Moro G.C., Stemberk J., Blahůt J., Coubal M., Košťák B., Zambrano M., Tondi E., 2018. Strain monitoring of active faults in the central Apennines (Italy) during the period 2002–2017. *Tecto*, <https://doi.org/10.1016/j.tecto.2018.10.033>
- Stramondo S., Tesauro M., Briole P., Sansosti E., Salvi S., Lanari R., Anzidei M., Baldi P., Fornaro G., Avallone A., Buongiorno M.F., Franceschetti G. and Boschi E.; 1999: The September 26, 1997 Colfiorito, Italy, earthquakes: modeled coseismic surface displacement from SAR interferometry and GPS. *Geophys. Res. Lett.*, 26(7), 883-886.
- Stramondo S., Vannoli P., Cannelli V., Polcari M., Melini D., Samsonov S., Moro M., Bignami C., Saroli M., 2014, X- and C-Band SAR Surface Displacement for the 2013 Lunigiana Earthquake (Northern Italy): A Breached Relay Ramp? *IEEE Journal of selected topics in applied Earth Observations and Remote Sensing*, vol. 7, no. 7.
- Strozzi, T., Wegmuller, U., Tosi, L., Bitelli, G., & Spreckels, V. (2001). Land subsidence monitoring with differential SAR interferometry. *Photogrammetric engineering and remote sensing*, 67(11), 1261-1270.
- Teatini, P., Tosi, L., & Strozzi, T. (2011). Quantitative evidence that compaction of Holocene sediments drives the present land subsidence of the Po Delta, Italy. *Journal of Geophysical Research: Solid Earth*, 116(B8).
- Tizzani P., Berardino P., Casu F., Euillades P., Manzo M., Ricciardi G.P., Zeni G. and Lanari R.; 2007: Surface deformation of Long Valley caldera and Mono Basin, California, investigated with the SBAS-InSAR approach. *Rem. Sens. Environ.*, 108(3), 277-289.
- Tobler W. R., 1970, A Computer Movie Simulating Urban Growth in the Detroit Region. *Economic Geography*, 46:sup1, 234-240, DOI: 10.2307/143141
- Tofani V., Segoni S., Agostini A., Catani F. and Casagli N.; 2013: Technical Note: Use of remote sensing for landslide studies in Europe. *Nat. Hazards Earth Syst. Sci.*, 13, 299-309.
- Tondi, E., Cello, G., Mazzoli, S., 1997. Strutture sismogenetiche in Appennino Centrale: potenziale sismico, analisi frattale e processi di crescita. *Il Quaternario* 10 (2), 409-414.
- Tortorici L., 1975. Osservazioni geologiche sul flysch di S. Bartolomeo nell'area compresa tra il fiume Trigno e Benevento (Italia meridionale). *Memorie della Società Geologica Italiana*, 94, 1791-1809.
- Tozer R.S.J., Butler R.W.H., Chiappini M., Corrado S., Mazzoli S., Speranza F., 2006. Testing thrust tectonic models at mountain fronts: where has the displacement gone? *J. Geol. Soc.* 162, 1–14.
- Turco E., Macchiavelli C., Mazzoli S., Schettino A., Pierantoni P.P., 2012. Kinematic evolution of Alpine Corsica in the framework of Mediterranean mountain belts. *Tectonophysics*, doi:10.1016/J.TECTO.2012.05.010.
- Turrini C, Rennison P., 2004. Structural Style from the Southern Apennines' Hydrocarbon Province-An Integrated View. *Thrust Tectonics and Petroleum Systems* (Ed. by K.R. Mc Clay). *AAPG Mem.*, 82, 558-578.

- Vai G.B., Martini I.P. (eds.), 2001. *Anatomy of an Orogen: the Apennines and Adjacent Mediterranean Basins*: Dordrecht, Kluwer Academic Publishers
- Valensise, G., Pantosti, D., 2001. Seismogenic faulting, moment release patterns and seismic hazard along the central and southern Apennines and Calabrian Arc, in Vai, G.B., Martini, I.P., eds., *Anatomy of an Orogen: The Apennines and Adjacent Mediterranean Basins*. Kluwer Academic Publishing, Dordrecht, 495– 512.
- Valoroso L., Chiaraluce L., Piccinini D., Di Stefano R., Schaff D. and Waldhauser F.; 2013: Radiography of a normal fault system by 64,000 high-precision earthquake locations: The 2009 L'Aquila (central Italy) case study. *J. Geophys. Res.: Solid Earth*, 118(3), 1156-1176, doi:10.1002/jgrb.50130.
- Van der Meulen M.J., Buitert S.J.H., Meulenkamp J.E., Wortel M.J.R., 2000. An early Pliocene uplift of the central Apenninic foredeep and its geodynamic significance. *Tectonics*, 19, 300–313.
- Van der Meulen M.J., Kouwenhoven T.J., Van der Zwaan G.J., Meulenkamp J.E., Wortel M.J.R., 1999. Late Miocene uplift in the Romagnan Apennines and the detachment of subducted lithosphere. *Tectonophysics*, 315, 319–335.
- Van der Meulen M.J., Meulenkamp, J.E. & Wortel, M.J.R. (1998) Lateral shifts of Apenninic foredeep depocentres reflecting detachment of subducted lithosphere. *Earth Planet. Sci. Lett.*, 154, 203–219.
- Ventura G., Di Giovambattista R., 2013. Fluid pressure, stress field and propagation style of coalescing thrusts from the analysis of the 20 May 2012 ML5.9 Emilia earthquake (Northern Apennines, Italy). *Terra Nova* 25, 72–78, <http://dx.doi.org/10.1111/ter.12007>.
- ViDEPI, 2009. Progetto Visibilità Dati Esplorazione Petrolifera in Italia, © 2009–2010 Ministero dello Sviluppo Economico UNMIG, Società Geologica Italiana, Assomineraria. <http://unmig.sviluppoeconomico.gov.it/videpi/>.
- Vilardo G., Ventura G., Terranova, C., Matano F. and Nardò S.; 2009: Ground deformation due to tectonic, hydrothermal, gravity, hydrogeological, and anthropic processes in the Campania Region (Southern Italy) from Permanent Scatterers Synthetic Aperture Radar Interferometry. *Rem. Sens. Environ.*, 113, 197-212.
- Vitale S., Ciarcia S., Mazzoli S., Iannace A. & Torre M. (2010) - Structural analysis of the 'Internal' Units of Cilento, Italy: new constraints on the Miocene tectonic evolution of the southern Apennine accretionary wedge. *Comptes Rendus - Geoscience*, 342, 475-482. doi:10.1016/J.CRTE.2010.03.005.
- Vitale S., Ciarcia S., Mazzoli S., Zaghloul M.N., 2011. Tectonic evolution of the 'Liguride' accretionary wedge in the Cilento area, southern Italy: A record of early Apennine geodynamics. *Journal of Geodynamics*, 51, 25-36, doi:10.1016/J.JOG.2010.06.002.
- Vitale S., Dati F., Mazzoli S., Ciarcia S., Guerriero V., Iannace A., 2012. Modes and timing of fracture network development in poly-deformed carbonate reservoir analogues, Mt. Chianello, southern Italy. *Journal of Structural Geology*, 37, 223-235, doi:10.1016/J.JSG.2012.01.005
- Vittori E., Cavinato G.P., Miccadei E., 1995. Active faulting along the northeastern edge of the Sulmona basin, central Apennines, Italy. In: Serva, L., Slemmons, D.B. (Eds.), *Perspectives in Paleoseismology*, Bulletin of the Association of Engineering Geologists. Special Publication, 6, 115–126.
- Vittori E., Maschio L., Ferreli L., Michetti A.M., Serva L., 1997. Carta e base di dati delle faglie capaci per l'Italia centro-meridionale: presentazione e stato di avanzamento del progetto ITHACA. *Italian Journal of Quaternary Sciences*, 10(2), 1997, 305-312.
- Vittori, E., Deiana, G., Esposito, E., Ferreli, L., Marchegiani, L., Mastrolorenzo, G., Michetti, A.M., Porfido, S., Serva, L., Simonelli, A.L., Tondi, E., 2000. Ground effects and surface faulting in the September–October 1997 Umbria–Marche (Central Italy) seismic sequence. *Journal of Geodynamics* 29, 535– 564.

- Walters R.J., Elliott J.R., D'Agostino N., England P.C., Hunstad I., Jackson J.A., Parsons B., Phillips R.J. and Roberts G.; 2009: The 2009 L'Aquila earthquake (central Italy): A source mechanism and implications for seismic hazard. *Geophys. Res. Lett.*, 36(17), <https://doi.org/10.1029/2009GL039337>.
- Ward S.N. 1998. On the consistency of earthquake moment release and space geodetic strain rates: Europe. *Geophysical Journal International*, 135, 1011–1018.
- Wasowski J., Ferretti A., Colesanti C., 2007a, Space-Borne SAR Interferometry for Long Term Monitoring of Slope Instability Hazards. *Proceeding of the First North American landslide Conference*, Vail, USA.
- Watson D. F. and Philip G. M., 1985, A Refinement of Inverse Distance Weighted Interpolation. *Geoprocessing* 2:315–327.
- Werner C., Wegmuller U., Strozzi T., Wiesmann A., 2003, Interferometric Point Target Analysis for Deformation Mapping, *Geoscience and Remote Sensing Symposium*, 2003. IGARSS '03. Proceedings. 2003 IEEE International. Volume: 7 DOI: 10.1109/IGARSS.2003.1295516
- Westaway, R. and Jackson, J., 1984, Surface faulting in the southern Italian Campania-Basilicata earthquake of 23 November 1980: *Nature*, 312, 436–438.
- Westaway, R. and Jackson, J., 1987, The earthquake of 1980 November 23 in Campania-Basilicata (Southern Italy): *Geophysical Journal of the Royal Astronomical Society*, 90, 375–443.
- Westaway, R., 1992, Seismic moment summation for historical earthquakes in Italy: tectonic implications: *Journal of Geophysical Research*, 97, 15437– 15464.
- Whittaker, A.C., Attal, M., Cowie, P.A., Tucker, G.E., Roberts, G.P., 2008. Decoding temporal and spatial patterns of fault uplift using transient river long profiles. *Geomorphology*, 100, 506–526.

Aknowledgements

A big thank you to the Earth to do what it does.